

**NON-STATISTICAL FLUCTUATION OF SINGLY
CHARGED PARTICLES PRODUCED IN ^{16}O -Ag/Br
INTERACTION AT 200A GeV/c**

**A thesis submitted to the University of North Bengal
in partial fulfilment of the requirements for the degree of
DOCTOR OF PHILOSOPHY
in Physics**

**By
Sanjib Kumar Manna**

SUPERVISOR

Prof. Amitabha Mukhopadhyay

CO-SUPERVISOR

Prof. Prabir Kumar Haldar

UNIVERSITY OF NORTH BENGAL

December 2021

DECLARATION

I declare that the thesis entitled, NON-STATISTICAL FLUCTUATION OF SINGLY CHARGED PARTICLES PRODUCED IN $^{16}\text{O-Ag/Br}$ INTERACTION AT 200A GeV/c, has been prepared by me under the guidance of Prof. Amitabha Mukhopadhyay, Department of Physics, University of North Bengal, and Prof. Prabir Kumar Haldar, Department of Physics, Cooch Behar Panchanan Barma University. No part of this thesis has been formed on the basis of any previously awarded degree or fellowship.

Date: 08/12/2021

Sanjib Kr. Manna.

Sanjib Kumar Manna

Department of Physics
University of North Bengal
Siliguri 734 013, Darjeeling, India

CERTIFICATE

This is to certify that the work contained in the thesis titled "NON-STATISTICAL FLUCTUATION OF SINGLY CHARGED PARTICLES PRODUCED IN ^{16}O -Ag/Br INTERACTION AT 200A GeV/c" submitted by Mr. Sanjib Kumar Manna, has been carried out in the Department of Physics, University of North Bengal under our supervision. This work has not been submitted elsewhere for any degree/diploma.

Amitabha Mukhopadhyay
Prof. Amitabha Mukhopadhyay
Supervisor

Department of Physics
University of North Bengal
Siliguri 734013, Darjeeling
West Bengal, India

Prabir Kumar Haldar
Prof. Prabir Kumar Haldar
Co-Supervisor

Department of Physics
Cooch Behar Panchanan Barma University
Cooch Behar 736101, West Bengal, India

Document Information

Analyzed document	Sanjib Kumar Manna_physics.pdf (D120440143)
Submitted	2021-11-30T08:06:00.0000000
Submitted by	University of North Bengal
Submitter email	nbuplg@nbu.ac.in
Similarity	2%
Analysis address	nbuplg.nbu@analysis.orkund.com

Sources included in the report

W	URL: https://www.researchgate.net/publication/231155574_Multifractal_moments_of_particles_produced_in_32S-AgBr_interaction_at_200_A_GeVc Fetched: 2020-01-02T11:48:14.7600000		12
W	URL: http://www.cs.fredonia.edu/singh/PhysicaA-2015.pdf Fetched: 2021-07-05T08:15:25.0700000		35
W	URL: https://daneshyari.com/article/preview/973840.pdf Fetched: 2021-07-05T08:15:24.9470000		6
W	URL: https://nl.wikipedia.org/wiki/Kettingbreuk Fetched: 2021-11-30T08:17:00.0000000		2

NON-STATISTICAL FLUCTUATION OF SINGLY CHARGED PARTICLES
PRODUCED IN ^{16}O -Ag/Br INTERACTION AT 200A GeV/c

ABSTRACT

One of the major objectives of doing research in the field of high-energy heavy-ion physics is to study the properties of nuclear matter under extreme thermodynamic conditions. It is generally held that nucleons, i.e. color neutral baryons, if and when subjected to very high temperature and/or pressure, are going to lose their individual identities and melt into a soup of more fundamental constituents of matter namely, the quarks and gluons. Depending upon the initial conditions of the collision, a quark-gluon matter may equilibrate to form a transient state called the quark-gluon plasma (QGP). With evolving time such a state expands and cools down, and ultimately freezes out to form a number of color neutral hadrons in the final state of the collision. It is claimed that a strongly interacting quark-gluon state at a high-temperature and low baryon density, has already been created in the heavy-ion experiments held at the Relativistic Heavy-ion Collider (RHIC), and Large Hadron Collider (LHC). It is however not the case that a higher energy will necessarily favor a QGP formation. In this regard issues like baryon stopping and nuclear transparency have serious implications. It has been speculated that a QGP at a high baryon density can be created even at a lower temperature than that produced in the RHIC/LHC. In this context experiments involving lower collision energies and analysis of the data obtained thereof have their importances.

The present thesis is based on some results obtained from a series of analysis made on the local structures of the phase space distribution of singly charged particles produced in ^{16}O -Ag/Br interaction at an incident momentum $p_{\text{lab}} = 200A$ GeV/c. The experimental data used in this investigation have been collected from a nuclear emulsion experiment (EMU-08) held in the year 1987 at the Super-Proton Synchrotron of CERN, Geneva. We have systematically examined various issues related to multiparticle production like, (i) the dynamical fluctuations present in the pseudorapidity (η) and azimuthal angle (φ) distributions, (ii) the self-similar and/or self-affine behavior of such fluctuations with diminishing phase space resolution, (iii) correlations between particles present in different phase space points, (iv) (multi)fractal nature of the dynamical fluctuations, (v) presence of unusual structures in the η and φ -distributions and cluster formation, and (vi) correlation among particles produced in the forward and backward η -hemispheres. The experimental results have been systematically compared with a microscopic transport model known as the ultra-relativistic quantum molecular dynamics (UrQMD). In addition, we have implemented a charge reassignment

algorithm that mimics the Bose-Einstein Correlation (BEC) between identical mesons as an after burner to the UrQMD output. On several occasions we have also compared the experimental results with those obtained from the $^{32}\text{S-Ag/Br}$ interaction at $p_{\text{lab}} = 200A$ GeV/c. We summarize below the contents of different chapters presented in this thesis.

In **Chapter 1** we have qualitatively reviewed various aspects of high-energy nucleus-nucleus (AB) collisions. The importance of AB collision in the context of QGP formation in laboratories, gross physical properties of the QGP along with its astrophysical and cosmological relevances have been summarily discussed. The kinematic variables that are used to formulate the dynamics of an AB collision are systematically introduced. Different stages of the space-time evolution of AB collision are serially outlined. The QCD phase diagram (*temperature – chemical potential* plot) has been explained in the context of a QGP \rightarrow hadron transition and some other phases that may be created in AB collisions under different kinematic conditions. The global scenario of AB collision experiments is summarily discussed. Some general features of the QGP, like its thermodynamics, hydrodynamics, observables that can be used to diagnose the QGP formation etc., are summarily described. Major experimental signatures of the QGP formation in high-energy AB collisions are summarily described. A review of the experimental results on global features of multiparticle emission in AB collisions has been summarized.

In **Chapter 2** we have discussed some salient features of the nuclear emulsion technique, like the scanning of emulsion plates, track formation and track structure, track selection and event selection criteria, and angle measurement etc.. The present investigation is confined only to the distributions of shower tracks, i.e. singly charged particles moving with relativistic speed, produced in the $^{16}\text{O-Ag/Br}$ interaction at $p_{\text{lab}} = 200A$ GeV/c. Gross characteristics of the experimental data, like the η -distribution, φ -distribution and distribution of the pseudorapidity density $\rho = N_{ev}^{-1} (dn_s/d\eta)$ of the shower tracks coming from $^{16}\text{O-Ag/Br}$ interaction, are presented in this chapter. For comparison, similar results obtained from the $^{32}\text{S-Ag/Br}$ interaction at the same incident momentum per nucleon have also been incorporated. A charge reassignment algorithm that can mimic the Bose-Einstein correlation into the UrQMD output has been described. Distributions obtained from the event samples generated by the UrQMD and modified by the charge reassignment algorithm, have also been shown for comparison. The simulation results reasonably well match the gross features of corresponding experiments.

Chapter 3 presents the results obtained from an intermittency analysis of the spatial fluctuations of shower track densities in the $^{16}\text{O-Ag/Br}$ interaction at $p_{\text{lab}} = 200A$ GeV/c. The intermittency analysis is performed by evaluating the scaled factorial moments (SFMs) in the η -space, in the φ -space and in the (η, φ) -plane. Our analysis shows that dynamical components in particle density fluctuations are present in η , φ and (η, φ) spaces. We find

that in one dimension such fluctuations are self-similar in nature, while the same is self-affine in two-dimension. Factorial correlators, cumulant moments and oscillatory moments are some other issues that are closely related with the intermittency analysis. Our results on factorial correlators indicate that short range correlations among the shower tracks are present not only in narrow phase space intervals but also in intervals that are separated by a distance along the pseudorapidity axis. The results are consistent with the predictions of a simple intermittency (α) model. Oscillatory moments on the other hand are derived from the factorial cumulants, where correlations present in every higher order moment are made free from those coming from the corresponding lower order moments. The observation is consistent with the prediction of a QCD parton shower model. In almost all cases the UrQMD simulations can not match the experimental results on intermittency and related issues. Inclusion of BEC in the simulation does not significantly improve the situation either.

While most of the SFMs calculated for individual events are not large valued, SFMs with very large values are not very rare to find out. These large valued SFMs result from high multiplicities in narrow phase space intervals. We have calculated the SFMs on an event-by-event basis and studied their fluctuations for the ^{16}O -Ag/Br event sample in terms of the erraticity moments and erraticity parameters. The results obtained from erraticity analysis are also incorporated in **Chapter 3**. We find that the event space fluctuations of the SFMs are chaotic in nature, both in experiment and in simulation. In this regard the ^{16}O -Ag/Br and ^{32}S -Ag/Br experimental data do not behave very differently. The simulation produces significantly smaller values of chaoticity parameter than the respective experiment.

We have characterized the self-similar nature of η -density of particles in terms of the multifractal moments and presented the results obtained from this analysis in **Chapter 4**. Several methods of analysis like (i) Hwa's moments, (ii) Takagi's moments, (iii) the multifractal detrended methods, and (iv) the visibility graph & sandbox algorithm have been adopted in our analysis. We find that our experimental data on the ^{16}O -Ag/Br and ^{32}S -Ag/Br interactions can be described in terms of a set of regularly behaving multifractal parameters, but so can be the simulated data too. If multifractality is really an outcome of some kind of hadronic or partonic cascading process, then this should not be the case. We have noticed that none of these methods can filter out the statistical noise present in the experimental data. However, the outcome of our visibility graph (VG) analysis is quite different from those obtained from the other methods. In the VG method statistically significant differences in the multifractal spectra between the experiment and respective simulation are observed. Large fluctuations in the density values that are not very frequently available, are multifractal in nature, whereas more abundant small fluctuations are found to be almost monofractal.

In **Chapter 5** we have looked for clusters of particles in the η and φ -distributions of the shower tracks. Presence of ring and/or jet-like structures is predicted as a possible outcome of Cerenkov gluon emission and/or Mach shock wave formation in the nuclear/partonic medium. Shower track emission data in the $^{16}\text{O-Ag/Br}$ and $^{32}\text{S-Ag/Br}$ interactions at $200A$ GeV/c are analyzed to find out jet/ring-like structures. Jet structures restricted within narrow regions of (η, φ) are found in our data. Such structures are more pronounced in the $^{32}\text{S-Ag/Br}$ than in the $^{16}\text{O-Ag/Br}$ interaction. In this chapter we have also presented a continuous wavelet analysis of the shower track η -distributions. Presence of cluster structures in the experimental data is confirmed from this analysis. The scale and location of such clusters are determined. Statistically significant differences between the experiment and respective UrQMD simulation are found.

In **Chapter 6** short and long-range correlations in the shower track emission data have been examined. Relative covariances of shower track multiplicities in the η -windows located in the forward and backward hemispheres are measured by varying the separation between the windows and the window size. Evidences of short range correlations have been confirmed from the study, which could not be reproduced either by the UrQMD or the UrQMD+BEC simulations. Such correlations are more pronounced in the $^{32}\text{S-Ag/Br}$ data than in the $^{16}\text{O-Ag/Br}$ data. This chapter also presents a study on a roughness parameter associated with the η -distributions of the shower tracks. Presence of large particle concentrations within narrow η -intervals is verified by using this method. The data have been analyzed in terms of the ω -measure and Φ -measure. The results indicate the presence of non-Poissonian multiplicity distributions in narrow η -intervals, and presence of short range correlations. We find that the AB collisions considered in this analysis are not mere incoherent superpositions of many nucleon-nucleon collisions.

In memory of my Grandparents

Acknowledgments

While preparing this thesis I cannot resist myself from walking down the memory lane. I started this research in the year 2009 as a Junior Research Fellow in a project funded by the Department of Science and Technology (DST), Govt. of India. I gratefully acknowledge the financial support that I received from the DST. Over the years I have come across many persons from whom I have benefited a lot directly or indirectly. I would like to recall their contributions.

First of all I would like to express my deepest gratitude to my thesis supervisors, Prof. Amitabha Mukhopadhyay of Physics Department, University of North Bengal, and Prof. Prabir Kumar Haldar of Physics Department, Cooch Behar Panchanan Barma University, for their guidance, encouragement and motivation towards my research. I am immensely indebted to Dr. Provash Mali, Department of Physics, University of North Bengal, for his all encompassing support which helped me to continue this research and prepare this thesis. His contribution will remain unforgettable. I would like to thank all the members of the Department of Physics, University of North Bengal, for providing a suitable academic environment throughout my research period. I express my deepest sense of gratitude to Late Professor P. L. Jain of the State University of New York at Buffalo, USA for providing us the emulsion plates and associated information. I also like to thank my colleagues Dr. Malay Kumar Ghosh, Mr. Soumya Sarkar and Mr. Somnath Ghosh of the Physics Department of North Bengal University for their help and support. I like to thank all the faculty members and supporting staffs of Chakdaha College, Nadia for their encouragement and support. I also like to express my gratitude to all my teachers in the School, College and University where I studied, especially to Mr. Sankar Chandra Khatua, my childhood teacher, and Dr. Swapan Kumar Das for their inspiration and help in all respect. Last but not the least, I must acknowledge my family for their constant moral support. At the end, I apologize to the persons whose names could not be acknowledged due to lack of space, though they have a significant contribution in this journey.

Sanjib Kr. Manna

Sanjib Kumar Manna

Date: 8/12/2021

Contents

Declaration	i
Certificate	ii
Abstract	iv
Acknowledgments	ix
List of Tables	xiii
List of Figures	xv
1 A brief review of high-energy nuclear collisions	1
1.1 Introduction	1
1.2 Nucleus-nucleus collision at high-energy	5
1.2.1 Kinematics of high-energy interaction	8
1.2.2 Geometry of nucleus-nucleus collision	12
1.2.3 Stopping in nucleus-nucleus collision	15
1.2.4 Evolution of nucleus-nucleus collision	18
1.2.5 Thermodynamics of the fireball	19
1.2.6 Hydrodynamics of the fireball	23
1.2.7 QCD phase diagram	28
1.3 QGP signals	30
1.4 Multiparticle production	34
1.4.1 Multiplicity distribution	34
1.4.2 Pseudorapidity distribution	36
1.4.3 Transverse momentum distribution	37
1.4.4 Azimuthal angle distribution	38
2 Experiment and simulation	45
2.1 Introduction	45
2.2 Properties of emulsion tracks	46
2.3 Scanning of emulsion plates	50
2.4 Measurement methods	51
2.5 Data characteristics	54

2.5.1	Event selection	55
2.5.2	Track classification	55
2.6	Advantages and disadvantages of emulsion experiments	56
2.7	Simulation	58
2.7.1	Modeling Bose-Einstein correlation	61
2.7.2	Sampling the simulated events	64
2.8	Basic distributions	65
3	Intermittency and related issues	69
3.1	Introduction	69
3.2	Literature review	71
3.3	Scaled factorial moments	73
3.3.1	Intermittency in $1d$	76
3.3.2	Intermittency in $2d$	83
3.4	Factorial correlators	88
3.5	Oscillatory moments	92
3.6	Erraticity moments	94
3.7	Summary	102
4	Multifractality and related issues	109
4.1	Introduction	109
4.2	Literature review	111
4.3	Hwa's multifractal moment	113
4.4	Takagi's multifractal moment	118
4.5	Detrended multifractal moments	121
4.5.1	Detrended methods and multifractal parameters	124
4.5.2	Results of MFDFA and MFDMA methods	125
4.6	Visibility graph and sandbox algorithm	131
4.6.1	Visibility graph	131
4.6.2	Degree distribution of visibility graph	133
4.6.3	Sandbox method of multifractality analysis	136
4.7	Summary	145
5	Ring-jet structure and wavelet analysis	151
5.1	Introduction	151
5.2	Literature review	153
5.3	Ring and jet-like structures	154
5.4	Wavelet analysis	161
5.5	Summary	169
6	Multiplicity fluctuation and forward-backward multiplicity correlation	172
6.1	Introduction	172
6.2	Literature review	173

6.3	Roughness in η -distribution	175
6.4	Forward-backward multiplicity correlation	177
6.5	ω -measure	182
6.6	Φ -measure	183
6.7	Summary	186
Concluding remarks		190
List of publications		196

List of Tables

1.1	Accelerator facilities in relativistic heavy-ion physics..	7
2.1	Chemical composition of standard emulsion.	46
3.1	The values of $1d$ intermittency exponent for order $q = 2 - 6$ in the $^{16}\text{O-Ag/Br}$ interaction at $200A$ GeV/c. The errors are of statistical origin.	78
3.2	The values of $1d$ intermittency exponent for order $q = 2 - 6$ in $^{32}\text{S-Ag/Br}$ interaction at $200A$ GeV/c. The errors are of statistical origin only.	79
3.3	Multifractal specific heat C calculated from the SFM analysis. The C values evaluated at different q -regions are specified.	82
3.4	$2d$ self-affine intermittency indices for the $^{16}\text{O-Ag/Br}$ interaction at $200A$ GeV/c. The errors are statistical only.	84
3.5	$2d$ self-affine intermittency indices for the $^{32}\text{S-Ag/Br}$ interaction at $200A$ GeV/c. The errors are statistical only.	84
3.6	Intermittency strength based on a random cascading α -model and Rényi dimensions for $^{16}\text{O-Ag/Br}$ and $^{32}\text{S-Ag/Br}$ interactions in $2d$. The errors are of statistical origin.	86
3.7	Values of fit parameters of $\ln\langle F_2^{(2)} \rangle$ against $\ln M$ plot by using a quadratic function like $f(x) = ax^2 + bx + c$ for the $^{16}\text{O-Ag/Br}$ interaction. The errors are of statistical origin.	88
3.8	Values of fit parameters of $\ln\langle F_2^{(2)} \rangle$ against $\ln M$ plot by using a quadratic function like $f(x) = ax^2 + bx + c$ for the $^{32}\text{S-Ag/Br}$ interaction. The errors are of statistical origin.	89
3.9	The ϕ_{pq} exponents of the FC scaling for several different combinations of (p, q) for the $^{16}\text{O-Ag/Br}$ interaction.	91
3.10	The ϕ_{pq} exponents of the FC scaling for several different combinations of (p, q) for the $^{32}\text{S-Ag/Br}$ interaction.	91
3.11	The values of slope parameter (δ) obtained from the ϕ_{pq} vs $(p \cdot q)$ plot.	92
3.12	Values of b , $\tilde{\psi}(2, 2)$ & $\tilde{\mu}_2$ for the experiment, the UrQMD and the UrQMD+BEC data.	99
3.13	Erraticity parameters in the $^{16}\text{O-Ag/Br}$ interaction at $200A$ GeV/c.	101
3.14	Erraticity parameters in the $^{32}\text{S-Ag/Br}$ interaction at $200A$ GeV/c.	102

4.1	The values of the Lévy stable index μ obtained at two different regions of q for the ^{16}O -Ag/Br and ^{32}S -Ag/Br interactions at $200A$ GeV/c.	117
4.2	The values of information dimension D_1 obtained from the T_q moments for the ^{16}O -Ag/Br and ^{32}S -Ag/Br interactions at $200A$ GeV/c.	120
4.3	The values of multifractal specific heat C calculated from the F_q , G_q and T_q moment analysis for the ^{16}O -Ag/Br and ^{32}S -Ag/Br interactions at $200A$ GeV/c.	121
4.4	The values of generalized Hurst exponent $h(q = 2)$	128
4.5	The centroid (α_0), the width ($\Delta\alpha$) and the skewness (r) parameters of the multifractal spectra for the studied interactions.	129
4.6	The ML estimated values of the exponent γ , see Equation (4.42).	136
4.7	The peak position α_0 , the FWHM $\Delta\omega$ and the asymmetry parameter r of the multifractal spectra shown in Figure 4.24.	144
6.1	The values of $\langle\gamma_k^2\rangle$ and $\sigma(\gamma_k^2)$ for the ^{16}O - and ^{32}S -induced Ag/Br interactions at $200A$ GeV/c. The values are calculated for pseudorapidity window $\delta\eta = 0.2$ and 0.1	177

List of Figures

1.1	A schematic of the time history of the universe [3].	2
1.2	Chromoelectric flux between a $q\bar{q}$ pair [13].	4
1.3	Schematic of a nucleus-nucleus collision [25].	12
1.4	Multiplicity distribution and centrality of AB collisions.	13
1.5	Stopping in nucleus-nucleus collisions.	17
1.6	Illustration of space-time evolution of an AB collision.	19
1.7	Sketch of QCD Phase Diagram [13].	29
2.1	Schematic of a secondary track geometry with respect to the projectile.	51
2.2	The Bose-Einstein correlation function $C_2(Q = q_{inv})$ for $\pi^- \pi^-$ pairs using the charge reassignment algorithm (left panel) and the weighting method (right panel). Gaussian fits are shown in each diagram. The figure is taken from ref. [32]	62
2.3	(a) η -distribution for an event in ^{16}O -Ag/Br interaction. (b) η -distribution for the ^{16}O sample compared with the UrQMD+BEC model simulation. The lower panel is same as in the upper panel but for the ^{32}S data. In all the cases the experimental distributions are fitted by a Gaussian distribution.	64
2.4	Distributions of φ (a) for ^{16}O -Ag/Br and (b) for ^{32}S -Ag/Br interactions. The UrQMD+BEC simulations are shown with the experiments.	65
2.5	Distributions of local pseudorapidity density of shower tracks for ^{16}O -Ag/Br (Figure (a, b)) and ^{32}S -Ag/Br (Figure (c, d)) interaction at 200A GeV/c. Two region is chosen for distribution, $\eta_0 - 1 < \eta < \eta_0$ and $\eta_0 < \eta < \eta_0 + 1$ for $\delta\eta=0.2$	66
3.1	Variation of the event averaged SFM of shower tracks with phase space partition number M in the η -space for the ^{16}O -Ag/Br interaction at 200A GeV/c. Best fitted straight lines to the data points are shown.	76
3.2	Same as in Figure 3.1 but in φ -space.	76
3.3	Normalized intermittency exponents as a function of order number q for the ^{16}O -Ag/Br interaction at 200A GeV/c. Lines joining points are drawn to guide the eye.	79
3.4	The same as in Figure 3.3 but for the ^{32}S -Ag/Br interaction at 200A GeV/c.	80

3.5	(a) Plot of λ_q versus q . The no-intermittency line corresponding to $\phi_q = 0$ is also shown. (b) Plot of intermittency strength α_q with q . (c) Plot of generalized Rényi dimension D_q with $\ln q/(q - 1)$. The curves are drawn to guide the eye. The plots are for the ^{16}O -Ag/Br interaction at 200A GeV/c.	81
3.6	The same as in Figure 3.5 but for the ^{32}S -Ag/Br interaction at 200A GeV/c.	81
3.7	The scaling of 2d SFMs for $q = 2 - 6$ in ^{16}O -Ag/Br interaction at 200A GeV/c. The solid curves are drawn to guide the eye.	83
3.8	A schematic of partitioning 2d phase space for (a) $H = 1$ corresponds to equal partitioning, (b) $H > 1$ corresponds to finer division along the vertical direction, and (c) $H < 1$ corresponds to finer division along the horizontal direction.	84
3.9	Two-dimensional SFM $\ln\langle F_2^{(2)} \rangle$ plotted against $\ln M$ for different Hurst parameters in the ^{16}O -Ag/Br interaction at 200A GeV/c. The solid curves represent quadratic fit to the data points.	87
3.10	The same as in Figure 3.9 but for the ^{32}S -Ag/Br interaction at 200A GeV/c.	87
3.11	Plot showing the dependence of factorial correlators of different orders against correlation length for the ^{16}O -Ag/Br interaction at 200A GeV/c. Points represent (a) experimental values, (b)UrQMD values and (c)UrQMD+BEC values in η -space. For clarity correlators of successive orders are shifted by one unit along the vertical axis as shown in the diagram. Lines joining points are drawn to guide the eye.	90
3.12	Plot of ϕ_{pq} versus p,q in η -space according to the predictions of the α -model. The solid line is the best-fit straight line to the experimental values.	91
3.13	Plot showing independence of factorial correlators with respect to phase space partition size δX_η at fixed D for the ^{16}O -Ag/Br interaction at 200A GeV/c. The dotted lines are best fit straight lines to the data.	92
3.14	Oscillatory moments H_q for different widths of η interval. In each η interval, experiment, UrQMD and UrQMD+BEC results are plotted together. $H_q = 0$ is the horizontal solid line. The graph is for the ^{16}O -Ag/Br interaction at 200A GeV/c.	93
3.15	The same as in Figure 3.14 but for the ^{32}S -Ag/Br interaction at 200A GeV/c.	94
3.16	Distributions of F_2^e in the ^{16}O -Ag/Br interaction at 200A GeV/c for two different values of η space partition number (a) $M = 5$ and (b) $M = 10$	95
3.17	Erraticity moments $C_{p,q}$ plotted as functions of phase space partition number M for the ^{16}O -Ag/Br interaction. The solid curves are drawn to guide the eye.	97
3.18	Plot of $\ln C_{2,2}$ and Σ_2 with $\ln f(M) = \ln M^b$ for the ^{16}O -Ag/Br interaction. The lines represent best linear fits to the data points.	97
3.19	Plot of $\ln C_{p,2}$ with $\ln C_{2,2}$ for the ^{16}O -Ag/Br interaction. The best fitted straight lines are shown.	98

3.20	Variation of $\chi(p, q)$ with p for the $^{16}\text{O-Ag/Br}$ interaction. The curves represent the best quadratic fits.	98
3.21	Plot of Σ_q with $\ln M$ for the $^{16}\text{O-Ag/Br}$ interaction. The lines joining points are drawn to guide the eye.	100
3.22	Plot of Σ_q against Σ_2 for the $^{16}\text{O-Ag/Br}$ interaction. The lines represent best linear fits to the data points in the $M \leq 12$ region.	100
3.23	Plot of the entropy index $\tilde{\mu}_q$ against order number q calculated from (a) Equation (3.39) and (b) Equation (3.41) for the $^{16}\text{O-Ag/Br}$ interaction. Lines joining the data points are shown.	101
4.1	Multifractal G_q moment plotted with phase space partition number in $^{16}\text{O-Ag/Br}$ interaction at $200A$ GeV/c. Lines joining points are drawn to guide the eye.	114
4.2	(a) The order dependence of the mass exponent $\tau(q)$ and the Lipschitz-Hölder exponent $\alpha(q)$ and (b) the multifractal spectral function $f(\alpha)$ obtained from $^{16}\text{O-Ag/Br}$ interaction at $200A$ GeV/c.	115
4.3	Plots of $[q - 1 - \tau(q)^{\text{dyn}}]$, $[q - 1 - \tau(q)]$ and the intermittency exponent ϕ_q with order number q for $^{16}\text{O-Ag/Br}$ interaction at $200A$ GeV/c. In all the graphs lines joining points are drawn to guide the eye.	116
4.4	Plot of $\ln(B - \alpha)$ versus $\ln(1 - f(\alpha))$ for $^{16}\text{O-Ag/Br}$ interaction at $200A$ GeV/c. In all diagrams the dotted (solid) lines represent linear fits to the data points in the low (high)- q region.	117
4.5	Multifractal T_q moments plotted with the number of particles in phase space interval for $^{16}\text{O-Ag/Br}$ interaction at $200A$ GeV/c. The best fitted straight lines are shown in all diagrams.	119
4.6	Generalized dimensions D_q with order number q calculated from the SFM F_q , G_q -moment and T_q -moment analysis for $^{16}\text{O-Ag/Br}$ interaction at $200A$ GeV/c. The lines joining points are shown to guide the eye.	120
4.7	Plot of D_q with $\ln q/(q - 1)$ for the $^{16}\text{O-Ag/Br}$ interaction at $200A$ GeV/c. The D_q values obtained from G_q and T_q moment analysis are compared. The lines represent the best linear fits to the data points.	121
4.8	Scaling behavior of the event averaged MFDFA moments $\langle W_q(s) \rangle$ for $q = 0, \pm 2$ and ± 5 . Left panel: $^{16}\text{O-Ag/Br}$ collision at $200A$ GeV/c and right panel: $^{32}\text{S-Ag/Br}$ collision at $200A$ GeV/c.	126
4.9	The same as in Figure 4.8 but for the MFDMA method.	127
4.10	The generalized Hurst exponent $h(q)$ and the multifractal exponent $\tau(q)$ obtained from the MFDFA method. Left panel: $^{16}\text{O-Ag/Br}$ collision at $200A$ GeV/c, right panel: $^{32}\text{S-Ag/Br}$ collision at $200A$ GeV/c.	128

4.11	The same as in Figure 4.10 but for the MFDMA method.	129
4.12	The multifractal singularity spectra obtained from the MF DFA method for (a) $^{16}\text{O-Ag/Br}$ interaction and (b) $^{32}\text{S-Ag/Br}$ interaction both at $200A$ GeV/c. Lines joining points are shown only to guide the eye.	130
4.13	The same as in Figure 4.12 but for the MFDMA method.	130
4.14	Order dependence of the generalized fractal dimension D_q for (a) $^{16}\text{O-Ag/Br}$ interaction and (b) $^{32}\text{S-Ag/Br}$ interaction both at $200A$ GeV/c.	131
4.15	An illustration of converting a time series to the corresponding visibility graph: (a) A time series of 15 measurements is converted to a visibility graph and (b) the same series is converted to a horizontal visibility graph.	132
4.16	(a) Pseudorapidity distribution of an $^{16}\text{O-Ag/Br}$ event having shower track multiplic- ity 240. (b) The η distribution shown in diagram (a) is modified using Equation (4.40).	133
4.17	A schematic of the HVG constructed from the distribution shown in Figure 4.16(b). The numbers within circles indicate the nodes of the graph and the lines represent the connectivity between a pair of nodes.	134
4.18	Combined degree distributions of all the VGs (upper panel) and HVGs (lower panel) generated from the $^{16}\text{O-Ag/Br}$ data (left) and $^{32}\text{S-Ag/Br}$ data (right). The straight lines in the HVG plots follow Equation (4.41).	135
4.19	An illustration of the sandbox algorithm.	138
4.20	X_q versus $\ln r$ plots for several different q values for $^{16}\text{O-Ag/Br}$ (left) and $^{32}\text{S-Ag/Br}$ (right) interactions at $200A$ GeV/c obtained from the visibility graphs. In the lower panels we show the UrQMD simulations of the data.	139
4.21	The same as in Figure 4.20 but for the horizontal visibility graphs.	140
4.22	The order dependence of the generalized fractal dimensions (upper panel) and the multifractal mass exponents (lower panel) calculated from the visibility graph analysis.	141
4.23	The same as in Figure 4.22 but for the horizontal visibility graph analysis.	142
4.24	Multifractal spectra obtained from the VG (upper panel) and HVG (lower panel) analysis for the interactions studied. Predictions from the mixed events are shown (follow text for details). The lines joining points represent Equa- tion (4.50) with the best fitted parameters given in Table 4.7.	143
5.1	Schematic representation of (a) a ring-like distribution and (b) a jet-like distribution of tracks in the target azimuth.	154
5.2	A schematic of $S_2/\langle S_2 \rangle$ distributions obtained for three cases, namely (1) ring-like events, (2) stochastic distribution and (3) jet-like events. The solid curve represents the resultant distribution.	155

5.3	Distributions of the S_1 parameter normalized by its stochastic expectation value $\langle S_1 \rangle$ for (a) ^{16}O -Ag/Br and (b) ^{32}S -Ag/Br interactions both at 200A GeV/c. The shaded region is experimental excess over UrQMD+BEC distribution and without shaded region is over UrQMD.	156
5.4	Same as in Figure 5.3 but for the S_2 parameter.	156
5.5	Average behavior of the S_1 parameter $\langle -\sum \ln(\Delta\varphi_i) \rangle$ for (a) ^{16}O -Ag/Br and (b) ^{32}S -Ag/Br interactions both at 200A GeV/c.	157
5.6	Same as in Figure 5.5 but for the S_2 parameter.	158
5.7	Cluster density distributions for (a) the ring-like region, $S_2/\langle S_2 \rangle < 1$ and (b) the jet-like region, $S_2/\langle S_2 \rangle > 1$ for ^{16}O -Ag/Br interactions at 200A GeV/c.	159
5.8	Same as in Figure 5.7 but for ^{32}S -Ag/Br interactions at 200A GeV/c.	159
5.9	Comparison of the φ -subgroup position distributed along the η axis for three different regions of $S_2/\langle S_2 \rangle$ for ^{16}O -Ag/Br interaction at 200A GeV/c.	160
5.10	Same as in Figure 5.9 but for ^{32}S -Ag/Br interactions at 200A GeV/c.	160
5.11	(a) Second derivative (Mexican hat wavelet) and (b) fourth derivative of the Gaussian function.	162
5.12	Wavelet coefficients $W_{g_2}(a, b)$ for a ^{16}O -Ag/Br event ($n_s = 202$) and a ^{32}S -Ag/Br event ($n_s = 276$) are plotted as functions of scale parameter a and translation parameter b [Equation (5.11)].	163
5.13	The same as in Figure 5.12 but for the g_4 wavelet.	163
5.14	Scalograms of the events for which the g_2 wavelets are shown in Figure 5.12.	164
5.15	g_2 wavelet pseudorapidity spectra for ^{16}O (left) and ^{32}S (right) interactions for different values of scale parameter a . In both the cases the experimental results are compared with the corresponding UrQMD+BEC simulation.	165
5.16	The same as in Figure 5.15 but for the g_4 wavelet.	166
5.17	Distributions of the local maxima (left) and the local minima (right) of the scalograms in ^{16}O -Ag/Br interactions at 200A GeV/c.	167
5.18	The same as in Figure 5.17 but for the ^{32}S -Ag/Br interactions.	167
5.19	Distributions of b_{\max} for different values of a_{\max} cut in ^{16}O -Ag/Br (left) and ^{32}S -Ag/Br (right) interactions at 200A GeV/c. In the lower panel shown are the results from the UrQMD+BEC simulations.	168
5.20	The same as in Figure 5.19 but for different scale windows (Δa_{\max}).	168
6.1	Distributions of γ_k^2 for pseudorapidity bin $\delta\eta = 0.2$	175
6.2	Distributions of d_{ik} for pseudorapidity bin $\delta\eta = 0.2$	176
6.3	A schematic diagram showing how the forward and backward windows are selected in η -distribution.	178

6.4	σ_c^2 as a function of pseudorapidity η measured about the centroid of the η -distribution. Continuous curves are drawn to visualize the trend of the data points.	179
6.5	σ_c^2 as a function of pseudorapidity windows $\Delta\eta$ at $\eta = \pm 1.5$ about the centroid of the η -distribution. Continuous curves are drawn to visualize the trend of the data points.	179
6.6	σ_c^2 as a function of pseudorapidity windows $\Delta\eta$ at $\eta = \pm 1.5$ about the centroid of the η -distribution for four different multiplicity classes. Continuous curves are drawn to visualize the trend of the data points.	180
6.7	Plot of forward-backward correlation parameter b as a function of pseudorapidity gap η . Continuous curves are drawn to visualize the trend of the data points.	181
6.8	b parameter plotted against pseudorapidity window size $\Delta\eta$. Continuous curves are drawn to visualize the trend of the data points.	182
6.9	Pseudorapidity dependence of the scaled variance ω of the multiplicity distribution.	183
6.10	The values of Φ_η -measure are shown as a function of pseudorapidity density ρ_η .	184
6.11	The values of Φ_η measure are shown as a function of overlapping pseudorapidity window $\Delta\eta$	185

Chapter 1

A brief review of high-energy nuclear collisions

1.1 Introduction

The characteristics of all elementary particles and the interactions experienced by them, are described by a unified, renormalizable gauge field theory, called the standard model (SM). The SM however, explains only three fundamental interactions namely the strong, the electromagnetic and the weak, out of the four that exist in nature. So far a similar renormalizable quantum theory for the fourth fundamental interaction, the gravitation, could not be developed. Quarks and leptons, the basic constituents of matter, participate in one or more of these interactions. High-energy heavy-ion interaction deals mainly with the bulk properties of hadronic/partonic matter, where the properties of these fundamental interactions are coupled with the macroscopic matter aspects of nuclear physics. For example, quantum chromodynamics (QCD), the non-abelian gauge theory of strong interaction, predicts that at high pressure and/or high temperature, the usual nuclear matter may undergo a transition to a color conducting deconfined state of quasi-free quarks and gluons called the quark-gluon plasma (QGP), and the QGP then makes a transition to a state of color neutral hadrons [1, 2]. In a strongly interacting extended QCD state phase transitions like these are not only a topic of interest, but they may also help us answer some of the basic questions that are related to the evolution of the universe after its birth, as well as to some astrophysical phenomena still taking place within it. It is speculated that

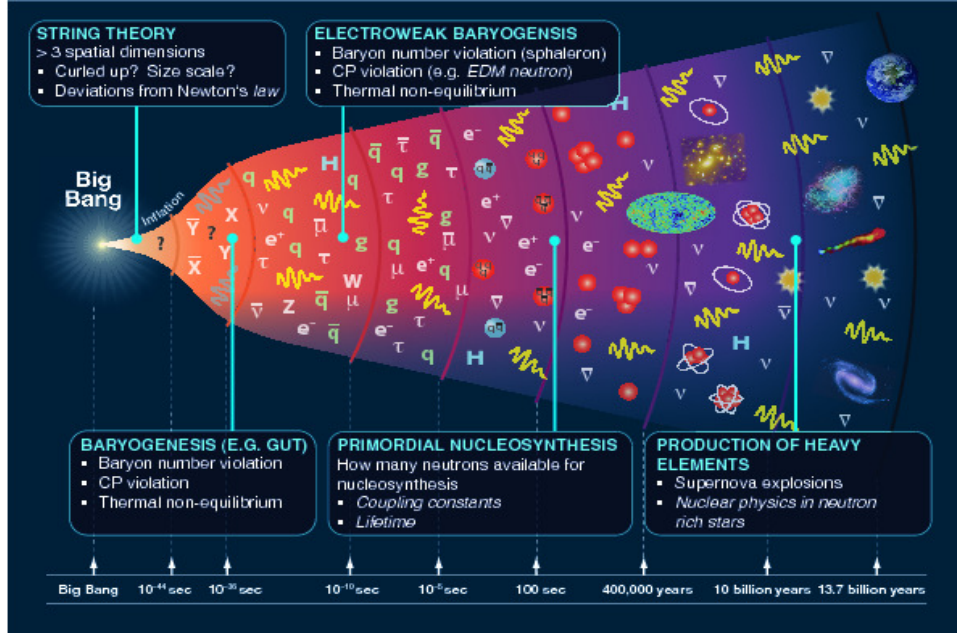


Figure 1.1: A schematic of the time history of the universe [3].

the early universe passed through a QGP \rightarrow hadron phase transition within the first few microseconds of its birth, popularly known as the big bang. In this respect high-energy heavy-ion interaction relates the science of small, i.e. the physics of elementary particles, to the science of large, the cosmology. Using the properties of QGP one can explore and test the predictions of QCD in its natural scale (Λ_{qcd}). In Figure 1.1 we show a schematic of the time (or equivalently the temperature) history of the universe. It is also speculated that shortly after the big bang, as the baby universe expanded and cooled down, it passed through several symmetry breaking processes that lead to different types of phase transitions. One such transition is associated with the electroweak symmetry breaking process that provides masses to the elementary particles. This transition took place at a temperature $T \gtrsim 200$ GeV. It is also related to the electroweak baryon number violating process that leads to the baryon-antibaryon abundance asymmetry observed in nature. Another transition from the QGP \rightarrow hadronic phase of matter took place at $T \lesssim 200$ MeV. This was due to the spontaneous breaking of chiral symmetry of the $SU_c(3)$ color group. Lattice QCD calculations suggest that both these transitions may not be accompanied at all with any kind of discontinuity in the temperature dependence of the free energy and/or its derivative(s). They are rather smooth cross-overs from one state to the other [4–7]. Lattice simulations also suggest that at vanishing baryochemical potential both the phase transitions might have taken place essentially at the same point. After hadronization, when the universe was just several seconds old, nucleosynthesis started. Gradually the radiation dominated universe turned into a matter dominated phase. After about $10 \mu\text{sec}$ of the big bang, when the temperature was a little less than 200 MeV, the entire universe was perhaps filled up with the QGP or a

QGP-like state [8–11]. Current high-energy heavy-ion experiments are trying to recreate the same sequence of events, although in the reverse order, by colliding two heavy-nuclei under the controlled conditions of a laboratory. The expectation is to create a temperature and material density similar to that prevailed around 10^{-5} sec after the birth of our universe. In laboratory such a state however occupies a tiny volume, typically $\sim 10^2 - 10^3 \text{ fm}^3$, and is going to survive momentarily for a time $\sim 50 \text{ fm}/c$. We may call this event *a little bang*, a very small replica of its much bigger cosmological counterpart.

With progressing advancement in the technology sector, powerful accelerators have become available. It is possible to collide two heavy-nuclei with each other at really very high-energies, at velocities very close to that of the light, and produce thereby a large number of new particles in the final state. Depending on the collision energy and the size of the interacting nuclei, the average number of the newly produced particles, most of which are π -mesons, can be anything between 10^2 and 10^4 per collision, much larger than the corresponding numbers produced in proton-proton collisions at similar energies. The process by which these new particles are produced, is known as multiparticle production. A large nucleus consists of many nucleons. In a high-energy collision between two such nuclei, individual nucleons belonging to one of the impinging nuclei are bound to suffer many rescattering with those belonging to the other, as well as with the hadrons/partons produced thereof. While the rescattering allows sufficient time for randomization of the micro-states accessible to the produced particles, a large average number of particles in the final state results in a small relative fluctuation in thermodynamic parameters. These two factors facilitate achieving a local thermal and chemical equilibrium, so that the intermediate stage of the colliding nuclei, in spite of the small volume that it occupies and the brief time interval for which it survives, can be treated as a well equilibrated thermodynamic state. If during the collision the nucleons are sufficiently compressed and heated up, then the boundaries of individual nucleons may melt down to coalesce into a new, exotic and extended state of deconfined quarks and gluons. To detect QGP formation from the debris of hundreds and thousands of particles in the final state, is not an easy task.

Strongly interacting matter has a rich phase structure, which includes a nuclear liquid phase, a hadronic gas phase, and the QGP. All these states are described by the rules of QCD, the theory of quarks, gluons and strong interaction. It is very pertinent to ask how do the collective and macroscopic properties of nuclear/hadronic/QGP matter emerge from the interactions of elementary quarks and gluons that constitute only the individual hadrons. With the help of QCD, high-energy heavy-ion interaction tries to address this issue under high-temperature and/or high-density conditions that are accessible to the experiments. QCD is a non-abelian gauge-field theory that is based on Yang and Mills $SU_c(3)$ color symmetry. Gluons, the color carrying gauge-bosons associated with the field, are self-interacting.

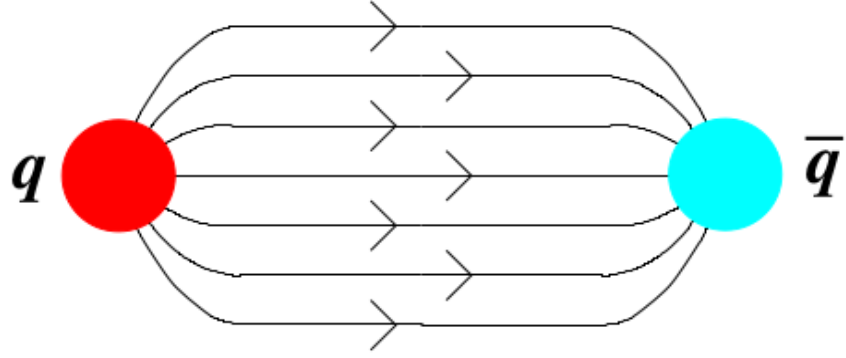


Figure 1.2: Chromoelectric flux between a $q\bar{q}$ pair [13].

Color-confinement and asymptotic freedom are two special properties of quarks and gluons. The interaction between a quark and an antiquark can be phenomenologically modelled by the so called Cornell potential [12],

$$V_s(r) = -\frac{4\alpha_s}{3r} + \kappa r \quad (1.1)$$

where $\alpha_s (= g_s^2/4\pi \approx 1)$ is the dimensionless strong coupling constant, r is the inter-quark spacing, and κ describes the long-range interaction. At short distances, or equivalently at large momentum transfers, the $1/r$ term dominates. Under such circumstances the quark - quark (qq) or the quark - anti-quark ($q\bar{q}$) interaction can be understood in terms of single gluon exchange or excitation of a single color string. With increasing distance more and more potential energy is stored within the intervening space, that can be viewed as a flux tube of color strings (see Figure 1.2). As the gluons are self-coupling and strong interaction is attractive in nature, the strings squeeze each other. As a result the color-force field effectively becomes uniform in the intervening space between the qq or the $q\bar{q}$ system. Therefore, in principle, infinite amount of energy should be required to separate one quark or anti-quark from the other. This in essence is the idea behind the permanent confinement of color degrees of freedom. On the other hand, if quantum effects are taken into account, the running (effective) coupling constant of QCD depends on the scale at which it is measured [14–16]. The dimensionful effective coupling constant in its leading order is given by,

$$g_s^2(q^2) \simeq \frac{16\pi^2}{\beta_0 \ln \frac{q^2}{\Lambda_{qcd}^2}} \quad ; \quad \beta_0 = \frac{11}{3} N_c - \frac{2}{3} N_f \quad (1.2)$$

where q is the 4-momentum transfer, Λ_{qcd} (~ 200 MeV) is the QCD renormalization parameter, N_c and N_f are respectively the numbers of color and flavor degrees of freedom. As $\beta_0 > 0$, with increasing q^2 the QCD coupling constant decreases logarithmically. At large momentum transfer, i.e. at small distances the qq or $q\bar{q}$ interaction potential becomes

weak, which basically is the essence of asymptotic freedom [17, 18]. In the limit $q^2 \gg \Lambda_{qcd}^2$ perturbative QCD can be employed, when $q^2 \sim \Lambda_{qcd}^2$ non-perturbative methods are required.

1.2 Nucleus-nucleus collision at high-energy

In high-energy collisions involving protons and/or electrons, the incident beam energy goes into a very small volume (a few – several fm³) equivalent to a point. On the other hand, in heavy-ion interactions a large amount of energy is deposited into an extended region of space ($10^2 - 10^3$ fm³) within a time of a few fm/ c , creating thereby a system known as the intermediate fireball. Depending on the initial conditions, the fireball energy density can rise to such a high value that new forms of matter may be created. As mentioned above, the search for such new phase(s) is the central objective of studying heavy-ion interactions. The history of high-energy nucleus-nucleus (AB) collisions dates back to the 1970s. There can be two types of AB experiments. One is called the fixed target experiments, where one of the colliding nuclei remains fixed in the laboratory. In the other, called the collider experiments, both the colliding nuclei are made to move towards each other from opposite directions. The advantage of collider facilities is that at the same incident beam energy (E), the energy available in the center of momentum system is much higher in magnitude ($\sim E$) than that available in a fixed target facility ($\sim \sqrt{E}$). The disadvantage is that, in colliders the collision rate is lower by a factor of $10^2 - 10^3$ than that in the fixed target experiments.

The first major attempt to study nuclear matter under extreme conditions was made at the Lawrence Berkeley Laboratory (LBL) by using the Bevalac facility. In those days the experimental scenario on AB interactions was dominated by the fixed target programs like, (i) the Bevatron at LBL, (ii) the Synchrophasotron (Synchro) at Joint Institute of Nuclear Research (JINR), (iii) the Alternating Gradient Synchrotron (AGS) at Brookhaven National Laboratory (BNL) and (iv) the Super Proton Synchrotron (SPS) at CERN. Though the JINR Synchrophasotron was commissioned before the Berkeley Bevalac, it was used to accelerate only the lighter ions. Both in the SPS and AGS, the facilities for accelerating nuclei came first at the late 1980's (lighter nuclei), and then again in the early 1990's (heavy nuclei). In both facilities many fixed target experiments were carried out, with a typical incident ion energy of a few hundred GeV per nucleon at the SPS, and ~ 10 GeV per nucleon at the AGS. Several indicators that can identify a probable QGP \rightarrow hadron phase transition, have been rigorously examined by analyzing the data available from these experiments. The experimental results have been compared with the models based on numerical simulations, the theories were modified and the results were repeatedly examined. Despite some experimental results suggesting early signal(s) of QGP formation [19, 20], no solid evidence of a colour deconfined state was available in the fixed target

experiments, thus eluding the expectations of a large number of researchers working in this field. In the beginning of the 21st century the experimental study of high-energy heavy-ion collision entered into a new era, when the Relativistic Heavy-Ion Collider (RHIC) started functioning at the BNL. This was followed by the establishment of the Large Hadron Collider (LHC) at CERN, making provision for a collision energy higher than that available in the RHIC by an order of magnitude. For the first time, in any terrestrial laboratory the experiments at RHIC and LHC started to indicate formation of a color deconfined extended QCD state like the QGP at high temperature and low baryonic potential. The data analysis, refinement of accumulated results, and physics analysis are still going on. Some of these results are going to be very briefly discussed later in the experimental review section of this chapter. To complement the RHIC and LHC experiments and to study the QCD state at high baryochemical potential, the Compressed Baryonic Matter (CBM) experiment is being designed and commissioned at the Facility for Anti-proton and Ion Research (FAIR) at GSI, Darmstadt [21]. Over the past forty years or so, there has been a tremendous advancement in the technology sector. As a result, there has been a $10^3 - 10^4$ times increase in the collision energy. The major heavy-ion programmes undertaken till date are listed in Table 1.1. The list will help us understand the chronology of this development in terms of the past, present and future accelerator facilities.

A nucleus consists of A nucleons. In the ground state it occupies a volume $V = 4\pi r_0^3 A/3$. It has a matter density

$$\rho = \frac{3}{4\pi r_0^3} \quad (1.3)$$

and it possesses an energy density

$$\epsilon = \frac{A \times m_N}{V} \quad (1.4)$$

Here $r_0 = 1.15$ fm is the nuclear radius parameter, and $m_N = 0.94$ GeV/ c^2 is the nucleon rest mass. Typical values are $\rho \approx 0.16$ nucleons/fm³ and $\epsilon \approx 0.15$ GeV/fm³. Whatever may be the constituent particles, if the intermediate fireball created in an AB collision has to qualify as a state, it should have well defined values of temperature, volume, pressure etc.. This is possible only when the motion of the constituent particles, after experiencing multiple rescattering, is sufficiently random. An order of magnitude calculation in this regard may be useful to realize the context. A hadron typically has a radius of 1 fm and it fills up a volume of $5 - 6$ fm³. So the hadronic matter density is about $n \sim 0.2$ per fm³. Typical cross-section of a high-energy hadronic interaction is $\sigma \sim 50$ mb or ~ 5 fm². Collisions between two heavy-nuclei increase the density by a few orders of magnitude. As a result the hadronic density increases to $n \sim 10$. The mean free path of the constituent particles will therefore be $\lambda \sim (n\sigma)^{-1} \approx 0.02$ fm. Therefore, one can expect multiple ($\sim 10^3$) hadronic rescattering taking place within a collision volume of dimension $10 - 15$ fm, which with all

Table 1.1: Accelerator facilities in relativistic heavy-ion physics..

Accelerator	Start Year	Projectiles	Max. Energy	Experiment	Status
Bevalac Berkeley	1984	$^{238}\text{U}, ^{84}\text{Kr},$ $^{40}\text{Ca}, ^{12}\text{C}$	<2A Gev	Fixed target	Closed
Synchro. JINR, Dubna	1975	$^{12}\text{C}, ^{24}\text{Mg},$ $^{20}\text{Ne}, ^{28}\text{Si}$	4.5A Gev	Fixed target	Closed
BNL-AGS Brookhaven	1986	^{28}Si	14.6A Gev	Fixed target	Closed
BNL-AGS Brookhaven	1992	^{197}Au	11A Gev	Fixed target	Closed
CERN-SPS Geneva	1986	$^{16}\text{O}, ^{32}\text{S}$	200A Gev	Fixed target	Closed
CERN-SPS Geneva	1994	^{208}Pb	200A Gev	Fixed target	Closed
GSI-SIS Darmstadt	2002	$^{84}\text{Kr}, ^{197}\text{Au}$	2A Gev	Fixed target	Operational
BNL-RHIC Brookhaven	2002	$^{39}\text{Cu}, ^{197}\text{Au}$	$\sqrt{s_{NN}}=200$ GeV	Collider	Operational
CERN-LHC Geneva	2008	$^{16}\text{O}, \text{Ar}, \text{Pb}$	$\sqrt{s_{NN}}=5.5$ Tev	Collider	Operational
GSI-SIS300 Darmstadt	2017	$^{59}\text{Ni}, ^{197}\text{Au}$	45A Gev	Fixed Target	Operational
NICA JINR, Dubna	2017	$^{197}\text{Au}, ^{238}\text{U}$	$\sqrt{s_{NN}} \sim 5$ GeV	Collider	Operational

probability will lead to equilibration. The thermodynamic conditions of the intermediate fireball that can be and have been reached in high-energy heavy-ion experiments using the above mentioned accelerator facilities, are listed below [22].

1. Temperature: $T = (100 - 1000)$ MeV (1 MeV \equiv 10 billion degrees) [up to a million times the temperature of the core of the sun].
2. Pressure: $P = (100 - 300)$ MeV/fm³ (1 MeV/fm³ \equiv 1028 atm.) [pressure at the center of the earth = 3.6 million atm.].
3. Density: $\rho = (5 - 10)\rho_0$ [ρ_0 is the density of a gold nucleus ~ 3000 g/cm³; density of a gold atom = 19 g/cm³].
4. Volume: nearly 1500 fm³, nucleus radius $R = 1.15 \times A^{1/3}$ fm [for an Au-nucleus $A \approx 200$, $R \simeq 7$ fm and $V = 4\pi R^3/3 \simeq 1500$ fm³].
5. Duration: $(10 - 50)$ fm/c $\sim 10^{-22}$ sec.
6. Baryochemical potential: $\mu = (400 - 600)$ GeV.
7. Magnetic field: $B \sim 10^{15} - 10^{16}$ Tesla [in neutron stars $B \sim 10^{11}$ Tesla].

1.2.1 Kinematics of high-energy interaction

Let us now discuss the kinematics of two-body interaction and some variables that are commonly used to characterize the particle production process in high-energy interactions. A detailed account of the topic can be found in [23, 24]. If otherwise not mentioned we shall stick to the natural unit system ($\hbar = c = k_B = 1$). Let us consider a two body collision where the projectile has a momentum \vec{p}_1 , energy E_1 and rest mass m_1 . On the other hand the target, fixed in the laboratory system (LS), has a rest mass m_2 only. The 4-momenta of these particles are respectively,

$$p_1 = (E_1, \vec{p}_1), \text{ and } p_2 = (m_2, \vec{0}) \quad (1.5)$$

In the center of momentum (CM) frame the momentum of two interacting particles are equal but oppositely directed. Let their 4-momentum in the CM frame be denoted by,

$$p_1^* = (E_1^*, \vec{p}_1^*), \text{ and } p_2^* = (E_2^*, \vec{p}_2^* = -\vec{p}_1^*) \quad (1.6)$$

The total energy (\sqrt{s}) available in the CM frame is equivalent to the invariant mass of the CM. The total 4-momentum in the CM frame is

$$(p_1^* + p_2^*)^2 = (E_1^* + E_2^*)^2 - (\vec{p}_1^* + \vec{p}_2^*)^2 = (E_1^* + E_2^*)^2 = E_{cm}^2 \equiv s \quad (1.7)$$

The total 4-momentum in the LS is

$$(p_1 + p_2)^2 = m_1^2 + m_2^2 + 2E_1 m_2 \quad (1.8)$$

The 4-momentum square of any system should be a Lorentz invariant quantity. Therefore,

$$E_{cm} = \sqrt{s} = \sqrt{m_1^2 + m_2^2 + 2m_2 E_{lab}} \quad (1.9)$$

where $E_{lab} = E_1$ is the projectile energy in LS. It is evident that at high-energies for a nucleon-nucleon (NN) system $\sqrt{s} \sim E_{lab}^{1/2}$, and the center of mass moves in the LS in the direction of \vec{p}_1 with a velocity $\beta_{cm}c$. Corresponding Lorentz factor $\gamma_{cm} = (1 - \beta_{cm}^2)^{-1/2}$. As $E = \gamma m$

$$\gamma_{cm} = \frac{E_1 + m_2}{\sqrt{s}} \quad \Rightarrow \quad \sqrt{s} \simeq E_{lab}/\gamma_{cm} \quad (1.10)$$

In a collider experiment if the incident energies are very high, i.e. ($E_1, E_2 \gg m_1, m_2$) then

$$E_{cm} \simeq \sqrt{4E_1 E_2} \quad (1.11)$$

If $E_1 = E_2 = E$ then $E_{cm} \simeq 2E$, and the CM energy increases linearly with E . If an AB collision is viewed as an independent superposition many elementary NN collisions then the AB collision is called incoherent. In such a case for a symmetric central collision between two identical nuclei ($A = B$), the total CM energy is related to the CM energy of an NN system ($\sqrt{s_{NN}}$) as $\sqrt{s} = A\sqrt{s_{NN}}$, and corresponding Lorentz factor given by,

$$\gamma_{cm} = \frac{E}{M} = \frac{\sqrt{s}}{2Am_N} = \frac{\sqrt{s_{NN}}}{2m_N} \quad (1.12)$$

If on the other hand, each colliding nucleus behaves like a single massive object then the collision is fully coherent. In non-central collisions between two identical nuclei, in asymmetric and coherent collisions, it is difficult to fix the effective CM frame, which depends on the impact parameter as well as on the degree of coherence of the collision. Therefore, the number of participating and spectator nucleons need to be determined first, posing extra problems particularly in soft processes. For hard processes that are more likely to be observed in the central collisions, the NN frame still works.

The rapidity variable

The rapidity variable is the relativistic measure of the velocity of a particle. It is a suitable choice to describe the dynamics of relativistic particles. It is a dimensionless quantity and can be used to locate a particle in the rapidity space. In high-energy collisions the beam line is conventionally taken along the z -axis, which may be called the longitudinal direction. The $(x-y)$ plane is called the transverse plane. It is convenient to decompose the momentum vector \vec{p} in two components, one in the longitudinal direction (p_l) and another in the transverse direction ($p_t = \sqrt{p_x^2 + p_y^2}$). p_t remains invariant under a Lorentz boost given along the longitudinal direction. In relativistic heavy-ion collisions the space-time rapidity of a particle is defined as

$$y = \frac{1}{2} \ln \left(\frac{t+z}{t-z} \right) \quad (1.13)$$

where t is the time and z is the space co-ordinate of the particle along the beam direction. For particles created exactly at the center of mass of the interacting system, $y = 0$. The space-time rapidity is however experimentally not measurable. It is used mainly for theoretical calculations. Therefore, the energy-momentum rapidity is introduced as,

$$y = \frac{1}{2} \ln \left(\frac{E + p_l}{E - p_l} \right) = \frac{1}{2} \ln \left(\frac{E + p_l}{m_t} \right) \quad (1.14)$$

Here $E = \sqrt{|\vec{p}|^2 + m^2}$ and $m_t = \sqrt{m^2 + p_t^2}$ is the transverse mass of the particle. The most interesting property of the rapidity variable is that, it is additive under Lorentz boost.

As a result, the overall shape of the rapidity distribution of particles remains unchanged under a longitudinal Lorentz boost. In the nonrelativistic limit, the rapidity of a particle traveling along the longitudinal direction is equal to the velocity of the particle measured in the unit of velocity of light in vacuum. The energy E and the longitudinal momentum p_l of a particle are related to the rapidity by the relation

$$E = m_t \cosh y \quad \text{and} \quad p_l = m_t \sinh y \quad (1.15)$$

The energy and momentum of the CMS in the LS are respectively, $\gamma_{cm}\sqrt{s}$ and $\beta_{cm}\gamma_{cm}\sqrt{s}$. The rapidity of the CM in the LS therefore, is

$$\begin{aligned} y_{cm} &= \frac{1}{2} \ln \left(\frac{\gamma_{cm}\sqrt{s} + \beta_{cm}\gamma_{cm}\sqrt{s}}{\gamma_{cm}\sqrt{s} - \beta_{cm}\gamma_{cm}\sqrt{s}} \right) \\ &= \frac{1}{2} \ln \left(\frac{1 + \beta_{cm}}{1 - \beta_{cm}} \right) \end{aligned} \quad (1.16)$$

Lorentz transformation between the CMS and the LS is given by the following equations,

$$E^* = \gamma E - \gamma\beta p_l; \quad p_l^* = -\gamma\beta E + \gamma p_l; \quad p_t^* = p_t \quad (1.17)$$

The star marked quantities are associated with the CMS. The rapidity values of a particle in the CMS and the LS are given respectively by,

$$y^* = \frac{1}{2} \ln \left(\frac{E^* + p_l^*}{E^* - p_l^*} \right) \quad \text{and} \quad y = \frac{1}{2} \ln \left(\frac{E + p_l}{E - p_l} \right) \quad (1.18)$$

Using Equation (1.17) in Equation (1.14) one gets,

$$\begin{aligned} y &= \frac{1}{2} \ln \left(\frac{E^* + p_l^*}{E^* - p_l^*} \right) + \frac{1}{2} \ln \left(\frac{1 + \beta}{1 - \beta} \right) \\ \Rightarrow y &= y^* + y_{cm} \end{aligned} \quad (1.19)$$

Therefore in a CMS \rightarrow LS transformation the rapidity distribution remains unaltered, with the y -scale shifted by an amount equal to y_{cm} . For a fixed target experiment, the beam rapidity can be obtained by using the relation (1.15). For the beam particle p_t is zero. The rapidity of beam particle (y_1) is given by,

$$\begin{aligned} y_1 &= \cosh^{-1} \left(\frac{E}{m_1} \right) = \cosh^{-1} \left(\frac{\sqrt{s_{NN}}}{2m_N} \right) \\ \Rightarrow y_1 &= \sinh^{-1} \left(\frac{p_l}{m_1} \right) \end{aligned} \quad (1.20)$$

where m_1 is the rest mass of the beam particle.

The pseudorapidity variable

Both the energy and the longitudinal momentum of a particle are necessary to determine the rapidity of that particle. But in many experiments it is not possible to measure both. In such cases it is instead convenient to use the pseudorapidity variable (η). Suppose a particle is emitted at an angle θ with respect to the beam axis. From Equation (1.14) we get the rapidity as,

$$y = \frac{1}{2} \ln \left(\frac{(m^2 + |\bar{p}|^2)^{1/2} + |\bar{p}| \cos \theta}{(m^2 + |\bar{p}|^2)^{1/2} - |\bar{p}| \cos \theta} \right) \quad (1.21)$$

If the kinetic energy of the particle is very high ($|\bar{p}| \gg m$) then Equation (1.21) reduces to

$$\begin{aligned} y &= \frac{1}{2} \ln \left(\frac{|\bar{p}| + |\bar{p}| \cos \theta}{|\bar{p}| - |\bar{p}| \cos \theta} \right) \\ &= -\ln \tan \left(\frac{\theta}{2} \right) = \eta \end{aligned} \quad (1.22)$$

In terms of the linear momentum components η is expressed as

$$\eta = \frac{1}{2} \ln \left(\frac{|\bar{p}| + p_l}{|\bar{p}| - p_l} \right) \quad (1.23)$$

$$e^\eta = \sqrt{\left(\frac{|\bar{p}| + p_l}{|\bar{p}| - p_l} \right)} \quad (1.24)$$

and

$$e^{-\eta} = \sqrt{\left(\frac{|\bar{p}| - p_l}{|\bar{p}| + p_l} \right)} \quad (1.25)$$

From Equations (1.24) and (1.25) the following relations are obtained,

$$|\bar{p}| = p_t \cosh \eta \quad \text{and} \quad p_l = p_t \sinh \eta \quad (1.26)$$

Rapidity and pseudorapidity are interchangeable and are related to each other by,

$$y = \frac{1}{2} \ln \left(\frac{\sqrt{p_t^2 \cosh^2 \eta + m^2} + p_t \sinh \eta}{\sqrt{p_t^2 \cosh^2 \eta + m^2} - p_t \sinh \eta} \right) \quad (1.27)$$

and

$$\eta = \frac{1}{2} \ln \left(\frac{\sqrt{m_t^2 \cosh^2 y - m^2} + m_t \sinh y}{\sqrt{m_t^2 \cosh^2 y - m^2} - m_t \sinh y} \right) \quad (1.28)$$

η is used as an approximation of y when the angular distribution of the produced particles is measured, and only when the relation $E \cong |\bar{p}| \gg m$ holds good. In high-energy interactions the approximation $\eta \cong y$ is good for the pions and other light weight particles.

1.2.2 Geometry of nucleus-nucleus collision

In a high-energy collision the colliding nuclei look like two Lorentz contracted discs or pancakes in their CM frame, the contractions being along their directions of motion. The impact parameter of a collision lies in $0 \leq b \leq (R_A + R_B)$, where R_A and R_B are the transverse radii of the colliding nuclei. The entire set of AB events falling within this b -range is called the minimum bias sample of events. In central (peripheral) collisions b is closer to its minimum (maximum) value. The schematic of an AB collision for $b \neq 0$ is shown in Figure 1.3. In

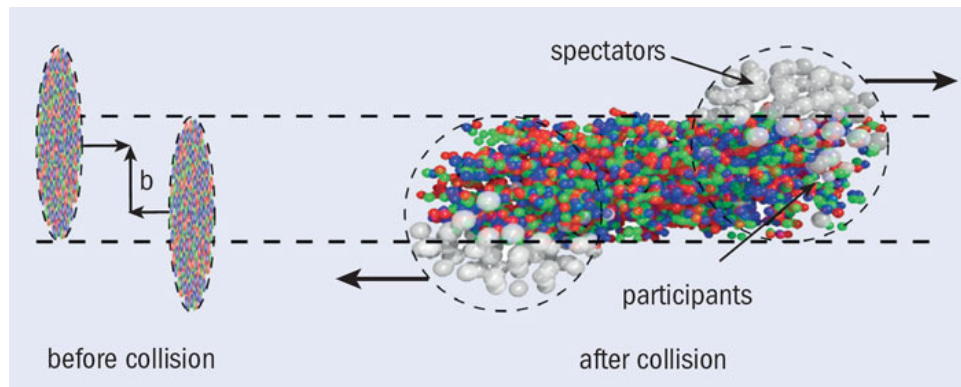


Figure 1.3: Schematic of a nucleus-nucleus collision [25].

the most peripheral collisions the interactions between the nuclei are primarily electromagnetic in nature. Either or both of the nuclei may absorb energy through giant resonances, proton-neutron clusters, higher lying nucleon resonances, and/or decay by emission of one or more nucleons. A small fraction of the total number of nucleons belonging to each nucleus are actually affected in such interactions, while most others remain unaffected. In a purely geometrical picture the cross-section of an AB reaction is given by the Bradt-Peter's formula, $\sigma_{\text{geo}} = \pi r_0^2 (A^{1/3} + B^{1/3} - \delta)^2$ [26]. However, b cannot be directly measured in an experiment. Generally, any observable that varies monotonically with b can be used as its representative measure. As for example the average charged particle multiplicity N_{ch} , the total transverse energy ($E_t = \sum_i E_i \sin \theta_i$) or the energy deposited by the spectator nucleons in the Zero Degree Calorimeter (E_{ZDC}) – the missing forward energy etc., are considered as suitable experimental measures of b . It is natural to assume that on an average, the energy released in a collision will be directly proportional to the number of nucleons participating in the collision, and the particle multiplicity will be proportional to the participating nucleon number. So the particle multiplicity is proportional to the energy liberated in the collision. For the minimum-bias event sample one can measure the N_{ch} -distribution or the E_t -distribution. High values of N_{ch} or E_t correspond to more central collisions and lower

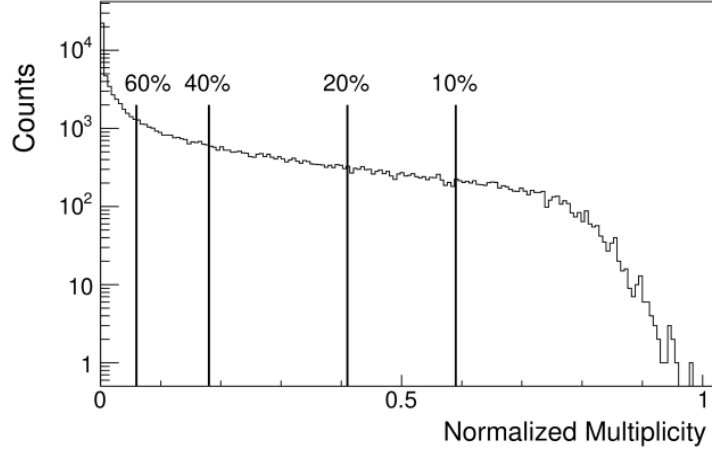


Figure 1.4: Multiplicity distribution and centrality of AB collisions.

values correspond to more peripheral collisions. The N_{ch} or the E_t distribution can therefore be utilized for the centrality determination of AB interactions. Figure 1.4 illustrates the schematic of a multiplicity distribution of charged particles for a minimum-bias event sample that can be used to assign the collision centrality. Starting from the maximum observed value of N_{ch} the area under the multiplicity distribution may be sliced into sequential intervals. The top 10% events with the highest N_{ch} values corresponds to the (0 – 10)% centrality class and so on. A similar exercise is possible for the E_t distribution too.

The Glauber model

The correlation between centrality and the number of participating nucleons has also been expounded in detail by the Glauber-type calculations using different functional forms of the nuclear density [27, 28]. The model treats an AB interaction as a superposition of multiple independent NN collisions, and at high energies the nucleons carry enough momentum to remain almost undeflected as the impinging nuclei pass through each other. It is also assumed that the nucleons move independently in the nucleus and that the size of the nucleus is large compared to the range of the NN interaction. Effectively the nucleons move on straight-line paths, and at any stage of the collision the inelastic NN cross-section (σ_{in}) is assumed to be independent of the number of NN collisions that a nucleon has already suffered. In that sense it is a classical model of the interaction. As the two nuclei collide at an impact parameter \mathbf{b} , the probability of n inelastic NN interactions is given by,

$$P(n, \mathbf{b}) = \binom{AB}{n} [T(\mathbf{b}) \sigma_{in}]^n [1 - T(\mathbf{b}) \sigma_{in}]^{(AB-n)}$$

where $T(\mathbf{b}) = \int \rho_A(\mathbf{b}_A, z_A) d\mathbf{b}_A dz_A \rho_B(\mathbf{b}_B, z_B) d\mathbf{b}_B dz_B t(\mathbf{b} - \mathbf{b}_A - \mathbf{b}_B)$ is the normalized thickness function for the AB collision. The total probability of having an inelastic event in the collision between A and B is,

$$\frac{d^2\sigma_{\text{in}}}{db^2} = \sum_{n=1}^{AB} P(n, b) = 1 - [1 - T(b) \sigma_{\text{in}}]^{AB}$$

The total inelastic cross-section is therefore,

$$\sigma_{\text{in}}^{AB} = \int 2\pi b db [1 - (1 - T(b) \sigma_{\text{in}})^{AB}]$$

In the framework of the Glauber model the total number of nucleons that underwent at least one interaction (N_{part}), or the total number of binary NN interactions (N_{coll}) per event, can be analytically obtained as,

$$\begin{aligned} N_{\text{part}}(b) &= \int d^2\mathbf{s} T_A(\mathbf{s}) [1 - \exp(-\sigma_{\text{in}}^{NN} T_B(\mathbf{s}))] + \int d^2\mathbf{s} T_B(\mathbf{s} - \mathbf{b}) [1 - \exp(-\sigma_{\text{in}}^{NN} T_A(\mathbf{s}))] \\ N_{\text{coll}}(b) &= \int d^2\mathbf{s} \sigma_{\text{in}}^{NN} T_A(\mathbf{s}) T_B(\mathbf{b} - \mathbf{s}) \equiv \sigma_{\text{in}}^{NN} T_{AB}(\mathbf{b}) \end{aligned} \quad (1.29)$$

where $T_A(\mathbf{s}) = \int dz \rho_A(z, \mathbf{s})$ is the thickness function for the nucleus A , $T_B(\mathbf{s})$ is the same for the nucleus B , and $T_{AB}(\mathbf{b})$ is the nuclear overlap function. It is assumed that an NN interaction takes place if the inter-nucleon distance d in the plane orthogonal to the beam-axis satisfies the condition $\pi d^2 \leq \sigma_{\text{in}}$. An arbitrary number of such AB collisions can be generated by the Monte Carlo Glauber model [29] and the resulting distributions of $d\sigma/N_{\text{part}}$, $d\sigma/N_{\text{coll}}$ and $d\sigma/db$ are obtained. The systematic uncertainties in the mean values of N_{part} and N_{coll} for each centrality class are estimated by varying the parameters of nuclear density function, by varying the value of σ_{in} , and from the uncertainty in the determination of the total AB interaction cross-section. These sources of uncertainties are treated as fully correlated in the final systematic uncertainty in the above measured variables. If certain cross-sections scale with the number of participants, they are associated with soft or small momentum transfer processes – the low- p_t hadron production, which accounts for almost 95% of the bulk hadron multiplicity, are phenomenologically described by non-perturbative models. On the other hand, in the hard QCD processes, like the jet formation, heavy flavor production etc., the cross-section scales with the number of primordial NN collisions N_{coll} . In a particular centrality class N_{part} grows like A , whereas N_{coll} grows like $A^{4/3}$, hence N_{coll} is always equal to or higher than N_{part} . Sometimes, the charged particle multiplicity is given in terms of the contributions of both soft and hard processes by a two-component model [30, 31] like,

$$N_{ch} = f \times N_{\text{part}} + (1 - f) \times N_{\text{coll}} \quad (1.30)$$

where f , typically valued at 85 – 90%, is the fractional contribution from soft processes.

1.2.3 Stopping in nucleus-nucleus collision

In an AB collision each incoming nucleus may be considered as a coherent cloud of nucleons. As the nuclei collide the nucleons undergo successive collisions, and transverse degrees of freedom are excited. A significant fraction of the incoming kinetic energy is deposited in the central region. This leads to the formation of a high-energy, high-density fireball, a state not anywhere close to the equilibrium. A finite amount of proper time (a few fm/c) is needed to liberate the partons in this state. Subsequent collisions lead to a locally thermalized state, which again takes a few fm/c of proper time. If the incident energy involved is extremely high, i.e. \gtrsim the highest RHIC energy, the participating nucleons are far apart in the phase space. Under such a condition the colliding nuclei are to a large extent transparent to each other. Significant amount of energy will still be deposited in the central rapidity region, which is used to form $q\bar{q}$ pairs. Baryons become as abundant as the antibaryons and the net baryon content of the state becomes small. Most of the final state particles are produced in the form of mesons. This may eventually lead to a QGP at high-temperature and low chemical potential. A similar state perhaps has already been created in the RHIC and LHC experiments. The system subsequently evolves like a relativistic imperfect fluid. Models based on perturbative QCD and hydrodynamics are used to theoretically study such states. Nuclear stopping measures the efficiency of slowing down the incoming nucleons and the ability to convert the incoming kinetic energy to transverse degrees of freedom. If the stopping is high, the total baryon number carried by the interacting nucleons is significantly redistributed, leading to a high baryo-chemical potential of the equilibrated fireball. The underlying physics issues are addressed by non-perturbative QCD and/or hadronic transport models. The stopping is large when a complete overlap between the projectile and target nuclei is achieved. It is measured by the average rapidity loss as [24],

$$\langle \delta y \rangle = y_P - \langle y_B \rangle = y_P - \frac{2}{N_{part}} \int_0^{y_P} y \frac{dN_{B-\bar{B}}}{dy} dy \quad (1.31)$$

where $\langle y_B \rangle$ is the net average baryon rapidity after the collision. The average scaled rapidity shift does not significantly change up to the SPS energy. We find $\langle \delta y / y_P \rangle \approx 0.27$ at $E_{lab} = 200 \text{ AGeV}$ [32]. For comparable system size the normalized rapidity density does not change with beam energy. Corresponding energy loss (ΔE) is

$$\Delta E = \int_{-y_P}^{y_P} \langle m_t(y) \rangle \frac{dN_{B-\bar{B}}}{dy} \cosh y dy \quad (1.32)$$

which comes out to be $\Delta E = 25.7 \pm 2.1$ TeV at the top RHIC energy [33]. It should also be noted that an incomplete stopping and a longitudinally expanding source lead to similar rapidity distributions.

The energy available for particle production in an AB collision depends globally on $\sqrt{s_{NN}}$ and collision centrality, and locally on p_t and y . The p_t -spectra of produced particles can in general be divided into a low- p_t and a high- p_t part. The low- p_t part is due to the random kinetic and collective motion of the particles present in the fireball, which has a thermal origin and can be described by an exponentially decaying function. The high- p_t part on the other hand, is dominated by hard processes and can be described by a power-law. The inverse slope of the p_t -spectrum is the effective temperature (T_e) of the source from which the particles are originating. T_e can be measured from our knowledge of the p_t -distribution. If the distribution can be approximated as exponentially decaying, then for $\langle p_t \rangle \gg m$ one gets $\langle m_t \rangle \approx \langle p_t \rangle \approx 2T_e$. Integrating the invariant yield over the entire p_t region one gets the rapidity distribution dN/dy of produced particles. Significant amount of information on AB collisions can be extracted by studying the rapidity distribution. Particle identification is necessary for rapidity measurement, which may not be possible in all experiments. Under such circumstances the pseudorapidity distributions are used. At very high-energies dN/dy should exhibit a plateau, which due to the transformation given in Equation (1.28) gets depleted by a small extent around $\eta^* = 0$. In the CMS the depletion factor reads as $(1 - m^2 / \langle m_t^2 \rangle)^{1/2}$, whereas in the LS the peak of the distribution is located at around half of the beam rapidity ($y_p/2$), and the depletion factor is $[1 - m^2 / \{ \langle m_t^2 \rangle \cosh^2(y_p/2) \}]^{1/2}$. Due to the additive property of the rapidity variable under Lorentz boost, the rapidity distribution remains unchanged as one moves from one reference frame to the other. In any relativistic AB collision usually there is a central particle producing region which results from the nucleons directly participating in the collision, and two baryon rich fragmentation regions (target and projectile) dominated by the spectator nucleons. If the colliding nuclei are transparent with respect to each other, they leave a trail of energy in the form of stretched out strings. The strings subsequently fragment and the central region is populated mostly by different types of mesons. Apart from a down-shift in their rapidity values necessary to conserve energy, the baryons (nucleons) continue to move out of the central rapidity region. On the other hand when the colliding nuclei substantially stop each other, the central rapidity region is filled up with both energy and baryons. Under complete stopping the projectile and target nucleons lose all memories of their initial states. Correspondingly, the difference (if there is any) between the energy and baryon number distributions in longitudinal and transverse directions with respect to the collision axis is very little. These two extreme situations are schematically represented in Figure 1.5. The difference between the rapidity values of the projectile and the target, $\Delta y = y_p - y_T$ is important for characterization of the central region. For targets fixed in

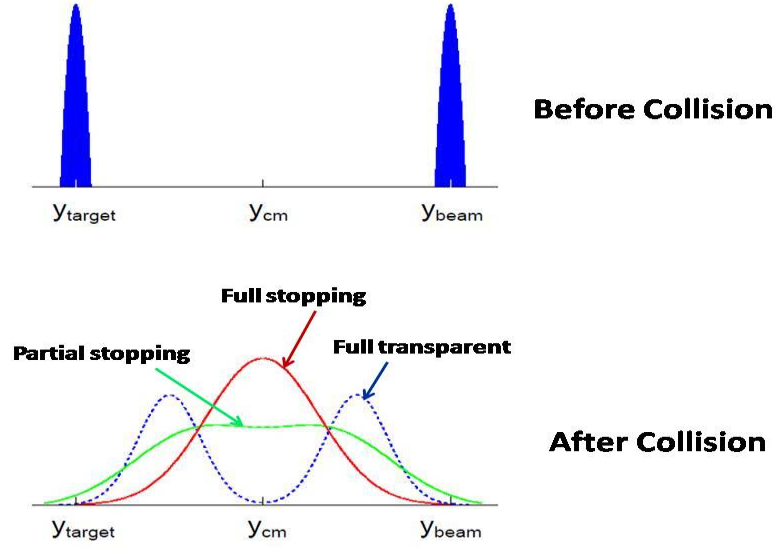


Figure 1.5: Stopping in nucleus-nucleus collisions.

the LS, $y_T = 0$ and $\Delta y = y_P$. Accordingly $\cosh \Delta y = E_P/m_P$. In a symmetric collider experiment the CMS is at rest in the LS, and for a head on collision $\Delta y/2$ is the rapidity of the projectile/target. With increasing $\sqrt{s_{NN}}$ the rapidity gap increases as, $\Delta y \propto \ln \sqrt{s_{NN}}$ [34]. This enables us to study the central region without actually having to account for particles spilling over from the fragmentation regions. Up to the SPS energy the rapidity distribution does not show any plateau and can in stead be described by a single Gaussian curve having a width $\sigma(y) \simeq 2 - 3$ rapidity units. Any system having a preferentially longitudinal expansion of the particle emitting source, will therefore have a reasonably large rapidity gap ($\Delta y > 3$), which occurs beyond the SPS energy. Experimental data suggest that nuclear/partonic stopping is present in the primordial, first generation collisions at the microscopic level. Rapidity distributions of particle multiplicity and/or transverse energy exhibit qualitatively similar shape, which on one hand evolve similarly with \sqrt{s} in pp , $p\bar{p}$ and e^+e^- reactions, and in central AB collisions on the other. For the bulk hadron rapidity distributions one can formulate a nuclear modification factor [24] as,

$$R_{AA}(p_t) = \frac{1}{\langle N_{coll} \rangle} \times \frac{\frac{d^2 N_{AA}}{dp_t dy}}{\frac{d^2 N_{pp}}{dp_t dy}} \quad (1.33)$$

The numerator of the ratio is the single particle p_t -distribution in a symmetric AA collision, while the denominator part is the single particle distribution of the same species of particles produced in pp collisions at the same incident energy per nucleon. In the above we assume that the AA collision is an incoherent superposition of many binary NN collisions. If the contribution to the total particle yield from each NN pair is considered to be same as that coming from a pp collision at the same \sqrt{s} , then $R_{AA} = 1$. However, in RHIC and LHC experiments R_{AA} is found to be larger than unity, indicating thereby a higher stopping in

nuclear collisions.

1.2.4 Evolution of nucleus-nucleus collision

The fireball system created in a high-energy heavy-ion collision passes through several different stages. Different probes that are sensitive to different stages of its space-time evolution, are used to determine the properties of the fireball. A schematic of different stages of an AB collision process is shown in Figure 1.6, and a brief qualitative description of each stage is sequentially summarized below.

- **Pre-equilibrium stage** - The initial AB collision takes place within a time span of $2R/\gamma_{cm}$, where R is the nuclear radius and γ_{cm} is the Lorentz factor in the CMS. For symmetric and central collisions between two heavy-nuclei, this amounts to a passing time of the order of a few fm/c. As for example in a $Au + Au$ or a $Pb + Pb$ collision at $E_{lab} = 200$ GeV the γ_{cm} factor ~ 10 and $2R/\gamma_{cm} \simeq 1.4$ fm/c. The initial stage of the collision is labeled as the pre-equilibrium stage. Processes like parton-parton hard scattering predominantly take place in the overlap region of the colliding nuclei, depositing thereby a large amount of energy in the central ($z \sim 0$) region. This stage can be investigated by using high- p_t probes such as jets, heavy-quarks and direct photons. During this stage intense matter compression and heating take place.
- **Equilibration of the fireball** - After the short pre-equilibration stage a fireball is created. Depending on the initial conditions due to multiple rescattering among the participating nucleons, thermal equilibrium may be established. In relativistic hydrodynamical models the equilibration process is very fast. It takes place within ~ 1 fm/c, while lacking an exact mechanism for this to happen. If the matter and/or energy density is sufficiently high, a QGP-like state may also be formed, which will be dominated by parton-parton and/or string-string scattering. The transition from the QGP to a hadron gas may occur at and around the Hagedorn limit of temperature $T_H \approx 170$ MeV [35–37]. After a local thermal equilibrium is achieved, due to an extremely large pressure gradient against the surrounding vacuum, the fireball system starts expanding. Relativistic hydrodynamics describes the evolution of the system. The specific viscosity of the system, though may not exactly vanish, is very close to its ideal limit, making the expansion to behave almost like a perfect fluid.
- **Chemical freeze-out** - As the system expands, it cools down until the temperature drops below a critical value, T_c say. It induces a phase transition causing the quarks and gluons to recombine and form color neutral hadrons. The expanding fireball first reaches a chemical freeze-out stage when the inelastic interactions between the partons

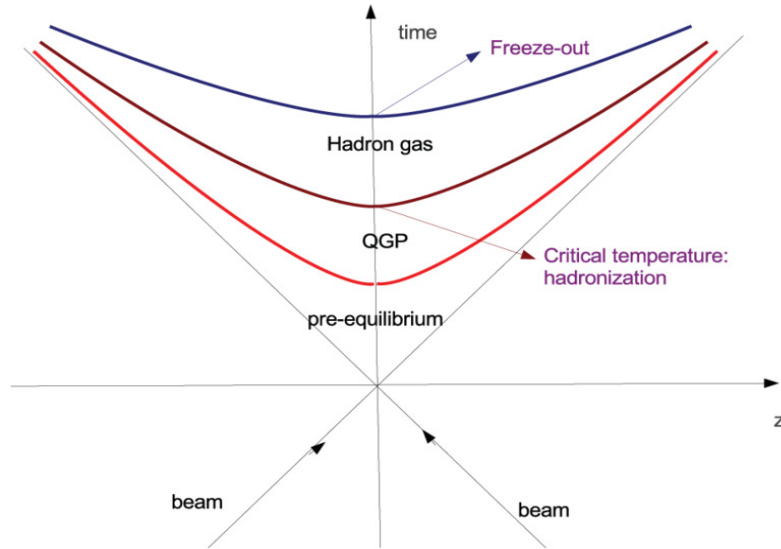


Figure 1.6: Illustration of space-time evolution of an AB collision.

cease to take place, and the relative abundance of every single particle species does not change anymore. It is considered as a mixed phase that exists between the QGP and hadronic gas. The entropy density is transferred to lower degrees of freedom and therefore, the system is prevented from a fast expansion and cooling due to the softest point defined by a minimum value of the energy density/pressure (ε/p) ratio in the equation of state. The exact mechanism of hadronization is yet unknown. Due to inelastic interactions the system can still maintain local thermal equilibrium.

- **Kinetic freeze-out** - In the hadronic phase the system maintains a collective expansion via hadron-hadron elastic interactions, thereby further decreasing the temperature of the fireball. The thermal or kinetic freeze out is triggered by this expansion, when the time scale associated with the collision mean free path of the particles becomes larger than the time scale associated with the collective expansion. As a result the elastic collisions between the particles slow down, a strongly coupled system evolves into a weakly coupled one, and the final state particles freely stream out from the fireball medium.

1.2.5 Thermodynamics of the fireball

It was none other than E. Fermi who first applied statistical physics and thermodynamics to multiple meson production in high-energy collisions [38]. Fermi assumed that when two nucleons collide, they release their energies within a very small volume $V = 2m_N V_0 / \sqrt{s_{NN}}$, where $V_0 = 4\pi R_\pi^3 / 3$ and $R_\pi = 1/m_\pi$ is the characteristic length (Lorentz contracted)

associated with the pion field. At the instant of collision, a large number of particles are formed. The mean free path of these particles is small compared to the dimension of the interaction volume, and a statistical equilibrium is set up. Subsequently the system decays into one of the many accessible multiparticle states. The decay probability is calculated in the framework of standard statistical physics. The main reason for the introduction of statistical concepts was the breakdown of perturbation theory in describing strongly interacting systems. A large value of the coupling constant prohibits any application of perturbative methods. On the other hand, the large coupling is responsible for multiparticle production, which is a very characteristic feature of strong interaction. The transition probability from an initial to a given final state is proportional to the modulus square of the transition matrix element and to the density of states. The matrix element is treated as a constant. The main effect comes from the available phase space, which grows with increasing collision energy. The probability of having an n -particle final state is proportional to

$$S(n) = \left[\frac{V}{(2\pi)^3} \right]^{(n-1)} \frac{dN}{dE}$$

Here dN/dE is the density of states. The power $(n-1)$ comes because only $(n-1)$ particles have independent momentum. Fermi argued that at very high energies even a detailed statistical description may not be necessary [38]. Assuming that the matter is thermalized, one can calculate the temperature of the produced hadronic system from thermodynamic considerations valid for massless particles. Fermi considered production of pions, nucleons and antinucleons, and obtained the total energy density in the center-of-mass frame as,

$$\varepsilon = \varepsilon_\pi + \varepsilon_{N+\bar{N}} = \frac{\pi^2 T^4}{3}$$

Using the expression for the Lorentz contracted volume we may rewrite the above relation,

$$T^4 = \frac{3\varepsilon^2}{2\pi^2 V_0 m_N} = \frac{9\varepsilon^2 m_\pi^3}{8\pi^3 m_N}$$

This equation may be used to calculate the abundance of produced particles from the thermodynamic relations giving the particle densities in terms of temperature.

As mentioned above a transition from the color neutral hadrons to the color conducting plasma consisting of nearly free quarks and gluons, can be accomplished through high-energy heavy-ion interactions. Using the accelerator facilities like RHIC and LHC it is possible to create such transient states of high energy and/or matter density that have definite equilibrium properties. The fireball however is not a static system and it evolves with space-time. It has been experimentally established that the fireball behaves more like an imperfect fluid possessing a small but finite viscosity, rather than like an ideal gas. To

begin with a static idealization of the fireball system would still be quite instructive, which has been done below in the framework of the MIT bag model [39]. Complexities and finer details that are needed for a more realistic system can gradually be added on at later stages.

In the MIT Bag model a hadron is considered to be a closed spherical bag of radius R composed of non-interacting quarks and/or anti-quarks. Due to the presence of the quarks (anti-quarks) the normal QCD vacuum is destroyed within the bag and we have a perturbative QCD vacuum inside. Energy and momentum conservation at the bag surface is ensured by introducing an external pressure at the bag surface to balance the internal pressure of the confined quarks. Each quark and/or antiquark is a spin- $\frac{1}{2}$ Fermion, massless inside the bag but infinitely massive outside. Therefore, each quark (antiquark) can be described by Dirac's equation for a massless free particle. Using the MIT bag model we can arrive at the thermodynamic conditions necessary to create the QGP [23]. To begin with we treat the quark (anti-quark) system as an ideal relativistic gas of massless ($\epsilon = pc$) Fermions at an equilibrium temperature T . The number density n_q of quarks in such a system can be derived by using the Fermi-Dirac distribution,

$$n_q = g_q \left(\frac{1}{2\pi} \right)^3 \int_0^\infty \frac{1}{e^{(p-\mu_q)/T} + 1} 4\pi p^2 dp$$

The corresponding energy density ε_q is

$$\varepsilon_q = g_q \left(\frac{1}{2\pi} \right)^3 \int_0^\infty \frac{p}{e^{(p-\mu_q)/T} + 1} 4\pi p^2 dp$$

Here μ_q is the quark chemical potential, and the quark-degeneracy factor

$$g_q = g_{spin} \times g_{color} \times g_{flavor}$$

is same as that ($g_{\bar{q}}$) of the anti-quark. If only two flavors (up and down) constitute the gas then $g_q = g_{\bar{q}} = 12$, and if three flavors (up, down and strange) are involved then $g_q = g_{\bar{q}} = 18$. For $\mu_q \neq 0$ neither of the above integrations can be individually worked out because the quark number density is not fixed, though the difference between the quark and anti-quark number density is. Moreover, as a quark can annihilate an anti-quark to produce a quantum of radiation, for a baryon-free gas one can write $\mu_q + \mu_{\bar{q}} = 0$. Presence of an anti-quark of energy ϵ in the gas system can be viewed as the absence of a quark of energy $-\epsilon$. Therefore, the corresponding expressions for an ideal anti-quark-gas will be

$$\begin{aligned} n_{\bar{q}} &= g_{\bar{q}} \left(\frac{1}{2\pi} \right)^3 \int_0^\infty \frac{1}{e^{(p+\mu_q)/T} + 1} 4\pi p^2 dp \\ \varepsilon_{\bar{q}} &= g_{\bar{q}} \left(\frac{1}{2\pi} \right)^3 \int_0^\infty \frac{p}{e^{(p+\mu_q)/T} + 1} 4\pi p^2 dp \end{aligned}$$

Putting the number density expressions together for an ideal massless quark and anti-quark gas we get,

$$n_q - n_{\bar{q}} = g_q \times \left(\frac{\mu_q}{6} T^2 + \frac{\mu_q^3}{6\pi^2} \right)$$

For a two flavor system ($g_q = 12$) we can now determine the net baryon number density as,

$$n_B = \frac{n_q - n_{\bar{q}}}{3} = \frac{2\mu_q}{3} T^2 + \frac{2\mu_q^3}{3\pi^2} = \frac{2\mu_B}{9} T^2 + \frac{2\mu_B^3}{81}$$

since $\mu_B = 3\mu_q$. Similarly we get the energy density as,

$$\varepsilon_q + \varepsilon_{\bar{q}} = g_q \times \left(\frac{7\pi^2}{30} T^4 + \frac{\mu_q^2}{4} T^2 + \frac{\mu_q^4}{8\pi^2} \right)$$

The gluons are massless and there is no conservation rule to restrict their number. The chemical potential $\mu_g = 0$. The number density and the energy density of an ideal gluon gas can be respectively obtained by using the Bose-Einstein distribution function,

$$\begin{aligned} n_g &= g_g \left(\frac{1}{2\pi} \right)^3 \int_0^\infty \frac{1}{e^{p/T} - 1} 4\pi p^2 dp = \frac{g_g}{\pi^2} \zeta(3) T^3 \\ \varepsilon_g &= g_g \left(\frac{1}{2\pi} \right)^3 \int_0^\infty \frac{p}{e^{p/T} - 1} 4\pi p^2 dp = g_g \frac{\pi^2}{30} T^4 \end{aligned}$$

The gluon degeneracy factor

$$g_g = 2(\text{spin}) \times 8(\text{color}) = 16$$

Adding the quark, antiquark and gluon energy densities together and combining the degeneracy factors we get [40],

$$\varepsilon_{qgp} = \varepsilon_q + \varepsilon_{\bar{q}} + \varepsilon_g = \left(\frac{37\pi^2}{30} T^4 + 3\mu_q^2 T^2 + \frac{3\mu_q^4}{2\pi^2} \right)$$

One expects a stable QGP when the pressure inside $P = \frac{1}{3}\varepsilon \geq B$, the equality holds at the boundary of stability. The condition may be used to arrive at the limiting critical values of the temperature T_c , the chemical potential μ_c and the baryon number density n_c ,

$$\begin{aligned} T_c(\mu_q = 0) &= \left(\frac{90B}{37\pi^2} \right)^{\frac{1}{4}} \approx 147 \text{ MeV} \\ \mu_c(T = 0) &= (2\pi^2 B)^{\frac{1}{2}} = 0.43 \text{ GeV} \\ n_c(T = 0) &= \frac{2}{3\pi^2} (2\pi^2 B)^{\frac{3}{4}} = 0.72 \text{ fm}^{-3} \end{aligned} \tag{1.34}$$

If the quark – quark and quark – anti-quark interactions are taken into account then the above expression of energy density is modified as [41],

$$\varepsilon = \left(\frac{37\pi^2}{30} - \frac{11\pi}{3}\alpha_s \right) T^4 + \left(1 - \frac{2}{\pi}\alpha_s \right) 3\mu_q^2 T^2 + \left(1 - \frac{2}{\pi}\alpha_s \right) \frac{3\mu_q^4}{2\pi^2}$$

Using the stability condition and setting the corresponding chemical potential μ_c and temperature T_c we get

$$B = \left(\frac{37\pi^2}{90} - \frac{11\pi}{9}\alpha_s \right) T_c^4 + \left(1 - \frac{2}{\pi}\alpha_s \right) \mu_c^2 T_c^2 + \left(1 - \frac{2}{\pi}\alpha_s \right) \frac{\mu_c^4}{2\pi^2}$$

Under the limiting conditions

$$\begin{aligned} T_c &= \left[\frac{B}{\left(\frac{37\pi^2}{90} - \frac{11\pi}{9}\alpha_s \right)} \right]^{\frac{1}{4}} \quad \text{at } \mu_q = 0, \\ \text{and } \mu_c &= \left[\frac{2\pi^2 B}{\left(1 - \frac{2}{\pi}\alpha_s \right)} \right]^{\frac{1}{4}} \quad \text{at } T = 0 \end{aligned} \quad (1.35)$$

Depending on the values of B and α_s chosen, the critical temperature T_c would lie somewhere between 150 – 200 MeV and the chemical potential μ_c somewhere between 450 – 600 MeV.

1.2.6 Hydrodynamics of the fireball

Relativistic hydrodynamics provides a simple picture of the space-time evolution of the hot and dense matter produced in the central rapidity region of a relativistic AB collision. It is assumed that the expanding system stays in local thermodynamical equilibrium. Without going into the details of any microscopic aspect, hydrodynamics then allows us to describe all the stages of expansion of the fireball, starting possibly from the QGP, through hadronization and ending at the freeze out. Hydrodynamics, although classical in concept and formulation, provides an important computational tool to describe the gross features of AB collisions. It uses the fundamental conservation laws of energy and momentum to build an equation of state for the evolving system.

Landau's hydrodynamic model

Landau [42, 43] reexamined Fermi's original idea, and argued that one should not expect the number of finally emitted particles to be determined only from the equilibrium condition at the instant of collision. Rather the system remains strongly interacting even after the initial stages of the collision, and the number of particles becomes definite only when they

are far apart in phase space. Landau too assumed that a compound system is formed, and energy is deposited in a small volume V which is subjected to a Lorentz contraction in the longitudinal direction. At the instant of the collision a large number of particles are formed. In comparison with the dimension of the collision volume the mean free path of these particles is small, and a statistical equilibrium is set up. If two equal sized nuclei, each of mass number A , collide head on ($b = 0$) with each other, then the total energy of the colliding system in the center of mass frame (E_{cm}) is

$$E_{cm} = A\sqrt{s} = 2Am_N\gamma_{cm} \quad (1.36)$$

The initial energy density ε is then given by

$$\varepsilon = \frac{E_{cm}}{V} = \frac{2Am_N\gamma_{cm}}{V_{rest}/\gamma_{cm}} = 2\varepsilon_{nm}\gamma_{cm}^2 \quad (1.37)$$

where $\varepsilon_{nm} = Am_n V_{rest} \approx 0.15 \text{ GeV/fm}^3$ is the energy density of nuclear matter, $V_{rest} = 4\pi R^3/3 = 4\pi r_0^3 A/3$ is the volume of each nucleus at rest, and r_0 is the nuclear radius parameter. Similarly, the initial baryon number density is

$$\rho_B = \frac{2A}{V} = \frac{2A}{V_{rest}/\gamma_{cm}} = 2\rho_{nm}\gamma_{cm} \approx 0.16 \text{ GeV/fm}^3 \quad (1.38)$$

where $\rho_{nm} = A/V_{rest}$ is the baryon number density of nuclear matter. In terms of the inelasticity factor (K) the initial energy density is then given by,

$$\varepsilon = K \frac{\sqrt{s}}{V} = 2\gamma_{cm}^2 K \varepsilon_h \quad (1.39)$$

where ε_h is the energy density of a hadron. In the second stage of the collision, under the influence of a longitudinal velocity gradient the system starts expanding. The transverse gradients are also present, but initially the longitudinal gradient is predominant and the early expansion is approximated as one-dimensional. The expanding system is regarded as an ideal fluid with zero viscosity and zero thermal conductivity. During the expansion the mean free path of the particles constituting the system still remains small in comparison with the dimension of the interaction volume, and the velocities of the particles are comparable to that of the light, justifying thereby the use of relativistic hydrodynamics. Particles are formed and absorbed in the system throughout the first and second stages of the collision. As the system expands, the mean free path of the particles becomes comparable to the dimension of the colliding system, and the interaction between the particles becomes weak. The expanding system then breaks up into individual particles when its temperature $T \sim m_\pi$. For a perfect fluid only one equation of state is necessary to describe the hydrodynamic expansion. If P is the pressure and ε is the energy density of the fluid, mainly composed of pions, then

following the black body radiation law $P = \frac{1}{3}\varepsilon$. Assuming that in comparison with the temperature T the baryon chemical potential μ_B is small, we get

$$Ts = \varepsilon + P \Rightarrow Tds = d\varepsilon$$

where s is the entropy density. Combining the above two relations we find that

$$s \propto \varepsilon^{3/4} \quad \text{and} \quad T \propto \varepsilon^{1/4}$$

The initial energy density $\varepsilon \propto \gamma_{cm}^2$, $E_{cm} \propto \gamma_{cm}$, and $\varepsilon \propto E_{cm}^2$. As a result,

$$s \propto \varepsilon^{3/4} \propto E_{cm}^{3/2}$$

A perfect fluid does not have any viscosity and during the hydrodynamic expansion the total entropy of the system remains unchanged. According to the black-body radiation formula,

$$N_\pi \propto sV \propto E_{cm}^{3/2} V_{rest} / \gamma_{cm} \propto AE_{cm}^{1/2} \propto AE_{lab}^{1/4}$$

which implies that heavy nuclei are better suited for pion production and that pion multiplicity grows slowly with collision energy. Landau solved the hydrodynamic equations in one and three-dimensions. An exact solution was obtained in one-dimension [44] which gave the same result as Landau's in the asymptotic region.

A necessary condition for the applicability of the Landau's picture to central relativistic AB collisions is that the nucleons in the front part of each of the colliding nuclei, while traversing through the other nucleus, must lose all of their kinetic energies in the center of mass frame. This demands that the average energy loss of these nucleons per unit length should be greater than a critical value given by,

$$\left| \frac{dE}{dz} \right|_{cr} = \frac{E_{cm}/2}{(2R/\gamma_{cm})} \quad (1.40)$$

Although at low energies ($E_{cm} < 10$ GeV) Landau's theory gives satisfactory results, but at ultra-relativistic energies ($E_{cm} = 200$ GeV) the condition becomes too stringent to be attained. Hence, Landau's picture breaks down when the required stopping power becomes too large. Furthermore, in contrast to the requirements of Fermi's and/or Landau's approach, the thickness of the colliding nuclei cannot be infinitely small even in the ultra-relativistic region. Also, in this model the boundary condition is specified at the time of maximum compression, whereas the entire matter is distributed over a small but finite volume. However, particle production is not an instantaneous process and it shows the characteristics of space-time correlation – fast particles are produced later and further away from the collision

center than the slow particles, which is not taken into account in Landau's model. The main criticisms of Landau's model are that, the leading particle effect is neglected, and in order to achieve full stopping, removal of radiation energy due to deceleration is required. These difficulties can be removed if one assumes that during the collision the valence quarks move without much interaction, and the energy carried by the gluon fields is stopped within the collision volume [45–47]. The assumption is justified because, due to color degeneracy the gluon-gluon interaction cross-section is larger than the quark-quark cross-section. To be consistent with the initial condition of Landau's model the gluon field should thermalize after a certain time.

Bjorken's hydrodynamical model

Bjorken introduced a hydrodynamic model [48] that is based on the assumption that at sufficiently high-energy the rapidity distribution of the final state particles is uniform in the mid-rapidity region. The space-time evolution of the system should look essentially same in all center-of-mass frames. It is also assumed that the strongly interacting matter present within the collision volume, reaches a state of local thermal equilibrium after the collision and subsequently expands adiabatically. The evolution of the system is determined by the initial conditions, and an equation of state (EoS) that transfers the energy and baryon density to the pressure exerted by the system, and which is subjected to the constraints of local conservation of energy-momentum and currents [49, 50]. The EoS for a non-dissipative ideal fluid can be mathematically formulated as

$$\begin{aligned}\partial_\mu T^{\mu\nu}(x) &= \partial_\mu [(\varepsilon(x) + P(x))u^\mu u^\nu - g^{\mu\nu}P(x)] = 0 \\ \partial_\mu j_B^\mu(x) &= \partial_\mu [n_B(x)u^\mu(x)] = 0\end{aligned}\tag{1.41}$$

where

$$T^{\mu\nu} = [\varepsilon + P] u^\mu u^\nu - g^{\mu\nu} P$$

is the relativistic stress energy tensor, ε is the energy density, P is the pressure, j_B^μ is the charge-current density, n_B is the baryon number density, and $u^\mu = (\gamma, \gamma \bar{v})$ is the four-velocity, all defined in the local rest frame (x) of the fluid. In Bjorken's theory all thermodynamic quantities characterizing the central region should depend only on the longitudinal proper time $\tau = \sqrt{t^2 - z^2}$ and longitudinal velocity $u_z = z/t = \tanh y$, so that $u^\mu = (t/\tau, 0, 0, z/\tau)$. Bjorken's equation is now transformed as,

$$\frac{\partial \varepsilon}{\partial \tau} + \frac{\varepsilon + P}{\tau} = 0\tag{1.42}$$

Using $\varepsilon = \lambda P$, where $\lambda = dP/d\varepsilon$ measures the elastic wave velocity in the medium, and the thermodynamic relation, $\varepsilon + P = Ts + \mu_B n_B$, we get,

$$\varepsilon(\tau_f) = \varepsilon(\tau_i) \left(\frac{\tau_i}{\tau_f} \right)^{1+\lambda} \quad (1.43)$$

For zero baryon density,

$$s(\tau_f) = s(\tau_i) \left(\frac{\tau_i}{\tau_f} \right) \quad \text{and} \quad T(\tau_f) = T(\tau_i) \left(\frac{\tau_i}{\tau_f} \right)^\lambda \quad (1.44)$$

A QGP to hadron gas phase transition causes softening of the EoS. As the temperature crosses its critical value, the energy and entropy densities quickly increase while the pressure rises slowly. The derivative $dP/d\varepsilon$ has a minimum at the end of the mixed phase, known as the softest point. The diminishing driving force slows down the build-up of flow. The preliminary conditions, which are input parameters, define the initiation of the hydrodynamic evolution and the relevant macroscopic density distributions at that point of time. The hydrodynamic evolution is terminated by implementing the freeze out condition, which describes the breakdown of local equilibrium due to decreasing local thermalization rates. In non-central collisions, driven by its inner asymmetric pressure gradients, the system will expand more prominently in the direction of the reaction plane than in the direction perpendicular to the reaction plane. As the time evolves, the system becomes less and less deformed. To estimate the initial energy density of a Bjorken-type fluid element one has to go to the fluid rest frame. All particles are originating from a cylindrical volume of cross-section area A , which actually is the overlap area of the interacting nuclei, and of length $v_z t$. We concentrate on a thin slab of thickness dz centered between the two pancake-like moving nuclei. The point of impact is assumed to be the origin ($z = 0$) of our frame of reference. Therefore $dz = \tau \cosh y dy$, and ignoring the collisions among produced hadrons one gets the energy density as,

$$\varepsilon_{BJ} = \frac{\Delta E}{\Delta V} = \frac{E dN}{A dz} = \frac{m_t dN}{\pi R^2 \tau dy} = \frac{1}{\pi R^2 \tau} \frac{dE_t}{dy} \quad (1.45)$$

Taking the proper time $\tau \approx 1$ fm/c and dN/dy to be the central rapidity density of produced particles, this relation was first derived by Bjorken [48]. However, a perfect fluid must undergo an isentropic expansion, and the entropy of the expanding fireball should be a conserved quantity. In terms of the entropy density $s = S/V$ for a one-dimensional expansion. In order to compensate the Lorentz contraction, a relation like $s_i \tau_i = s_f \tau_f$ should hold between the initial and final proper time. For massless particles $\varepsilon \propto T^4$ and $s \propto T^3$. Correspondingly,

$$\varepsilon_f = \varepsilon_i \left(\frac{\tau_i}{\tau_f} \right)^{4/3} \quad (1.46)$$

which contradicts Bjorken's formula, $\varepsilon_{BJ} \sim \tau^{-1}$. The energy density formula should therefore be modified as,

$$\varepsilon = \frac{1}{\pi R^2 \tau_0} \frac{dE_t}{dy} \left(\frac{\tau_f}{\tau_i} \right)^{1/3} = 2 \varepsilon_{BJ} \quad (1.47)$$

1.2.7 QCD phase diagram

The study of QCD phase diagram is an important and one of the primary goals of high-energy heavy-ion physics research. The QCD phase diagram shown in Figure 1.7, uses temperature (T) and baryo-chemical potential (μ_B) as independent variables. It shows the location of different states of nuclear, hadronic and partonic matter, indicates the type of transition from one phase to another, and marks the critical point(s) and the phase boundaries. These are some of the major issues that are still under intense investigation [51, 52]. There are two extreme conditions of QGP to hadron phase transition, (i) at high temperature and zero net baryon density, and (ii) at high baryon density and zero temperature. The $T = 0$ and $\mu_B = 0$ point corresponds to the QCD vacuum. Nuclear matter exists at T close to zero and $\mu_B = 940$ MeV, the first non-vacuum state along the μ_B -axis and a strongly correlated super-fluid composed of non-relativistic nucleons. At a higher μ_B and low T the state of matter can be described as a degenerate neutron gas, which is expected to be common in neutron stars. Since the NN interaction is somewhat like the Van-der-Waals interaction between molecules, with increasing temperature a transition similar to the liquid-gas phase transition takes place. This ends at a critical temperature $T \simeq 18$ MeV. Further heating results in a weakly interacting gas of hadronic resonances, in which the density of states grows exponentially for both mesons and baryons [35]. This suggests that hadronic matter below T_c behaves like a Hagedorn gas. One route to achieve the color deconfinement is to increase the pressure, and as such the density. Increase in pressure will push the nucleons closer until their typical size becomes larger than the average inter-nucleon distance. This will make the nucleons overlap and the boundaries of individual nucleons to melt. If the pressure is increased beyond $1 \text{ GeV}/\text{fm}^3$ the degenerate neutron gas no longer remains stable, because the degeneracy pressure is not sufficient to sustain a stable equilibrium. This will result in a transition to a gas of quarks, that are no longer confined within the nucleons. Further increasing the pressure is expected to result in a color superconductor. In this phase, some of the quarks will form a condensate of $q\bar{q}$ Cooper-pairs which will induce a color Meissner effect. At even higher densities the QCD interaction weakens, which opens up the possibility of a so called color-flavor locked (CFL) phase. This is a super-fluid which is an electromagnetic insulator and breaks chiral symmetry. If on the other hand, the nucleon gas is heated up to $T > 100$ MeV it becomes a hadron gas. Several hadronic species like pions and excited nucleons exist in equilibrium. Increasing the temperature further will

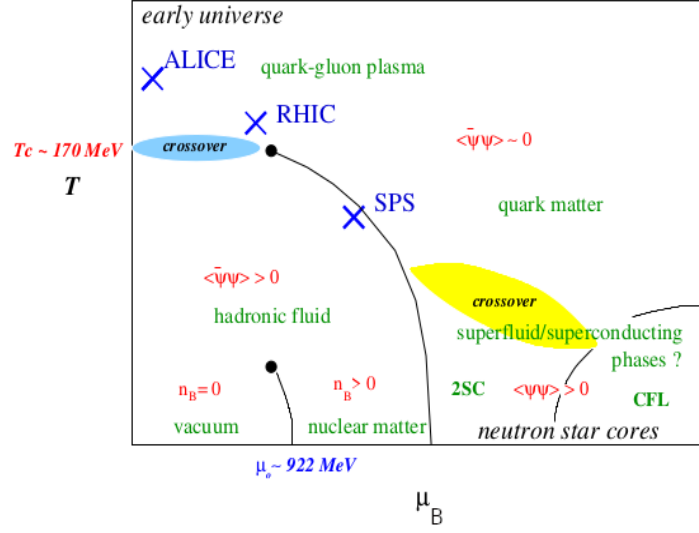


Figure 1.7: Sketch of QCD Phase Diagram [13].

cause a transition to the QGP phase. The low T and high μ_B region of the phase diagram has not been extensively studied either in experiments or in theory. We shall perhaps have to wait until the results from STAR beam energy scan program and/or CBM-FAIR become available.

The high T and low μ_B region of the QCD phase diagram has been investigated quite extensively in heavy-ion experiments held at the LHC and RHIC. The high T and low μ_B QGP should behave like a dilute gas of weakly coupled partons. However, contrary to the expectations the LHC and RHIC results suggest that the QGP so created in these experiments rather behave like a strongly coupled liquid. The parameter that decides the material property of such a QGP is its specific viscosity. According to our current understanding about the evolution of the early universe, there were two symmetry breaking processes and therefore two phase transitions, (i) the spontaneous breaking of electroweak symmetry taking place at a few hundred MeV, and (ii) the spontaneous breaking of chiral symmetry of the SU(3) color group at $T < 200$ MeV. For finite quark mass the lattice QCD and common wisdom suggest that at least at small μ_B both should occur at a common T_c . At near-zero net baryon density non-perturbative lattice QCD places this confinement - deconfinement transition at an energy density of about a few GeV/fm^3 , and at a critical temperature $T_c \approx 170$ MeV [53–58]. At $\mu_q \approx 0$ the transition is a cross-over at around $T \sim 150 - 170$ MeV, whereas QCD predicts that in a baryon rich environment the transition to deconfinement is of first order. One should therefore expect a QCD critical end point (CEP) where the first order transition line ends up at the cross over. To locate the CEP is of current research interest. At the CEP the first order transition becomes continuous, resulting in long range correlations and fluctuations at all length scales. For a system in between, the above two

limits i.e. (i) $\mu_B = 0$ and high T , and (ii) $T = 0$ and high μ_B , there is a pressure arising from the thermal motion of the particles as well as from the degeneracy of the Fermion gas. The study of the intermediate region of the phase diagram is quite complicated as perturbation theory cannot be applied to the QCD near T_c . Furthermore at finite baryon density the usual lattice approach fails [23, 54, 59]. There exist however, various other effective theories and phenomenological models [8, 60] which form the basis of the QCD phase diagram shown very naively in Figure 1.7.

1.3 QGP signals

One must identify appropriate signals that can detect a QGP state created in high-energy heavy-ion collisions. Formation of QGP is followed by expansion and cooling of the fireball. Below the confining temperature T_c , color neutral hadrons are formed and freeze-out. A hot and dense HG forms the background in this case. The task is to identify the QGP signals from a debris of hundreds, sometimes thousands of particles. This is rather difficult because one requires a precise knowledge of the HG under extreme conditions of temperature and density. The picture for a HG that we employ, either involves an equilibrated statistical system or an ideal, non-interacting system or we consider nuclear collisions as multiple, coherent hadron-hadron collisions etc. We are not sure whether such idealized pictures can describe the ultra-relativistic heavy-ion collisions in a realistic manner. The standard method used in the QGP diagnostics is to compare the prediction of heavy-ion collisions incorporating the presence of QGP with the prediction of models that involves the dynamics of a hot and dense HG. In case we find any anomaly or difference between the two pictures, we can subscribe it to an exotic phenomenon, e.g. QGP formation. In high-energy nuclear collisions we expect multiple scatterings and hence a rapid increase in the entropy followed by a quick thermalization. An important question is whether confinement survives this thermalization or not. In case it does, we have hadrons in the system, if it does not we have a QGP in the fireball. Some of the signatures commonly used to detect the QGP or a QGP-like state are very qualitatively summarized below.

1. **J/Ψ Suppression:** Quarkonia are bound states of heavy quark-antiquark pairs. They are smaller than even the light hadrons and are much tightly bound. Therefore, they can survive in a QGP even above the deconfinement temperature and melt down only when the color screening radius drops down to the quarkonium size. Since different quarkonium states have different sizes and binding energies, this will lead to a sequential suppression of the quarkonia, first the larger and loosely bound excited states, and then the smaller and tightly bound states [61]. Such patterns can provide a spectral

analysis of the QGP, similar to that obtained for the sun by studying the solar spectra. An alternative explanation for the J/Ψ suppression involves J/Ψ collisions with the hard deconfined partons present in the QGP [62]. A J/Ψ produced somewhere in the fireball has to cross a certain region of hadronic/partonic matter before escaping the collision region, and because it can interact inelastically with particles on its way out, it may be destroyed. A survival probability can be defined as, $\exp(-L/\lambda)$, where L is the distance traveled by the J/Ψ , $\lambda = (n\sigma_{abs})^{-1}$ is the absorption mean free path and n is the particle number density within the fireball medium [63].

As a hard process charm production in nuclear collisions increases with collision energy much faster than that of the light quarks. At sufficiently high energy the produced medium should contain more charm quarks than present in a QGP at chemical equilibrium. If at the hadronization point the charm and anticharm quarks combine statistically to form charmonium states, the combination mechanism should lead to an enhanced J/Ψ production, even if all the direct J/Ψ -s are dissociated [64]. The sequential suppression and statistical regeneration, thus present two opposite patterns. It should be emphasized that statistical recombination would on one hand provide clear evidence for the presence of a thermal medium. On the other, it presupposes a statistical charmonium production mechanism, quite distinct from the hard production that is generally discussed.

2. **Jet Quenching:** In very high-energy collisions, when a parton belonging to a nucleon of one of the incoming nuclei collides with that of the other coming from the opposite direction, high p_t partons are produced. They are commonly referred as jet-partons, they fly off in every possible directions from the collision point, and finally fragment into hadrons emitted in narrow cones. When some of these jet-partons enter a thermalized fireball, they interact with the medium and lose their energies and momenta before hadronization [65]. This loss is commonly known as the jet quenching, and is estimated through a mathematical ratio known as the nuclear modification factor (see Equation (1.33)). If there is no jet quenching then the ratio must be unity for all jet momenta. However, if the ratio tends to be less than unity, it serves as a definite measure of jet suppression in the medium [66–71]. This particular mathematical entity is a suitable candidate for the signature of formation of a thermalized medium of deconfined quarks and gluons.
3. **Photon production:** One of the proposed signals of QGP is the direct photon production. The direct photons are defined to be all produced photons, except those coming from hadron decays in the last stage of the collision. There are several processes that can produce the direct photons [72]. The dominant contributions come from the annihilation processes like $q\bar{q} \rightarrow g\gamma$, $q\bar{q} \rightarrow \gamma\gamma$, from the QCD Compton processes

like $qg \rightarrow q\gamma$, $\bar{q}g \rightarrow \bar{q}\gamma$, and from the electromagnetic Bremsstrahlung of quarks, $q \rightarrow q\gamma$. The photon mean free paths are much larger than the transverse size of the region of hot matter created in any nuclear collision, because photons interact only electromagnetically with the medium. As a result, photons with high-energy created in the core of the strongly interacting plasma, can generally pass through the surrounding matter without much interaction, carrying information directly from wherever they are formed. In the hadronic phase the dominant contributions come from processes like $\pi\pi \rightarrow \rho\gamma$, $\pi\rho \rightarrow \pi\gamma$, $\pi\pi \rightarrow \eta\gamma$, $\pi\eta \rightarrow \pi\gamma$ reactions and the $\omega \rightarrow \pi^0\gamma$, $\rho^0 \rightarrow \pi^+\pi^-\gamma$ decays. Thus there is a huge amount of background radiation. For ultra-relativistic nuclear interactions it will be an exceptional thermometer if the thermally produced photon component can be separated from the background. The high- p_t photons can be used to estimate the momentum of the associated parton, allowing a characterization of the in-medium parton energy loss. The prompt photons carry information about the initial state and its possible modifications in nuclei, and should thus be one of the best probes of gluon saturation. The thermal photons emitted from the fireball matter carry information on its temperature. Since quarks and gluons have different momentum distributions in the QGP and hadronic phase, one can get information about a transition to the QGP phase by analyzing the photon spectrum. Hydrodynamic models applied to QGP have shown that the increase in photon number at large p_t is a QGP signal [73].

4. **Lepton pair production:** Production of direct lepton pairs like e^+e^- or $\mu^+\mu^-$ is one of the reliable probes of hot and dense fireball [74]. Leptons interact only electroweakly with the fireball medium and subsequently leave the interphase region without any much interaction carrying information about the properties of the matter at the time when they were produced. Dileptons are mainly produced by thermal $q\bar{q}$ annihilation ($q\bar{q} \rightarrow e^+e^-$ or $q\bar{q} \rightarrow \mu^+\mu^-$) in the QGP phase, and by the decay of ρ , ω and ϕ mesons in the mixed phase. Furthermore, the decays and Bremsstrahlung processes of mesons and baryons after hadronization can produce leptons. ρ meson provides a special opening to observe in-medium modifications of the vector meson properties such as mass and/or width, which may be associated to the chiral symmetry restoration because of a very short lifetime. For ρ meson $\tau = 1.3$ fm/c, as compared to the typical fireball lifetime of 10 – 20 fm/c at SPS energies. In the analysis of the invariant mass spectrum of the lepton pairs, the primary problem lies in differentiating the contributions coming from different processes. Taking into account of the chiral symmetry restoration, modification of the ρ meson decay channels predicts an increase in the lepton pairs in the intermediate mass region which is supported by experimental results [75].

5. **Charge fluctuations:** Estimation of charge fluctuations would tell us if we have created a system of quarks and gluons [76, 77]). In the QGP phase the unit of charge is $\pm e/3$, while in the hadronic phase the unit of charge is $\pm e$. The net charge of course does not depend on such subtleties, but the fluctuation in the net charge depends on which phase it originates from. Measurement of charge fluctuation is affected by volume fluctuation, which can be avoided if one considers the ratio fluctuations. The task is to find a suitable ratio whose fluctuation is easy to measure and simply related to the net charge fluctuation. An obvious candidate can be the ratio $H = Q/N_{ch}$, where $Q = N_+ - N_-$ is the net charge and $N_{ch} = N_+ + N_-$ is the total charge. N_+ and N_- are respectively the number of positively and negatively charged particles. Instead of using H one may as well consider the charge ratio $R_{ch} = N_+/N_-$. The charged particle multiplicity is directly related to the entropy production. The observable

$$\xi \equiv \langle N_{ch} \rangle \langle \delta R_{ch}^2 \rangle = 4 \langle N_{ch} \rangle \langle \delta H^2 \rangle = 4 \langle \delta Q^2 \rangle / \langle N_{ch} \rangle \quad (1.48)$$

provides a measure of the charge fluctuation per unit entropy. The observable differs between a hadronic system and a QGP. For a pion gas $\xi_\pi \approx 4.0$. Relating the final state charged particle multiplicity N_{ch} to the number of primordial quarks and gluons is not simple. One has to use entropy conservation [76] which leads to $\xi_{QGP} \simeq 3/4$. Event-by-event fluctuation study of conserved quantities like electrical charge, baryon number, strangeness etc. may allow us to locate the CEP.

6. **Hanbury-Brown-Twiss effect:** Correlation between identical particles or interferometry, provides information about the reaction geometry, and hence gives major information about the spacetime structure of the particle emitting source in AB collisions. The information can be extracted by using the two-particle intensity interferometry technique, also known as the Hanbury-Brown-Twiss (HBT) effect [78, 79]. The method was initially developed to measure the angular size of distant stars [80]. The two-particle correlation arises from the interference of particle wave-functions. This kind of correlation depends on whether the particles are bosons or fermions. The degree of interference depends on the degree of coherence of the particle emitting source(s), which is maximum for a completely incoherent source. The source size increases with event multiplicity and decreases with transverse momentum. If QGP is produced it will hadronize populating the central rapidity region. Following the second law of thermodynamics the volume V and entropy S of the QGP and hadronic phase will be related as $V_{qgp} \times S_{qgp} \leq V_{had} \times S_{had}$. Information regarding the final hadronic phase can therefore be used to understand the nature of the intermediate phase(s).

1.4 Multiparticle production

In any collision involving two elementary objects, be they hadrons, nucleons or nuclei, the interaction cross-section (σ) is of primary importance. In emulsion experiments the cross-section is determined by measuring the interaction mean free path. The theoretical framework of cross-section determination is often given by a geometrical (participant-spectator) or optical model. A good parameterization of the AB interaction cross-section is done by using the Bradt-Peters formula [26],

$$\sigma_{AB} = \pi r_0^2 \left(A^{1/3} + B^{1/3} - \delta \right)^2 \quad (1.49)$$

where r_0 and δ are two parameters determined by fitting the measured cross-sections. Detailed studies on the cross-section measurement showed that δ also depends on the mass number of the colliding nuclei and in the CERN-SPS energy region its variation can be parameterized as,

$$\delta = \delta_0 \left(A^{-1/3} + B^{-1/3} \right)$$

No significant energy dependence has been observed for the nuclear inelastic scattering cross-section. The total inelastic cross-section however, shows variation with energy because of the contribution from Electromagnetic Dissociation (ED) events, which becomes significant at higher energies. In relativistic heavy-ion collisions ED of the projectile nucleus takes place via the exchange of a virtual photon between the projectile and target nuclei. At CERN-SPS energies ($E_{\text{lab}} = 200A$ GeV) the maximum energy of the photons that can be exchanged between the interacting nuclei may be as high as $E_\gamma = 4$ GeV. For a low energy photon exchange the nuclei may electromagnetically interact through a dipole (multipole) resonance, causing the target nucleus to excite and then to deexcite by evaporating fragments. On the other hand for a high energy photon they may interact by exciting a Δ (1232) resonance that decays into a nucleon and a pion, either of which can initiate a two-step process of intranuclear cascade accompanied by evaporation tracks [81]. A comprehensive review of multiparticle production in AB collisions at RHIC energies by using thermal and hadronic models can be found in [82]

1.4.1 Multiplicity distribution

It is customary to write down a two body $\rightarrow n$ -particle inclusive reaction as,

$$A + B \Rightarrow p_1 + p_2 + \cdots + p_n + X$$

where X stands for anything, i.e. all possible particles that are not subjected to observation in a given experiment. In contrast, a reaction like

$$A + B \Rightarrow p_1 + p_2 + \cdots + p_n$$

where all the final-state particles are detected, is called an exclusive one. A high-energy AB interaction can be represented as,

$$\text{Projectile (A)} + \text{Target (B)} \Rightarrow \text{Nuclear fragments} + \text{Produced particles}$$

In this type of collisions different types of new particles are produced, most of which ($\gtrsim 90\%$) are π -mesons. The number of particles belonging to a particular species in an event is called the multiplicity of that particular species. By measuring the multiplicity one gets an idea about the degrees of freedom released in the collision process. In AB collisions the term multiplicity usually refers to the number of charged hadrons, if not mentioned otherwise. As mentioned before the multiplicity distribution can also be used to determine the impact parameter of the AB collisions. The multiplicity distribution of charged hadrons was found to be well described by the negative binomial distribution (NBD)

$$P_{\text{NBD}}(n; \mu, k) = \frac{\Gamma(n+k)}{\Gamma(n+1)\Gamma(k)} \frac{(\mu/k)^n}{(1+\mu/k)^n} \quad (1.50)$$

for the first time in $p\bar{p}$ collisions [83], and then for other high-energy collisions involving hadrons, leptons, and nuclei. Equation (1.50) uses two free parameters μ and k related respectively to the mean multiplicity as $\mu = \bar{n}$, and its dispersion as $D = \bar{n} + (\bar{n})^2/k$. Sometimes a double-NBD is required to satisfactorily describe the tail of the distribution. The physical interpretation of NBD was given in terms of a clan picture [84]. Several independent clans are produced in the pp collision. Particles belonging to a particular clan have a common history and they are strongly correlated. In high-energy AB collisions the same idea is used to describe the multiplicity distributions in narrow centrality intervals. For a particular centrality class the clan number is given by,

$$N_{\text{clan}} = w \times N_{\text{part}} + (1-w) \times N_{\text{coll}} \quad (1.51)$$

As mentioned before N_{part} corresponds to soft processes and N_{coll} to hard processes, while w is a weight factor. The charged hadron multiplicity for AB collisions at a given impact parameter is generated by sampling N_{clan} times the pp , or equivalently the NN multiplicity, the latter being generated by NBD. Finally a χ^2 minimization is done by fitting the charged particle multiplicity data obtained from the experiment. The χ^2 minimization gives us the values of w , μ and k , and allows us to connect the experiment with the Glauber model [85].

1.4.2 Pseudorapidity distribution

The (pseudo)rapidity distribution of charged hadrons produced in heavy-ion collisions is an extremely useful global observable that helps us understand several important aspects of multiparticle production. It tells us to what extent the incoming beam energy is utilized to produce new particles. The distributions are single Gaussian shaped when the baryon stopping is significant. For relatively transparent collisions, as is the case in RHIC or LHC experiments, they look like double Gaussian. The distribution is divided into three regions, the projectile fragmentation, the central and the target fragmentation region. At AGS/SPS energies the central region is narrow, and is rich in baryons. On the other hand at top RHIC/LHC energies the central region is wide and almost flat with a small dip at the center. As predicted by the Landau's model the distributions have a functional form like, $dN_{ch}/dy \propto \exp \sqrt{(y_P^2 - y^2)}$, where $y_P = \ln(\sqrt{s_{NN}}/m_p)$ is the projectile rapidity [86]. At higher energies the central (pseudo)rapidity density of charged hadrons $dN_{ch}/d\eta|_{\eta_0}$ becomes higher. We have already seen how in the framework of Bjorken's hydrodynamic model, this central density can be used to determine the initial energy density produced in the AB collisions. For a particular centrality class $dN_{ch}/d\eta|_{\eta_0}$ is also a good measure of the collision centrality. The tails of the distributions are found to be independent of the collision energy, a feature known as longitudinal scaling. If the distributions are plotted as functions of $y' = y - y_P$, they look identical around $y' = 0$. According to the limiting fragmentation hypothesis, the observed (pseudo)rapidity density of particles approaches a limiting value in the fragmentation region even if the colliding energy is increased. Landau's hydrodynamical model predicts that the (pseudo)rapidity spectra of the produced particles should follow a Gaussian distribution [42, 43]. However, fitting a double Gaussian function to the pseudorapidity spectra is motivated by the trend of the data coming from the SPS, RHIC and LHC. The extracted width-parameter is used to study the dynamics of the system. With increase in energy the width of (pseudo)rapidity distribution increases. Using Landau's model this can be related to the longitudinal flow and velocity of sound (c_s) in the fireball medium,

$$\sigma_y^2 = \frac{8}{3} \frac{c_s^2}{1 - c_s^4} \ln \left(\frac{\sqrt{s_{NN}}}{2m_p} \right)$$

where m_p is the proton mass and σ_y is the width of the (pseudo)rapidity distribution. For an ideal gas $c_s^2 = 1/3$. The central (pseudo)rapidity density of charged hadrons shows a linear-log energy dependence in the SiS100 to RHIC range ($\sqrt{s_{NN}} = 2 - 200$ GeV). A weighted combination of the experimental values of particle yield (central particle density per participant pair) in central AB collisions follows an empirical relation like [87, 88],

$$\frac{2}{N_{\text{part}}} \times \left. \frac{dN_{ch}}{d\eta} \right|_{\eta=0} = \alpha + \beta \ln \sqrt{s_{NN}} \quad (1.52)$$

where α and β are fit parameters. Such a behavior seems well justified by the participant-driven picture of the N_{part} scaling of the central density. In addition, as the data show, the process of bulk production is largely characterized by N_{part} or soft scaling, rather than by the number of binary collisions, N_{coll} , the latter being attributed to hard scaling. On the other hand the energy dependence of the particle yield in the top RHIC to LHC range can be fitted by a power law,

$$\frac{2}{N_{\text{part}}} \times \left. \frac{dN_{ch}}{d\eta} \right|_{\eta=0} = \alpha (\sqrt{s_{NN}})^\beta \quad (1.53)$$

but overestimates the lower energy measurements. The fit parameters α , β are obviously different from the previous equation. The energy dependence of the mean multiplicities, integrated over a finite region of central (pseudo)rapidity, are seen to follow a second-order logarithmic polynomial like [87],

$$\frac{2}{N_{\text{part}}} \times N_{ch} \Big|_{\eta=0} = \alpha + \beta \ln(s_{NN}) + \gamma [\ln(s_{NN})]^2 \quad (1.54)$$

once again with a new set of fit parameters. This trend holds even for relatively low-energies. Such a behavior is expected to be a natural consequence of a combination of the Gaussian shape of the (pseudo)rapidity distribution as predicated in Landau's model, the logarithmic increase of the midrapidity density with the c.m. energy, and the limiting fragmentation. The NN inelastic scattering cross-section increases with energy, which affects the N_{coll} value in AB collisions. As a result the particle yield will have a significant energy and centrality dependence. It is observed that the charged hadron yield at mid-rapidity can be factorized in terms of its energy and centrality dependence in the following way [88],

$$\frac{2}{N_{\text{part}}} \times N_{ch} \Big|_{\eta=0} = f(\sqrt{s}) \times g(N_{\text{part}}) \quad (1.55)$$

A fit result to the experimental data provides the following functional forms,

$$\begin{aligned} f(\sqrt{s}) &= \alpha + \beta (\ln s)^2 \\ g(N_{\text{part}}) &= 1 + \beta' N_{\text{part}}^{1/3} \end{aligned} \quad (1.56)$$

1.4.3 Transverse momentum distribution

The hard scattering in nuclear collisions was for the first time reported at CERN ISR [89]. Since this discovery the inclusive p_T measurement has become an important tool in high-energy interactions. An exponential fall of the invariant p_T spectra at low to moderate p_T is a characteristic of a thermalized hadronic system [90]. Any deviation from the exponential

form may therefore be attributed to the partonic structure or some other exotic phenomena [91]. One example of such observation is the suppression of high p_T hadron production in Au+Au collisions at top RHIC energy relative to the pp case at the same energy [90]. The JACEE collaboration, while studying ultra-relativistic cosmic-ray events, observed a rapid increase in the $\langle p_T \rangle$ from its typical range $\langle p_T \rangle \approx 0.34 - 0.4$ GeV/c measured at the collider experiments. For some events the observed value was even ≥ 1 GeV/c, while the energy density of those events was about $2 - 3$ GeV/fm³ [92]. According to [93] a sudden increase in the $\langle p_T \rangle$ value could be an indicator of QGP to hadron transition. Although energy densities comparable to the JACEE events have been achieved in the laboratory, no striking change in the p_T spectra has been observed so far [94]. Some results based on hydrodynamical calculations predict only a modest increase in the $\langle p_T \rangle$ -value for inclusive charged hadrons, even when the QGP phase is taken into account [95]. A hydrodynamical calculation with strong and electromagnetic decays of resonances upto mass 1.4 GeV [96], cannot predict the SPS data on Pb+Pb interactions at $\sqrt{s} = 17$ GeV [97]. Recently, the transverse momentum spectra of strange hadrons within extensive and nonextensive statistics have been studied over a wide range of collision energy [98]. The hadronic cascade model UrQMD gives much steeper p_T spectra at SPS energies [99], and at RHIC the model prediction given an even steeper p_T spectra. This signifies that the UrQMD is not quite capable to produce enough radial flow. Recently the STAR experiment at RHIC published their beam energy scan results for Au+Au interactions [90]. The p_T spectra for identified hadrons measured by the STAR show a mass ordering, that is the inverse slope of the spectra follow an ordering like $\pi < K < p$. The STAR results can be reproduced by a simple thermal model [100], which indicates a possibility of thermalization of the hadronic matter at RHIC. The p_T spectra can also be used to extract the baryo-chemical potential [90], which enriches our information regarding the QCD phase diagram.

1.4.4 Azimuthal angle distribution

In high-energy heavy-ion collisions the particles produced show a high degree of collective behavior which is termed as flow [101]. Due to a spatial asymmetry present in the overlapping volume of the colliding nuclei, a pressure gradient is generated at an early stage of the collision, that leads to an anisotropic transverse collective flow during the expansion of the hot and dense matter [102]. By characterizing the asymmetric azimuthal distribution of particles (commonly charged hadrons) emitted from non-central collisions, we can quantify the outward pressure. The non-zero Fourier components of the invariant azimuthal distribution

$$E \frac{d^3 N}{d^3 p} = \frac{1}{2\pi} \frac{d^2 N}{p_t dp_t dy} \left(1 + 2 \sum_{n=1}^N v_n \cos[n(\varphi - \Psi_R)] \right) \quad (1.57)$$

can be used to characterize the collective behavior of the particles. Here Ψ_R is the azimuthal angle of the reaction plane, a plane spanned by the impact parameter and the beam direction. v_1 measures the total amount of in-plane transverse flow. In an AB collision as the participating nucleons try to stop each other, due to a bounce-off effect exerted by the compressed and heated fireball, the spectator nucleons of the impinging nuclei are deflected away from the beam axis. The directed flow of high- p_T particles produced at the very early stage of an AB collision, continues to evolve until the very late stages. Therefore, directed flow can be used to look into the early time thermalization or even into the pre-equilibrium stage of an AB collision. The v_2 coefficient, also called the elliptic flow parameter, originates from the geometrical asymmetry present initially in the almond shaped transverse overlap region of the colliding system. This spatial asymmetry results in an asymmetry in the momentum space, which in turn gets converted to a pressure gradient in the reaction plane, and ultimately to an azimuthal anisotropy in the final state. At high energies the longitudinal dimension of the Lorentz contracted nuclei is negligible in comparison with their transverse dimension. Correspondingly, the time taken by the nuclei to cross each other, becomes small compared to the characteristic time taken by the elliptic flow to develop. The triangular flow parameter v_3 on the other hand originates from the fluctuations of the initial collision geometry. Unlike the elliptic flow, it should not be very sensitive to the centrality of the collision. The triangular flow parameter v_3 has been found to be able to explain the ‘near side ridge’ and the ‘away side shoulder’ observed in the two-particle correlations [103]. An investigation based on the viscous hydrodynamics shows that the triangular flow is more sensitive to the QGP viscosity than the elliptic flow [104]. Such type of Fourier decomposition really measures particle emission directly correlated with the orientation of the density gradients as shown by the fact that v_2 for all charged particles at low transverse momenta scales linearly with the eccentricity of the overlap region of the colliding nuclei [105]. In the high- p_t region hadronization occurs through fragmentation, whereas in the medium- p_t region it is modeled by quark recombination or coalescence. The phenomenon of constituent quark number scaling gives experimental support to this model. When scaled by the constituent quark number, the v_2 against E_t curves merge into one universal curve, suggesting that elliptic flow actually develops at the quark level, and hadrons form through combination of constituent quarks.

Bibliography

- [1] J. C. Collins and M. J. Perry, Phys. Rev. Lett. 34, 1353 (1975).
- [2] E. V. Shuryak, Phys. Rep. 61, 71 (1980).

-
- [3] D. J. Weir, Gravitational Waves from a First Order Phase Transition, <https://saoghal.net/slides/brda/>, University of Helsinki (2019).
- [4] L. P. Csernai and J. I. Kapusta, Phys. Rev. Lett. 69, 737 (1992).
- [5] J. Berges and K. Rajagopal, Nucl. Phys. B 538, 215 (1999).
- [6] M. A. Stephanov, K. Rajagopal and E. V. Shuryak, Phys. Rev. Lett. 81, 4816 (1998).
- [7] Z. Fodor and S. D. Katz, JHEP 0404, 050 (2004).
- [8] H. Satz, Extreme States of Matter in Strong Interaction Physics, Lect. Notes in Phys. 841, 1 (2012).
- [9] F. Karsch, Lect. Notes Phys. 583, 209 (2002).
- [10] F. Karsch, Nucl. Phys. A 698, 199 (2002).
- [11] R. S. Bhalerao, CERN-2014-001, pp. 219-239 (2013), arXiv:1404.3294v1.
- [12] E. Eichten, K. Gottfried, T. Kinoshita, J. Kogut, K. D. Lane, and T.-M. Yan, Phys. Rev. Lett. 34, 369 (1975).
- [13] S. Hands, Contemp. Phys. 42, 209-225 (2001), arXiv:0105022v1.
- [14] D. Griffiths, Introduction to Elementary Particles, John Wiley and Sons Inc. (1987).
- [15] J. Beringer *et al.* (Particle Data Group), Phys. Rev. D 86, 010001 (2012).
- [16] A. Deur, S. J. Brodsky, G. F. de Teramond, Prog. Part. Nuc. Phys. 90, 1 (2016).
- [17] D. J. Gross and F. Wilczek, Phys. Rev. Lett. 30, 1343 (1973).
- [18] H. D. Politzer, Phys. Rev. Lett. 30, 1346 (1973).
- [19] U. Heinz and M. Jacob, arXiv:nucl-th/0002042 (2000).
- [20] J. Rafelski, Eur. Phys. Jr. A 51, 114 (2015).
- [21] B. Friman, C. Höhne, J. Knoll, S. Leupold, J. Randrup, R. Rapp and P. Senger (Eds.), The CBM Physics Book, Springer (2010).
- [22] J. P. Lansberg, Physics of Ultrarelativistic Heavy-ion Collisions, Talk given in the Energy Atlas Workshop, Benasque, Spain (2015).
- [23] C. Y. Wong, Introduction to High-Energy Heavy-Ion Collisions, World Scientific (1994).

- [24] M. Kliemant, R. Sahoo, T. Schuster and R. Stock, Lect. Notes Phys. 785, 23 (2010), The Physics of the Quark-Gluon Plasma: Introductory Lectures, (Eds.) S. Sarkar, S. Satz and B. Sinha, Springer-Verlag, Berlin, Germany (2010).
- [25] <https://cerncourier.com/a/participants-and-spectators-at-the-heavy-ion-fireball/>.
- [26] H. L. Bradt and B. Peters, Phys. Rev. 77, 54 (1950).
- [27] P. Shukla, arXiv:nucl-th/0112039v1 (2001).
- [28] G. H. Corral, arXiv:1010.3164v1, Lectures given at the 5th CERN-Latin-American School of High-Energy Physics, Recinto Quirama, Colombia, 15 - 28 Mar 2009.
- [29] M. L. Miller, K. Reygers, S. J. Sanders, and P. Steinberg, Ann. Rev. Nucl. Part. Sci. 57, 205 (2007).
- [30] D. Kharzeev and M. Nardi, Phys. Lett. B 507, 121 (2001).
- [31] X.-N. Wang and M. Gyulassy, Phys. Rev. Lett. 86, 3496 (2001).
- [32] N. Herrmann *et al.*, Ann. Rev. Nucl. Part. Sci. 49, 581 (1999).
- [33] J. Adams *et al.* (STAR Collaboration), Nucl. Phys. A 757, 102 (2005).
- [34] J. Letessier and J. Rafelski, Hadrons and Quark-Gluon Plasma, Cambridge University Press, Cambridge (2004).
- [35] R. Hagedorn, Nuovo Cim. Suppl. 3, 147 (1965).
- [36] R. Hagedorn and J. Rafelski, Phys. Lett. B 97, 136 (1980).
- [37] R. Hagedorn, Z. Phys. C 17, 265 (1983).
- [38] E. Fermi, Prog. Theo. Phys. 5, 570 (1950).
- [39] A. Chodos, B. L. Jaffe, K. Johnson, C. B. Thorn and V. F. Weisskopf, Phys. Rev. D 9, 3471 (1974); A. Chodos, B. L. Jaffe, K. Johnson and C. B. Thorn, Phys. Rev. D 10, 2599 (1974).
- [40] R. Vogt, Ultrarelativistic Heavy-Ion Collisions, Elsevier, Amsterdam, The Netherlands (2007).
- [41] D. Evans, QCD and the Quark-Gluon Plasma, Talk given in the Summer School, Queen's University, Belfast, UK (2017).
- [42] L. D. Landau, Izv. Akad. Nauk. Ser. Fiz. 17, 51 (1953).
- [43] S. Z. Belensky and L. D. Landau, Usp. Fiz. Nauk. 56, 309 (1955).

- [44] I. M. Khalatnikov, J. Exp. Theor. Phys. 26, 529 (1954).
- [45] P. Carruthers and M. Duong-Van, Phys. Rev. D. 28, 130 (1983).
- [46] S. Pokorski and L. Van Hove, Acta. Phys. Pol. B 5, 229 (1974).
- [47] L. Van Hove and S. Pokoroski, Nucl. Phys. B 86, 243 (1975).
- [48] J. D. Bjorken, Phys. Rev. D 27, 140 (1983).
- [49] K. Yagi, T. Hatsuda and Y. Miake, Quark-Gluon Plasma, From Big Bang to Little Bang (Cambridge University Press, Cambridge, 2005).
- [50] P. Kolb and U. Heinz, Quark-Gluon Plasma 3, (Eds.) R. C. Hwa and X. N. Wang, World Scientific, Singapore (2003).
- [51] M. Stephanov, Prog. Theo. Phys. Suppl. 153, 139 (2004).
- [52] M. Gazdzicki, M. Gorenstein and P. Seyboth, Act. Phys. Pol. B 42(2), 307 (2011).
- [53] L. Susskind, Phys. Rev. D 20, 2610 (1979).
- [54] J. Kuti, J. Polónyi and K. Szlachányi, Phys. Lett. B 98, 199 (1981).
- [55] J. Engels, F. Karsch, I. Montvay and H. Satz, Phys. Lett. B 101, 89 (1981).
- [56] F. R. Brown *et al.*, Phys. Rev. Lett. 65, 2491 (1990).
- [57] F. Karsch, Nucl. Phys. A 590, 367 (1995).
- [58] R. Stock, hep-ph/9901415 24.
- [59] L. D. McLerran *et al.*, Phys. Lett. B 98, 195 (1981); Phys. Rev. D 24, 450 (1981).
- [60] A. Ayala *et al.*, Nucl. Phys. B 897, 77 (2015).
- [61] T. Matsui and H. Satz, Phys. Lett. B 178, 416 (1986).
- [62] D. Kharzeev and H. Satz, Phys. Lett. B 334, 155 (1994).
- [63] D. Kharzeev, C. Lourenco, M. Nardi and H. Satz, Z. Phys. C 74, 307 (1997).
- [64] P. Braun-Munzinger and J. Stachel, Nucl. Phys. A 690, 119 (2001);
R. L. Thews, M. Schroedter and J. Rafelski, Phys. Rev. C 63, 054905 (2001).
- [65] J. D. Bjorken, Fermilab-Pub-82/59-THY, Batavia (1982).
- [66] M. Gyulassy and M. Plümer, Phys. Lett. B 243, 432 (1990).
- [67] M. H. Thoma, Quark Gluon Plasma 2, (Ed.) R. C. Hwa, p.51, (World Scientific, 1995).

- [68] R. Baier, Nucl. Phys. A 715, 209c (2003).
- [69] R. Karabowicz (BRAHMS Collaboration), Nucl. Phys. A 774, 477 (2006).
- [70] A. Grelli (ALICE Collaboration), Nucl. Phys. A 904, 635c (2013).
- [71] M. B. Tonjes (CMS Collaboration), Nucl. Phys. A 904, 713c (2013).
- [72] J. Kapusta, P. Lichard and D. Seibert, Phys. Rev. D 44, 2774 (1991).
- [73] P. Huovinen and P. V. Ruuskanen, Ann. Rev. Nucl. Part. Sc. 56, 163 (2006).
- [74] E. L. Feinberg, Nuovo Cimento A 34, 391 (1976).
- [75] I. Tserruya, Nucl. Phys. A 681, 133c (2001).
- [76] S. Jeon and V. Koch, Phys. Rev. Lett. 85, 2076 (2000).
- [77] M. Asakawa, U. Heinz and B. Müller, Phys. Rev. Lett. 85, 2072 (2000).
- [78] G. Goldhaber *et al.*, Phys. Rev. 120, 300 (1960).
- [79] U. A. Wiedemann and U. W. Heinz, Phys. Rept. 319, 145 (1999).
- [80] R. Hanbury-Brown and R. Q. Twiss, Nature 178, 1046 (1956).
- [81] G. Singh, K. Sengupta and P. L. Jain, Phys. Rev. C 41, 999 (1990).
- [82] A. Tawfik and E. Abbas, Phys. Part. Nucl. Lett. 12, 521 (2015); F. Karsch, K. Redlich and A. Tawfik, Eur. Phys. J. C 29, 549 (2003); A. Tawfik, Phys. Rev. D 71 054502 (2005); F. Karsch, K. Redlich and A. Tawfik, Phys. Lett. B 571, 67 (2003).
- [83] G.J. Alner *et al.* (UA5 Collaboration), Phys. Lett. B 160, 193 (1985); *ibid* 160, 199 (1985).
- [84] A. Giovannini and L. Van Hove, Z. Phys. C 30, 391 (1986).
- [85] R. Sahoo *et al.*, Adv. High Energy Phys. 2015, 612390 (2015).
- [86] L. D. Landau, Multiple production of particles under collision of rapid particles, in Collected Papers of L. D. Landau, Ed. D. Ter-Haar, pp. 569–585, Pergamon Press, Oxford, UK, 1965.
- [87] E. K. G. Sarkisyan and A. S. Sakharov, Eur. Phys. J. C 70, 533 (2010).
- [88] B. Alver *et al.* (PHOBOS Collaboration), Phys. Rev. C 83, 024913 (2011).
- [89] B. Alper *et al.*, Phys. Lett B 44, 52 (1973);
M. Banner *et al.*, Phys. Lett. B 44, 537 (1973).

-
- [90] L. Adamczyk *et al.* (STAR Collaboration), Phys. Rev. C 96, 044904 (2017).
- [91] J. Schukraft, International Workshop on Quark Gluon Plasma Signatures, 127-143, Cern Report number: CERN-PPE-91-04.
- [92] T. H. Burnett *et al.*, Phys. Rev. Lett. 57, 3249 (1986).
- [93] L. Van Hove, Phys. Lett. B 118, 138 (1982);
E. V. Shuryak and O. V. Zirhov, Phys. Lett. B 89, 253 (1980).
- [94] J. Schukraft, Proc. 19th Int. Symp. on Multiparticle Dynamics, Arles 1988 (World Scientific, 1988).
- [95] M. Kataja *et al.*, Phys. Rev. D 34, 2755 (1986);
J. P. Blaizot and J. Y. Ollitrault, Nucl. Phys. A 458, 745 (1986);
X. N. Wang and R. C. Hwa, Phys. Rev. D 35, 3409 (1987).
- [96] P. Huovinen *et al.*, Phys. Lett. 503, 58 (2001).
- [97] H. Appelshäuser *et al.* (NA49 Collaboration), Phys. Rev. Lett. 82, 2471 (1999).
- [98] A. N. Tawfik, Adv. High Eng. Phys. 2019, 4604608 (2019); H. Yassin, E. R. Abo Elyazeed and A. N. Tawfik, Phys. Scr. 95, 075305 (2020).
- [99] M. J. Bleicher *et al.*, Phys. Rev. C 62, 024904 (2000).
- [100] W. Florkowski and W. Broniowski, Nucl. Phys. A 715, 875 (2003).
- [101] H. A. Gustafsson *et al.*, Phys. Rev. Lett. 52, 1590 (1984).
- [102] J.-Y. Ollitrault, Phys. Rev. D 46, 229 (1992).
- [103] B. Alver and G. Roland, Phys. Rev. C 81, 054905 (2010); *ibid.* 82, 039903 (2010).
- [104] B. Schenke *et al.*, Phys. Rev. Lett. 106, 042301 (2011).
- [105] C. Adler *et al.* (STAR Collaboration), Phys. Rev. Lett. 87, 182301 (2001).

Chapter 2

Experiment and simulation

2.1 Introduction

Nuclear emulsion is a dispersion of silver halide crystals in a gelatin matrix. The medium is used to record charged particle tracks of silver halide micro-crystals fixed into about equal parts in volume, a matrix material consisting of gelatin and water with a small amount of glycerol and a few other substances. An electrically charged particle while passing through the medium produces a latent image. Under proper chemical treatment the image appears as trails of black colloidal grains of metallic silver along the trajectory of the particle. The photo-sensitive silver halide material (mostly AgBr) has three to four times more concentration in nuclear emulsion than that in a conventional photographic plate. The AgBr grains in nuclear emulsions are well separated and are much smaller in size (less than a micron in diameter), whereas the AgBr grains in an ordinary photographic plate are interlocked and they can be as large as several microns. The Ilford G5 emulsion plates used in this experiment have a grain diameter of about 0.3 micron. However, the mean crystal grain diameters are different in different types of emulsions. It is observed that the contrast of nuclear emulsion may be improved if the grains are uniform in size, and the sensitivity goes up with increasing grain size. The dimension of each Ilford G5 emulsion pellicle used in the present investigation is 18 cm. \times 7 cm. \times 600 microns. Gelatin being a hygroscopic material, emulsion can absorb water from the atmosphere. Therefore, while citing the relative size and composition of emulsions, it is necessary to mention the *shrinkage factor* of

Table 2.1: Chemical composition of standard emulsion.

Element	Atomic weight (A)	No. of atoms per cc $\times 10^{20}$	Moles per cc $\times 10^{-3}$	Concentration at 58% R.H.
I	129.93	0.565	0.094	0.012
Ag	107.88	101.01	16.764	1.817
Br	79.92	100.41	16.673	1.338
S	32.06	1.353	0.216	0.249
O	16.0	94.97	16.050	0.007
N	14.01	31.68	5.147	0.053
C	12.0	138.30	22.698	0.227
H	1.008	321.56	53.571	0.074

the medium, and the real time relative humidity of the surrounding. The chemical composition of a standard research emulsion (such as Ilford G5) is given in Table 2.1. In emulsion the total number of atoms is 7.898×10^{22} per cc, whereas the total number of electrons is 1.0446×10^{24} per cc. Taking the nuclear radius parameter $r_0 = 1.2$ fm, the geometrical mean free path of all the elements present in nuclear emulsion comes out ≈ 37 cm. However, the actual interaction mean free path is quite different from this geometrical value.

2.2 Properties of emulsion tracks

The nature of a track formed within emulsion medium depends upon the particle type, energy etc. For instance, a high velocity/energy particle will create rarer grain density that leads to a thinner track. A comprehensive description of the development of tracks created by charged particles in nuclear photo-emulsion is given in [1]. Here we briefly describe some of the important features of the tracks formed in nuclear emulsions.

- (a) **Grain density:** The development of grains in emulsion takes place due to the energy lost by charged particles through ionization while passing through the medium. The grain density is measured to characterize lowly ionizing and fast moving charged particles. The number of grains deposited per micron of a track is defined as the grain density, which is proportional to, (i) the rate of energy lost by the moving particle dT/dx (in KeV per micron), and (ii) the square of the charge (Z) of the particle. A relationship between the grain density dn/dx and the rate of energy loss dT/dx like

$$\frac{dn}{dx} = c \left[1 - \exp \left\{ b Z \left(\frac{dT}{dx} \right)^{1/2} - a^{1/2} \right\} \right] \quad (2.1)$$

has been experimentally verified [2]. Here a , b and c are empirical constants. Consequently, the grain density will have a maximum value near the end of the track. It was found that, as the velocity (β) of charged particle increases, the corresponding grain density initially decreases and reaches a minimum at $\beta \approx 0.45$, and then it saturates slightly above the least value [3–6]. The rise in grain density above the minimum value is due to the distortion of the field associated with the particle – an increase in velocity leads to the longitudinal contraction and lateral extension of the field of the moving particle [1]. The rate of energy loss is found to be $\delta E \sim \log E$. However, this is not reflected in the grain density, as the energy dissipation mostly takes place outside the core of the track. Nevertheless, some of the additional energy loss may lead to the formation of the so-called δ rays, which contribute to the observed limited increase in the grain density. The Cerenkov radiation also contributes to the grain density. Gelatine which has a refractive index ≈ 1.5 will be a source of Cerenkov radiation when $\beta > 2/3$ [7]. Sometimes instead of grain density, the blob density B is measured. A blob is a resolvable spot in which more than one grains are present. The estimation of blob number is equivalent to measuring the number of gaps between two blobs. It is observed that the frequency distribution of gap length exponentially decreases with increasing gap length [8]. The number density of the gaps H exceeding a gap-length l is given by [9]

$$H = B \exp(-gl) \quad (2.2)$$

The slope parameter g is a measure of grain density, but is not exactly equal to the grain density dn/dx . Fowler and Perkins gave an alternative relation for the blob density [9]

$$B = g \exp(-g\alpha) \quad (2.3)$$

where α is a parameter determined by the average grain size. From these two relations one can determine g as a useful ionizing parameter.

(b) **Lacunarity and opacity:** The lacunarity of a track

$$L = \int_0^\infty -l \left(\frac{dH}{dl} \right) dl = \exp(-g\alpha) \quad (2.4)$$

is defined as the fraction of the track made up of gaps. From Equation (2.3) and Equation (2.4) we get, $g = B/L$ and $\alpha = -(L/B) \ln L$. For particles with low Z and high velocity ($\beta \sim 1$) the specific energy loss is small. In such cases the following proportionality holds

$$\frac{dE}{dx} \propto \frac{dn}{dx} \quad (2.5)$$

Assuming $g \propto dn/dx$, one may get $Z^2 \propto -\ln L$. Opacity \mathcal{O} on the other hand, is defined as the fraction of a track that is made up of blobs, and therefore it is related to lacunarity as $\mathcal{O} = 1 - L$. The charge of the track forming particle can be determined either by measuring its lacunarity or opacity. By default for low Z ($Z = 2 - 3$), a high degree of accuracy for the charge measurement can be achieved in this method, because of a dependence like

$$\delta Z \propto \frac{1}{Z} \frac{\delta L}{L} \quad (2.6)$$

Here the error $\delta L = \sigma_L/\sqrt{N_c}$ can arbitrarily be reduced by increasing N_c , the number of cells of equal length over which the measurement of L has been made, and $\sigma_L = \sqrt{\langle L^2 \rangle - \langle L \rangle^2}$ is the variance in L .

- (c) **Delta-rays:** For large Z the rate of energy loss of the moving particle is high, and secondary electrons are produced with sufficient kinetic energies. Some of these electrons may have observable tracks within emulsion. Such electron tracks are referred to as δ -rays. The number of delta-rays n_δ per unit length depends on the specific energy loss as,

$$-\frac{dE}{dx} = \frac{4\pi e^4 Z_p^2 N Z_t}{mv^2} \left[\ln \left(\frac{2mv^2}{I} \right) - \ln(1 - \beta^2) - \beta^2 \right] \quad (2.7)$$

where N is the number of atoms per unit volume of the emulsion material, Z_t and I are respectively, the mean atomic number and ionization potential of the emulsion nuclei and Z_p is the projectile charge number. Therefore, when the lacunarity measurement is not permitted, the method of delta ray counting can be utilized to determine the charge of a particle. For a particle of charge Ze the number of delta rays with energies between W and $W + dW$ is given by [10, 11],

$$dn_\delta = \frac{2\pi N Z_p^2 e^4}{m_e v^2} \frac{dW}{W} \left[1 - \beta^2 \frac{W}{W_{\max}} \right] \quad (2.8)$$

where the upper limit of energy that the electron may receive is

$$W_{\max} = \frac{2m_e v^2 \gamma^2}{1 + 2\gamma \frac{m_e}{m} + \left(\frac{m_e}{m}\right)^2} \quad (2.9)$$

and $\gamma = 1/\sqrt{1 - \beta^2}$ is the Lorentz factor. The lower limit of delta-ray energy is approximately 10 KeV. Integrating Equation (2.8) we get $n_\delta \propto Z^2/\beta^2$. This formula can be utilized to determine the charge of the particle.

- (d) **Particle range:** Charged particles loose energy through collisions with the atoms present in the medium through which they traverse. When the energy of the moving particle becomes less than the ionization potential of the atoms present in the medium, the particle in motion suffers multiple elastic scattering and ultimately stops within

the medium. The track length of the particle is the distance along the trajectory starting from its point of origin to the last developed grain. It is also known as the residual range (R). The true range can then be defined as the distance traveled by the particle before it stops within the emulsion. Knowing the specific energy loss dE/dx and initial energy E_0 , the range of a particle can be determined from the following formula,

$$R(E_0) = \int_0^{E_0} \frac{1}{dE/dx} dE \quad (2.10)$$

Using Equation (2.7) we get from the above

$$R(E_0) = \frac{m}{Z^2} f(v_0) \quad (2.11)$$

where $f(v_0)$ depends only on the initial velocity v_0 . In the non-relativistic limit ($E_0 \ll mc^2$) a range-energy relation for any particle is similar to that of a proton, $R_p = K E_p^n$, where R_p is in microns and the kinetic energy E_p is in MeV, $K \approx 0.262$ and $n \approx 0.575$ are experimentally obtained parameters. For a particle of mass m and charge Ze the range-energy relation reads as [12],

$$E = K \left(\frac{m}{m_p} \right)^{(1-n)} Z^{2n} R^n \quad (2.12)$$

where m_p is the rest mass of proton. Due to different statistical effects, ranges of even mono-energetic particles exhibit straggling. A straggling parameter is defined as,

$$\Gamma_R = \frac{\pi}{2} \left[\frac{\sum_{i=1}^N (R_i - \bar{R})^2}{N} \right]^{1/2} \quad (2.13)$$

The FWHM (ΔR) of the differential range distribution is related to Γ_R by $\Delta R = 0.94\Gamma_R$.

- (e) **Track width:** For a highly ionizing particle the linear track structure contains little information in terms of grain or blob density as n_δ becomes too large to count [13]. In those cases the track width is a useful parameter to identify the charge of a particle. The track width depends on various factors. For instance, the type of emulsion and the developer used, the particle charge, its mass, velocity etc. Experimentally it is found that the track width increases linearly with Z (for $Z > 10$). As the track caused by a heavy-ion reaches toward its end, a thinning down (tapering) of the track is observed due to electron capture, which reduces the effective charge of the ion. The length of this tapered portion (L_t) of the track may also be used to find out the atomic number

of the particle [14]. The following empirical relation is obtained in this regard,

$$L_t \sim Z^\nu, \quad \text{where } \nu \approx 1.0 \quad (2.14)$$

- (f) **Shrinkage factor:** Gelatin and glycerin are both hygroscopic materials. The actual equilibrium thickness and refractive index of both processed and unprocessed emulsion depends on the surrounding humidity. For a qualitative measurement of the track densities, range and angles in emulsion, the original thickness of the emulsion has to be known. The shrinkage factor of emulsion is a parameter that relates the actual thickness of the emulsion plate with its measured thickness. The shrinkage factor S , generally supplied by the manufacturer, is defined by

$$S = \frac{\text{thickness of emulsion layer during exposure}}{\text{thickness of emulsion layer during scanning}} \quad (2.15)$$

2.3 Scanning of emulsion plates

Scanning of an emulsion plate is performed by using along-the-track method under the view of the microscopes. Two different scanning methods are generally employed.

- (a) **Area or volume scanning:** In an area scanning the focal surface of an emulsion plate is swept up and down from the surface of an emulsion to the supporting glass plate. This is done by rolling the fine focus control while observing the events successively coming into and going out of view. Each field of view is scanned from one surface of the emulsion to the other. That means a definite area (actually a volume) of the plate is scanned. Area scanning is employed under the following circumstances, (i) when the events of a particular type in a given volume are to be found, and (ii) when the situation demands a representative sample. Preliminary volume or line scanning may be performed under a magnification of $300 - 400\times$, but the angle measurement and track identification should finally be done under a higher magnification ($\gtrsim 1000\times$). The area scanning however is not an efficient method to find out the single diffractive dissociation events, interactions with the hydrogen nuclei, and therefore to build up a minimum bias event sample.
- (b) **Along the track scanning:** If a stack of emulsion pellicles is exposed to a beam of particles, or if one wishes to study the density and distribution of the beam tracks in the stack, then the procedure for finding the tracks is to traverse each plate parallel to the leading edge and perpendicular to the incoming tracks. This type of scanning is known as *along the track scanning*. The scanning operation is often tiresome and

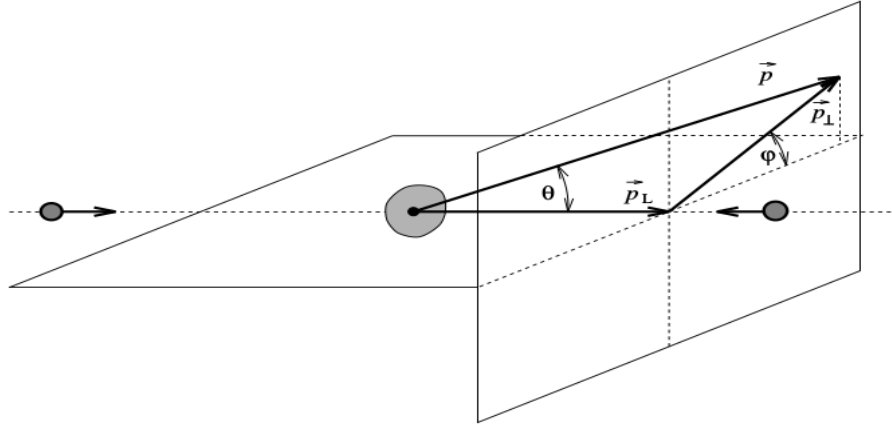


Figure 2.1: Schematic of a secondary track geometry with respect to the projectile.

time consuming. It requires a lot of concentration on the part of the scanner, and the experimental results depend largely upon the correct decision. Care should be taken to avoid personal bias and subjectivity in the decision. To avoid individual bias, the same data sample may be counter checked by independent observers. Electronic counting will no doubt be a faster process, but it would not be an intelligent method of scanning. Like in the case of area scanning, the preliminary scanning along the track may be performed under a magnification of $300 - 400\times$, though the final selection of events has to be done under a higher magnifications ($\sim 1000\times$). By adopting the along the track scanning method it is possible to build up a sample of minimum bias events in emulsion experiments.

2.4 Measurement methods

- (a) **Counting and statistics:** Nuclear-emulsion can discriminate between various types of events as well as tracks originating from different types of events. The ionization of a track may be measured by counting the number of grains or blobs over a particular segment of the track (say $100 \mu m$ of length). Delta-rays over a similar length interval may be counted to identify the charge of the particle producing the track. Energy spectra are determined by counting the number of tracks within a particular range interval. Angular distributions are determined by counting the number of tracks within the prescribed angular intervals. In order to establish the reliability of the collected data, a practical knowledge of counting statistics is therefore required. The track geometry is schematically presented in Figure 2.1. In high-energy interactions often a large number ($10^2 - 10^3$) of new particles are produced. The resulting tracks come out from the interaction vertex within a narrow forward angular interval. Often it becomes

very difficult to distinguish one track from the other. The problem is more profound in the forward direction of an event, that is densely populated by jets of particles. In such cases one may have to take help of a nearby projectile track located within the same field of view, that is essentially moving parallel to the projectile track under consideration. It is to be noted that if the projectile tracks are close to each other, they will experience almost identical distortions in the emulsion. Heavy-ion interactions are rich sources of highly energetic photons. These photons may interact with the Coulomb/nuclear field(s) available in the emulsion medium, and produce e^-e^+ pairs. The angular separations between the electron and positron tracks are often very small, and therefore it is often extremely difficult to identify them as two separate tracks. Moreover, if the $\gamma \rightarrow e^-e^+$ conversion takes place near the interaction vertex, it is very likely that the e^-e^+ tracks will be confused with tracks originating from the primary interaction vertex. When the coordinates of points are recorded at a large distance from a particular interaction vertex, there may be interference with the tracks coming from other interactions as well. These problems can be solved by recording the coordinates of several points on a single track, and through a reconstruction program one may obtain the best fitted track. One may also extrapolate the fit to check whether the straight line is passing through the coordinates of the interaction vertex or not.

- (b) **Dip angle:** The dip angle ξ of a straight track is defined as,

$$\tan \xi = \Delta z / L \quad (2.16)$$

where Δz is the true difference of depth between any two points on the track and L is the length of the projection of the track between these two points. If dry objectives are used, the apparent depth d_a will be less than the corresponding true depth ($d_t = \mu_e d_a$). For oil-immersion objectives d_a and d_t are more or less equal because the refractive index of the immersion oil is roughly equal to that of the emulsion medium, $\mu_{\text{oil}} \approx \mu_{\text{emul}} = 1.52$. The true dip angle ξ_t at the time of passage of the particle is then given by

$$\tan \xi_t = S \tan \xi = S \Delta z / L = S \mu \Delta z / L \quad (2.17)$$

where S is the shrinkage factor.

- (c) **Space angle:** The space angle or the emission angle θ of a track with respect to the beam direction, may also be measured by a simple coordinate method. If two tracks are characterized by their direction cosines (l_1, m_1, n_1) and (l_2, m_2, n_2) , then θ is given by,

$$\cos \theta = l_1 l_2 + m_1 m_2 + n_1 n_2 \quad (2.18)$$

The direction cosine of a track is related to the spatial coordinates of two points on the track (x_1, y_1, z_1) and (x_2, y_2, z_2) by the relation

$$l = \frac{(x_2 - x_1)}{d}; \quad m = \frac{(y_2 - y_1)}{d}; \quad n = \frac{(z_2 - z_1)}{d} \quad (2.19)$$

for $d = [(x_2 - x_1)^2 + (y_2 - y_1)^2 + (z_2 - z_1)^2]^{1/2}$. In order to find out the emission angle of a secondary track one needs to find out the direction cosines of the track as well as the direction cosines of the projectile track.

- (d) **Azimuthal angle:** The azimuthal plane of an interaction is defined as a plane perpendicular to the direction of motion of the projectile nucleus. The track direction projected in this plane with respect to some reference direction may be defined as the azimuthal angle φ of a track (measured counter clockwise). If the projectile direction coincides with one of the directions of the horizontal stage movement (say the x -direction), then

$$\varphi = \tan^{-1} \left(\frac{S\Delta z}{\Delta y} \right) \quad (2.20)$$

If the projectile direction does not completely coincide with the x -direction of the stage motion, then φ for the track is measured by setting the corresponding quantity for the projectile track to zero.

- (e) **Range measurement:** Due to scattering the track of a charged particle in emulsion may not always be straight. The particle under consideration may deviate from its original direction due to Coulomb scattering. Therefore, it is convenient to break up a track into M number of linear segments, and the residual range of the particle may be determined from the relation,

$$R = \sum_{i=1}^M [(x_i - x_{i-1})^2 + (y_i - y_{i-1})^2 + S^2(z_i - z_{i-1})^2]^{1/2} \quad (2.21)$$

where S is the shrinkage factor along the vertical direction. For mounted plates generally no shrinkage factor is associated along the horizontal directions.

- (f) **Momentum measurement:** While passing through the emulsion medium, charged particles experience frequent small deflections due to elastic scatterings effected by the Coulomb field of the atomic nuclei present in the medium. According to [15], the mean projected absolute angle of deviation $\bar{\Theta}$ is given by,

$$\bar{\Theta} = \frac{kZ}{p\beta} \left(\frac{t}{100} \right)^{1/2} \quad (2.22)$$

Here t is the track length followed, Z is the average atomic number of nuclear emulsion, and k is the scattering constant given by,

$$k = e^2 Z Z_p N^{1/2} \left[\ln \left(\frac{\phi_1}{\phi_2} \right) \right]^{1/2} \quad (2.23)$$

N is the number of atoms per unit volume in emulsion, Z_p is the atomic number of the particle moving with velocity $\beta = v/c$ and momentum p , and ϕ_1 (ϕ_2) is the maximum (minimum) value of the projected angle in the plane of the particle trajectory. For an accurate measurement of $\bar{\Theta}$ one can follow the procedure outlined in [16]. Accordingly, the plate is placed on a mechanical stage in such a way that the track is approximately parallel to one of the sides of the stage, say the x -direction. The coordinate (x_0, y_0) of an arbitrary point on the track is measured. The plate is then displaced by a distance t along the x -direction, and the ordinate y_1 of the point is determined by means of an eye-piece scale. The measurement should be performed under a very high magnification ($> 1500\times$), and the ordinate eye-piece scale is commonly replaced by a flair micrometer, which is capable of reading distances within a few hundreds of micron. Once again the stage is moved through the standard distance t , and the ordinate y_2 is recorded. The operation is repeated several times along the length of the track. The absolute value of the second differences, $D_i = |y_{i+2} - 2y_{i+1} + y_i|$ of successive such measurements are determined. The mean absolute value of the second difference between successive chords of length t , corrected for the stage noise and cell length, $\bar{D} = \sum_i^n D_i/n$, can be used to find out $\bar{\Theta}$,

$$\bar{\Theta} = \left(\frac{180}{\pi} \right) \left(\frac{\bar{D}}{t} \right) \quad (2.24)$$

From Equation (2.22) and Equation (2.24) one can determine $p\beta$. It is assumed that the energy loss in a given cell length t of the track is negligible.

2.5 Data characteristics

The data used in this investigation are obtained from the stacks of Ilford G5 nuclear emulsion plates horizontally irradiated by the ^{16}O beam at an incident momentum $p_{\text{lab}} = 200 \text{ GeV}/c$ per nucleon. The equivalent CM energy is $\sqrt{s_{NN}} = 20.05 \text{ GeV}$. The experiment (EMU-08) was performed at the Super-proton Synchrotron (SPS) of CERN by the SUNY at Buffalo group [17]. ^{16}O -emulsion events are found by adopting along the track scanning method

using Leitz microscopes under a total magnification $300\times$. The angle measurements, categorization and counting of tracks etc. are performed by using Koristka microscopes under a magnification $1500\times$.

2.5.1 Event selection

To reduce the loss of tracks and minimize the errors in angle measurements, we exclude events found within $20\mu\text{m}$ thickness from either the top or bottom surface of the plates and events found within 1 mm from the edges of the plates. Proper care was taken to discard interactions induced by the secondary tracks. Using along the track scanning method the total path length followed for ^{16}O -projectile tracks was 117.19 mt. Total number of inelastic ^{16}O +emulsion events found within this path length was 1070. Out of these 957 were inelastic collisions with the emulsion nuclei and 113 were electromagnetic dissociation events [18]. The mean free path for nuclear interactions was $\lambda_{\text{nucl}} = 12.25 \pm 0.40$ cm and that for the electromagnetic dissociation events was $\lambda_{\text{ED}} = 103.71 \pm 9.76$ cm. Corresponding interaction cross-sections were $\sigma_{\text{nucl}} = 1033 \pm 38$ mb. and $\sigma_{\text{ED}} = 592 \pm 57$ mb. respectively. The corresponding numbers for the ^{32}S -projectile can be found elsewhere [19].

2.5.2 Track classification

The tracks emitted from an interaction are classified into the following categories.

1. **Shower tracks:** The shower tracks are produced by singly charged particles moving with speed $\beta > 0.7$. The shower tracks comprise mostly of charged pions with a few percent admixture of charged kaons. The shower tracks have an ionization $I \leq 1.4I_0$, where I_0 is the minimum ionization due to any track observed within the emulsion plate. The multiplicity of such tracks in an event is denoted by n_s .
2. **Gray tracks:** The gray tracks are generally produced by the protons that directly participate in an interaction and are knocked out from the target nuclei. The energy range of gray tracks is usually 30–400 MeV. The ionization of gray tracks lies between $1.4 I_0$ and $10 I_0$. In nuclear emulsion their range exceeds 3 mm. The velocity range of these particles is $0.3c$ to $0.7c$. The multiplicity of gray tracks in an event is denoted by n_g .
3. **Black tracks:** Black tracks predominantly originate from the slowly moving protons and other heavier fragments emitted by the excited target nucleus after an interaction has taken place. A proton generated black track may have kinetic energy < 30 MeV

and velocity $< 0.3c$. The ionization of the black tracks $I > 10I_0$ and their range < 3 mm in emulsion. The multiplicity of black tracks in an event is denoted by n_b .

4. **Projectile fragments:** The projectile fragments are a different class of tracks with constant ionization, long range and small emission angle. They remain confined within an extremely narrow forward cone of semi-vertex angle (θ_f), that depends on the momentum of the incoming nucleus. The tracks are very straight as they suffer very small Coulomb scattering. According to the Fermi gas model of nucleus, the Fermi energy of a nucleon is given by,

$$E_f = \frac{\hbar^2}{2m_p} \left(\frac{3}{2}\pi^2 n_p \right)^{2/3} \quad (2.25)$$

where m_p and n_p are, respectively the nucleon mass and nucleon number density. Numerically E_f is estimated to be 21 MeV and the corresponding Fermi momentum $p_f = \sqrt{2m_p E_f} \approx 200$ MeV/c. For an incident beam with $p_{lab} = 200A$ GeV/c, $\theta_f \approx$ a few mrad. The multiplicity of projectile fragments in an event is denoted by n_f .

The total number of heavy tracks (n_h) emitted from a primary ^{16}O -emulsion event is given by $n_h = n_b + n_g$. If in an event $n_h \geq 8$ with at least one heavy track with $Z \geq 2$, then it should be an interaction with a Ag/Br nucleus. In this investigation we have considered only those ^{16}O -AgBr events for which the projectile nuclei completely fragment in the collisions. The events have no projectile fragment of charge $Z \geq 2$. Only the shower tracks are used in this analysis. To avoid contamination, likely to arise from the fast moving protons, shower tracks falling within the forward Fermi cone as mentioned above, have been excluded from the scope of our analysis. Our final event samples consist of 280 ^{16}O -Ag/Br and 200 ^{32}S -Ag/Br events. The average shower track multiplicity for the ^{16}O -Ag/Br sample is $\langle n_s \rangle = 119.26 \pm 3.59$, whereas $\langle n_s \rangle = 217.79 \pm 6.16$ for the ^{32}S -Ag/Br sample.

2.6 Advantages and disadvantages of emulsion experiments

The nuclear emulsion is used simultaneously as a detector of charged particles and a target medium comprising of nuclei of varying mass numbers. As mentioned above, standard emulsions consist of H, C, N, O, Ag and Br nuclei. As far as high-energy interactions are concerned, information regarding target nucleus mass can be obtained from the characteristic structures of the heavy fragments in an event. Nuclear emulsion has the ability to detect all charged particles coming out of an event (also called a star), i.e. as a detector it has a 4π acceptance. Though, the detection efficiency is not equally good in all directions. Particularly along the vertical direction (toward or away from the direction of vision) the

efficiency is not good. Due to its high density the stopping power of nuclear emulsion is usually very high, and therefore, the interaction probability between a projectile particle and a target nucleus is also very large. Nuclear emulsions are light weight, very easy to handle and less costly compared to other detectors. The sensitivity of undeveloped nuclear emulsion plates lasts for a few weeks. Hence all charged particles passing through it are able to get their tracks permanently recorded for a reasonably long span of time. That makes nuclear emulsion a suitable detector for balloon flight and satellite experiments to study the cosmic-ray events, where heavy projectiles are seldom found. Neutral particles can also be indirectly detected in emulsions as and when they interact with the other nuclei, and produce tracks of charged particles. Nuclear emulsion can be used over a wide range of temperature, from the temperature of liquid Helium up to the boiling point of water. The most striking advantage of nuclear emulsion is its high spatial resolution. For horizontally irradiated stacks of emulsion pellicles an accuracy of 0.1 unit of pseudorapidity can be achieved. This unique feature makes the emulsion experiments important to investigate distributions of produced particles in narrow intervals of pseudorapidity.

There are some difficulties associated with the emulsion experiments too. It is not possible to identify the sign of a charged particle unless a magnetic field is applied. But it is also very difficult to get the magnetic field penetrate into the emulsion material, and to produce enough curvature in the track of a particle moving with relativistic speed. The sensitivity and thickness of emulsion pellicles are affected by temperature, humidity, age etc. Unless special care is taken these factors always introduce errors in the data. The track lengths of most of the produced particles in emulsion are at best a few mm. long. So high magnification devices such as high power microscopes are required to scan and collect the data. Even the automated devices could not speed up the scanning very significantly. This makes the data acquisition process a tedious and time consuming job. For AB interactions in the GeV range, where a few hundreds of particles may come out of an event, the time taken to build up even a moderate statistics requires huge effort. The collected data can never be made fully free from personal bias and errors. Measurement of momentum through elastic scattering is an even more tedious and time consuming process, making it almost impossible for any statistically significant number of tracks. Identification of the target fragments often becomes extremely difficult, and sometimes even impossible. However, a gross distinction between the light group (H, C, N, O) and the heavy group (Ag, Br) of target nuclei can be made.

2.7 Simulation

In this analysis we use the the Ultra-relativistic Quantum Molecular Dynamics (UrQMD) [20] model to simulate the experiment. UrQMD is a microscopic transport model where an AB interaction is considered as a superposition of many elementary NN interactions. UrQMD simulates the space-time evolution of an AB interaction, starting from its initial pre-equilibrium stage to the final freeze-out stage. At low and intermediate energies ($\sqrt{s_{NN}} < 5$ GeV) the model describes the phenomenology of hadronic interactions in terms of interactions between known hadrons and their resonances. At higher energies, typically at $\sqrt{s_{NN}} = 5$ GeV and above, the excitation of color strings and their subsequent fragmentation into hadrons are taken into account. The model was proposed mainly to give a microscopic description of the AB interactions. Until now there is no concrete theory of hadronic interactions, with their vastly different characteristics at different incident energies and in different kinematic regions. Perturbative quantum chromodynamics (pQCD) can be applied to describe hard processes where the four-momentum (Q^2) transfer is large. But pQCD is formally inappropriate for the description of soft processes (low- p_t physics) because of strong coupling. Therefore, low- p_t collisions are described in terms of phenomenological models. Now-a-days a variety of models for hadronic and nuclear collisions are available. The UrQMD is one of them which is quite appropriate for the collision energy involved in the present experiment.

The UrQMD is based upon covariant propagation of hadrons considered on the (quasi)particle level on classical trajectories in combination with stochastic binary scatterings, color string formation and resonance decays. It represents a Monte-Carlo solution of a large set of coupled partial integro-differential equations for the time evolution of various phase space densities of particle species like N , Δ , Λ , π etc. In this model nuclei are treated as a Fermi-gas with a Gaussian density distribution. The wave function of the nucleus is defined as the product of single nucleon Gaussian functions without invoking the Slater determinant that is necessary for proper anti-symmetrization of a many particle state. The nuclear (N -particle) wave function is given by,

$$\Phi = \prod_i \varphi_i(x_j, p_j, t) \quad (2.26)$$

Here a single particle wave function is

$$\varphi_j(x_j, p_j, t) = \left(\frac{2\alpha}{\pi}\right)^{3/4} \exp \left[-\alpha \{x_j - r_j(t)\}^2 + \frac{i}{\hbar} p_j(t) x_j \right] \quad (2.27)$$

In configuration space the centroids of the Gaussian function are distributed at random within a sphere of radius

$$R(A) = r_0 \left(\frac{1}{2} \left[A + (A^{1/3} - 1)^3 \right] \right)^{1/3} : r_0 = \left(\frac{3}{4\pi\rho_0} \right)^{1/3} \quad (2.28)$$

where ρ_0 is the nuclear matter density in the ground state. The finite width of these Gaussians result in a diffused surface region beyond the radius of that sphere. The initial momenta of the nucleons are chosen at random between 0 and local Thomas-Fermi momentum $p_f^{\max} = \hbar c(3\pi^2\rho)^{1/3}$, where ρ is the corresponding local nucleon density. A disadvantage of the initialization mentioned above is that the initialized nuclei are not really in their ground states with respect to the Hamiltonian used for their propagation. However, the parameters of the Hamiltonian are tuned to the equation of state for a finite sized nucleus and to the properties of finite nuclei. If however, the energy of the nucleons within the nucleus is minimized in a self consistent way, then the nucleus would collapse to a single point in momentum space because of the non-inclusion of Pauli's principle. One possible solution to this problem is the inclusion of fermionic properties of the nucleons via the antisymmetrization of the wave function of the nucleus. This ansatz has been implemented in the framework of the Fermionic Molecular Dynamics (FMD) [21]. But the FMD equations of motion are computationally very expensive. To get rid of the problems one can use the so called Pauli potential [22] in the Hamiltonian. Its advantage is that the initialized nuclei remain absolutely stable, whereas in the conventional initialization and propagation without the Pauli potential, the nuclei start evaporating single nucleons after $\approx 20 - 30$ fm/c. A drawback of such a potential is that the kinetic momenta of the nucleons are not equivalent to their canonical momenta, i.e. the nucleons carry the correct Fermi-momentum, but their velocities are zero. Furthermore, the Pauli potential leads to a wrong specific heat and changes the dynamics of string fragmentation.

For nuclear collisions the interaction potential used in UrQMD is the density dependent Skyrme potential [23]. This potential consists of a sum of a two and three-body interaction terms. The two-body term (E^{Sk2}) has a linear density dependence, and models the long-range attractive component of the NN interaction. Whereas the three-body term (E^{Sk3}) is responsible for the short-range repulsive part of the interaction. In addition to the Skyrme potential, the Yukawa (E^{Yuk}), the Coulomb (E^{Coul}) and the Pauli (E^{Pauli}) (optional) potentials are also included in UrQMD. In finite nuclei the usage of a Yukawa term has the advantage that the parameter can be tuned to the proper surface potential of the nuclei without changing the equation of state. With these interactions the classical

UrQMD Hamiltonian reads as,

$$H = \sum_{j=1}^N E_j^{kin} + \frac{1}{2} \sum_{j,k=1}^N \left(E_{jk}^{Sk2} + E_{jk}^{Yuk} + E_{jk}^{Coul} + E_{jk}^{Pauli} \right) + \frac{1}{6} \sum_{j,k,l=1}^N E_{jkl}^{Sk3} \quad (2.29)$$

The time evolution of the system is obtained by the requirement that the corresponding action is stationary under the allowed variation of the wave function. This yields an Euler-Lagrange equation for each parameter,

$$\dot{p}_i = -\frac{\partial \langle H \rangle}{\partial q_i} = -\nabla_{q_i} \sum_{j \neq i} \langle V_{ij} \rangle = -\nabla_{q_i} \langle H \rangle \quad (2.30)$$

$$\dot{q}_i = \frac{\partial \langle H \rangle}{\partial p_i} = \frac{p_i}{m} + \nabla_{p_i} \sum_j \langle V_{ij} \rangle = \nabla_{p_i} \langle H \rangle \quad (2.31)$$

The potential element is given by

$$\langle V_{ij} \rangle = \int d^3x_1 d^3x_2 \varphi_i^* \varphi_j^* V(x_1, x_2) \varphi_i \varphi_j \quad (2.32)$$

These equations are solved numerically. Impact parameter of a collision is sampled according to the quadratic measure, $dW \sim bdb$. Two particles collide if their relative distance $d \leq d_0 = \sqrt{\sigma_{tot}/\pi}$. The total cross-section σ_{tot} depends on the center of mass energy $\sqrt{s_{NN}}$, the particle type and its isospin, which is taken to be symmetric. In the limit $\sqrt{s_{NN}} \geq 5$ GeV the CERN/HERA parametrization for the pp cross section is used [24]. Since the functional dependence of σ_{tot} on $\sqrt{s_{NN}}$ at low energies has a complicated shape, UrQMD uses a set of numerical values for that purpose.

Particle production in UrQMD either takes place via the decay of a meson or baryon resonance or via a string excitation and its fragmentation. For beam energies of about 10 GeV/nucleon particle production in UrQMD is dominated by resonance decays. Production cross-sections for the excitation of individual resonances can be calculated in the framework of one-pion exchange (OPE) or one-boson exchange (OBE) models [25]. Considering the number of resonances generated by the UrQMD, and the limited energy range of their applicability for cross section determination within OPE and OBE models, the calculation of all resonance excitation cross sections in the framework of these models is not practical. Therefore, an effective parametrization based on simple phase space considerations has been employed, and free parameters are tuned to experimental measurements. After the fragmentation, decay of the resonances proceeds according to the branching ratios compiled by the Particle Data Group [24]. The resonance decay products have isotropic distributions in the rest frame of the resonance. If a resonance is among the outgoing particles, its mass must be determined at first in accordance to the Breit-Wigner formula. If the resonance

decays into more than two particles, then the corresponding N -body phase space is used to calculate their momenta. If the outgoing phase space is occupied, the Pauli principle is applied to hadronic collisions. The collision term in UrQMD includes more than fifty baryon species (including nucleon, delta and hyperon resonances with masses up to 2.25 GeV) and five meson nonets (including strange meson resonances). The particles are supplemented by their corresponding anti-particles and all isospin-projected states. The states can either be produced in string decays, s -channel collisions or resonance decays. For excitations with masses more than 2 GeV, a string picture is used. Full baryon/antibaryon symmetry is included in the UrQMD model.

2.7.1 Modeling Bose-Einstein correlation

The Bose-Einstein correlation (BEC) is one of the primary reasons of observing particle correlations in relativistic nuclear collisions. The BEC between identical mesons is a quantum statistical effect that is not present in the UrQMD model. We know that intensity correlations appear due to the symmetrization of the two-particle states. Accordingly, any two particles having momenta q_1 and q_2 , can form a state with amplitude

$$\tilde{A} \propto \frac{1}{\sqrt{2}} \left[e^{i(q_1 x_1 + q_2 x_2)} + e^{i(q_1 x_2 + q_2 x_1)} \right] \quad (2.33)$$

where x_i ($i = 1, 2$) is the emission point of the i -th particle. If the particles are emitted incoherently, the observed two-particle spectrum is expressed in terms of single particle density function $\rho(p)$ as,

$$\rho_2(q_1, q_2) \propto \int dx_1 \rho_1(x_1) \int dx_2 \rho_1(x_2) |\tilde{A}(q_1, q_2)|^2 \quad (2.34)$$

and the two-particle intensity correlation function is given by,

$$C_2(Q) = \frac{\rho_2(q_1, q_2)}{\rho_1(q_1)\rho_1(q_2)} = 1 \pm |R(Q)|^2 \quad (2.35)$$

where the sign $+(-)$ corresponds to bosons (fermions) and $R(Q)$ is the normalized Fourier transform of ρ , the source density [26]

$$R(Q) = \frac{\int dx \rho(x) e^{i(q_1 - q_2)x}}{\int dx \rho(x)} \quad (2.36)$$

This quantity is often parametrized in terms of a source radius R_{inv} , related to the size of the emission region, and a chaoticity parameter λ , which measures the strength of the effect.

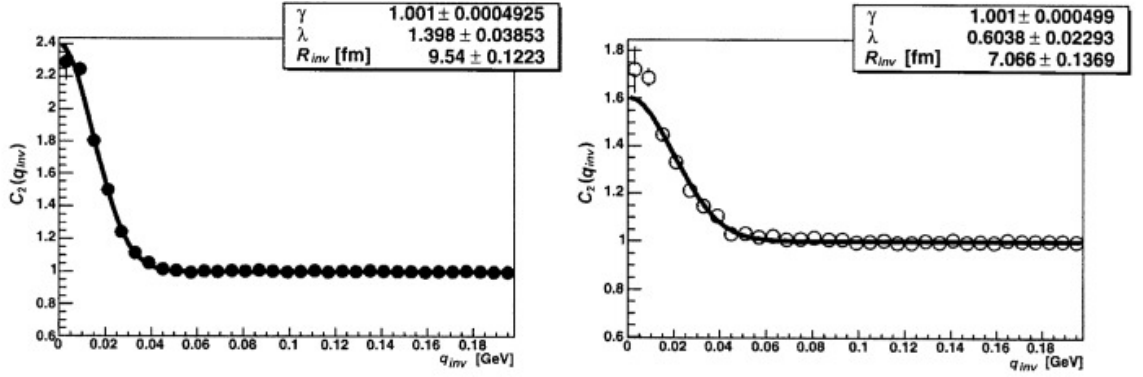


Figure 2.2: The Bose-Einstein correlation function $C_2(Q = q_{inv})$ for $\pi^-\pi^-$ pairs using the charge reassignment algorithm (left panel) and the weighting method (right panel). Gaussian fits are shown in each diagram. The figure is taken from ref. [32]

From the above equation one derives,

$$|R(Q)|^2 = \lambda e^{-R_{inv}^2 Q^2} \quad (2.37)$$

after assuming a spherical emission volume with a Gaussian density distribution. The study of BEC among identical meson pairs is carried out by using the ratio of correlation obtained from the data to the same obtained from a Monte-Carlo (MC). The common method of introducing BEC among particles generated via classical MC simulations is the weighting method with a two-boson weight factor,

$$f_{BEC}(q_{inv}, x) = 1 + \cos[(q_1 - q_2) \cdot (x_1 - x_2)] \quad (2.38)$$

The weighting method computes f_{BEC} using particle momenta and coordinates at the freeze-out. A drawback of this method is that it cannot simulate multi-boson correlations. However, with transport models the weighting method is well justified, as the phase-space densities generated by the transport models are rather low. Recently, a new algorithm has been suggested [27], which claims to overcome this limitation. The algorithm is based on reassigning charges of produced pions and results in formation of quantum Bose-Einstein cells in phase-space, in which the number of identical bosons is enhanced. It conserves the energy-momenta and does not alter any single particle inclusive distribution. Since its original study [28], the BEC of various particle pairs has been studied for a large variety of interacting systems over a wide range of energies [29, 30]. It has been observed that like-charge particle correlations are much stronger than those between unlike-charge particles [31]. We include the BEC effect numerically in the form of an *after burner* [27] making use of the output of the event generator. As mentioned, the algorithm is based on the reassignment of electrical charges of particles, while keeping the particle coordinates unaltered. The particle information are contained in the UrQMD output file *test.f19* written in the OSCAR

format. Only the (event-wise) pi-mesons are taken from the output file. Each particle entry in an event contains a serial number, the particle ID, the particle freeze-out 4-momenta (p_x, p_y, p_z, E) , the particle mass m , and the final freeze-out 4-coordinates (x, y, z, t) . The steps followed in the charge reassignment algorithm are listed below.

- (i) Choose a meson at random from an event, call it the i -th one, and assign a charge ‘sign’ i.e., $+$, $-$ or 0 to it, irrespective of its original charge, with weight factors respectively given by $p_+ = n_+/n$, $p_- = n_-/n$ and $p_0 = n_0/n$. Here n_+ , n_- , n_0 are, respectively the number of $+ve$, $-ve$ and neutral mesons in the event, and $n(= n_+ + n_- + n_0)$ is the total number of mesons present in that event. The chosen meson, i.e. the i -th one, defines a phase space cell.
- (ii) Calculate the distances in 4-momenta $\delta_{ij}(p) = |p_i - p_j|$, and 4-coordinates $\delta_{ij}(x) = |x_i - x_j|$ between the already chosen meson (the i -th one) and all other mesons (indexed by j) that are not yet assigned any charge sign.
- (iii) Assign a weight factor

$$P_{ij} = \exp \left[-\frac{1}{2} \delta_{ij}^2(p) \delta_{ij}^2(x) \right] \quad (2.39)$$
 to each of the j -th particles. The weight factor actually characterizes the bunching probability of the particles in a given cell.
- (iv) Then start generating uniformly distributed random numbers $r \in (0, +1)$. If $r < P_{ij}$, reassign to the j -th meson the same charge sign as the i -th one. Continue the process until either r exceeds P_{ij} , or until all mesons in the event having the same charge sign as the i -th one are exhausted.
- (v) Repeat the whole set of operations for all other mesons for which the charge reassignment has not yet been done. Obviously, the weight factors p_{\pm} and p_0 will now be modified, as some of the particles present in the event are already used up. The algorithm is repeated until the mesons belonging to all charge varieties in the event are used up.

The UrQMD model provides all pion pairs with $Q^2 = (p_i - p_j)^2 = (\Delta E)^2 - (\delta p)^2 < 0$. In order to keep the value of the factor (P_{ij}) below unity, only the pion pairs having a space-like separation, $-R^2 = (x_i - x_j)^2 = (\Delta t)^2 - (\Delta x)^2 < 0$ are accepted [32]. Without changing the overall set of 4-momenta, 4-coordinates, or total meson charge of the system, we can in this way generate clusters of identical charge states of mesons. In Figure 2.2 we illustrate the correlation function $C_2(Q = q_{inv})$ for $\pi^- \pi^-$ pairs computed from the charge reassignment procedure (left panel) and the weighting procedure (right panel) for Au+Au interactions at $\sqrt{s_{NN}} = 200$ GeV generated by the UrQMD model. The results complement each other.

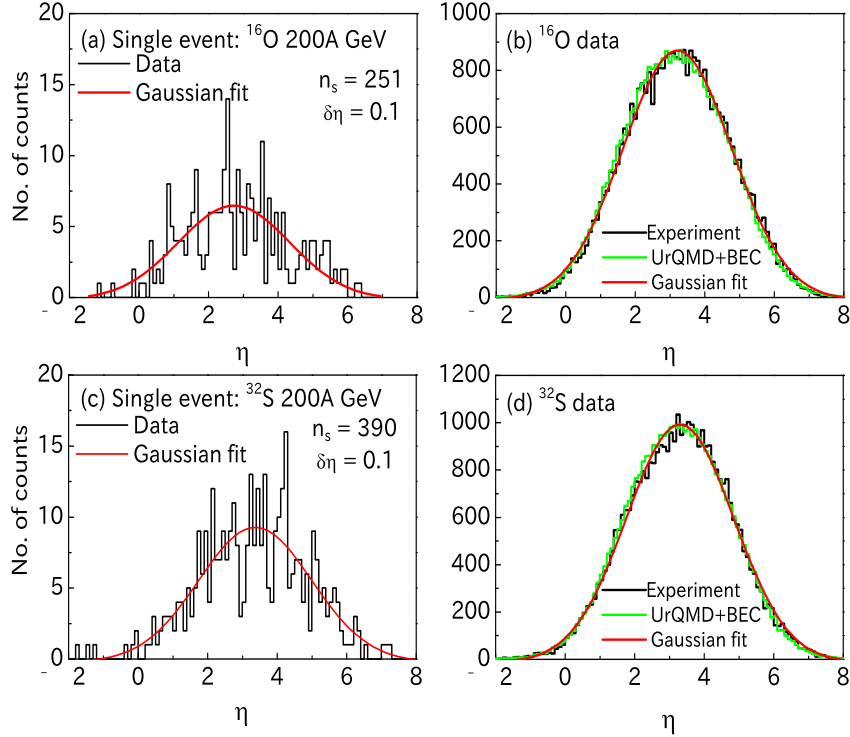


Figure 2.3: (a) η -distribution for an event in ^{16}O -Ag/Br interaction. (b) η -distribution for the ^{16}O sample compared with the UrQMD+BEC model simulation. The lower panel is same as in the upper panel but for the ^{32}S data. In all the cases the experimental distributions are fitted by a Gaussian distribution.

2.7.2 Sampling the simulated events

Using the UrQMD code we simulate the ^{16}O -Ag/Br and ^{32}S -Ag/Br events at $p_{\text{lab}} = 200A$ GeV/c. We first generate minimum bias samples in the laboratory frame separately for the Ag and Br targets and for each projectile. These independent event samples corresponding to Ag and Br targets are then mixed up at random to generate a minimum bias event samples on ^{16}O -Ag/Br and ^{32}S -Ag/Br interactions. The proportional abundance of Ag and Br nuclei in G5 emulsion [13] is maintained during the mixing procedure. All newly produced mesons in the simulated events are retained in the respective output files. The event samples are then passed through the charge reassignment algorithm described in the previous section. From each minimum bias sample we select such events as to match the corresponding experimental shower track multiplicity distribution. Obviously the average shower track multiplicity of the simulated sample is same as the experimental one. The event sample simulated for each projectile is five times as large as that of the experiment. The UrQMD simulation that includes the BEC is denoted by UrQMD+BEC in this document.

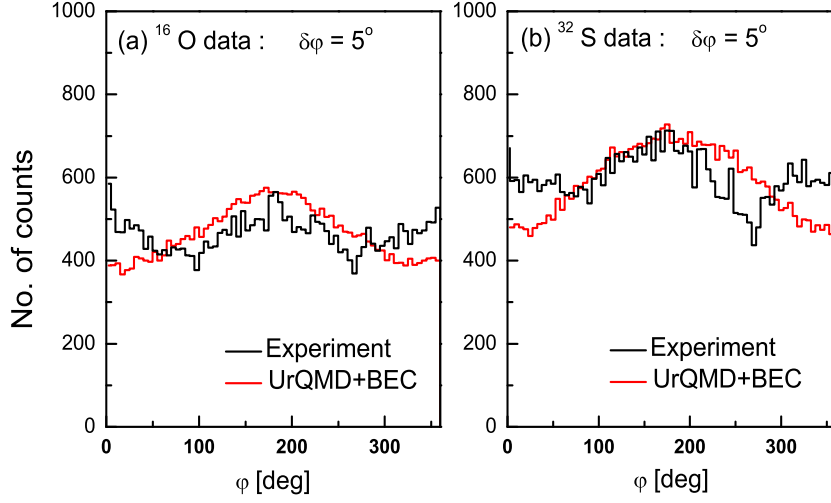


Figure 2.4: Distributions of φ (a) for ^{16}O -Ag/Br and (b) for ^{32}S -Ag/Br interactions. The UrQMD+BEC simulations are shown with the experiments.

2.8 Basic distributions

By measuring the emission angle θ of a shower track with respect to the projectile track the pseudorapidity variable of a particle is determined,

$$\eta = -\ln [\tan(\theta/2)] \quad (2.40)$$

The resolution in η is

$$\delta\eta = -\frac{1}{\sin\theta} \delta\theta \quad (2.41)$$

Therefore, at small angles only a small error in θ ensures a good resolution in η . The accuracy of our η -measurement is $\delta\eta \approx 0.1$ unit. In a 1-dimensional analysis we take η as the basic variable, while it is the (η, φ) plane for a 2-dimensional analysis.

In Figure 2.3 the η -distributions of the shower tracks for two individual events, as well as those for the ^{16}O -Ag/Br and ^{32}S -Ag/Br event samples are shown. The η -distribution of shower tracks for a single event has a lot of spikes and valleys, apparently devoid of any fixed pattern. The background of such event-wise distributions can be very roughly approximated by Gaussian curves, as shown in the figure. For a large sample of events these fluctuations are however smoothed out. The event averaged η -distributions for both projectiles can also be described by Gaussian functions. We fit Gaussian curves to the data and obtain the following fit parameters. The centroid $\eta_0 = 3.32 \pm 0.01$, the peak density $N_{\text{ev}}^{-1} dn_s/d\eta|_{\eta_0} = 31.19 \pm 0.11$, and the width $\sigma_\eta = 1.55 \pm 0.01$ for the ^{16}O -Ag/Br sample. Corresponding values for For the ^{32}S -Ag/Br sample are, $\eta_0 = 3.37 \pm 0.01$, $N_{\text{ev}}^{-1} dn_s/d\eta|_{\eta_0} = 56.34 \pm 0.24$ and $\sigma_\eta = 1.55 \pm 0.01$. In these diagrams of we have included the η -distributions of charged hadrons obtained from the UrQMD generated ^{16}O -Ag/Br and ^{32}S -Ag/Br events, where as

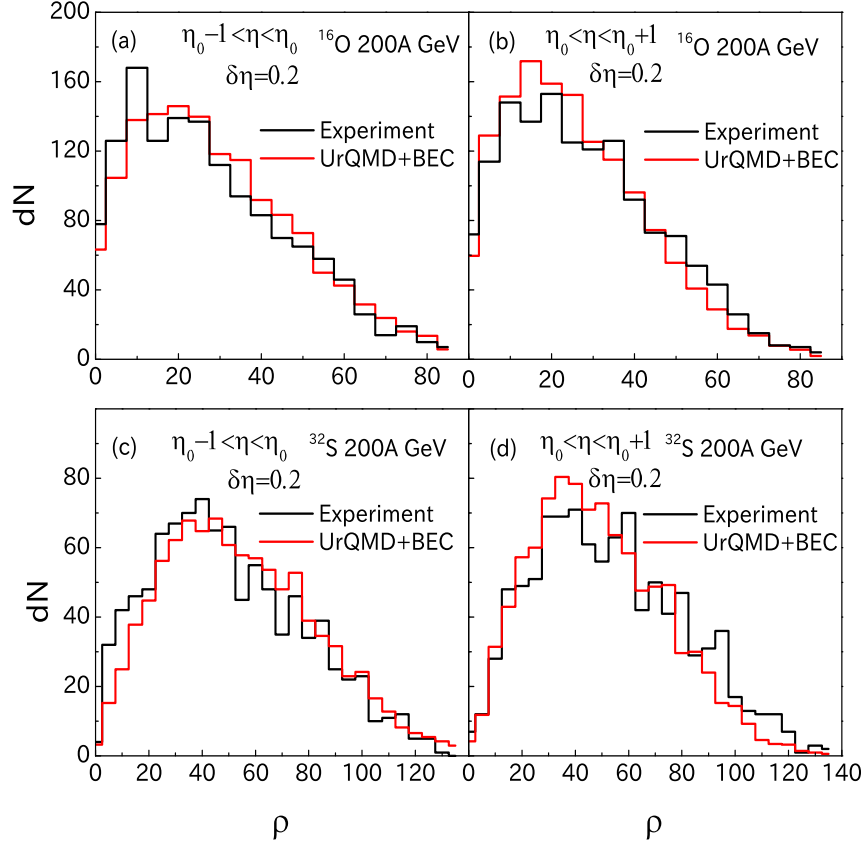


Figure 2.5: Distributions of local pseudorapidity density of shower tracks for ^{16}O -Ag/Br (Figure (a, b)) and ^{32}S -Ag/Br (Figure (c, d)) interaction at 200A GeV/c. Two region is chosen for distribution, $\eta_0 - 1 < \eta < \eta_0$ and $\eta_0 < \eta < \eta_0 + 1$ for $\delta\eta=0.2$.

mentioned in section 2.7, the BEC has been mimicked as an after burner to the simulated data through a charge reassignment algorithm. Following Bjorken's hydrodynamical model [33] one can calculate the initial energy density (ϵ) for each event sample by using the peak density of the particles,

$$\epsilon = \frac{m_t}{\tau \hat{A}} \left. \frac{d\langle n_{all} \rangle}{d\eta} \right|_{\eta=\eta_0} \quad (2.42)$$

where ϵ is averaged over the transverse area \hat{A} , and where τ the proper time in which the matter present within the collision volume should equilibrate. We consider $n_{all} = 1.5 n_s$, assuming equal abundance of all three charge species ($\pm 1e, 0$). We set the transverse mass of a pion at $\langle m_t \rangle = 0.38$ GeV, choose $\tau = 1$ fm/c, assume that \hat{A} is roughly the geometrical cross-sectional area of the ^{16}O -nucleus, and replace $\left. \frac{d\langle n_{all} \rangle}{d\eta} \right|_{\eta=\eta_0}$ by $1.5\rho_0$. The initial energy density values come out as $\epsilon \approx 0.82$ GeV/fm³ in ^{16}O -Ag/Br interaction and $\epsilon \approx 0.92$ GeV/fm³ in ^{32}S -Ag/Br interaction. We note that these ϵ -values are just below the threshold mark ($\epsilon = \text{a few GeV/fm}^3$) needed for the QGP formation in AB collisions. The azimuthal angle (φ) distributions of shower tracks are shown in Figure 2.4. We see that the φ -distributions have dips around $\varphi = 90^\circ$ and 270° . Most probable reasons of such azimuthal

asymmetries are, (i) inefficient recording of the shower tracks directly toward or away from the direction of vision, and (ii) the collective flow of charged hadrons. The UrQMD+BEC generated distributions are plotted together with the respective experiment. The distributions of shower track density values in the central particle producing regions, ($\rho = dn_s/d\eta$) for our $^{16}\text{O-Ag/Br}$ and $^{32}\text{S-Ag/Br}$ data samples are shown in Figure 2.5 (a) (left panel) $(\eta_0 - 1) < \eta < \eta_0$ and (b) (right panel) $\eta_0 < \eta < (\eta_0 + 1)$. The UrQMD+BEC simulated distributions are incorporated in these diagrams too. The distributions are asymmetric and each simulation can more or less reproduce the corresponding experiment. Particle densities 3–4 times as large as the most probable density value are observed both in the experiments and in the simulations. In the following chapters we are going to investigate the small scale structures of these high-valued density fluctuations.

Bibliography

- [1] C. F. Powell, P. H. Fowler and D. H. Perkins, *The study of elementary particles by photographic method*, Pergamon, Oxford (1959).
- [2] A. E. S. Green, *Nuclear Physics*, McGraw-Hill Book Company (1955).
- [3] L. Voyvodic, *Bristol Conf. Rep. Dec.* (1951).
- [4] L. Voyvodic and E. Pickup, *Phys. Rev.* 85, 91 (1952).
- [5] A. H. Morrish, *Phil. Mag.* 43, 533 (1952).
- [6] R. R. Daniel, J. H. Davis, J. H. Mulvay and D. H. Perkins, *Phil. Mag.* 43, 753 (1952).
- [7] R. M. Sternheimer, *Phys. Rev.* 89, 1148 (1953).
- [8] C. O’Ceallaigh, *Phil. Mag.* 42, 1032 (1951).
- [9] P. H. Fowler and D. H. Perkins, *Phil. Mag.* 46, 587 (1955).
- [10] N. F. Mott, *Proc. Roy. Soc. (London)*, 124, 425 (1929).
- [11] B. Rossi, *High Energy Particles*, Prentice Hall, Englewood Cliffs, New Jersey (1952).
- [12] C. M. G. Lattes *et al.*, *Proc. Phys. Soc. (London)* 61, 173 (1948).
- [13] W. H. Barkas, *Nuclear Research Emulsions*, Vols. I & II, Academic Press (1963).
- [14] P. Freier, E. J. Lofgren, E. P. Ney and F. Oppenheimer, *Phys. Rev.* 74, 1818 (1948).
- [15] E. J. Williams, *Phys. Rev.* 58, 292 (1940).

-
- [16] P. H. Fowler, *Phil. Mag.* 41, 169 (1950).
- [17] J. Thomas and P. Jacobs, High Energy Heavy Ion Experiments, Eleventh International Conference on Ultra-Relativistic Nucleus-Nucleus Collisions, 9-13 January 1995, Quark Matter '95, p. 28-29, Monterey, California, USA.
- [18] G. Singh and P. L. Jain, *Z. Phys. A* 344, 73 (1992).
- [19] M. K. Ghosh, Some Aspects of Multiparticle Production in ^{32}S -Ag/Br Interactions at 200A GeV/c (Ph.D. Thesis, North Bengal University, 2008).
- [20] S. A. Bass *et al.*, *Prog. Nucl. Part. Phys.* 41, 255 (1998);
M. Bleicher *et al.*, *J. Phys. G* 25, 1859 (1999).
- [21] H. Feldmeier, *Nucl. Phys. A* 515, 147 (1990).
- [22] L. Wilets *et al.*, *Nucl. Phys. A* 282, 341 (1977).
- [23] T. H. R. Skyrme, *Nucl. Phys.* 9, 615 (1959).
- [24] R. Barnett *et al.*, *Phys. Rev. D* 54, 1 (1996).
- [25] M. Berenguer (Ph.D. Thesis, Goethe University, Frankfurt am Main, Germany, 1993).
- [26] M. G. Bowler, *Z. Phys. C* 29, 617 (1985).
- [27] O. V. Utyuzh, G. Wilk and Z. Wlodarczyk, *Phys. Lett. B* 522, 273 (2001).
- [28] G. Goldhaber *et al.*, *Phys. Rev. Lett.* 3, 181 (1959) ; *Phys. Rev.* 120, 300 (1960).
- [29] E. A. Wolf, *Proc. XXVII, Int. Conf. High Energy Physics, Glasgow*, Eds. P. J. Bussy and I. J. Knowles, p.1281 (1994).
- [30] G. Alexander, I. Cohen and E. Levin, *Phys. Lett. B* 452, 159 (1999).
- [31] A. D. Angelis, *Mod. Phys. Lett. A* 5, 2395 (1990).
- [32] M. Bystersky, *Nucleonica Supplement*, 49, s37 (2004).
- [33] J. D. Bjorken, *Phys. Rev. D* 27, 140 (1983).

Chapter 3

Intermittency and related issues

3.1 Introduction

The investigation of single particle density fluctuations in narrow phase space intervals has been a popular method to study the mechanism of multiparticle production [1–5]. Most of the analyses in this regard are based on the measurement of scaled factorial moment (SFM), that can eliminate Poisson distributed statistical noise. Bialas and Peschanski [6, 7] first pointed out that the single particle density functions should be examined locally within narrow intervals and not over the entire region of phase space accessible to an experiment. They employed the SFM-technique to analyze the JACEE events induced by ultra-relativistic cosmic ray nuclei [8], and found that the q -th order SFM (F_q) for integer q , increases with decreasing phase space resolution size δX as,

$$F_q \propto (\delta X)^{-\phi_q} \quad \text{as } \delta X \rightarrow 0 \quad (3.1)$$

In high-energy physics the phenomenon is known as ‘intermittency’. A scale invariant exponent ϕ_q extracted from the phase space dependence of F_q , represents the intermittency strength and characterizes the dynamical part of the density fluctuations. Several speculative suggestions have so far been made to interpret the origin of dynamical components in particle density fluctuation. The most common trivial reasons of fluctuation are the statistical noise, kinematic conservation laws, quantum correlations etc. The dynamical

fluctuations on the other hand may arise due to (i) collective flow (ii) formation of mini-jets, (iii) emission of Cerenkov gluons [9] (iv) a random cascading effect in the space-time evolution of the collision process [10], (v) a parton-hadron phase transition [11], and (vi) a combination of more than one or all of the above [9, 12–15].

In order to better understand the characteristics of local density fluctuations, an intermittency analysis is usually supplemented by the factorial correlator (FC), oscillatory moment (OM) and erraticity moment analysis. While the SFM accounts for local fluctuations about a particular phase space point, the correlation among particles at different phase space points, located at a distance larger than the scale size at which the correlations are being examined and generated by the intermittency type of fluctuations, are usually characterized by the two-fold factorial correlator (FC) [6, 7]. Both the SFM and the FC are actually integrals of the same underlying correlation function, but they differ only with respect to the respective domains of analysis. This close relationship between the two can be traced back into the sum rules involving the SFM and the FC. Both moments are sensitive to the projection (dimensional reduction) effects and both contain contributions from the corresponding lower-order moments. The OM on the other hand, provides a deeper insight to the multiparticle dynamics [16, 17], e.g., the gluon-dynamical equation predicts a minimum in the OM at a rank $q \approx 5$. One should however keep in mind that the OM is effective only to the partonic multiparticle dynamics [17]. The nature of event-by-event fluctuations beyond intermittency is investigated by using the erraticity moments [18–20], which are free from some of the disadvantages of the SFMs. One such limitation is that the SFMs are incapable of locating the position of a spike or a sharp void in an event. Moreover, while averaging over a large event sample, the characteristic event space fluctuations of the SFMs are smoothed out. Two important pieces information can be extracted from an erraticity analysis. First, it quantifies the chaotic nature of spatial fluctuations in the event space, and second, it is capable of characterizing the degree of fluctuation of the parton multiplicity that initiates the QCD branching processes. It is claimed that in order to describe the chaoticity of multiparticle production in high-energy interactions, the entropy index (μ_q) is as effective as the *Lyapunov exponent* is for describing a classical deterministic nonlinear system [19, 20]. Non-vanishing positive values of μ_q can be used as a criterion for the purpose. In this chapter we present some results on the intermittency and related issues for the ^{16}O -Ag/Br interaction at an incident momentum of $200A$ GeV/c. The results are sometimes compared with the results obtained by using a set of ^{32}S -Ag/Br data at $200A$ GeV/c presented in a previous analysis [21]. We also systematically compare the experimental results with those obtained from the UrQMD and UrQMD+BEC simulations.

3.2 Literature review

As mentioned above the analysis of local density fluctuations of particles within narrow intervals of phase space in terms the SFM was for the first time suggested by Bialas and Peschanski [6] for the cosmic-ray induced AgBr events recorded by the JACEE collaboration [8]. It was found that the SFM in general increases with decreasing rapidity resolution (δy) following a scale invariant power law. The word intermittency was coined from the turbulence in hydrodynamics. The intermittency phenomenon proves that the particle density fluctuations must have some dynamical origin [18–20, 22, 23]. Holynski *et al.* [24] studied the SFM in proton-emulsion interactions at 200 and 800 GeV, and in ^{16}O -emulsion interactions at 60A and 200A GeV. Clear evidence of short-range dynamical correlations was observed from the data that could not be explained by Monte Carlo (MC) simulations. Standard models of multiparticle production could not explain the intermittent behavior either [25]. On the other hand, a jet model that used a scale-invariant decay function, appeared to be consistent with the intermittency results. From the $1d$ and $2d$ SFM analysis in p -nucleus, ^{16}O -AgBr and ^{32}S -Ag/Br interactions at 200A GeV (EMU07 experiments), it was found that the intermittency phenomenon is much stronger in the (η, φ) -space than in the η -space [26]. The intermittent pattern was more pronounced in the p -nucleus interaction than in the AB interactions. The results of intermittency analysis in $^{32}\text{S}+\text{Au}$ interaction at 200A GeV (EMU01 collaboration) were compared with the results simulated by the Lund Monte-Carlo model, FRITIOF [27]. The FRITIOF results showed a bin size dependence only for a horizontal averaging scheme of the SFM, but was found to be uniform with $\delta\eta$ for the vertical averaging. Using the ^{16}O -emulsion and ^{32}S -emulsion data at 60A and 200A GeV (EMU08 Expt.) [28–30], and p -emulsion data at 800 GeV (FNAL Expt. No. 751) [31, 32], it was shown that at a given incident energy the $1d$ intermittency strength decreases with increasing event multiplicity. However, the same strength slowly increases with the mass number of the projectile nucleus. In nuclear emulsion experiments held at a few GeV/nucleon energy range, presence of intermittency was found in the η and φ -distributions of the shower tracks [33]. However, the generalized dimensions (D_q) computed from the intermittency index did not depend either on the reaction type or on the energy of the collision [32–35]. In another study of the p -nucleus interaction at 800 GeV [36], the intermittency index was found to corroborate the above observation on D_q . An energy dependence of the intermittency exponent obtained from the $^{16}\text{O}+\text{Ag/Br}$ interaction at 60A and 200A GeV was reported [37]. In a comprehensive study on the intermittency and cumulant moments using the ^{28}Si -emulsion and ^{197}Au -emulsion data in the 10A GeV energy range, existence of a few particle correlations was established, which showed larger intermittency exponents in $2d$ than in $1d$ [38]. Evidence of a few-particle correlations was also found in the ^{32}S -Ag/Br interaction at 200A GeV and ^{28}Si -Ag/Br interaction at 14.5A GeV [21, 39]. These results

could not be explained either by the FRITIOF or by the UrQMD model. On the other hand, a partonic AMPT model grossly reproduced the ^{16}O -Ag/Br interaction data on the SFM at $E_{\text{lab}} = 4.5A, 14.5A, 60A$ and $200A$ GeV (EMU01 experiment) [40].

The intermittency phenomenon has also been studied in leptonic (ll) and hadronic (hh) interactions at relativistic energies. The experiments on π^+p and K^+p collisions at $p_{\text{lab}} = 250$ GeV/c (NA22 experiment) gave an evidence of intermittency in the rapidity space [41]. The results were compared with the FRITIOF-2.0, FRITIOF-3.0 and DPM models [42, 43]. The e^+e^- annihilation data at $\sqrt{s} = 29$ GeV [44] produced somewhat weaker intermittency than what was observed in hh interactions [41]. However, the strength of intermittency was found to be larger in ll interactions than in the AB collisions at a comparable collision energy. The above observation favors a jet cascading over a hadronic reaction mechanism as a possible interpretation of the intermittency phenomenon [41, 45, 46]. The UA1 collaboration [47] had also reported the results of intermittency analysis for the $\bar{p}p$ collisions at $\sqrt{s} = 630$ GeV. They showed that the quantitative measures of intermittency in different variables like η , y and φ are almost identical. The intermittency index increases with decreasing event multiplicity. A simple Monte Carlo model could not reproduce either the intermittency results for a sample of low p_T tracks, or its multiplicity dependence. The DELPHI experiment [48] showed that the rapidity scaling of SFMs in e^+e^- annihilation data at $\sqrt{s} = 91$ GeV is consistent with the JETSET-6.3 PS model prediction [49]. Intermittency of rapidity distributions in the e^+e^- annihilation data obtained from PEP and PETRA [44, 50, 51] was also examined in terms of a QCD bunching process [52]. The investigation suggests that for most of the observables the dynamics can be described by soft hadronization, and the perturbative gluon radiation is of lesser importance. In a three (y, p_t, φ) and two dimensional (y, p_t), (y, φ), (p_t, φ) analysis of the SFM on π^+p and K^+p interactions at $E_{\text{lab}} = 250$ GeV (NA22 Collaboration) [53], an evidence of dimensional reduction in the intermittency strength was observed. It was also found that the density fluctuations in the final stages of these interactions are self-similar in the transverse plane, but self-affine in the longitudinal one. In AB collisions also, the intermittency exponent was reduced when projected from a higher to lower sub-dimensions [38].

The event space fluctuations of the SFMs are described by a set of moments called the erraticity moments [18]. The erraticity moments in AB , hadronic and leptonic collisions at relativistic energies were measured [18–20, 54–60]. Most of these results indicated the existence of event to event fluctuations, which for an integer order q , was quantified by a parameter called the entropy index μ_q . The NA27 data on pp collisions at 400 GeV showed an increase in μ_q with decreasing average multiplicities of the final state particles [58]. The experimental observation was close to the prediction of a Monte-Carlo simulation based on the quark jets which used a very small fixed coupling constant α_s [61]. The same erraticity

results of the NA27 experiment could be explained also by a purely statistical model that used the negative binomial multiplicity distribution [62]. However, a soft-interaction model called the ECOMB, was unable to describe the NA22 results on e^+e^- collision [41, 63], and NA27 results on pp collision [20]. The erraticity results on π^+p and K^+p collisions at 250 GeV/c (NA22 Collaboration) [64] were compared with the PYTHIA 5.720 model [65]. The erratic nature of event to event fluctuations in the data could not be matched by PYTHIA 5.720, and the erraticity moments are found to be dominated by statistical noise [66].

The multiplicity dependence of the erraticity parameters are observed in ^{28}Si -nucleus interactions at $4.5A$ and $14.5A$ GeV/c [67, 68]. It was found that the magnitude of erraticity moments decreased with increasing multiplicity and were essentially insensitive to the incident beam energy and mass of the beam/target nuclei [66]. A comparison of these results with those reported by other experiments [55–57], suggested that the erratic fluctuations present in the data were due to statistical reasons, and no unambiguous evidence of dynamical fluctuations could be established. The results more or less matched with the prediction of the FRITIOF model. However, FRITIOF could not account for the observed erraticity measures in ^{16}O -Ag/Br and ^{32}S -Ag/Br interactions at $200A$ GeV [22], indicating the presence of dynamical components in the erraticity measures. A comparison of the results of [23] with those obtained from the ECOMB-generated hadronic events [20], as well as with the results obtained from other experiments [58, 59, 69] showed that, the erraticity parameters were significantly smaller in the ^{32}S -Ag/Br experiment than those obtained from other experiments at a similar energy. The entropy index was calculated for the target fragments emitted in the ^{32}S -Ag/Br interaction at $200A$ GeV (CERN SPS) and ^{28}Si -Ag/Br interaction at $14.5A$ GeV (BNL AGS). The results were in conformity with the chaotic behavior of target fragmentation. For the ^{28}Si -data the entropy index was much greater (~ 2.6 times) than that for the ^{32}S -data [70]. Moreover the entropy indices in the target fragmentation region showed an increasing trend with an increase in the charged particle multiplicity [59, 60, 71, 72].

3.3 Scaled factorial moments

We know that a statistical distribution can be characterized by its moments. For a given discrete probability distribution P_n ($n = 1, 2, \dots$) the ordinary q -th order moment is obtained as,

$$\langle n^q \rangle = \sum_{n=0}^{\infty} n^q P_n \quad : \quad \text{for } q = 0, 1, 2, \dots \quad (3.2)$$

The event averaged q -th order factorial moment (FM) on the other hand is defined as,

$$\langle f_q \rangle = \langle n^{[q]} \rangle = \langle n(n-1)\cdots(n-q+1) \rangle \quad (3.3)$$

Here n represents the frequency (number of particles) of an arbitrary phase space interval, and $\langle \rangle$ denotes that the quantity is averaged over the event sample. In terms of the inclusive distribution $\rho_q(y_1, y_2, \dots, y_q)$ for q particles in the variable y over a domain Ω , the FMs is given by

$$\langle f_q \rangle = \int_{\Omega} dy_1 \cdots \int_{\Omega} dy_q \rho_q(y_1, y_2, \dots, y_q) \quad (3.4)$$

The normalized or scaled factorial moment (SFM) is defined as,

$$\begin{aligned} F_q &= \frac{\int_{\Omega} dy_1 \cdots \int_{\Omega} dy_q \rho_q(y_1, y_2, \dots, y_q)}{[\int_{\Omega} dy \rho_1(y)]^q} \\ &= \frac{\sum_{n=0}^{\infty} n(n-1)\cdots(n-q+1)P_n}{\langle n \rangle^q} \end{aligned} \quad (3.5)$$

Whereas the ordinary moments cannot eliminate the statistical components of the fluctuations, the factorial moments can take care of Poisson type noise. For instance, in an arbitrary bin having a multiplicity n , if we denote the dynamical component by $D(t)$ then,

$$P_n = \int_0^{\infty} \frac{t^n}{n!} e^{-t} D(t) dt \quad (3.6)$$

For a large event sample the bin-multiplicity n can run from zero to a very large value, effectively infinity. Therefore,

$$\begin{aligned} \langle f_q \rangle &= \sum_{n=0}^{\infty} n(n-1)\cdots(n-q+1)P_n = \sum_{n=q}^{\infty} \frac{n!}{(n-q)!} P_n \\ &= \sum_{n=q}^{\infty} \int_0^{\infty} \frac{t^n}{(n-q)!} e^{-t} D(t) dt \\ &= \int_0^{\infty} t^q D(t) dt \end{aligned} \quad (3.7)$$

This shows that $\langle f_q \rangle$ is identical to the ordinary q -th order moment of the dynamical component of the distribution, and Poisson type statistical fluctuations can be successfully eliminated. The normalization property of the Poisson distribution is employed in the above derivation. A detailed discussion on multiplicity moments, especially those related to the multiparticle emission physics, can be found in [1, 73]. The idea of [6] was to study the structure of particle density in rapidity or any other suitable phase space variable. We may consider the pseudorapidity (η) variable for our discussion. It can be shown that the SFM averaged over M sub-intervals, each of width $\delta\eta$ considered within an acceptance

$\Delta\eta = M\delta\eta$, corresponds to the moment of the probability density in those bins. Based on the normalization method adopted, the SFM is said to be a *horizontally averaged* or a *vertically averaged* factorial moment [7]. In terms of the inclusive distribution $\rho_q(\eta)$ the horizontally averaged SFM is defined as,

$$\begin{aligned} F_q^H(\eta) &= \frac{1}{M} \sum_{m=1}^M \frac{\int_{\delta\eta} \rho_q(\eta_1, \dots, \eta_q) \prod_{i=1}^q d\eta_i}{\left(\int_{\delta\eta} \rho(\eta) d\eta / M\right)^q} \\ &= \frac{1}{M} \sum_{m=1}^M \frac{\langle n_m^{[q]} \rangle}{\langle \bar{n}_m \rangle^q} \end{aligned} \quad (3.8)$$

where $\langle \bar{n}_m \rangle = \langle n \rangle / M$, $n = \sum_m n_m$ is the total number of particles present within $\Delta\eta$ in an event. The vertically averaged SFM on the other hand is defined as,

$$\begin{aligned} F_q^V(\eta) &= \frac{1}{M} \sum_{m=1}^M \frac{\int_{\delta\eta} \rho_q(\eta_1, \dots, \eta_q) \prod_{i=1}^q d\eta_i}{\left(\int_{\delta\eta} \rho(\eta) d\eta\right)^q} \\ &= \frac{1}{M} \sum_{m=1}^M \frac{\langle n_m^{[q]} \rangle}{\langle n_m \rangle^q} \end{aligned} \quad (3.9)$$

Here $\langle n_m \rangle$ is the number of particles in the m -th bin averaged over the event sample. Both the moments F_q^H and F_q^V scale with phase space resolution size ($\delta\eta$) or equivalently with the partition number (M) like,

$$F_q^s \sim M^{\phi_q} \quad \text{for large } M \quad (3.10)$$

where $s = H$ or V . Irrespective of the averaging technique adopted, the SFM is capable of suppressing any Poisson distributed statistical noise. The vertically averaged SFMs are more sensitive to the bin-to-bin density variations but they are unstable at small bin sizes. Whereas the horizontally averaged SFMs are sensitive only to the local fluctuations of the particle density, but they remain stable over a large $\delta\eta$ -range. Both the moments are equal for $M = 1$ and also when the underlying distribution in the particular phase space variable is uniform. The latter criterion is achieved by using a cumulant variable X_η defined as [74]

$$X_\eta = \int_{\eta_{\min}}^{\eta} \rho(\eta) d\eta / \int_{\eta_{\min}}^{\eta_{\max}} \rho(\eta) d\eta \quad (3.11)$$

where η_{\min} (η_{\max}) is the minimum (maximum) value of η , and the single particle inclusive density in η is $\rho(\eta) = N_{ev}^{-1}(dn/d\eta)$. Irrespective of its original form, density distribution in terms of X_η is always uniform $\in [0, 1]$. The present analysis is based on the distributions of cumulant variables corresponding to the η and/or φ variables. We shall however continue to call the corresponding variables η and φ .

3.3.1 Intermittency in $1d$

We compute the event averaged SFMs denoted by $\langle F_q \rangle$ as functions of phase space partition number M for the $^{16}\text{O-Ag/Br}$ interaction at $200A$ GeV/c. Figure 3.1 shows our results in the η -space and Figure 3.2 in the φ -space. In both the figures we include the results obtained from the UrQMD and UrQMD+BEC simulations. We find that the event averaged SFMs for $q = 2$ to 6 obey a power law type scaling relation like Equation (3.10), indicating an intermittent pattern of particle density functions in both the η and φ spaces. The straight

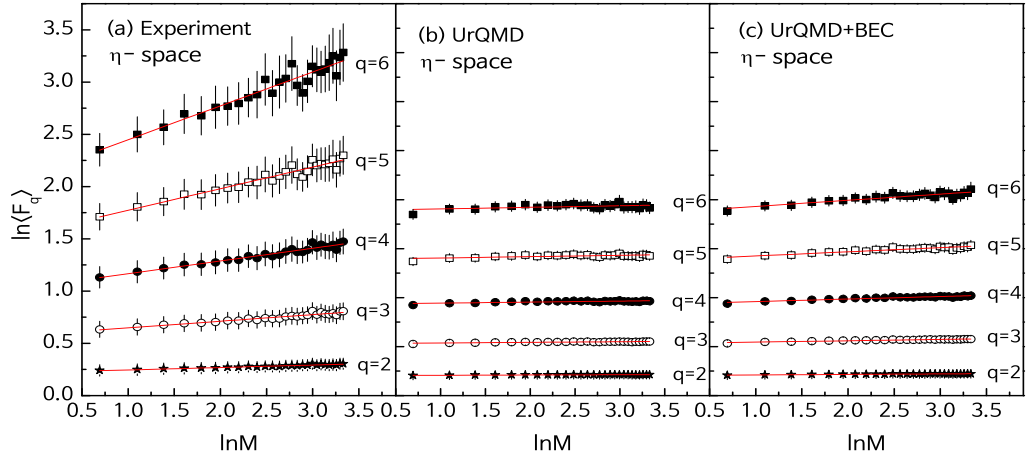


Figure 3.1: Variation of the event averaged SFM of shower tracks with phase space partition number M in the η -space for the $^{16}\text{O-Ag/Br}$ interaction at $200A$ GeV/c. Best fitted straight lines to the data points are shown.

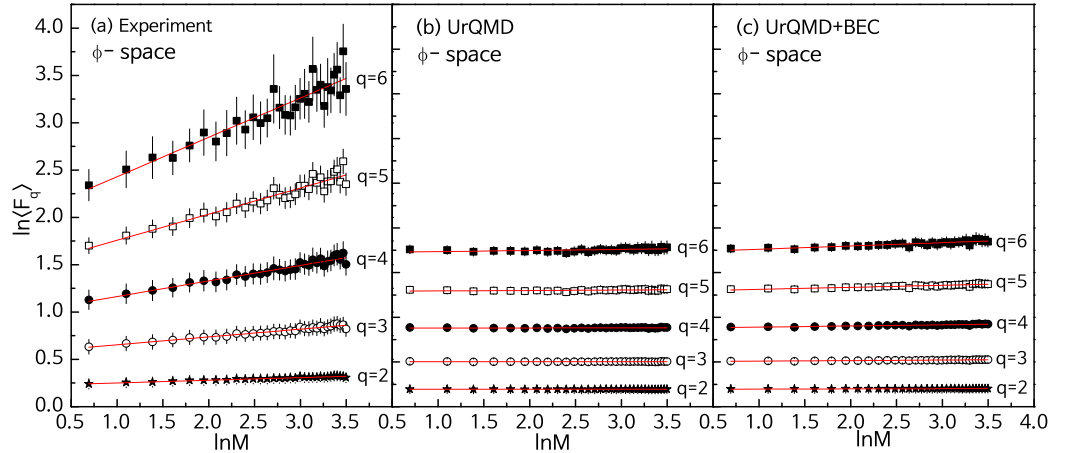


Figure 3.2: Same as in Figure 3.1 but in φ -space.

lines in these figures represent the best fitted scaling function of Equation (3.10) with ϕ_q as a free parameter. The ϕ_q exponents called the *intermittency index*, are given in Table 3.1. In order to avoid the kinematic constraints [75] a few points at the lowest values of M are

excluded while fitting the straight lines. We have also computed the $1d$ intermittency exponents for the $^{32}\text{S-Ag/Br}$ interaction at $200A$ GeV/ c , and the values are given in Table 3.2. The diagrams as well as the tables suggest that the intermittency exponents are significantly larger in the experiments than in the simulations. The UrQMD+BEC generated values of ϕ_q are slightly larger than the corresponding UrQMD generated values. The errors associated with ϕ_q are estimated by assuming that for each event F_q is an error free quantity. Thus the standard error in $\langle F_q \rangle$ originates only from the event space fluctuation of the SFM. At this point it should be mentioned that, as the SFMs are computed in the same domain ($\Delta\eta$) with varying bin size ($\delta\eta$), in Figure 3.1 and Figure 3.2 for a given q the data points are highly correlated. Thus the error estimation of ϕ_q requires special precaution [76]. We have generated 10 independent samples, each equal in size as the respective experimental sample, by using the Lund model FRITIOF [77]. Gross characteristics of the data like the multiplicity and η -distribution of each FRITIOF generated sample are identical to the respective experiment. We then calculate ϕ_q for each FRITIOF generated sample and obtain their statistical spread as,

$$\sigma(\phi_q) = \sqrt{\langle \phi_q^2 \rangle - \langle \phi_q \rangle^2} \quad (3.12)$$

over the 10 sets of MC data used. The $\sigma(\phi_q)$ values obtained in this way are quoted as errors of ϕ_q in the η -space. For the error estimation in φ -space we follow the same procedure, but the FRITIOF data are now replaced by (pseudo)random numbers $\in [0, 2\pi]$. Since the FRITIOF model as well as the random number generated samples contain either none or very little dynamical effect, the estimated errors of the intermittency exponents are only of statistical origin. The goodness of linear regression is represented by the Pearson's coefficient (R^2) [78]. In almost all the cases the R^2 values are very close to unity, confirming the linearity of $\ln F_q$ with $\ln M$. We see that the intermittency indexes in the φ -space are higher in magnitude than those in the η -space. Such a phase space dependence of the intermittency index is found to be valid for both the $^{16}\text{O-Ag/Br}$ and $^{32}\text{S-Ag/Br}$ interactions, and is consistent with our previous observation for the $^{28}\text{Si-Ag/Br}$ interaction at $14.5A$ GeV as well [79]. The findings of our analysis however contradict the observation of [76], where a phase space independence was observed in this regard. We also find that the ϕ_q values in the $^{16}\text{O-Ag/Br}$ interaction are 2 to 3 times larger in magnitude than those in the $^{32}\text{S-Ag/Br}$ interaction, which might be an effect of projectile mass difference. It is found that at comparable energies the intermittency indices in leptonic and hadronic interactions are higher in magnitude than those in the AB interactions [41, 44, 50, 53, 80]. One may argue that due to intermixing of many particle producing sources, the correlations coming from elementary NN interactions are to some extent washed out, and the intermittency phenomenon in AB collisions is therefore partially suppressed [81]. For both the systems studied in this investigation, the UrQMD generated data do not produce intermittency. The SFMs are almost independent of the phase space partition number. Alternatively, we can say

that the model does not generate enough dynamical fluctuation. The inclusion of BEC into the UrQMD generated events introduces only a small but finite amount of correlation that is visible in the figures as well as in the tables. To check whether the observed intermittency effects are due to the contributions coming from lower order correlations, for $q \geq 2$ we define a set of normalized exponents ξ_q as [76],

$$\xi_q = \phi_q / \binom{q}{2} \quad (3.13)$$

A true three-particle correlation is then given by,

$$\xi_q^{(3)} = (q-2)\xi_3 - (q-3)\xi_2 \quad (3.14)$$

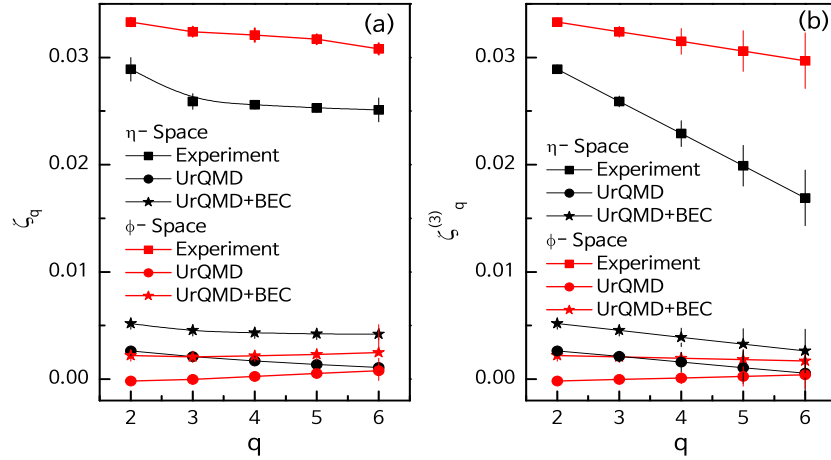
In Figure 3.3 we show the variations of ξ_q and $\xi_q^{(3)}$ with q in both η and φ -space for the ^{16}O -Ag/Br interaction, whereas similar diagrams for the ^{32}S -Ag/Br interaction are shown in Figure 3.4. In these diagrams the experimental results are compared with the corresponding UrQMD and UrQMD+BEC simulations. For the ^{16}O -Ag/Br experiment the normalized three-particle correlation parameter $\xi_q^{(3)}$ is seen to linearly decrease with increasing q . In the φ -space $\xi^{(3)}$ is consistently higher than that in the η -space. Corresponding UrQMD and UrQMD+BEC simulated results are significantly smaller than the experiment. In φ -space the UrQMD simulated values of $\xi^{(3)}$ are very close to zero. On the other hand, for the ^{32}S -Ag/Br experiment the $\xi_q^{(3)}$ values in the φ -space are not only larger in magnitude than those in the η -space, but they are also found to linearly rise with increasing q . In the

Table 3.1: The values of 1d intermittency exponent for order $q = 2 - 6$ in the ^{16}O -Ag/Br interaction at 200A GeV/c. The errors are of statistical origin.

	Order	η -space		φ -space	
		ϕ_q	R^2	ϕ_q	R^2
Experiment	2	0.0289±0.0011	0.939	0.0333±0.0002	0.984
	3	0.0779±0.0022	0.935	0.0972±0.0014	0.951
	4	0.1534±0.0061	0.930	0.1925±0.0038	0.945
	5	0.2534±0.0103	0.927	0.3172±0.0047	0.947
	6	0.3771±0.0167	0.915	0.4618±0.0081	0.918
UrQMD	2	0.0026±0.0003	0.979	-0.0002±0.0002	0.931
	3	0.0063±0.0008	0.932	-0.0001±0.0005	0.931
	4	0.0101±0.0018	0.947	0.0016±0.0011	0.931
	5	0.0136±0.0034	0.921	0.0052±0.0020	0.923
	6	0.0162±0.0060	0.975	0.0126±0.0037	0.925
UrQMD+BEC	2	0.0052±0.0003	0.956	0.0022±0.0002	0.907
	3	0.0136±0.0008	0.958	0.0062±0.0005	0.913
	4	0.0259±0.0017	0.949	0.0130±0.0011	0.908
	5	0.0423±0.0032	0.934	0.0231±0.0022	0.990
	6	0.0630±0.0060	0.907	0.0371±0.0390	0.964

Table 3.2: The values of $1d$ intermittency exponent for order $q = 2 - 6$ in $^{32}\text{S-Ag/Br}$ interaction at $200A$ GeV/c. The errors are of statistical origin only.

	Order	η -space		φ -space	
		ϕ_q	R^2	ϕ_q	R^2
Experiment	2	0.013 ± 0.003	0.982	0.014 ± 0.0006	0.967
	3	0.032 ± 0.003	0.977	0.044 ± 0.002	0.972
	4	0.056 ± 0.007	0.961	0.099 ± 0.005	0.967
	5	0.082 ± 0.013	0.937	0.201 ± 0.011	0.946
	6	0.112 ± 0.021	0.905	0.371 ± 0.021	0.915
UrQMD	2	0.001 ± 0.0001	0.986	0.012 ± 0.0006	0.953
	3	0.004 ± 0.0004	0.939	0.033 ± 0.0015	0.956
	4	0.009 ± 0.0008	0.946	0.062 ± 0.0027	0.958
	5	0.017 ± 0.0017	0.930	0.097 ± 0.0042	0.959
	6	0.032 ± 0.0035	0.999	0.138 ± 0.0061	0.957
UrQMD+BEC	2	0.002 ± 0.0002	0.953	0.029 ± 0.0009	0.976
	3	0.005 ± 0.0005	0.952	0.078 ± 0.0025	0.967
	4	0.009 ± 0.0010	0.920	0.143 ± 0.0045	0.987
	5	0.016 ± 0.0021	0.955	0.224 ± 0.0073	0.975
	6	0.026 ± 0.0042	0.969	0.323 ± 0.0113	0.972

**Figure 3.3:** Normalized intermittency exponents as a function of order number q for the $^{16}\text{O-Ag/Br}$ interaction at $200A$ GeV/c. Lines joining points are drawn to guide the eye.

η -space the UrQMD and UrQMD+BEC simulated $\xi_q^{(3)}$ values both are again very close to zero. However, in the φ -space very surprisingly the UrQMD+BEC simulation significantly exceeds the experiment until $q = 6$. The overall observation indicates that the higher order ($q \geq 2$) intermittency present in the experiments cannot simply be explained in terms of the lower order two and three-particle correlations.

A self-similar cascade mechanism may occur in different phases, leading to different kinds of spiky events. In some events there are many spikes, such as in the JACEE events [8], while in some other only one or two large spikes are seen [82]. In high-energy AB interactions when

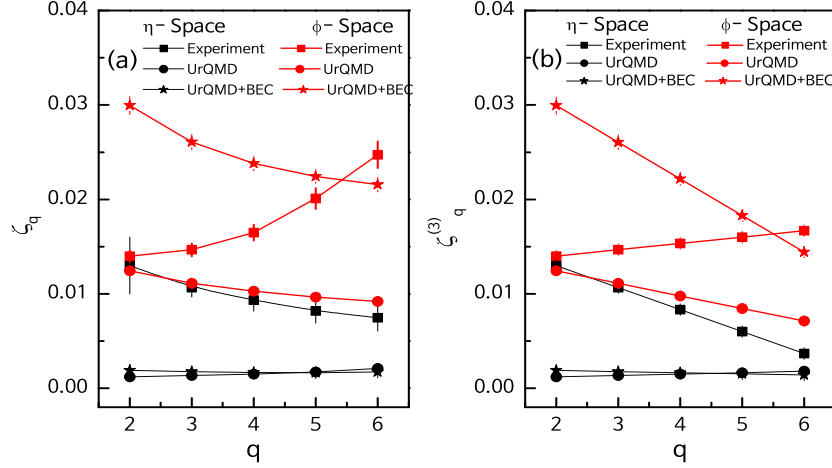


Figure 3.4: The same as in Figure 3.3 but for the $^{32}\text{S-Ag/Br}$ interaction at $200A$ GeV/c.

the normal hadronic phase dominates, the events are populated by many spikes and valleys. On the other hand, a few large spikes are observed in events dominated by a spin-glass like phase. If the two phases are simultaneously present, then the parameter

$$\lambda_q = (\phi_q + 1)/q \quad (3.15)$$

should exhibit a minimum at a certain order number q , say at $q = q_c$, that is not necessarily an integer [11]. In the region $q < q_c$ a self-similar multiparticle system would behave differently from that in the $q > q_c$ -region. Whereas the $q < q_c$ -region is dominated by numerous fluctuations involving smaller numbers of particles in one bin, the $q > q_c$ -region is dominated by a small number of very large fluctuations [83]. The situation can be described as a mixture of a *liquid phase* of many small fluctuations and a *dust phase* of a few grains of very large fluctuations. The liquid-dust phases can coexist. However, when the system was examined by using moments of rank $q < q_c$ and $q > q_c$, one found that either the *liquid* or the *dust* phase dominates [11]. In Figure 3.5(a) and Figure 3.6(a) we have plotted λ_q against q , respectively for the $^{16}\text{O-Ag/Br}$ and $^{32}\text{S-Ag/Br}$ interactions at $200A$ GeV/c. In both diagrams the experimental results are shown along with the respective UrQMD and UrQMD+BEC simulations. The figures show that the experimental values of λ_q in both η and φ -space deviate to a small extent from the respective no-intermittency lines. The simulated values of λ_c on the other hand are always very close to the no-intermittency line. According to [84] the observed q -dependence represents a weak $1d$ intermittency in the experiment(s). It may be noted that the deviation from the no-intermittency line is slightly larger in φ -space than what it is in the η -space.

A more direct measure of the intermittency strength can be obtained from its connection with (multi)fractality, at first in the framework of the α -model [7], and subsequently in a

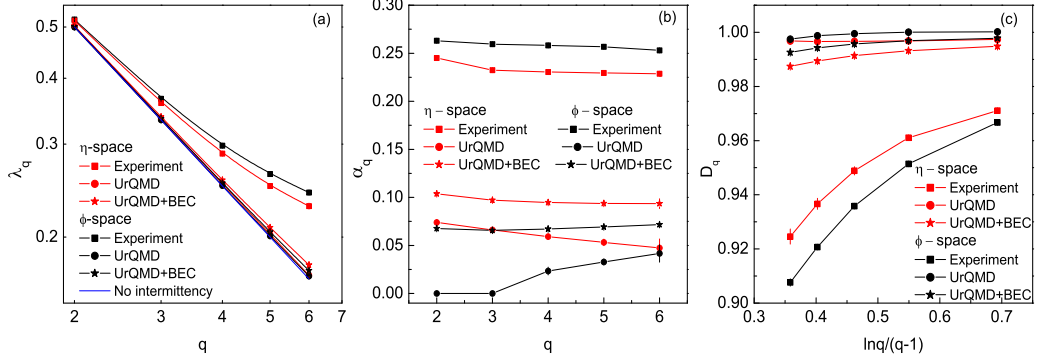


Figure 3.5: (a) Plot of λ_q versus q . The no-intermittency line corresponding to $\phi_q = 0$ is also shown. (b) Plot of intermittency strength α_q with q . (c) Plot of generalized Rényi dimension D_q with $\ln q/(q-1)$. The curves are drawn to guide the eye. The plots are for the $^{16}\text{O-Ag/Br}$ interaction at 200A GeV/c.

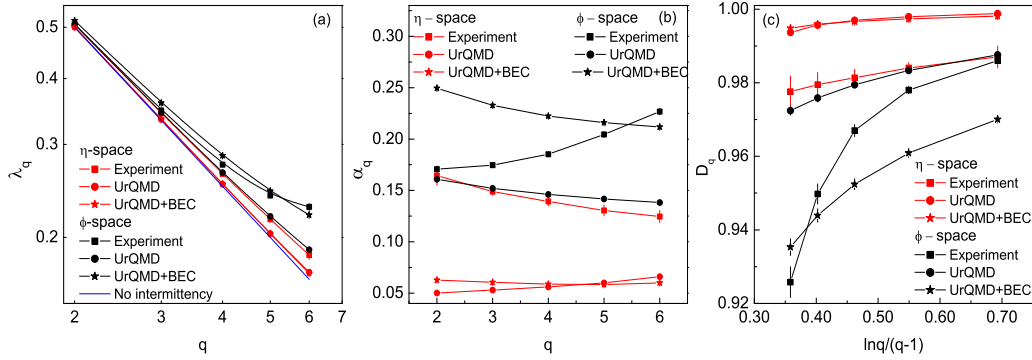


Figure 3.6: The same as in Figure 3.5 but for the $^{32}\text{S-Ag/Br}$ interaction at 200A GeV/c.

model independent way that does not invoke any particular hypothesized mechanism of particle production [85]. The generalized Rényi dimension of multifractality can be determined from the intermittency exponent ϕ_q by using the following relation,

$$D_q = D_T - \frac{\phi_q}{(q-1)} \quad (3.16)$$

where D_T is the topological dimension of the supporting space, i.e. $D_T = 1$ (2) in a $1d$ ($2d$) analysis. According to the α -model the strength parameter α_q is related to D_q as,

$$\alpha_q = \sqrt{\frac{6 \ln 2}{q} (D_T - D_q)} \quad (3.17)$$

The α_q parameter as a function of q is plotted in Figure 3.5(b) for the $^{16}\text{O-Ag/Br}$ interaction and in Figure 3.6(b) for the $^{32}\text{S-Ag/Br}$ interaction. In the $^{16}\text{O-Ag/Br}$ interaction

the experimental values of $\alpha_q \approx 0.25$ and they are almost independent of q , whereas the simulated α_q -values are found to vary in the $0 - 0.1$ range. The α_q against q plots for the $^{32}\text{S-Ag/Br}$ interaction are quite different. In the experiment α_q increases in the φ -space and decreases in the η -space. Once again the UrQMD+BEC simulated values of the parameter are significantly larger than those of the experiment in the $q = 2$ to 5 range. From the above discussion it cannot be claimed in clear terms as to which process, i.e. a second-order phase transition or a random cascading, is actually responsible for the intermittency observed in the experiments. For an arbitrary underlying dynamics it is however possible to define an effective fluctuation strength as [85],

$$\alpha_{\text{eff}} \propto \sqrt{2\phi_2} \quad (3.18)$$

The values of α_{eff} are found to be $\alpha_{\text{eff}}(\eta) = 0.240 \pm 0.005$ and $\alpha_{\text{eff}}(\varphi) = 0.258 \pm 0.0008$ for the $^{16}\text{O-Ag/Br}$ experiment, and $\alpha_{\text{eff}}(\eta) = 0.161 \pm 0.019$ and $\alpha_{\text{eff}}(\varphi) = 0.167 \pm 0.004$ for the $^{32}\text{S-Ag/Br}$ experiment.

Table 3.3: Multifractal specific heat C calculated from the SFM analysis. The C values evaluated at different q -regions are specified.

Interaction		Fit Region	η -space	φ -space
$^{16}\text{O-Ag/Br}$ interaction at $200A$ GeV/c	Experiment	$2 \leq q \leq 5$	0.1148 ± 0.0199	0.1540 ± 0.0214
		$2 \leq q \leq 4$	0.0936 ± 0.0186	0.1309 ± 0.0192
		$4 \leq q \leq 6$	0.2324 ± 0.0195	0.2707 ± 0.0122
	UrQMD	$2 \leq q \leq 5$	0.0028 ± 0.0004	0.0047 ± 0.0017
		$2 \leq q \leq 4$	0.0032 ± 0.0003	0.0028 ± 0.0015
		$4 \leq q \leq 6$	-0.0011 ± 0.0012	0.0188 ± 0.0041
	UrQMD+BEC	$2 \leq q \leq 5$	0.0179 ± 0.0030	0.0118 ± 0.0025
		$2 \leq q \leq 4$	0.0146 ± 0.0025	0.0089 ± 0.0021
		$4 \leq q \leq 6$	0.0380 ± 0.0039	0.0294 ± 0.0036
$^{32}\text{S-Ag/Br}$ interaction at $200A$ GeV/c	Experiment	$2 \leq q \leq 5$	0.0257 ± 0.0019	0.1161 ± 0.0313
		$2 \leq q \leq 4$	0.0242 ± 0.0026	0.0796 ± 0.0188
		$4 \leq q \leq 6$	0.0357 ± 0.0035	0.3909 ± 0.0715
	UrQMD	$2 \leq q \leq 5$	0.0102 ± 0.0022	0.0394 ± 0.0045
		$2 \leq q \leq 4$	0.0077 ± 0.0015	0.0345 ± 0.0040
		$4 \leq q \leq 6$	0.0310 ± 0.0064	0.0673 ± 0.0047
	UrQMD+BEC	$2 \leq q \leq 5$	0.0073 ± 0.0010	0.0875 ± 0.0111
		$2 \leq q \leq 4$	0.0061 ± 0.0007	0.0751 ± 0.0089
		$4 \leq q \leq 6$	0.0177 ± 0.0034	0.1634 ± 0.0149

A thermodynamic interpretation of multifractality has been given in terms of a constant specific heat C that is related to the Rényi dimension as [86],

$$D_q = D_\infty + C \frac{\ln q}{q-1} \quad (3.19)$$

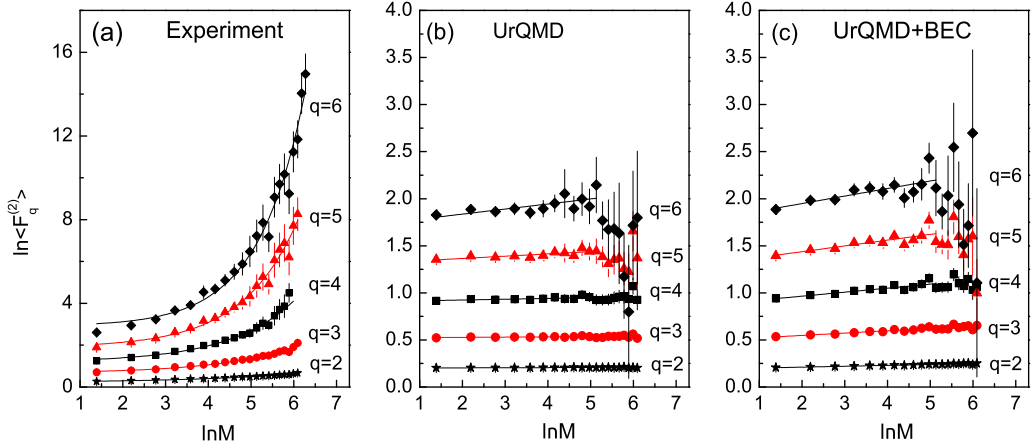


Figure 3.7: The scaling of $2d$ SFMs for $q = 2 - 6$ in ^{16}O -Ag/Br interaction at $200A$ GeV/ c . The solid curves are drawn to guide the eye.

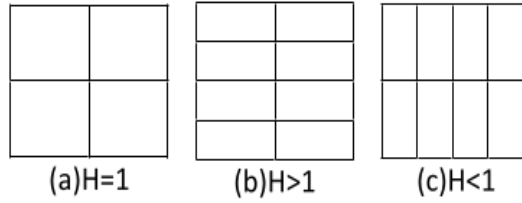
While deriving the above relation it has been assumed that only Bernoulli type of fluctuations are responsible for a transition from monofractality to multifractality. A monofractal to multifractal transition corresponds to a jump in the value of C from zero to a nonzero positive value. By examining the variation of D_q with $\ln q/(q-1)$ one can obtain the value of C . Such results for our investigation are shown in Figure 3.5(c) for the ^{16}O -Ag/Br interaction and in Figure 3.6(c) for the ^{32}S -Ag/Br interaction. The experimental values of D_q increase nonlinearly with increasing $\ln q/(q-1)$. For both interactions the nonlinearity in φ -space is more prominent than that in the η -space. The C value will obviously depend on the order number q . The simulated values in all cases are very close to unity, the topological dimension of the supporting space. We have computed C in three different domains of q . Table 3.3 summarizes our results. It shows that the C values obtained from the experimental data are always positive. The simulated values are very close to zero or at least about an order less than the corresponding experimental values. We also observe that the values of C are not consistent with the universality of the parameter as claimed in [86].

3.3.2 Intermittency in $2d$

In a $2d$ analysis of intermittency we consider the (η, φ) -plane as our phase space. In order to make the results independent of the underlying distribution functions, the cumulative variables (X_η, X_φ) have been used [74]. Therefore, all the particles are distributed uniformly over a square of unit side. The q -th order SFM is calculated following Equation (3.8), where the phase space partition number is taken as $M = M_\eta \cdot M_\varphi$, and M_η (M_φ) is the number of partitions along the η (φ) direction. For a self-similar structure the $2d$ -SFM are expected to follow a scaling relation like Equation (3.10) in the (η, φ) -plane. In Figure 3.7 we show the plots of event averaged $2d$ SFMs $\langle F_q^{(2)} \rangle$ against M for the ^{16}O -Ag/Br data. Here we have set

Table 3.4: $2d$ self-affine intermittency indices for the $^{16}\text{O-Ag/Br}$ interaction at 200A GeV/c. The errors are statistical only.

q	Experiment		UrQMD		UrQMD+BEC	
	$\phi_q^{(2)}$	R^2	$\phi_q^{(2)}$	R^2	$\phi_q^{(2)}$	R^2
2	0.125 ± 0.025	0.994	0.001 ± 0.0004	0.476	0.009 ± 0.0004	0.983
3	0.339 ± 0.045	0.987	0.002 ± 0.001	0.218	0.025 ± 0.003	0.909
4	0.857 ± 0.115	0.983	0.008 ± 0.004	0.316	0.043 ± 0.008	0.759
5	1.596 ± 0.198	0.986	0.024 ± 0.006	0.643	0.061 ± 0.016	0.589
6	3.059 ± 0.270	0.983	0.054 ± 0.018	0.467	0.080 ± 0.026	0.494

**Figure 3.8:** A schematic of partitioning $2d$ phase space for (a) $H = 1$ corresponds to equal partitioning, (b) $H > 1$ corresponds to finer division along the vertical direction, and (c) $H < 1$ corresponds to finer division along the horizontal direction.

$M_\eta = M_\varphi$ which corresponds to a self-affine partitioning of the phase space. The experiment, UrQMD and UrQMD+BEC generated results are plotted together in this figure. Due to the anisotropy present in the fluctuations in two different directions (i.e., a self-affine structure) of phase space, the variation of $\ln\langle F_q^{(2)} \rangle$ against $\ln M$ is not linear over the entire $\ln M$ range. To obtain a measure of the self-affine intermittency index in $2d$ one can perform a polynomial fit to the $\ln\langle F_q^{(2)} \rangle$ versus $\ln M$ data, and then retain only the linear coefficient by setting all other coefficients zero. For the $^{16}\text{O-Ag/Br}$ interaction the $2d$ self-affine intermittency index $\phi_q^{(2)}$ obtained in this way is presented in Table 3.4. Once again the fit quality is measured by the Pearson's coefficient R^2 [78] and their values are quoted in Table 3.4. The same set of exponents for the $^{32}\text{S-Ag/Br}$ interaction at 200A GeV/c are given in Table 3.5. The errors quoted in these tables are only of statistical origin. The procedure of error estimation is

Table 3.5: $2d$ self-affine intermittency indices for the $^{32}\text{S-Ag/Br}$ interaction at 200A GeV/c. The errors are statistical only.

q	Experiment		UrQMD		UrQMD+BEC	
	$\phi_q^{(2)}$	R^2	$\phi_q^{(2)}$	R^2	$\phi_q^{(2)}$	R^2
2	0.075 ± 0.003	0.974	0.003 ± 0.0002	0.978	0.009 ± 0.0003	0.996
3	0.384 ± 0.038	0.984	0.009 ± 0.001	0.974	0.026 ± 0.0009	0.993
4	1.030 ± 0.170	0.969	0.017 ± 0.003	0.967	0.048 ± 0.002	0.985
5	1.560 ± 0.290	0.946	0.026 ± 0.003	0.944	0.072 ± 0.006	0.960
6	2.022 ± 0.099	0.958	0.049 ± 0.004	0.983	0.103 ± 0.009	0.977

similar to that used in our $1d$ intermittency analysis. It is seen that the $2d$ intermittency exponents for the UrQMD and UrQMD+BEC simulations are comparatively lower valued than the corresponding experiment. For a given q the $^{16}\text{O-Ag/Br}$ experiment produces larger $\phi_q^{(2)}$ value than the $^{32}\text{S-Ag/Br}$ experiment. The $\alpha_q^{(2)}$ values for the $^{16}\text{O-Ag/Br}$ experiment increase with increasing q , but for the $^{32}\text{S-Ag/Br}$ experiment the values initially rise and then saturate near $q = 4$. It has been conjectured [10, 87] that beside some kind of collective phenomena there are other possibilities, e.g. a branching process or a second order phase transition, that lead to the $2d$ intermittency within a scale invariant dynamics. To check whether or not these mechanisms are acceptable in the present analysis for our $^{16}\text{O-Ag/Br}$ and $^{32}\text{S-Ag/Br}$ data, the $\phi_q^{(2)}$ values, shown in Table 3.4 and Table 3.5, are put to different tests. Our observations in this regard are listed below.

- (i) Unlike the $1d$ intermittency exponents the $\phi_q^{(2)}$ values do not follow the predictions of a self-similar cascade mechanism. Neither a log-normal distribution under Gaussian approximation [6, 7] nor a log-Lévy stable distribution works for the observed values [88, 89], thereby ruling out a self-similar cascade process in $2d$. The Rényi dimensions, shown in Table 3.6, are however fractional valued and decrease with increasing q , which indicates a (multi)fractal nature of the underlying dynamical fluctuation.
- (ii) The intermittency parameter λ_q obtained from $\phi_q^{(2)}$ does not exhibit any clear minimum. Hence the possibility of coexistence of two different phases (e.g., liquid-gas) is also ruled out for both $^{16}\text{O-Ag/Br}$ and $^{32}\text{S-Ag/Br}$ interactions at $200A$ GeV/c.
- (iii) For both interactions the $\phi_q^{(2)}$ values are not consistent with a monofractal structure of particle production either, as required by a system at the critical temperature for a second order phase transition [90]. The Landau-Ginzburg parameter ν is also significantly different from its universal value ($\nu = 1.304$) to warrant any kind of thermal (second order) phase transition [91].

Following Equation (3.17) we determine the $2d$ intermittency strength $\alpha_q^{(2)}$ for the $^{16}\text{O-Ag/Br}$ and $^{32}\text{S-Ag/Br}$ interactions, and their values are given in Table 3.6. From the values of $\alpha_q^{(2)}$ and the plots of $1d$ intermittency strength shown in Figure 3.5 and Figure 3.6, one can conclude that the fluctuation strength in $^{16}\text{O-Ag/Br}$ interaction is consistently greater than that in the $^{32}\text{S-Ag/Br}$ interaction. We also observe that $\alpha_q^{(2)} > 2\alpha_q$. Nonlinearity in the partition number dependence of the $2d$ SFMs, as observed in Figure 3.7, is due to an anisotropy present in the (η, φ) plane. For a particular interaction the kinematically allowed η -range depends on the collision energy and/or momentum, whereas the φ range irrespective of the colliding system and/or collision energy lies always in between 0 and 2π . It is therefore suggested that the phase space should be so partitioned as to appropriately

Table 3.6: Intermittency strength based on a random cascading α -model and Rényi dimensions for ^{16}O -Ag/Br and ^{32}S -Ag/Br interactions in $2d$. The errors are of statistical origin.

Order(q)	^{16}O -Ag/Br		^{32}S -Ag/Br	
	$D_q^{(2)}$	$\alpha_q^{(2)}$	$D_q^{(2)}$	$\alpha_q^{(2)}$
	Experiment			
2	1.875±0.025	0.487±0.006	1.925±0.003	0.395±0.006
3	1.831±0.023	0.502±0.012	1.808±0.039	0.516±0.010
4	1.714±0.038	0.549±0.032	1.657±0.057	0.597±0.051
5	1.601±0.049	0.612±0.063	1.610±0.073	0.570±0.083
6	1.388±0.054	0.643±0.084	1.596±0.020	0.528±0.106
	UrQMD			
2	1.999±0.0004	0.046±0.005	1.997±0.0002	0.079±0.001
3	1.999±0.0005	0.036±0.005	1.996±0.0005	0.079±0.002
4	1.997±0.001	0.053±0.007	1.994±0.001	0.077±0.003
5	1.994±0.002	0.071±0.004	1.994±0.001	0.074±0.002
6	1.989±0.004	0.087±0.007	1.990±0.001	0.082 ±0.002
	UrQMD+BEC			
2	1.991±0.0004	0.137±0.002	1.991±0.0003	0.137±0.001
3	1.988±0.002	0.132±0.004	1.987±0.0004	0.134±0.001
	1.986±0.003	0.122±0.006	1.984±0.0006	0.129±0.002
5	1.985±0.004	0.113±0.007	1.982±0.002	0.122 ±0.003
6	1.984±0.005	0.105±0.009	1.979±0.002	0.119±0.003

take this anisotropy into account [92]. This is usually done by introducing a *roughness* parameter called the Hurst exponent (H). A schematic of how H is related to the unequal partitioning of the (η, φ) -plane is shown in Figure 3.8. Following [93] we introduce H for an asymmetric partitioning of the (η, φ) -plane which is referred to as a self-affine structure of the phase space. The scale factors in different directions are related as,

$$M_\eta = M_\varphi^H : 0 < H < 1 \quad \text{and} \quad M_\varphi = M_\eta^{(1/H)} : H > 1 \quad (3.20)$$

Both M_η and M_φ now cannot be simultaneously integer valued. Therefore, one has to leave a small fraction out of our consideration along either η or φ -direction, as the case may demand. However, such exclusion is not going to affect the final results, since the phase space variables X_η and X_φ are uniform $\in [0, 1]$. A self-affine analysis for $q = 2$ has been performed for a wide range of H values ($0.25 \leq H \leq 4.0$). Figure 3.9 illustrates the scaling of second order SFM $F_2^{(2)}$ for some selected values of H for the ^{16}O -Ag/Br interaction, while Figure 3.10 shows similar plots for the ^{32}S -Ag/Br interaction. From these figures one can see that as H differs from unity the phase space dependence of the $2d$ SFMs is gradually straightened out. For each H the $\langle F_2^{(2)} \rangle$ versus M data are fitted by the following quadratic equation,

$$y = ax^2 + bx + c \quad (3.21)$$

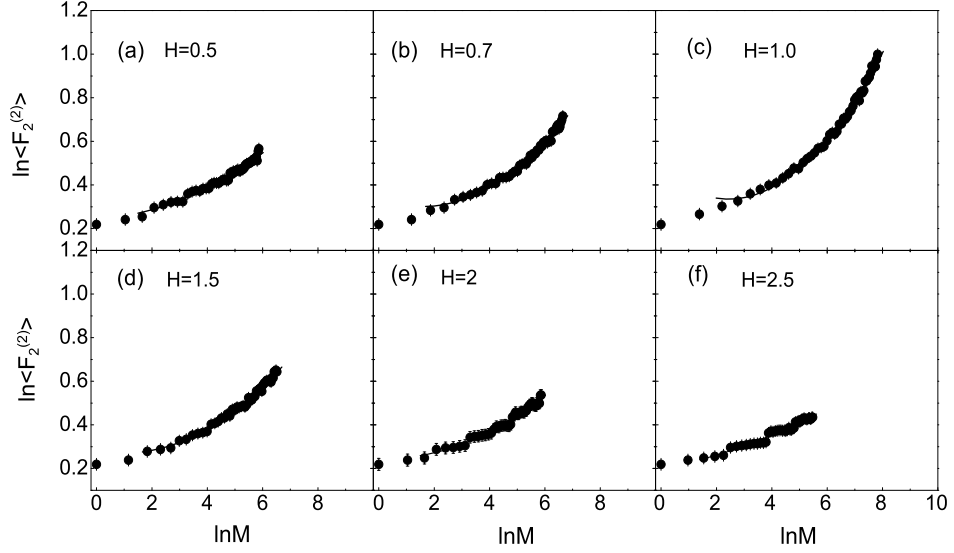


Figure 3.9: Two-dimensional SFM $\ln\langle F_2^{(2)} \rangle$ plotted against $\ln M$ for different Hurst parameters in the ^{16}O -Ag/Br interaction at 200A GeV/c. The solid curves represent quadratic fit to the data points.

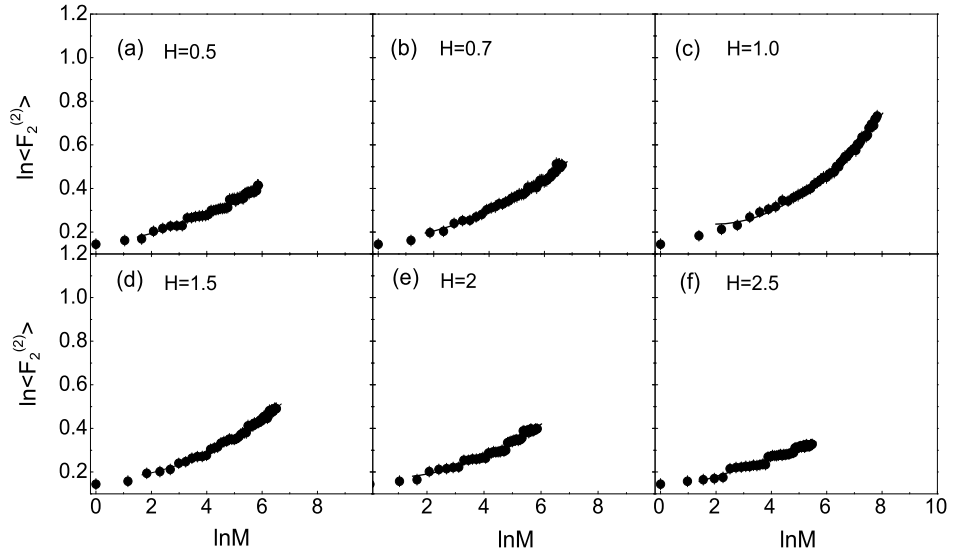


Figure 3.10: The same as in Figure 3.9 but for the ^{32}S -Ag/Br interaction at 200A GeV/c.

where $y = \ln\langle F_2^{(2)} \rangle$ and $x = \ln M$. In order to take care of the conservation rules depicted in [75] a couple of points at the lowest $\ln M$ region are omitted from the fits. Estimated values of the parameters a and b along with the R^2 coefficients are presented in Table 3.7 for the ^{16}O -Ag/Br interaction and in Table 3.8 for the ^{32}S -Ag/Br interaction. The errors quoted in these tables are statistical in nature. For both interactions the coefficient of the quadratic term in Equation (3.21) attains a maximum value at $H = 1.0$. Once the self-similarity of the underlying phase space is attained, one can estimate the effective fluctuation strength. A linear fit of the data as per Equation (3.10) now gives the required $\phi_q^{(2)}$ values at $H = 4.0$

Table 3.7: Values of fit parameters of $\ln\langle F_2^{(2)} \rangle$ against $\ln M$ plot by using a quadratic function like $f(x) = ax^2 + bx + c$ for the $^{16}\text{O-Ag/Br}$ interaction. The errors are of statistical origin.

Hurst Exponent(H)	a	b	R^2
0.25	0.0009±0.0021	0.0371±0.0144	0.908
0.30	0.0075±0.0025	-0.0016±0.0179	0.902
0.35	0.0021±0.0017	0.0376±0.0127	0.951
0.40	0.0034±0.0013	0.0319±0.0097	0.975
0.50	0.0073±0.0012	0.0066±0.0099	0.981
0.60	0.0111±0.0009	-0.0159±0.0086	0.990
0.70	0.0153±0.0010	-0.0491±0.0096	0.991
0.80	0.0184±0.0009	-0.0738±0.0095	0.993
1.0	0.0216±0.0010	-0.1051±0.0113	0.994
1.08	0.0182±0.0009	-0.0713±0.0104	0.994
1.1	0.0182±0.0010	-0.0712±0.0107	0.993
1.2	0.0154±0.0009	-0.0477±0.0100	0.992
1.4	0.0134±0.0008	-0.0335±0.0073	0.995
1.5	0.0122±0.0009	-0.0245±0.0084	0.992
1.6	0.0106±0.0009	-0.0106±0.0087	0.990
1.8	0.0092±0.0011	-0.0034±0.0093	0.986
2.0	0.0088±0.0013	-0.0053±0.0104	0.979
2.5	0.0039±0.0013	0.0223±0.0104	0.965
3.0	0.0055±0.0018	0.0068±0.0135	0.932
4.0	0.0006±0.0018	0.0309±0.0123	0.899

and 0.4, respectively for the $^{16}\text{O-Ag/Br}$ and $^{32}\text{S-Ag/Br}$ interactions. Note that the best linear dependence of $\ln\langle F_2^{(2)} \rangle$ on $\ln M$ is observed for the above specified values of H . We obtain the $2d$ intermittency index as $\phi_q^{(2)} = 0.0349 \pm 0.0017$ for the $^{16}\text{O-Ag/Br}$ interaction and $\phi_q^{(2)} = 0.0443 \pm 0.0012$ for the $^{32}\text{S-Ag/Br}$ interaction. The effective $2d$ intermittency strengths are $\alpha_{\text{eff}}^{(2)} = 0.2642 \pm 0.0064$ for the $^{16}\text{O-Ag/Br}$ interaction and $\alpha_{\text{eff}}^{(2)} = 0.2977 \pm 0.0040$ for the $^{32}\text{S-Ag/Br}$ interaction.

3.4 Factorial correlators

Factorial correlator (FC) introduced by Bialas and Peschanski [6, 7] is an important addition to the intermittency analysis of single particle density fluctuations. FCs can measure the local density fluctuations along with the bin-to-bin correlations present in the SFMs. The FCs are calculated for each combination of non-overlapping pair of bins (say jj' -th) separated by a distance D in the phase space. The FCs are defined as [6, 7],

$$F'_{pq} = \frac{\langle n_j^{[p]} n_{j'}^{[q]} \rangle}{F'_p F'_q} \quad (3.22)$$

Table 3.8: Values of fit parameters of $\ln\langle F_2^{(2)} \rangle$ against $\ln M$ plot by using a quadratic function like $f(x) = ax^2 + bx + c$ for the $^{32}\text{S-Ag/Br}$ interaction. The errors are of statistical origin.

Hurst Exponent(H)	a	b	R^2
0.25	-0.0004±0.0019	0.0391±0.0135	0.887
0.30	0.0026±0.0018	0.0222±0.0129	0.915
0.35	-0.0014±0.0013	0.0507±0.0097	0.950
0.40	-0.00004±0.0011	0.0446±0.0085	0.968
0.50	0.0046±0.0009	0.0175±0.0081	0.981
0.60	0.0039±0.0007	0.0286±0.0063	0.991
0.70	0.0071±0.0008	0.0036±0.0078	0.989
0.80	0.0085±0.0007	-0.0067±0.0068	0.993
1.0	0.0136±0.0007	-0.0515±0.0083	0.994
1.08	0.0108±0.0007	-0.0234±0.0078	0.993
1.1	0.0107±0.0007	-0.0224±0.0070	0.994
1.2	0.0094±0.0007	-0.0117±0.0067	0.994
1.4	0.0080±0.0006	-0.0019±0.0061	0.994
1.5	0.0079±0.0006	-0.0011±0.0059	0.994
1.6	0.0065±0.0009	0.0108±0.0078	0.988
1.8	0.0056±0.0009	0.0138±0.0078	0.986
2.0	0.0081±0.0012	-0.0082±0.0098	0.976
2.5	0.0014±0.0011	0.0331±0.0084	0.967
3.0	0.0029±0.0016	0.0196±0.0115	0.934
4.0	0.0005±0.0018	0.0295±0.0123	0.888

where $n_j^{[q]} = n_j(n_j - 1) \cdots (n_j - q + 1)$ is the single event q -th order SFM, $F'_q = \langle n_j^{[q]} \rangle$ and n_j ($n_{j'}$) is the number of tracks in the j -th (j' -th) interval. The above defined FCs are not symmetric in the indices p and q , and therefore they are symmetrized as,

$$\langle F_{pq} \rangle = \frac{1}{2} (F'_{pq} + F'_{qp}) \quad (3.23)$$

According to the α -model of intermittency [6, 7] F_{pq} should depend on the correlation length D but not on the phase space interval size δX , and they should follow a power-law relation like,

$$\langle F_{pq} \rangle \propto D^{-\phi_{pq}} \quad (3.24)$$

as $1/D$ approaches a large value. The exponent ϕ_{pq} measures the strength of correlation. Figure 3.11 shows event averaged FCs as functions of correlation length in the η -space for the $^{16}\text{O-Ag/Br}$ interaction at 200A GeV/c. The experimental results are supplemented by the corresponding UrQMD and UrQMD+BEC generated results. For each combination of (p, q) the experimental values of $\langle F_{pq} \rangle$ increase with increasing $-\ln D$. It is seen that there is a rapidly growing correlation at the beginning, a saturation next, and a moderate linear rise at the end. On the other hand, with increasing $-\ln D$ the simulated values of $\langle F_{pq} \rangle$ rise initially and then saturate. Since the $-\ln D$ versus $\langle F_{pq} \rangle$ plots are not linear over the

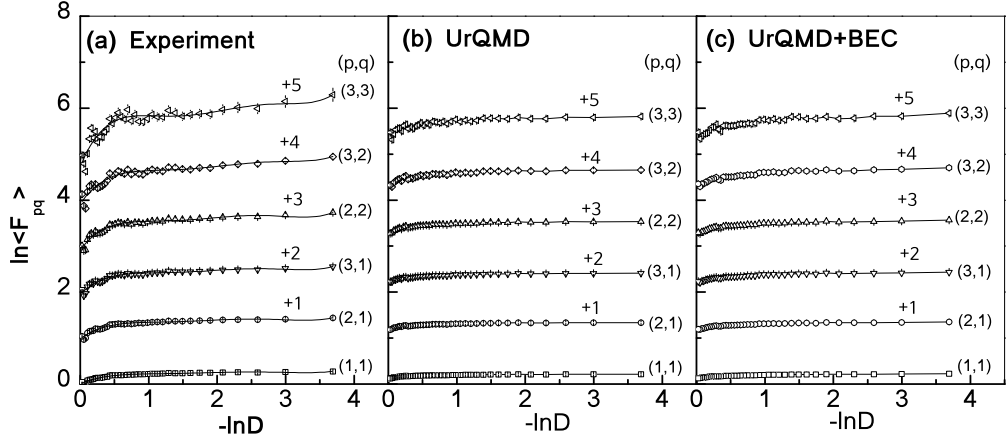


Figure 3.11: Plot showing the dependence of factorial correlators of different orders against correlation length for the ^{16}O -Ag/Br interaction at 200A GeV/c. Points represent (a) experimental values, (b)UrQMD values and (c)UrQMD+BEC values in η -space. For clarity correlators of successive orders are shifted by one unit along the vertical axis as shown in the diagram. Lines joining points are drawn to guide the eye.

entire range of $-\ln D$, the exponents ϕ_{pq} are obtained by fitting straight lines to the data only in the large $-\ln D$ region that corresponds to short-range correlations. The values of ϕ_{pq} , and the coefficient R^2 , a measure of the goodness of fits, are given in Table 3.9 for the ^{16}O -Ag/Br interaction. For an easy reference we show the values for the ^{32}S -Ag/Br interaction in Table 3.10. Both experiments produce almost identical values of the exponent ϕ_{pq} . Negligibly small values of ϕ_{pq} are obtained from the UrQMD simulation. Inclusion of BEC only marginally enhances the values of the exponent in both interactions. According to the α -model and log-normal approximation ϕ_{pq} exponents should follow a relation like

$$\phi_{pq} = \phi_{p+q} - \phi_p - \phi_q = (p \cdot q) \phi_{11} \quad (3.25)$$

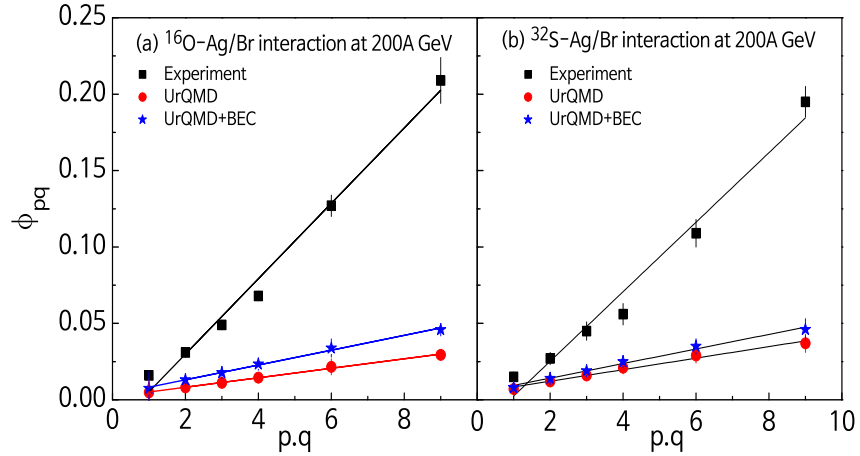
The validity of the above relation has been tested in Figure 3.12 by plotting ϕ_{pq} with the product $(p \cdot q)$ for both interactions. The results are consistent with a linear growth of the exponent ϕ_{pq} with the product $(p \cdot q)$, indicating the validity of the α -model in the ^{16}O -Ag/Br and ^{32}S -Ag/Br interactions at 200A GeV/c. UrQMD and UrQMD+BEC simulated results cannot match the respective experiment. The values of the slope parameter $\delta = \phi_{11}$ are given in Table 3.11. Another prediction of the α -model is that $\langle F_{pq} \rangle$ should be independent of δX_η . This aspect can be verified from Figure 3.13, where the values of $\langle F_{pq} \rangle$ obtained from the ^{16}O -Ag/Br data are plotted for several different values of δX_η at fixed D . Horizontal lines showing the uniformity of the $\langle F_{pq} \rangle$ distributions are drawn to guide the eye. Although a few points at large $-\ln \delta X_\eta$ and higher (p, q) slightly deviate from the average trend, in general considering the error bars, the prediction of the α -model is fulfilled in the ^{16}O -Ag/Br experiment. Similar results were also obtained for the ^{32}S -Ag/Br experiment [21]. It must

Table 3.9: The ϕ_{pq} exponents of the FC scaling for several different combinations of (p, q) for the ^{16}O -Ag/Br interaction.

(p,q)	Experiment		UrQMD		UrQMD+BEC	
	ϕ_{pq}	R^2	ϕ_{pq}	R^2	ϕ_{pq}	R^2
(1,1)	0.016 ± 0.001	0.952	0.005 ± 0.008	0.698	0.007 ± 0.011	0.886
(2,1)	0.031 ± 0.002	0.971	0.008 ± 0.002	0.685	0.013 ± 0.002	0.847
(3,1)	0.049 ± 0.002	0.980	0.011 ± 0.002	0.672	0.018 ± 0.003	0.825
(2,2)	0.068 ± 0.003	0.983	0.014 ± 0.003	0.665	0.023 ± 0.003	0.832
(3,2)	0.127 ± 0.007	0.977	0.022 ± 0.005	0.631	0.034 ± 0.006	0.767
(3,3)	0.209 ± 0.015	0.963	0.029 ± 0.001	0.554	0.046 ± 0.002	0.887

Table 3.10: The ϕ_{pq} exponents of the FC scaling for several different combinations of (p, q) for the ^{32}S -Ag/Br interaction.

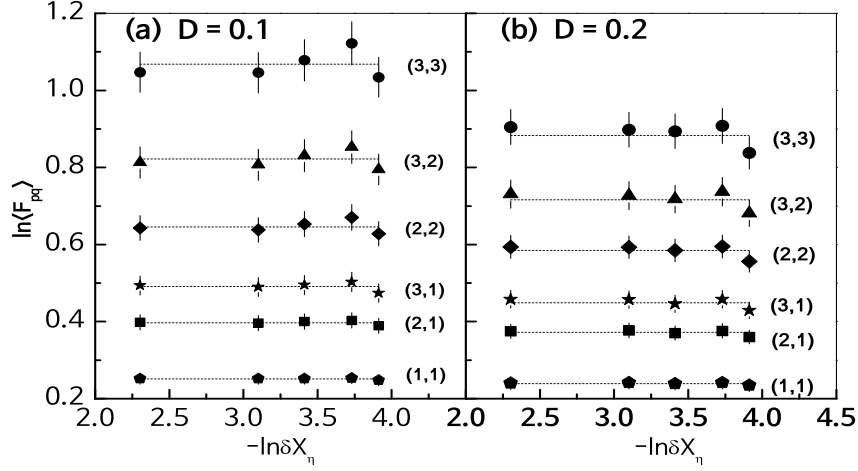
(p,q)	Experiment		UrQMD		UrQMD+BEC	
	ϕ_{pq}	R^2	ϕ_{pq}	R^2	ϕ_{pq}	R^2
(1,1)	0.015 ± 0.002	0.943	0.007 ± 0.001	0.783	0.008 ± 0.001	0.827
(2,1)	0.027 ± 0.004	0.927	0.012 ± 0.002	0.782	0.014 ± 0.002	0.838
(3,1)	0.045 ± 0.006	0.932	0.016 ± 0.003	0.780	0.019 ± 0.003	0.843
(2,2)	0.056 ± 0.007	0.948	0.021 ± 0.004	0.785	0.025 ± 0.003	0.844
(3,2)	0.109 ± 0.009	0.973	0.029 ± 0.005	0.800	0.035 ± 0.005	0.848
(3,3)	0.195 ± 0.010	0.990	0.037 ± 0.006	0.777	0.046 ± 0.007	0.831

**Figure 3.12:** Plot of ϕ_{pq} versus $p.q$ in η -space according to the predictions of the α -model. The solid line is the best-fit straight line to the experimental values.

be mentioned that such a property does not only hold for the α -model, but it is in general a feature of any model that takes short-range correlations into account [94]. Our results on FCs indicate the presence of short-range bin-to-bin correlations in the experiment, and the gross features of the experiments are consistent with the prediction of the α -model. The correlation strength in the UrQMD generated data sample for each interaction is negligibly small, much smaller (almost by an order of magnitude) than the corresponding experiment.

Table 3.11: The values of slope parameter (δ) obtained from the ϕ_{pq} vs $(p \cdot q)$ plot.

	$^{16}\text{O-Ag/Br}$		$^{32}\text{S-Ag/Br}$	
	δ	R^2	δ	R^2
Experiment	0.025 ± 0.001	0.994	0.023 ± 0.002	0.988
UrQMD	0.003 ± 0.0001	0.998	0.004 ± 0.0002	0.992
UrQMD+BEC	0.005 ± 0.0001	0.998	0.005 ± 0.0002	0.995

**Figure 3.13:** Plot showing independence of factorial correlators with respect to phase space partition size δX_η at fixed D for the $^{16}\text{O-Ag/Br}$ interaction at 200A GeV/c. The dotted lines are best fit straight lines to the data.

3.5 Oscillatory moments

The effect of multiparticle correlation can also be studied by using the factorial cumulant moments K_q [95]. They measure the genuine higher order correlations, where contributions from lower order correlations are eliminated. The K_q -moments are defined as,

$$K_q = F_q - \sum_{j=1}^{q-1} \binom{q-1}{j-1} F_{q-j} K_j \quad : \quad q = 2, 3, \dots \quad (3.26)$$

For Poisson distributed multiplicities $K_1 = 1$ and $K_{q>1} = 0$. Thus, nonzero values of K_q for $q \geq 2$, indicate the presence of two or more particle correlations in the inclusive density distribution of the produced particles. It has been predicted by a QCD-based parton shower cascade model that with increasing q the K_q moments would oscillate irregularly around zero. Both F_q and K_q possess strong energy and order dependence. In order to take care of such trivial dependences, a new set of normalized cumulant moments are defined [16] as,

$$H_q = K_q / F_q \quad (3.27)$$

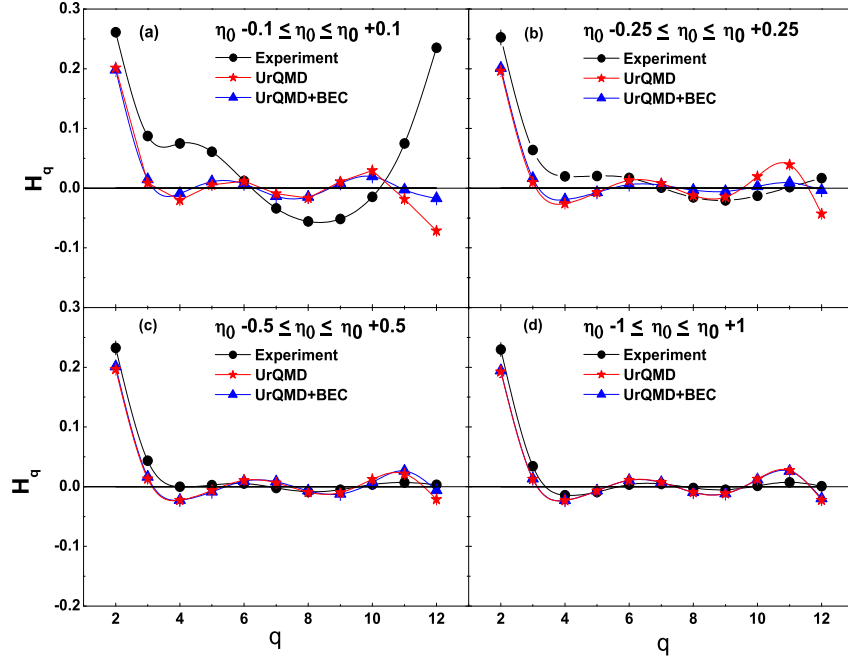


Figure 3.14: Oscillatory moments H_q for different widths of η interval. In each η interval, experiment, UrQMD and UrQMD+BEC results are plotted together. $H_q = 0$ is the horizontal solid line. The graph is for the $^{16}\text{O-Ag/Br}$ interaction at 200A GeV/c.

In high-energy e^+e^- , hadron-hadron (hh), and hadron-nucleus (hA) interactions, oscillatory behavior of the H_q -moments with increasing q has been experimentally confirmed [1–4, 17, 96]. For the e^+e^- and hh interactions the observed behavior has been attributed to a multicomponent structure of the particle production process, whereas for hA interactions the result has been explained in terms of a leading particle cascade model [97]. Empirically, a negative binomial distribution and/or a modified negative binomial distribution have/has been used to describe the multiplicity distributions in these interactions. But neither of them could explain the behavior of the cumulant moments [98]. The H_q moments computed for the $^{16}\text{O-Ag/Br}$ and $^{32}\text{S-Ag/Br}$ interactions at 200A GeV/c are shown in Figure 3.14 and Figure 3.15 respectively. In these figures the experimental results are compared with the UrQMD and UrQMD+BEC simulated results. The normalized oscillatory moments H_q are calculated in several different η -windows positioned symmetrically about the centroid (η_0) of the respective η -distribution like, (i) $\eta_0 - 0.1 \leq \eta \leq \eta_0 + 0.1$, (ii) $\eta_0 - 0.25 \leq \eta \leq \eta_0 + 0.25$, (iii) $\eta_0 - 0.5 \leq \eta \leq \eta_0 + 0.5$ and (iv) $\eta_0 - 1.0 \leq \eta \leq \eta_0 + 1.0$. One can see that only in the narrowest η -window the experimental results are significantly different from the UrQMD and UrQMD+BEC results. The extent of oscillation, particularly at large q , is much larger for the experiment than what it is either for the UrQMD or the UrQMD+BEC data. This is indicative of different characteristics of the jet structure in the experiment and simulation. At small q the oscillation starts even before H_q drops down to zero. The UrQMD and UrQMD+BEC data on the other hand, exhibit smaller amplitudes of oscillation

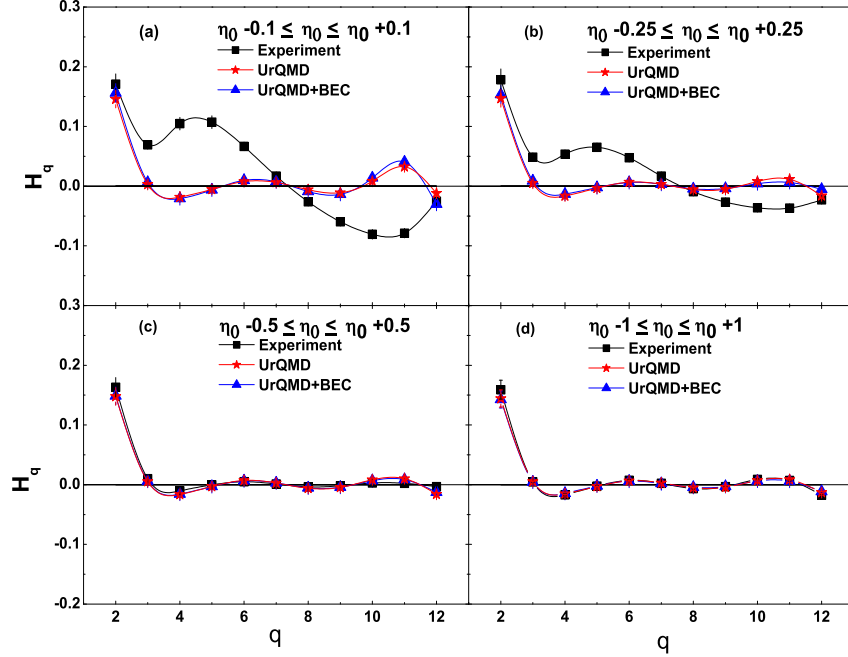


Figure 3.15: The same as in Figure 3.14 but for the ^{32}S -Ag/Br interaction at 200A GeV/c.

compared to the respective experiment. As the η -interval size increases, the difference between experiment and simulation tends to decrease. In large η -windows, particularly in $\eta_0 \pm 0.5$ and $\eta_0 \pm 1.0$, perhaps due to intermixing of particles coming from different sources, the correlation effects are washed out. The moments therefore show only very little or no oscillation, and the experimental results begin to coincide with the simulations. The above observations are more or less identical for both ^{16}O -Ag/Br and ^{32}S -Ag/Br interactions at 200A GeV/c.

3.6 Erraticity moments

As mentioned above the erraticity moments deal with the event space fluctuations of the factorial moments. We define a single event factorial moment F_q^e of order q as,

$$F_q^e = \frac{\frac{1}{M} \sum_{m=1}^M n_m (n_m - 1) \dots (n_m - q + 1)}{\left(\frac{1}{M} \sum_{m=1}^M n_m\right)^q} \quad (3.28)$$

M is the number of non-overlapping intervals in the η -space and n_m is the number of particles in the m -th such interval. Figure 3.16 shows the distributions of F_q^e for the ^{16}O -Ag/Br interaction for $M = 5$ and $M = 10$. The experimental results are compared with the corresponding UrQMD and UrQMD+BEC simulated events. It can be seen that majority of the F_q^e values are concentrated within an initial small range. However, a long, slowly decaying

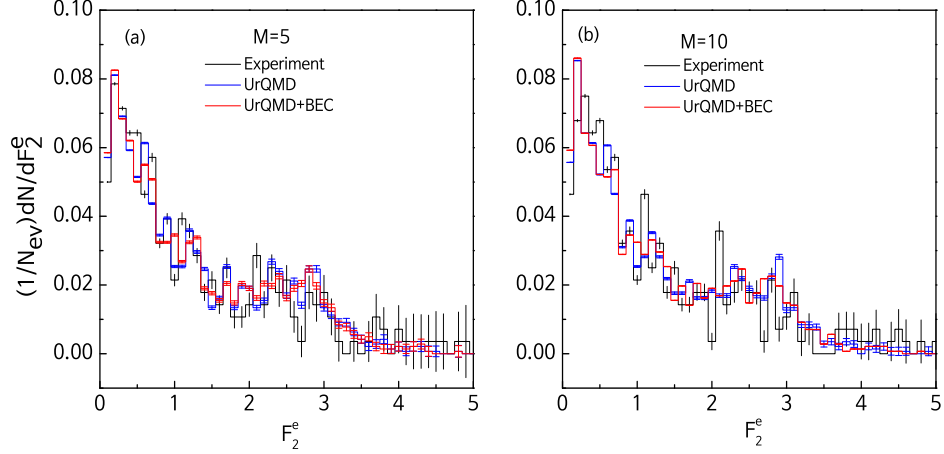


Figure 3.16: Distributions of F_2^e in the $^{16}\text{O-Ag/Br}$ interaction at 200A GeV/c for two different values of η space partition number (a) $M = 5$ and (b) $M = 10$.

tail that corresponds to growingly larger F_q^e values, is also visible in each distribution. It is our objective to quantify these large fluctuations in F_q^e in terms of the erraticity moments and associated parameters.

The method of erraticity analysis starts by introducing an event-wise normalized factorial moment $\Phi_q = F_q^e / \langle F_q^e \rangle$, and then by defining a couple of erraticity moments expressed in terms of Φ_q . The vertically averaged p -th order moment of Φ_q or the erraticity moment is defined as,

$$C_{p,q} = \langle \Phi_q^p \rangle \quad (3.29)$$

and an entropy like quantity Σ_q is defined as,

$$\Sigma_q = \langle \Phi_q \ln \Phi_q \rangle \quad (3.30)$$

In the $p > 1$ region $C_{p,q}$ characterizes the tails of F_q^e -distribution and is sensitive only to the spikes of the corresponding η -distribution. On the other hand $C_{p < 1, q}$ characterizes the small F_q^e behavior of the F_q^e -distribution, which is influenced mainly by η -bins with low multiplicities. A typical domain of analysis is $0 < p < 2$, which reveals enough information about the F_q^e -distribution. We are particularly interested in studying the erraticity behavior in the $p \approx 1$ region. In multiparticle dynamics the erraticity moments $C_{p,q}$ are found to follow a scaling-law with phase space partition number M (equivalently with the window size $\delta\eta$) like,

$$C_{p,q} \propto M^{\psi(p,q)} : M \rightarrow \infty \quad (3.31)$$

The above equation is referred to as *the erraticity*, and the exponent $\psi(p, q)$ is called *the erraticity index*. If the spatial pattern of particle density function does not change from

one event to another, the distribution $P(F_q^e)$ tends to a delta function. Under such circumstances, both ϕ_q and $C_{p,q}$ would reduce to unity and $\psi(p, q) \rightarrow 0$. Any deviation of $\psi(p, q)$ from zero value can therefore be considered as an erraticity measure. The slope parameter,

$$\mu_q = \left. \frac{d}{dp} \psi_q(p) \right|_{p=1} \quad (3.32)$$

is called the entropy index. In high-energy AB interactions $C_{p,q}$ may not exhibit as strict a scaling-law as prescribed in Equation (3.31), but would rather abide by a more generalized formula like,

$$C_{p,q} \propto f(M)^{\tilde{\psi}(p,q)} \quad (3.33)$$

where $f(M)$ is some well behaved function of M . Similar to Equation (3.33) one would expect a generalized scaling-law for the Σ_q moments like,

$$\Sigma_q \propto \tilde{\mu}_q \ln[f(M)] \quad (3.34)$$

From Equation (3.33) and Equation (3.34) it follows that

$$\tilde{\mu}_q = \left. \frac{d}{dp} \tilde{\psi}(p, q) \right|_{p=1} \quad (3.35)$$

The index $\tilde{\mu}_q$ is quite different from the entropy index μ_q , and therefore, should not be compared with each other. However, the exponent $\tilde{\mu}_q$ is again a measure of the erratic behavior of the event space fluctuation of the factorial moments [19, 20]. A small $\tilde{\mu}_q$ value corresponds to a less chaotic system, whereas a large $\tilde{\mu}_q$ value corresponds to a highly chaotic system.

In Figure (3.17) the $C_{p,q}$ moments for $q = 2$ and 3 over a wide range of p -values are plotted against M for the $^{16}\text{O-Ag/Br}$ interaction. For a better comparison the experiment and simulation are plotted together. From these graphs one can see that the experimental $C_{p,q}$ values vary over a wider range compared to the corresponding UrQMD and UrQMD+BEC generated values. A smooth but nonlinear increasing trend of $\ln C_{p,q}$ with $\ln M$ can be seen over its entire range, which indicates the justification of invoking a generalized power-law as prescribed in Equation (3.33). Several kinks (or discontinuities) seen at large M for all the plots might be an outcome of the limited statistics of our event sample(s). A similar pattern is also observed for the $^{32}\text{S-Ag/Br}$ interaction at $200A$ GeV/c. To establish a generalized scaling-law as suggested by Cao and Hwa [19, 20], we have assumed $\ln f(M) = (\ln M)^b$, taking b as a free parameter that may be adjusted from the linear fit of the $\ln C_{2,2}$ versus $\ln[f(M)]$ data. Such plots are shown in Figure 3.18 along with the respective best fitted straight lines. The values of b so obtained, are given in the third column of Table 3.12. In all the cases Pearson's coefficient R^2 , which decides the goodness of fit, are found to be > 0.98 .

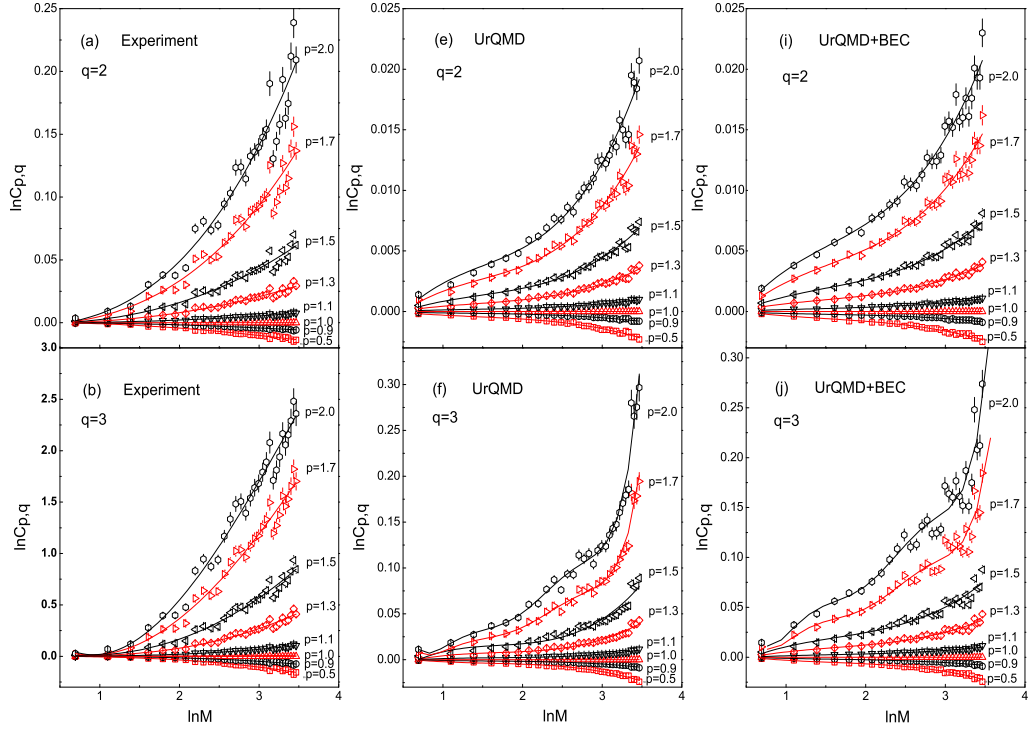


Figure 3.17: Erraticity moments $C_{p,q}$ plotted as functions of phase space partition number M for the $^{16}\text{O-Ag/Br}$ interaction. The solid curves are drawn to guide the eye.

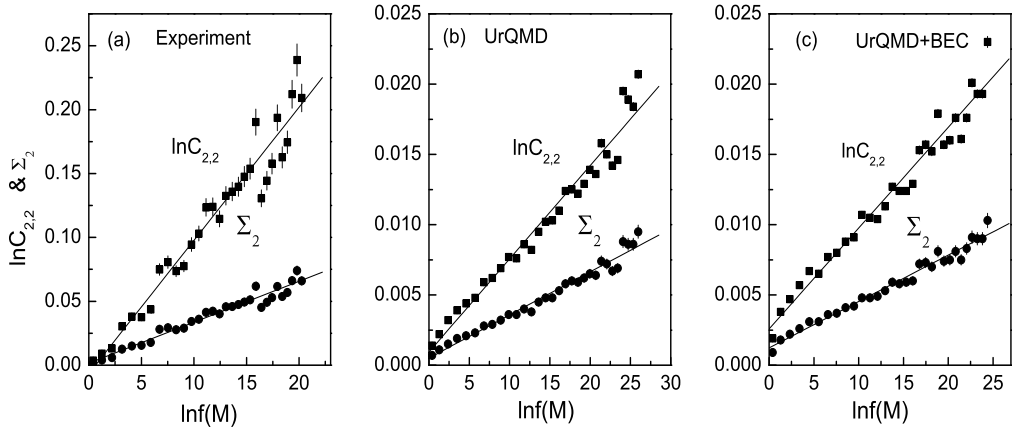


Figure 3.18: Plot of $\ln C_{2,2}$ and Σ_2 with $\ln f(M) = \ln M^b$ for the $^{16}\text{O-Ag/Br}$ interaction. The lines represent best linear fits to the data points.

The slope of the $\ln[f(M)]$ versus $\ln C_{2,2}$ straight line fit gives us another parameter ($\tilde{\psi}(2, 2)$) related to the erraticity analysis. The $\tilde{\psi}(2, 2)$ values are quoted in the fourth column of Table 3.12. The indices $\tilde{\mu}_2$ can now be obtained from the linear relationship between Σ_2 and $\ln[f(M)]$ using the b -values already obtained from the best fit. These plots are also included in Figure 3.18 and $\tilde{\mu}_2$ values are given in the fifth column of Table 3.12. Note that all the $C_{p,q}$ moments depend almost similarly on $\ln M$. In order to evaluate the erraticity

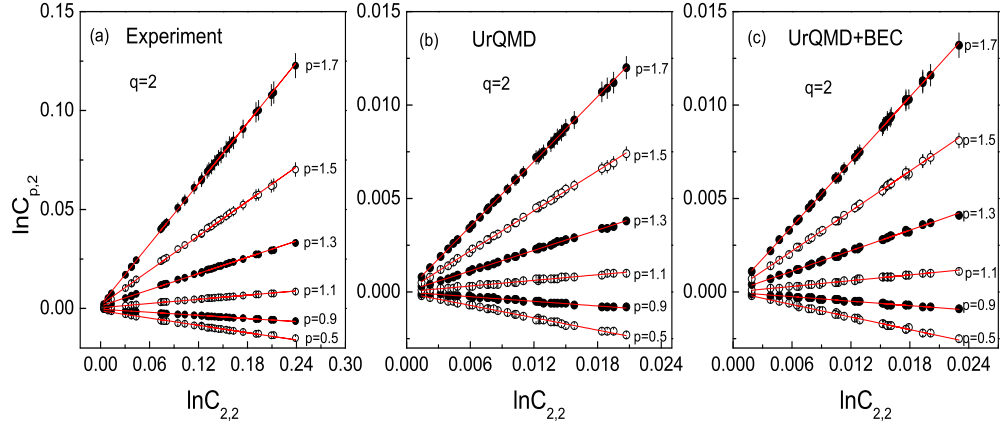


Figure 3.19: Plot of $\ln C_{p,2}$ with $\ln C_{2,2}$ for the $^{16}\text{O-Ag/Br}$ interaction. The best fitted straight lines are shown.

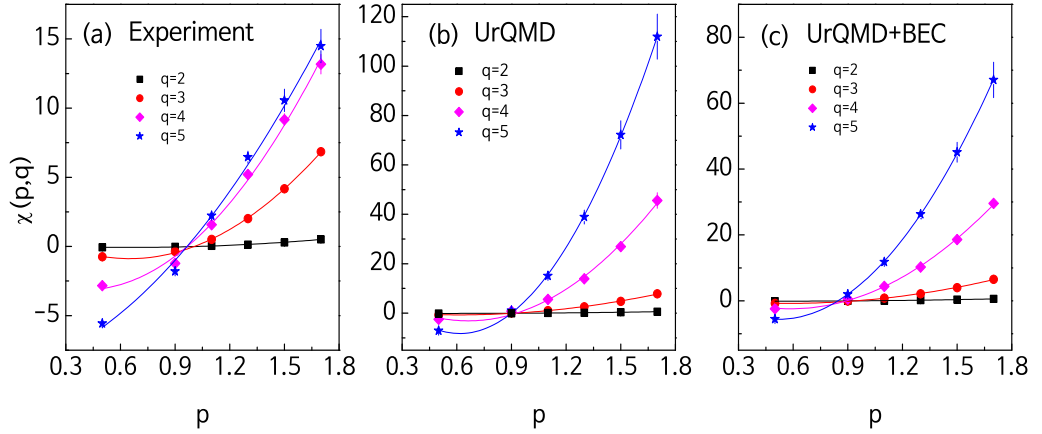


Figure 3.20: Variation of $\chi(p, q)$ with p for the $^{16}\text{O-Ag/Br}$ interaction. The curves represent the best quadratic fits.

parameters, one can therefore also use $\ln C_{2,2}$ in place of $\ln[f(M)]$. The scaling relation (Equation 3.33) then would reduce to a simple power law like,

$$C_{p,q} \propto (C_{2,2})^{\chi(p,q)} \quad (3.36)$$

We find that for $q = 2$ the expected linear dependence of $\ln C_{p,q}$ on $\ln C_{2,2}$ is almost exact. For different values of p the results are graphically presented in Figure 3.19 for the $^{16}\text{O-Ag/Br}$ interaction. For $q > 2$ the linear dependence is only approximate in the sense that it is valid only in the low- M region. The effects of finite multiplicity and limited statistics are visible at large M . For $q > 2$ we have obtained $\chi(p, q)$ through a linear fit of the $\ln C_{p,q}$ versus $\ln C_{2,2}$ data within a limited region of M (≤ 12), where $\ln C_{p,q}$ is found to behave systematically with $\ln C_{2,2}$. Figure 3.20 shows the $\chi(p, q)$ versus p plots for different q values for the $^{16}\text{O-Ag/Br}$ interaction. The solid lines in these diagrams represent a quadratic

Table 3.12: Values of b , $\tilde{\psi}(2,2)$ & $\tilde{\mu}_2$ for the experiment, the UrQMD and the UrQMD+BEC data.

Interaction	Data Set	b	$\tilde{\psi}(2,2)$	$\tilde{\mu}_2$
^{16}O -Ag/Br interaction at 200A GeV/c	Experiment	2.42	0.0104 ± 0.0005	0.0032 ± 0.0001
	UrQMD	2.62	0.0007 ± 0.00002	0.0003 ± 0.00009
	UrQMD+BEC	2.57	0.0007 ± 0.00009	0.00033 ± 0.00002
^{32}S -Ag/Br interaction at 200A GeV/c	Experiment	2.08	0.0029 ± 0.00007	0.00126 ± 0.00003
	UrQMD	2.52	0.00011 ± 0.000003	0.00006 ± 0.0000021
	UrQMD+BEC	2.22	0.0002 ± 0.000007	0.00009 ± 0.000004

function for a fixed q like,

$$\chi(p, q) = a_2 p^2 + a_1 p + a_0 \quad (3.37)$$

The first order derivatives of $\chi(p, q)$ at $p = 1$

$$\chi'_q = \frac{\partial}{\partial p} \chi(p, q)|_{p=1} \quad (3.38)$$

can now be used to determine the $\tilde{\mu}_q$ index from the following relation,

$$\tilde{\mu}_q = \tilde{\psi}(2, 2) \chi'_q \quad (3.39)$$

In Figure 3.21 the entropy-like moments Σ_q are also plotted against $\ln M$ for different q -values. As expected, these moments are also nonlinear functions of $\ln M$. However, for all positive q the variations look quite similar. This gives us a freedom to use Σ_2 as the independent variable in place of $f(M)$. The plots of Σ_q against Σ_2 are shown in Figure 3.22 for our ^{16}O -Ag/Br data and corresponding simulations. In each case the slope parameters

$$\omega_q = \frac{\partial \Sigma_q}{\partial \Sigma_2} \quad (3.40)$$

are obtained by making a linear fit of the Σ_q versus Σ_2 plots within a limited M (≤ 12) region. Subsequently, once again we derive the $\tilde{\mu}_q$ index by using the following relation,

$$\tilde{\mu}_q = \tilde{\mu}_2 \omega_q \quad (3.41)$$

All four erraticity parameters namely χ'_q , ω_q and two sets of $\tilde{\mu}_q$ obtained from Equation (3.39) and Equation (3.41), have been presented in Table 3.13 for the ^{16}O -Ag/Br interaction at 200A GeV/c. Table 3.14 on the other hand shows the corresponding values for the ^{32}S -Ag/Br interaction. The parameters obtained from the experiment as well as from the simulations are presented together for an easy comparison. Several observations can now be

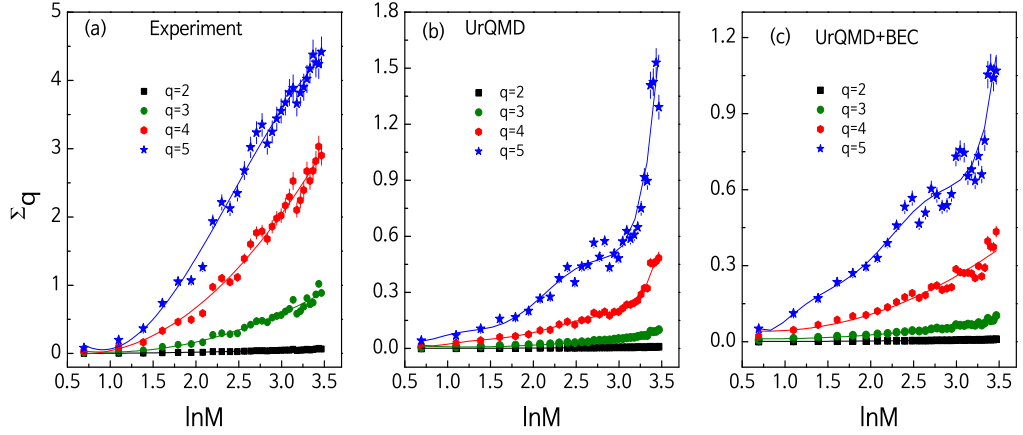


Figure 3.21: Plot of Σ_q with $\ln M$ for the ^{16}O -Ag/Br interaction. The lines joining points are drawn to guide the eye.

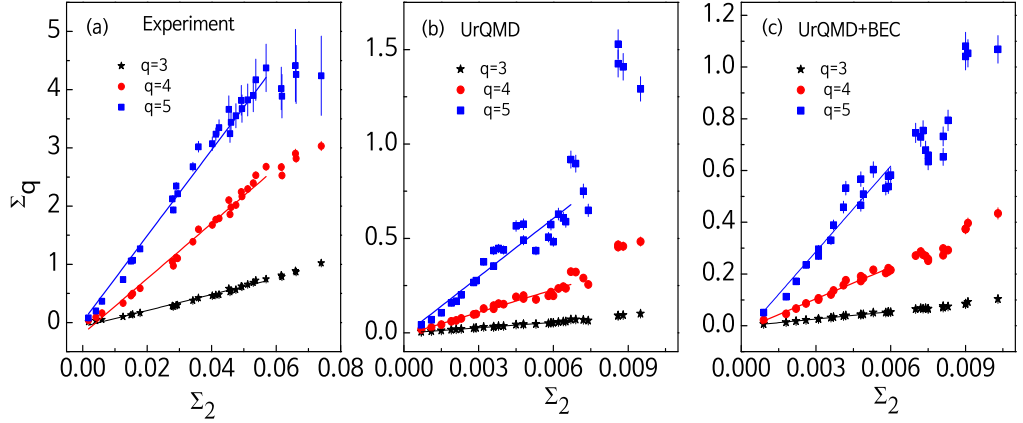


Figure 3.22: Plot of Σ_q against Σ_2 for the ^{16}O -Ag/Br interaction. The lines represent best linear fits to the data points in the $M \leq 12$ region.

made regarding the erraticity behavior of the interactions studied in this analysis. In general, erraticity in the particle production mechanism is observed for all the data sets used. The index $\tilde{\mu}_q$ obtained by using two different formulae, Equation (3.39) and Equation (3.41), within their statistical uncertainties, are very close to each other for both the interactions under consideration. In the ^{16}O -Ag/Br experiment the $\tilde{\mu}_q$ values are greater than the corresponding ^{32}S -Ag/Br values. For a better understanding $\tilde{\mu}_q$ values are plotted with q in Figure 3.23 for the ^{16}O -Ag/Br data. Figure 3.23(a) is drawn following Equation (3.39) and Figure 3.23(b) following Equation (3.41). In these diagrams the experimental $\tilde{\mu}_q$ values show a rapid growth with increasing q and the values are always larger than the corresponding simulated values. Almost an identical pattern was observed also for the ^{32}S -Ag/Br interaction at 200A GeV/c [23]. For the ^{28}Si -Ag/Br interaction at 14.5A GeV [79] the exponent values are found to be slightly less than that obtained either in the ^{16}O -Ag/Br or in the ^{32}S -Ag/Br interaction at 200A GeV/c. Comparing the results of our erraticity analysis with

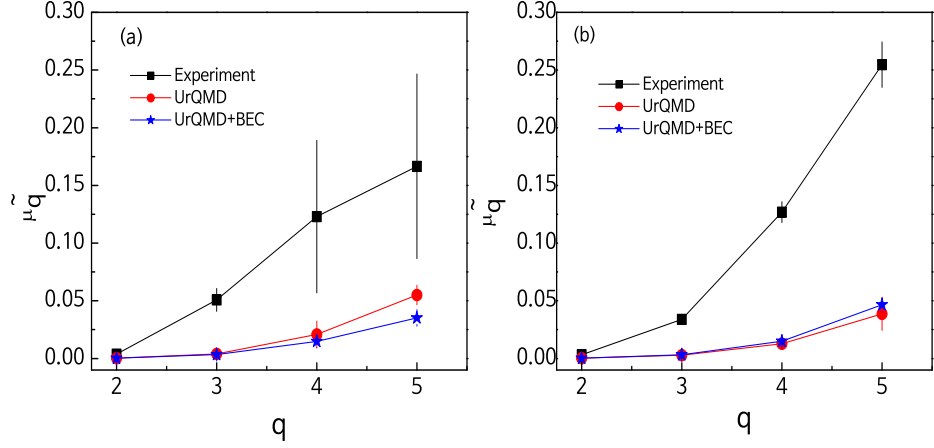


Figure 3.23: Plot of the entropy index $\tilde{\mu}_q$ against order number q calculated from (a) Equation (3.39) and (b) Equation (3.41) for the $^{16}\text{O-Ag/Br}$ interaction. Lines joining the data points are shown.

similar results available in literature [68, 79], one can argue that the parameters depend more on the colliding system (projectile mass number) than on the energy of the collision. An increase in the entropy index signals the augmentation of a possible quark-hadron phase transition [99]. This feature has indeed been observed for a possible non-thermal phase transition [100]. We find a similar increasing trend in the $\tilde{\mu}_q$ parameter for the present set of $^{16}\text{O-Ag/Br}$ and $^{32}\text{S-Ag/Br}$ data, that might be a signal of non-thermal phase transition. For all the parameters studied in connection with our erraticity analysis the UrQMD and UrQMD+BEC simulated results cannot match the respective experiment. It looks like that

Table 3.13: Erraticity parameters in the $^{16}\text{O-Ag/Br}$ interaction at $200A$ GeV/c.

Order	χ'_q	ω_q	$\tilde{\mu}_q = \tilde{\psi}(2, 2) \chi'_q$	$\tilde{\mu}_q = \tilde{\mu}_2 \omega_q$
-Experiment-				
2	0.3585 ± 0.1526	–	0.0037 ± 0.0018	0.0032 ± 0.0001
3	4.8897 ± 0.7076	10.5999 ± 0.2905	0.0509 ± 0.0099	0.0339 ± 0.0020
4	11.8182 ± 5.7735	39.5938 ± 1.4085	0.1231 ± 0.0661	0.1268 ± 0.0090
5	16.0123 ± 7.7193	79.5720 ± 2.8979	0.1668 ± 0.0880	0.2546 ± 0.0197
-UrQMD-				
2	0.4691 ± 0.0358	–	0.0003 ± 0.00003	0.0003 ± 0.0001
3	5.5574 ± 2.0006	9.4482 ± 0.2546	0.0039 ± 0.0015	0.0028 ± 0.0009
4	29.9204 ± 15.4343	42.3925 ± 2.0933	0.0209 ± 0.0114	0.0127 ± 0.0044
5	78.5247 ± 9.8705	129.1417 ± 9.5503	0.0549 ± 0.0085	0.0387 ± 0.0145
-UrQMD+BEC-				
2	0.4704 ± 0.0415	–	0.0003 ± 0.0001	0.0003 ± 0.00002
3	4.8484 ± 1.0341	9.9323 ± 0.2553	0.0034 ± 0.0012	0.0033 ± 0.0003
4	21.1468 ± 4.8363	45.5489 ± 2.3834	0.0148 ± 0.0053	0.0150 ± 0.0017
5	50.2871 ± 3.7539	140.9617 ± 10.0848	0.0352 ± 0.0072	0.0465 ± 0.0062

Table 3.14: Erraticity parameters in the ^{32}S -Ag/Br interaction at 200A GeV/c.

Order	χ'_q	ω_q	$\tilde{\mu}_q = \tilde{\psi}(2, 2) \chi'_q$	$\tilde{\mu}_q = \tilde{\mu}_2 \omega_q$
-Experiment-				
2	0.4370±0.0540	–	0.0013±0.0002	0.0013±0.00003
3	7.0600±1.7400	15.550±0.5400	0.0210±0.0050	0.0195±0.0008
4	33.980±3.1700	79.630±3.3300	0.0990±0.0090	0.1000±0.0050
5	72.260±17.370	191.20±4.9900	0.2100±0.0500	0.2400±0.0080
-UrQMD-				
2	0.4970±0.0760	–	0.0001±0.00001	0.0001±0.000002
3	4.2910±0.1640	8.4090±0.1630	0.0005±0.00003	0.0005±0.00003
4	18.6530±1.5790	35.987±1.1390	0.0021±0.0002	0.0022±0.0001
5	57.907±9.7320	108.523±4.8190	0.0064±0.0012	0.0065±0.0005
-UrQMD+BEC-				
2	0.4910±0.0600	–	0.0001±0.00002	0.0001±0.000004
3	4.9360±0.4970	9.7120±0.2480	0.0009±0.0001	0.0009±0.00006
4	26.4630±9.7890	47.5750±2.2710	0.0053±0.0021	0.0043±0.0004
5	104.978±65.882	167.643±12.791	0.0210±0.0139	0.0151 ±0.0018

the erraticity behavior comes merely as a statistical effect in the UrQMD model. Inclusion of BEC does not add any significant change in the observations.

3.7 Summary

In this chapter we have presented the results of our intermittency analysis and related issues on the shower track distribution in ^{16}O -Ag/Br interaction at 200A GeV/c. On many occasions our ^{16}O -Ag/Br results are compared with similar results obtained from the ^{32}S -Ag/Br interaction at 200A GeV/c. We also provide a systematic comparison of the experimental results with the predictions of the UrQMD and UrQMD+BEC models. Major observations of this analysis are summarized below.

- (i) We find an intermittent pattern of the density distribution of the shower tracks in the ^{16}O -Ag/Br interaction at 200A GeV/c which is self-similar in the η or φ , and self-affine in (η, φ) space. The intermittency observed in ^{16}O -Ag/Br data is stronger than that observed in the ^{32}S -Ag/Br data. Comparing the results of this analysis with similar results available in the literature, we understand that the $1d$ intermittency depends more on the colliding objects than on the collision energy. Higher order particle correlations in ^{16}O -Ag/Br interaction cannot be fully explained in terms of two and three-particle (lower order) correlations. Since the shower tracks consist of both positive and negative charged mesons, not strictly identical fields, the observed

correlations are not exactly Bose-Einstein type either. The order dependence of the intermittency indexes rule out the possibility of a second-order thermal phase transition in the $^{16}\text{O-Ag/Br}$ and $^{32}\text{S-Ag/Br}$ interactions. However, a weak sign of a multiplicative cascade mechanism is observed in the experiments. The multifractal specific heat C has been calculated from the generalized Rényi dimensions. However, the values of C do not match with the universal expected value ($C = 0.25$) of the parameter.

- (ii) Our analysis on factorial correlators indicate that short range bin-to-bin correlations are present in the data, and the experimental observations in this regard are consistent with the α -model. Once again the observed correlations could not be reproduced either by the UrQMD or by the UrQMD+BEC. The oscillatory moments are found to be quite sensitive to the type of correlations present in the experiment as well as in the simulations. The results on FCs and OMs therefore, cannot be simply interpreted in terms of a few particle correlations.
- (iii) The $2d$ intermittency strength is significantly higher compared to that in the $1d$, i.e. dimensional reduction of underlying space affects the intermittency phenomenon. As expected, the UrQMD simulated results show almost negligible intermittency for both $^{16}\text{O-Ag/Br}$ and $^{32}\text{S-Ag/Br}$ interactions at $200A$ GeV/c. However, a small amount of intermittency is observed when the BEC is incorporated into the UrQMD output. The experimental values of $2d$ intermittency index $\phi_q^{(2)}$ are several times larger than the UrQMD+BEC simulated values. The $2d$ intermittency results suggest that the underlying fractal structure of the dynamical fluctuation is not self-similar at all scales, rather it is self-affine. The self-similarity could be retrieved only when the anisotropy in the (η, φ) plane is properly addressed by using the Hurst exponent H . In this analysis we find that the anisotropy in the $2d$ space can be retrieved for two different values of H , with $H = 0.4$ and $H = 4.0$. We do not attribute any physical significance to the value $H > 1.0$. However, for $H \sim 0.4$ the data behave in a more systematic and consistent manner. The fluctuation strength in $2d$ are always greater in the $^{16}\text{O-Ag/Br}$ interaction than in the $^{32}\text{S-Ag/Br}$ interaction.
- (iv) A substantial amount of event-to-event fluctuations of the SFMs is observed in the $^{16}\text{O-Ag/Br}$ interaction at $200A$ GeV/c. The fluctuations are characterized by a power-law type of scaling of the erraticity moments $C_{p,q}$ and Σ_q against the partition number M . The event space fluctuations of the SFMs is found to be more chaotic in the $^{32}\text{S-Ag/Br}$ than in the $^{16}\text{O-Ag/Br}$ interaction. The UrQMD and UrQMD+BEC generated values of the SFM in both $^{16}\text{O-Ag/Br}$ and $^{32}\text{S-Ag/Br}$ interactions exhibit erraticity too. The chaoticity present in the UrQMD simulations are however not as prominent as they are in the experiments. A comparison of our results with those obtained from the transport model, as well as with the results obtained from other experiments on

hN , NN and AB interactions [20, 58, 59, 69] shows that, the chaoticity is significantly weaker in the present case than that obtained in other investigations.

Bibliography

- [1] W. Kittel and E. A. De Wolf, *Soft Multihadron Dynamics*, World Scientific (2005).
- [2] W. Kittel, *Proceedings of the Twentieth International Symposium on Multiparticle Dynamics*, Gut Holmeche, Germany (1990), Edited by R. Baier and D. Wegener, World Scientific, Singapore (1991).
- [3] I. M. Dremin and J. W. Gary, *Phys. Rep.* 349, 301 (2001).
- [4] E. A. De Wolf, I. M. Dremin and W. Kittel, *Phys. Rep.* 270, 1 (1996).
- [5] *Fluctuations and fractal structure*, *Proceedings of Ringberg Workshop on multiparticle production*, Ringberg Castle, Germany, 1991, Edited by R. C. Hwa, W. Ochs and N. Schmitz, World Scientific, Singapore (1992).
- [6] A. Bialas and R. Peschanski, *Nucl. Phys. B* 273, 703 (1986).
- [7] A. Bialas and R. Peschanski *Nucl. Phys. B* 308, 857 (1988).
- [8] T. H. Burnett *et al.*, *Phys. Rev. Lett.* 50, 2062 (1983).
- [9] I. M. Dremin, *Sov. J. Nucl. Phys.* 30, 726 (1981).
- [10] W. Ochs, *Phys. Lett. B* 247, 101 (1990).
- [11] A. Bialas and K. Zalewski, *Phys. Lett. B* 238, 413 (1990).
- [12] R. C. Hwa, *Phys. Lett. B* 201, 165 (1988).
- [13] I. M. Dremin, *JETP Lett.* 30, 152 (1980).
- [14] B. Andersson, P. Dahlquist and G. Gustafson, *Phys. Lett. B* 214, 604 (1988).
- [15] B. C. Chiu and R. C. Hwa, *Phys. Lett. B* 236, 466 (1990).
- [16] I. M. Dremin, *Phys. Lett. B* 313, 209 (1993).
- [17] I. M. Dremin *et al.*, *Phys. Lett. B* 336, 119 (1994).
- [18] Z. Cao and R. C. Hwa, *Phys. Rev. Lett.* 75, 1268 (1995).
- [19] Z. Cao and R. C. Hwa, *Phys. Rev. D* 53, 6608 (1996).

- [20] Z. Cao and R. C. Hwa, Phys. Rev. D 61, 074011 (2000).
- [21] M. K. Ghosh, A. Mukhopadhyay and G. Singh, J. Phys. G 34, 177 (2007).
- [22] D. Chanda, M. K. Ghosh *et al.*, Phys. Rev. C 71, 034904 (2005).
- [23] M. K. Ghosh and A. Mukhopadhyay, Phys. Rev. C 68, 034907 (2003).
- [24] R. Holynski *et al.*, Phys. Rev. Lett. 62, 733 (1989).
- [25] A. Bialas and R. Peschanski, Jagellonian University Report No. TPJU/4/88.
- [26] R. Holynski *et al.* (KLM Collaboration), Phys. Rev. C 40, R2449 (1989).
- [27] M. I. Adamovich *et al.*, Phys. Rev. Lett. 65, 412 (1990).
- [28] P. L. Jain *et al.*, Phys. Rev. Lett. 59, 2531 (1987).
- [29] G. Singh *et al.*, Phys. Rev. Lett. 61, 1073 (1988).
- [30] K. Sengupta *et al.*, Phys. Lett. B 213, 548 (1988).
- [31] P. L. Jain *et al.*, Phys. Lett. B 187, 175 (1987); Phys. Rev. D 34, 2886 (1986).
- [32] K. Sengupta *et al.*, Phys. Lett. B 236, 219 (1990).
- [33] G. Singh, A. Mukhopadhyay and P. L. Jain, Z. Phys. A 345, 305 (1993).
- [34] P. L. Jain and G. Singh, Phys. Rev. C 44, 854 (1991).
- [35] P. L. Jain and G. Singh Z. Phys. C 53, 355 (1992).
- [36] G. Das *et al.*, Phys. Rev. C 54, 2081 (1996).
- [37] D. Ghosh *et al.*, Phys. Rev. C 47, 1120 (1993).
- [38] P. L. Jain and G. Singh, Nucl. Phys. A 596, 700 (1996).
- [39] P. Mali, A. Mukhopadhyay and G. Singh, Phys. Scr. 85, 065202 (2012).
- [40] M. Mohisin Khan *et al.*, Int. J. Mod. Phys. E 23, 1450075 (2014).
- [41] I. V. Ajinenko *et al.*, Phys. Lett. B 222, 306 (1989).
- [42] A. Capella *et al.*, Phys Lett. B 81, 68 (1979); Z. Phys. C 3, 329 (1980).
- [43] M. Adamus *et al.*, (NA22 Collaboration), Z. Phys. C 39, 311 (1988).
- [44] B. Buschbeck *et al.*, Phys. Lett. B 215, 788 (1988).

-
- [45] R. Peschanski, Proc. 23èmes Rencontres de Moriond (Les Arcs, Savoie, March 1988), ed. Tran Thanh Van Editions Frontières, Gif-sur-Yvette) (1988).
- [46] T. Haupt (NA22 Collaboration), Proc. XIX Intern. Symp. on Multiparticle dynamics (1988), ed. Tran Thanh Van (Editions Frontières, Gif-sur-Yvette) (1988).
- [47] C. Albajar *et al.* (UA1 Collaboration), Nucl. Phys. B 345, 1 (1990).
- [48] P. Abreu *et al.* (DELPHI Collaboration), Phys. Lett. B 247, 137 (1990).
- [49] T. Sjöstrand, Comput. Phys. Commun. 27, 243 (1982); Comput. Phys. Commun. 28, 229 (1983); T. Sjöstrand and M. Bengtsson, Comput. Phys. Commun. 43, 367 (1987).
- [50] W. Braunschweig *et al.* (TASSO Collaboration), Phys. Lett. B 231, 548 (1989).
- [51] K. Sugano, (HRS Collaboration), Contribution to the Workshop on Intermittency in high energy collisions, Santa Fe, March (1990).
- [52] G. Gustafson and C. Sjögren, Phys. Lett. B 248, 430 (1990).
- [53] N. M. Agababyan *et al.* (EHS /NA22 Collaboration), Phys. Lett. B 382, 305 (1996).
- [54] S. Wang *et al.*, Phys. Lett. B 458, 505 (1999).
- [55] F. Jinghua *et al.*, Phys. Lett. B 472, 161 (2000).
- [56] L. Fuming *et al.*, Phys. Lett. B 516, 293 (2001).
- [57] Yi-Fei Zhou *et al.*, Chin. Phys. Lett. 18, 1179 (2001).
- [58] W. Shaoshun and W. Zhaomin Phys. Rev. D 57, 3036 (1998).
- [59] D. Ghosh *et al.*, Phys. Lett. B 540, 52 (2002).
- [60] D. Ghosh *et al.*, J. Phys. G 29, 2087 (2003).
- [61] Z. Cao and R. C. Hwa, Phys. Rev. D 54, 6674 (1996).
- [62] L. Zhixu, F. Jinghua and L. Lianshou, HZPP-9909, July 30 (1999).
- [63] I. V. Ajineko *et al.* (NA22 Collaboration), Phys. Lett. B 235, 373 (1990).
- [64] M. R. Atayan *et al.* (EHS/NA22 Collaboration), Phys. Lett. B 558, 29 (2003).
- [65] T. Sjöstrand, Comput. Phys. Commun. 82, 74 (1994).
- [66] M. R. Atayan *et al.*, (EHS/NA22 Collaboration), Phys. Lett. B 558, 22 (2003).
- [67] R. Hasan *et al.*, J. Phys. G 28, 2939 (2002).

- [68] S. Ahmad *et al.*, J. Phys. G 30, 1145 (2004).
- [69] M. R. Atayan *et al.*, (EHS/NA22 Collaboration), HEN 449 (2003).
- [70] D. Ghosh *et al.*, J. Phys. G 34, 2165 (2007).
- [71] D. Ghosh *et al.*, J Phys. G 31, 1083 (2005).
- [72] D. Ghosh *et al.*, Phys. Rev. C 68, 024908 (2003).
- [73] R. Botet and M. Ploszajczak, The Phenomenology of Hadronic Matter, World Scientific Lecture Notes in Physics Vol. 65, World Scientific (2002).
- [74] A. Bialas and M. Gazdzicki, Phys. Lett. B 252, 483 (1990).
- [75] M. I. Adamovich *et al.* (EMU01 Collaboration), Z. Phys. C 76, 659 (1997).
- [76] M. I. Adamovich *et al.* (EMU01 Collaboration), Nucl. Phys. B 388, 3 (1992).
- [77] H. Pi, Comp. Phys. Commun. 71, 173 (1992).
- [78] P. R. Bevington and D. K. Robinson, Data reduction and error analysis for the physical sciences. McGraw-Hill, New York. (2003).
- [79] P. Mali *et al.*, Can. J. Phys. 89, 949 (2011).
- [80] I. Derado *et al.*, Z. Phys. C 47, 23 (1990).
- [81] G. Alexander and E. K. G. Sarkisyan, Phys. Lett. B 487, 215 (2000); Nucl. Phys. B (Proc. Suppl.) 92, 211 (2001).
- [82] M. Adamus *et al.*, (NA22 Collaboration), Phys. Lett. B 185, 200 (1987).
- [83] E. K. G. Sarkisyan *et al.*, Phys. Lett. B 347, 439 (1995).
- [84] Ph. Brax and R. Peschanski, Nucl. Phys. B 346, 65 (1990).
- [85] L. Lianshou, F. Jinghua and W. Yuanfang, Phys. Lett. B 444, 563 (1998).
- [86] A. Bershadski, Phys. Rev. C 59, 364 (1999).
- [87] W. Ochs, Z. Phys.C 50, 339 (1991).
- [88] Ph. Brax and R. Peschanski, Phys. Lett. B 253, 225 (1991).
- [89] I. Sarcevic and H. Satz, Phys. Lett. B 233, 251 (1989).
- [90] H. Satz, Nucl. Phys. B 326, 613 (1989).
- [91] R. C. Hwa and M. T. Nazirov. Phys. Rev. Lett. 69, 741 (1992).

-
- [92] W. Yuanfang and L. Lianshou, Phys. Rev. Lett. 70, 3197 (1993).
- [93] L. Lianshou *et al.*, Z. Phys. C 69, 323 (1996).
- [94] E. A. De Wolf, In Proceeding of the Ringberg Workshop on Multiparticle Production, Edited by R. C. Hwa *et al.*, World Scientific, Singapore (1992).
- [95] P. Carruthers, H. C. Eggers and I. Sarcevic, Phys. Lett. B 254, 258 (1991);
P. Carruthers, H. C. Eggers and I. Sarcevic, Phys. Rev. C 44, 1629 (1991).
- [96] N. Suzuki *et al.*, Phys. Rev. C 58, 1720 (1998).
- [97] N. Suzuki and S. Suzuki, Prog. Theor. Phys. 62, 727 (1979).
- [98] E. K. G. Sarkisyan, Phys. Lett. B 477, 1 (2000);
G. Abbiendi *et al.* (OPAL Collaboration), Phys. Lett. B 523, 35 (2001).
- [99] R. C. Hwa, Proc. VII International Workshop on Multiparticle Production, World Scientific, Singapore, p.303 (1997).
- [100] L. K. Gelovani, G. L. Gogiberidze and E. K. Sarkisyan, Proc. VIII International Workshop on Multiparticle Production, Matrahaza, Hungary, p.334 (1998).

Chapter 4

Multifractality and related issues

4.1 Introduction

The intermittency analysis of our data suggests that some kind of scale invariant dynamics is responsible for the observed angular distributions of the shower tracks. In one dimension a self-similar nature of the intermittency phenomenon is well established. It has been suggested in theory [1–3] and observed in experiments [4–8] that, self-similarity in the particle density fluctuations should lead to a power-law scaling behavior of the multiplicity moments with decreasing phase space resolution size (δX). Such scaling laws can further be utilized to characterize apparently random fluctuations in event-wise particle numbers within narrow intervals of phase space in terms of a set of smoothly varying fractal parameters, and extract some universal fractal properties of the underlying dynamics of particle emission.

For a self-similar process the multifractal frequency moment of order q , also called the G_q -moment [1, 9, 10], exhibits a power-law dependence on δX . The technique adopted for evaluating G_q -moments has some advantages over that for the scaled factorial moments (SFMs), as well as a few shortcomings. One can use the G_q -moments to study the spikes (for $q > 0$) as well as the non-empty valleys (for $q < 0$), while the SFMs are useful only for the spikes in the density function. Unlike the SFM, in the G_q -moments the order number q is not limited only to positive integers, but they can also take up negative as well as fractional values. However, in the low multiplicity events the empty bin effect becomes important, and the G_q -moments saturate as $\delta X \rightarrow 0$. Moreover, the statistical noise present in the

density function cannot be automatically accounted for. The limiting condition $\delta X \rightarrow 0$ is a mathematical idealization, and the only achievable limit is up to the phase space resolution allowed by the detector granularity. Takagi introduced another set of multifractal moments, commonly known as the T_q -moments, which are defined only for the positive integer order q , and are not affected by the finiteness of the event multiplicity [11]. However, like G_q the T_q -moments too cannot automatically eliminate the statistical noise.

Recently some other methods, like the multifractal detrended fluctuation analysis (MFDFA) [12], the multifractal detrended moving average (MFDMA) analysis [13], the sandbox algorithm method [14], have become popular in the multifractal characterization of time series data, and have also been adopted in studying the multiparticle emission data. Actually, the MFDFA method is a kind of generalization of the detrended multifractal analysis (DMA) method developed in [15] to describe the long-range correlation in coding and decoding DNA nucleotide sequences [15, 16]. On the other hand, the MFDMA method is an advancement of the moving average technique, which was initially proposed to estimate the Hurst exponents in self-affine signals [17], and was further extended to the detrending moving average (DMA) method by considering second-order differences between the original signal and its moving average [18]. To a certain extent the MFDMA method is similar to the MFDFA method. However, in the MFDMA analysis one can select the position of the detrending moving window with respect to the value of interest to be detrended, which gives an extra freedom to this technique. On the other hand, in the MFDFA technique one can detrend the signal by using a polynomial of desired order, which certainly is an improvement over the MFDMA, where the signal has to be detrended only by the local averages. The analysis of networks and graphs provides an alternative way to characterize the time series data. Recently, the sandbox (SB) algorithm [14], commonly used for complex network analysis [19], has been employed in multifractal analysis of multiparticle emission data [20]. The combination of visibility graph (VG) and SB algorithm was perhaps for the first time used in [20] to obtain a satisfactory description of the multifractality in AB collisions. In this chapter we present the results of our multifractal analysis in $^{16}\text{O-Ag/Br}$ interaction at a beam momentum of $200A$ GeV/c. For the G_q and T_q moments we have analyzed only the $^{16}\text{O-Ag/Br}$ data at $200A$ GeV/c, and compared the experiment with UrQMD and UrQMD+BEC simulations. On the other hand for the MFDFA and MFDMA methods we have compared the $^{16}\text{O-Ag/Br}$ results with the $^{32}\text{S-Ag/Br}$ experiment as well as with the corresponding UrQMD simulations. For the sandbox algorithm the $^{16}\text{O-Ag/Br}$ and $^{32}\text{S-Ag/Br}$ experimental results are both compared with the UrQMD simulations.

4.2 Literature review

The multifractal analysis of single particle density fluctuations in high-energy collisions was proposed in the early 1990's. R. C. Hwa introduced the technique of G_q -moments for the multifractal description of multiparticle emission data [1, 9, 10]. Hwa and Pan computed various multifractal parameters like the fractal dimensions, the mass exponent, the multifractal spectral function etc., and observed that the parameters depend on the collision energy, centrality of collision, particle type etc. for the pp collision at $\sqrt{s} = 20$ GeV generated by the ECCO model [21]. Jain *et al.* explored the multifractal character of single particle density functions in the η -space for 60A and 200A GeV ^{16}O -Ag/Br interactions, and for 200A GeV ^{32}S -Ag/Br interaction in terms of the G_q moments [22]. In [10] the G_q -moment was modified to take care of the empty bin effect, and the generalized fractal dimensions D_q^{dyn} were estimated for the ECCO generated data. Sengupta *et al.* performed a G_q -moment analysis for the pA and AB interactions over a wide energy range in emulsion experiments [23]. The multifractal results obtained in [23] were influenced by statistical noise, and the results showed slight departure from those generated by the random numbers. The normalized entropy on the other hand, consistently deviated from the random number generated values. The results on G_q -moments obtained from the ^{197}Au -Ag/Br and ^{28}Si -Ag/Br interactions [24] and from the ^{32}S -Ag/Br interactions [25] revealed a rich multifractal structure in the respective η -density distributions of shower tracks. The G_q -moment method had also been employed to the $\mu+p$, $\mu+d$ interaction data of the EMC collaboration [5], and to the $\bar{p}p$ data of the UA1 Collaboration [4]. It was found that the EMC/UA1 data exhibit an asymptotic power-law behavior of $\langle G_q \rangle$ with phase space partition number. From the comparisons of the UA1 data with Monte Carlo models like GENCL and PYTHIA, it was found that none of the models could fully reproduce the experiment. The GENCL model however agreed a little better with the experiment than the PYTHIA. It was found that the G_q -moments in $2d$ also follow a power law behavior [26] that can be explained by the multifractal cascade model [27].

Takagi proposed a different approach (the T_q -moment) for the multifractal analysis of high-energy collisions [11]. He himself used the method to analyze the UA5 data on $\bar{p}p$ collisions at $\sqrt{s} = 200$ GeV and 900 GeV [28], and also to the TASSO and DELPHI data on e^+e^- interactions in the 14 – 43.6 GeV energy range [29, 30]. It was reported that both $\bar{p}p$ and e^+e^- interactions show similar multifractal structures, and that the generalized dimensions for a given reaction tend to increase with \sqrt{s} [11]. However, like the G_q -method, no attempt has been made in the T_q -moments to separate the statistical noise from the non-statistical component. The EMU01 data on ^{197}Au -Ag/Br at 10.7A GeV, ^{16}O -Ag/Br at 60A GeV and ^{32}S -Ag/Br at 200A GeV were analyzed in terms of G_q moments [7]. The experimental results

were found to match with a purely stochastic model. Evidence of multifractality in the target fragmentation is also observed in several studies [31]. The signature of multifractality was also observed in the particle production mechanism of muon-nucleus interaction at 420 ± 45 GeV [32], where both the G_q and T_q methods were adopted. Multifractal structure in the single particle η -distributions was also observed for the $^{28}\text{Si-Ag/Br}$ and $^{12}\text{C-Ag/Br}$ interactions at 4.5A GeV obtained from the JINR Synchrophasotron [33]. Ahmad *et al.* showed that the angular distribution of grey tracks produced in $^{197}\text{Au-Ag/Br}$ and $^{28}\text{Si-Ag/Br}$ interactions, respectively at 10.6A GeV and 14.5A GeV, are of multifractal nature, and the results can be reproduced by the Lund MC model FRITIOF [34]. However, the Lund model failed to describe the $^{32}\text{S-Ag/Br}$ data at 200A GeV/c [25]. Mali *et al.* studied the G_q and T_q -moments in $^{28}\text{Si-Ag/Br}$ interaction at 14.5A GeV, and the results were compared with the UrQMD model. It was found that UrQMD could describe some features of the multifractal parameters, indicating that the experimental data were largely influenced by the statistical noise [35]. From the EMU01 data on several interacting systems at different energies, a universal property of the multifractal specific heat C was established [36]. In [37] it was also found that the Monte Carlo model HIJING produced nearly the same values of C as observed in the experiment.

Recently the detrended multifractal methods, which are primarily used in the multifractal characterization of time series data, have been employed to analyze the η -distribution of particles produced in heavy-ion collisions. The MFDFA method has been used to investigate the fractal properties in the (η, φ) space in Au+Au collision at $\sqrt{s_{NN}} = 200$ GeV generated by the UrQMD [38]. The η -distribution of shower tracks in $^{28}\text{Si-Ag/Br}$ interaction at 14.5A GeV, in $^{16}\text{O-Ag/Br}$ and $^{32}\text{S-Ag/Br}$ interactions at 200A GeV, are characterized using the MFDFA and MFDMA methods [39–41]. In these studies the experimental data were compared with the UrQMD simulations. The results of these detrended analyses reveal the multifractal nature of the η -distributions of shower tracks, and the degree of multifractality in the experiments is found to be more or less similar to that of the simulations. That means the results of detrended methods are dominated by the statistical noise. The sandbox algorithm [14], a popular method used in the complex network analysis, has been adopted to analyze the visibility and horizontal visibility graphs generated from the η -distribution of singly charged particles produced in $^{16}\text{O-Ag/Br}$ and $^{32}\text{S-Ag/Br}$ interactions at 200A GeV [20, 42]. The multifractal variables derived from the sandbox method are found to be quite sensitive to the kind of fluctuations present in the data, and a qualitative difference between the experiment and corresponding UrQMD simulation has been observed.

4.3 Hwa's multifractal moment

The multifractal G_q -moment of order q calculated on an e-by-e basis, is defined for the i -th event as [10],

$$G_q^{(i)} = \sum_{j=1}^M \left[\frac{n_{ij}}{(n_s)_i} \right]^q \Theta(n_{ij} - q) \quad (4.1)$$

Here M is the number of intervals into which the entire phase space (in the present case it is the η -space) has been divided, n_{ij} is the number of particles in the j -th η -window of the i -th event, $(n_s)_i = \sum_{j=1}^M n_{ij}$ is the total number of particles (shower tracks) belonging to the i -th event, and Θ is a step function as defined in [10]. The Θ -function has been introduced to address the issue of empty bin effect. According to the theory of fractals if self-similar dynamical components are present in the density fluctuation, the event averaged G_q moment should exhibit the following scaling-law,

$$\langle G_q(\delta X_\eta) \rangle \propto (\delta X_\eta)^{\tau(q)}; \quad \text{as } \delta X_\eta \rightarrow 0 \quad (4.2)$$

The notation $\langle \rangle$ means that an average over the event sample has been taken. The exponent $\tau(q)$ is called the multifractal mass exponent or simply the fractal exponent, that can be related to the generalized Rényi (fractal) dimensions D_q through the relation,

$$\tau(q) = (q - 1)D_q \quad (4.3)$$

We calculate the G_q -moments as functions of phase space partition number M over a wide range of q -values for the ^{16}O -Ag/Br interaction at 200A GeV/c. The results for some selective values of q are shown in Figure 4.1, where $\ln\langle G_q \rangle$ has been plotted against $\ln M$ (a) for the experiment, (b) for the UrQMD, and (c) for the UrQMD+BEC simulated data. The cumulative variable X_η defined in Equation (3.11) correspond to the η -variable unless stated otherwise. The figure shows that the phase space dependence of G_q is more or less similar for all the three data samples. For instance $\ln\langle G_q \rangle$ increases for $q < 0$ and decreases for $q > 1$ with increasing M , and $\ln\langle G_q \rangle$ tends to saturate at large $\ln M$. The saturation effect might simply be an outcome of the finiteness of shower track multiplicities. For a given q the mass exponent $\tau(q)$ is calculated from these plots as,

$$\tau(q) = \lim_{\Delta \rightarrow 0} \frac{\Delta \ln\langle G_q \rangle}{\Delta \ln \delta X_\eta} \quad (4.4)$$

While fitting a straight line we have not considered the points falling in the saturation region. From the knowledge of $\tau(q)$ one can now establish a connection between intermittency and multifractality, evaluate the fractal dimensions, and construct the multifractal singularity

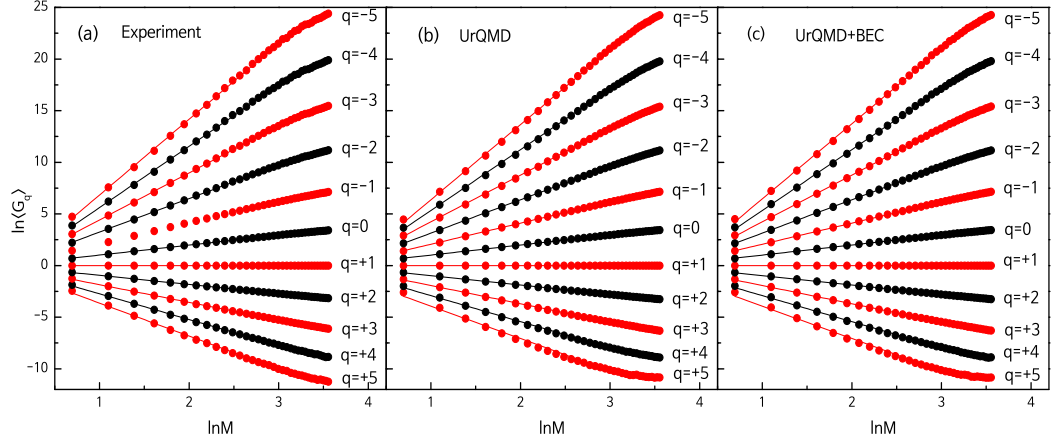


Figure 4.1: Multifractal G_q moment plotted with phase space partition number in ^{16}O -Ag/Br interaction at 200A GeV/c. Lines joining points are drawn to guide the eye.

spectrum as [43],

$$f(\alpha) = q\alpha(q) - \tau(q) \quad (4.5)$$

Here $\alpha(q) = \frac{\partial\tau(q)}{\partial q}$ is the Lipschitz-Hölder exponent. Figure 4.2(a) shows the exponents $\tau(q)$ and $\alpha(q)$ plotted against q , while Figure 4.2(b) shows the multifractal spectrum $f(\alpha)$ for the ^{16}O -Ag/Br interaction at 200A GeV/c along with the simulated results. It is observed that $\tau(q)$ and $\alpha(q)$ -values for the experiment and simulations do not differ significantly, $\tau(q)$ increases while $\alpha(q)$ decreases with q . A similar behavior has also been observed for the ^{32}S -Ag/Br interaction at 200A GeV/c [25]. The width of the multifractal spectrum is a direct measure of the degree of multifractality present in the data, which for a monofractal object should reduce to a delta function centered around a particular $\alpha(q) = \alpha_0$. A finite width of $f(\alpha)$ on the other hand, would suggest that the singularities in particle density, as the scaling law (4.2) suggests, may be different at different phase space points, and is not guided by any universal exponent. It is observed that the experimental distribution is slightly wider than both UrQMD and UrQMD+BEC simulated spectra, while the UrQMD+BEC generated spectrum is wider than the UrQMD spectrum. In this regard our ^{16}O -Ag/Br results in general qualitatively match with the ^{32}S -Ag/Br results. The features of $f(\alpha)$ -spectrum confirm a multifractal nature of the particle density fluctuations in ^{16}O -Ag/Br data. The left and right sides of the spectrum correspond respectively, to the dense and sparse regions of densities. The maximum values of $f(\alpha)$ in experiment and simulations are very close to unity, indicating that the empty bin effect particularly in the higher resolution region, is marginal in our case. For a $\bar{p}p$ interaction a similar feature has been observed while UA1 data were being compared with GENCL and PYTHIA predictions [4]. In the case of AB interactions multifractal characteristics were observed both in the experiment as well as in the Monte Carlo predictions based on a simple stochastic model [7].

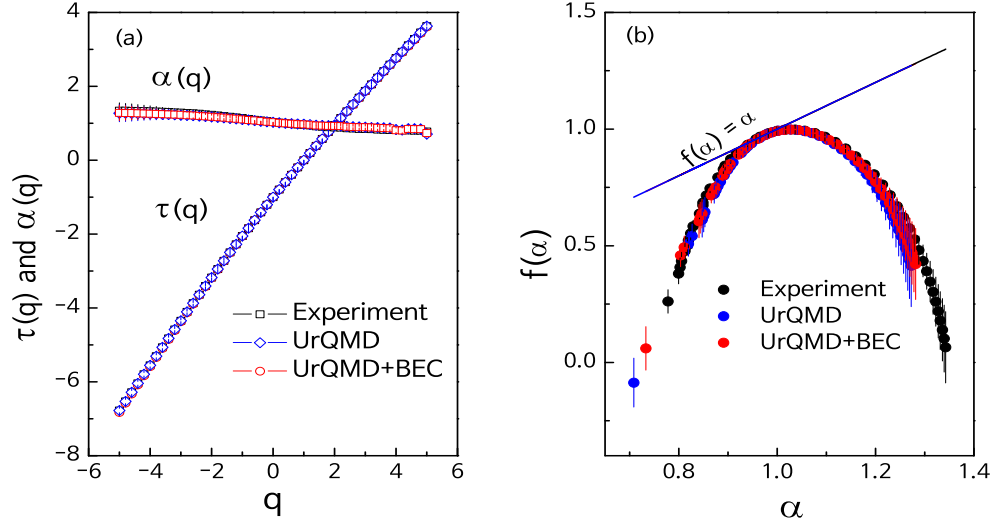


Figure 4.2: (a) The order dependence of the mass exponent $\tau(q)$ and the Lipschitz-Hölder exponent $\alpha(q)$ and (b) the multifractal spectral function $f(\alpha)$ obtained from ^{16}O -Ag/Br interaction at 200A GeV/c.

It is worthwhile to find out the dynamical component of multifractality, and to see whether it is consistent with our intermittency results. With the help of a set of pseudo-random numbers, one can calculate the statistical part of G_q and $\tau(q)$, denoted respectively by G_q^{sta} and $\tau(q)^{\text{sta}}$. It has been shown in ref. [10] that the dynamical component of $\tau(q)$, denoted by $\tau(q)^{\text{dyn}}$, is related to $\tau(q)^{\text{sta}}$ by the following relation,

$$\tau(q)^{\text{dyn}} = \tau(q) - \tau(q)^{\text{sta}} + q - 1 \quad (4.6)$$

For a trivial dynamics, $\tau(q)^{\text{dyn}}$ will be equal to $(q-1)$ [10]. So any deviation of $\tau(q)^{\text{dyn}}$ from $(q-1)$ is a signature of a nontrivial component. In that case $\tau(q)^{\text{dyn}}$ and the intermittency exponent ϕ_q will be related as [10],

$$q - 1 - \tau(q)^{\text{dyn}} \approx \phi_q \quad (4.7)$$

In Figure 4.3 $[q - 1 - \tau(q)]$, $[q - 1 - \tau(q)^{\text{dyn}}]$ and ϕ_q values are plotted together against q for the ^{16}O -Ag/Br interaction at 200A GeV/c. It is observed from this figure that after subtraction of the statistical component from $[q - 1 - \tau(q)]$, the quantity $[q - 1 - \tau(q)^{\text{dyn}}]$ comes closer to intermittency index ϕ_q , both for the experiment and for the UrQMD and UrQMD+BEC simulations. The experimental value of $[q - 1 - \tau(q)^{\text{dyn}}]$ rises steeper with q than the UrQMD and UrQMD+BEC generated values, though $[q - 1 - \tau(q)^{\text{dyn}}]$ in the experiment is a bit higher than the corresponding intermittency index obtained for the simulated data.

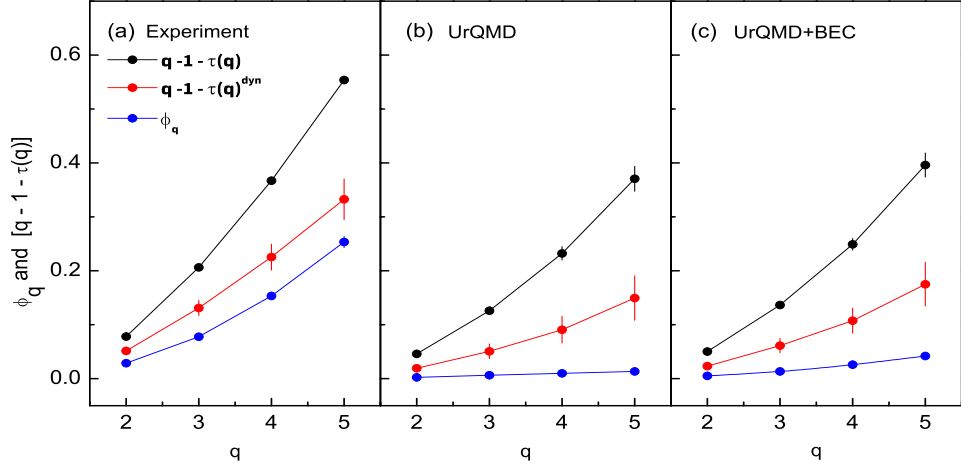


Figure 4.3: Plots of $[q-1-\tau(q)^{\text{dyn}}]$, $[q-1-\tau(q)]$ and the intermittency exponent ϕ_q with order number q for $^{16}\text{O-Ag/Br}$ interaction at 200A GeV/c. In all the graphs lines joining points are drawn to guide the eye.

The generalized Rényi dimensions D_q are computed as,

$$D_q = 1 - \frac{\phi_q}{(q-1)} \quad (4.8)$$

Using Equation (4.7) we get

$$D_q \approx \frac{\tau(q)^{\text{dyn}}}{(q-1)} \quad (4.9)$$

In this context we note that the the anomalous dimensions d_q are related to the Rényi dimensions by,

$$d_q = D - D_q \quad (4.10)$$

where D is the topological dimension of the supporting space. For one-dimensional analysis $D = 1$. The multifractality can also be classified by a parameter μ , known as the Lévy index. The parameter usually lies $\in [0, 2]$, and indicates the degree of multifractality and estimates the cascading rate in a self-similar branching process [44]. The Lévy index can also be utilized to decipher a possible mechanism of particle production. Such a characterization of multifractality is possible if the underlying density distribution can be described by a Lévy stable law. Under the Lévy law approximation, one can determine μ from the following relation [27, 45],

$$\frac{d_q}{d_2} = \frac{1}{(2^\mu - 2)} \frac{(q^\mu - q)}{(q-1)} \quad (4.11)$$

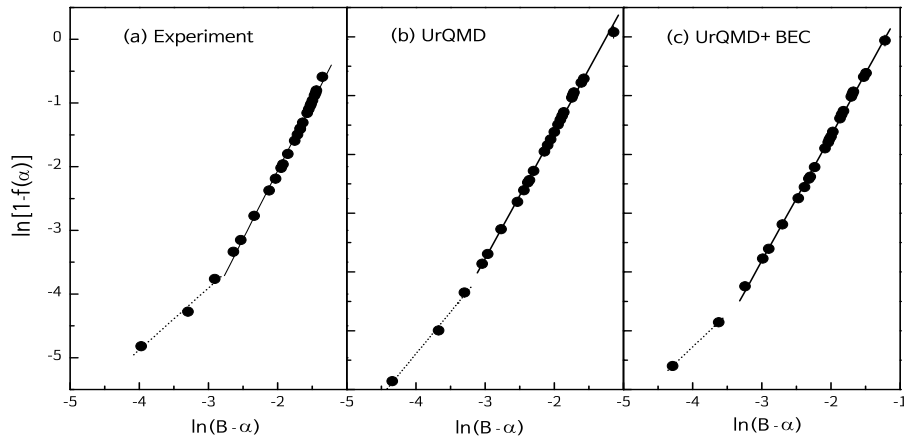
As we do not have too many D_q values in our analysis, the outcome is expected to be unreliable. Therefore, instead of using the above formula, we compute μ from the multifractal spectrum $f(\alpha)$. According to [46] $f(\alpha)$ is related to μ by,

$$1 - f(\alpha) \propto (B - \alpha)^{\mu/(\mu-1)} \quad \text{for } \alpha < B \quad (4.12)$$

Table 4.1: The values of the Lévy stable index μ obtained at two different regions of q for the ^{16}O -Ag/Br and ^{32}S -Ag/Br interactions at 200A GeV/c.

Interaction	Fit Region	Experiment	UrQMD	UrQMD+BEC
^{16}O -Ag/Br interaction at 200A GeV/c	Low- q region	-34.8295 ± 25.1512	3.3426 ± 2.8125	9.4972 ± 7.2267
	High- q region	1.8769 ± 1.7308	1.8691 ± 1.7528	1.8859 ± 1.7522
^{32}S -Ag/Br interaction at 200A GeV/c	Low- q region	-2.8521 ± 2.2629	2.7783 ± 2.4661	2.7405 ± 2.4313
	High- q region	2.3154 ± 2.1758	1.8275 ± 1.7406	1.8016 ± 1.7159

where $B = 1 + (1 - D_2)/(2^\mu - 2)$. It is observed in Figure 4.2(b) that $f(\alpha)$ varies smoothly with α . The slope of the $\ln(1 - f(\alpha))$ versus $\ln(B - \alpha)$ graph is therefore equal to $\mu/(\mu - 1)$. The value of μ can be extracted from the slope in the region $\alpha(q) < B$. The calculation of μ by using Equation (4.12) is constrained by $f(B) = 1$. The $\ln(1 - f(\alpha))$ versus $\ln(B - \alpha)$ graph is shown in Figure 4.4 for the experiment and corresponding UrQMD simulations. The points are best fitted by straight line in two different regions, one in the low- q ($0.2 \leq q \leq 0.6$) region, and the other in the high- q ($0.8 \leq q \leq 5.0$) region. The values of μ extracted from the graph are shown in Table 4.1. In this table we also include the μ values obtained for the ^{32}S -Ag/Br interaction at 200A GeV/c. The UrQMD and UrQMD+BEC simulated values are also quoted in this table. For the ^{16}O -Ag/Br interaction the μ values in the high- q region are reasonable, but for the ^{32}S -Ag/Br interaction only the simulated values fall within the acceptable domain of μ in the high- q range. In all the other cases the Lévy stable index is found to be beyond the accepted range of $[0, 2]$.

**Figure 4.4:** Plot of $\ln(B - \alpha)$ versus $\ln(1 - f(\alpha))$ for ^{16}O -Ag/Br interaction at 200A GeV/c. In all diagrams the dotted (solid) lines represent linear fits to the data points in the low (high)- q region.

4.4 Takagi's multifractal moment

Takagi introduced a new set of multifractal moments T_q that are not affected by the empty bin effect and finiteness of the charge particle multiplicities as is the case for the G_q -moments [11]. The T_q -moments are however defined only for a positive integer q as,

$$T_q(\delta X_\eta) = \ln \sum_{i=1}^{N_{ev}} \sum_{j=1}^M (p_{ij})^q \quad (4.13)$$

Here $p_{ij}(= n_{ij}/K)$ is the normalized density function, K is the total number of particles present in the whole event sample, M is the number of partitions in phase space, and n_{ij} is the number of particles falling within the j -th such partition of the i -th event. Takagi's method is based on two assumptions. First, the density function ρ is uniform over the phase-space interval considered, and second, the multiplicity distribution P_n does not depend on the location of the phase space interval. According to the theory of multifractality, T_q should be a linear function of the logarithm of the phase space resolution like,

$$T_q(\delta X_\eta) = A_q + B_q \ln(\delta X_\eta) \quad (4.14)$$

where A_q and B_q are constants. If this kind of linear relationship holds for a wide range of resolution, then the generalized fractal dimensions can be calculated by using the following formula,

$$D_q = B_q / (q - 1); \quad \text{for } q \geq 2 \quad (4.15)$$

If the number of events is large enough then

$$\sum_{i=1}^{N_{ev}} \sum_{j=1}^M (p_{ij})^q = \frac{\langle n^q \rangle}{K^{q-1} \langle n \rangle} \quad (4.16)$$

where $\langle n \rangle$ represents the average bin multiplicity. Now replacing δX_η by $\langle n \rangle$ one can derive an expression for the generalized dimension D_q for $q \geq 2$ as,

$$\ln \langle n^q \rangle = A_q + \{(q - 1)D_q + 1\} \ln \langle n \rangle \quad (4.17)$$

For $q = 1$ the dimension D_1 is called the information dimension, which provides the information of how much of a phase space interval is filled up with the distribution of particles (tracks). D_1 is obtained by taking an appropriate limit to Equation (4.15) [47]. For this purpose we define an entropy like quantity,

$$S(\delta X_\eta) = - \sum_{i=1}^{N_{ev}} \sum_{j=1}^M p_{ij} \ln p_{ij} \quad (4.18)$$

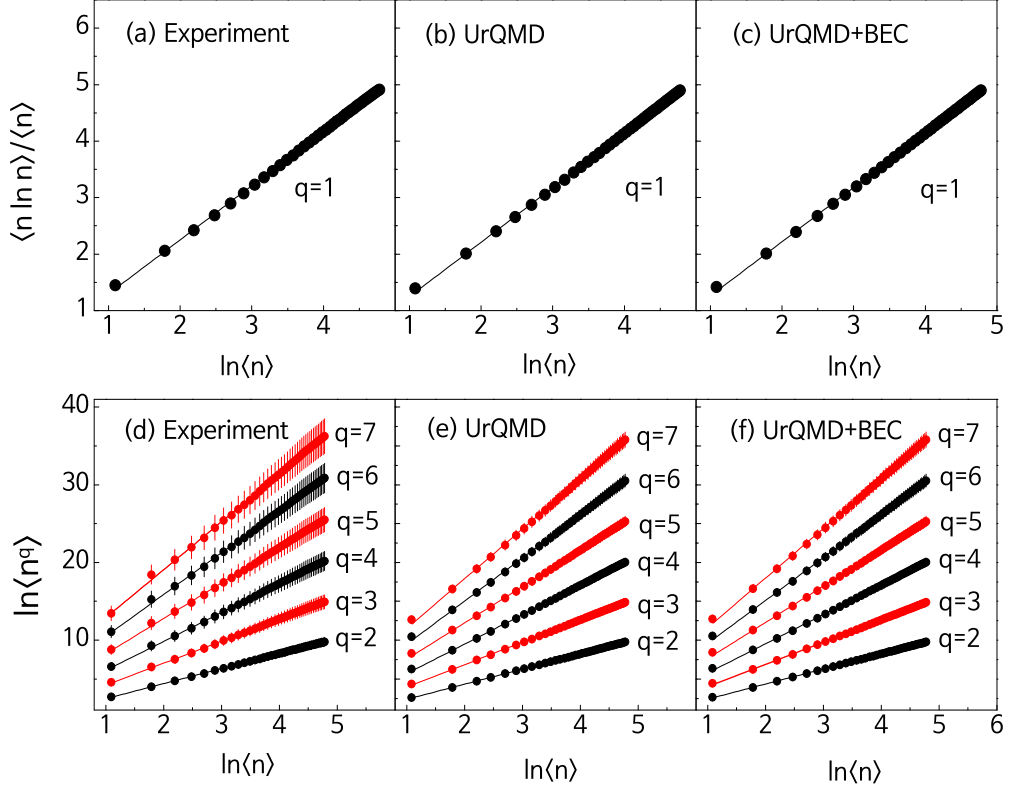


Figure 4.5: Multifractal T_q moments plotted with the number of particles in phase space interval for ^{16}O -Ag/Br interaction at 200A GeV/c. The best fitted straight lines are shown in all diagrams.

and study its linear dependence on $\ln(\delta X_\eta)$ like,

$$S(\delta X_\eta) = -D_1 \ln(\delta X_\eta) + \text{constant} \quad (4.19)$$

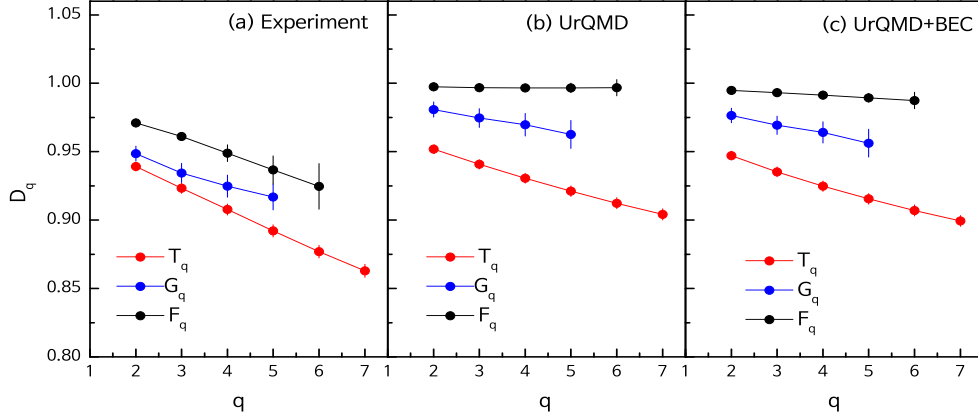
Using Equation (4.16) we get from the above equation

$$\langle n \ln n \rangle / \langle n \rangle = C_1 + D_1 \ln \langle n \rangle \quad (4.20)$$

In order to extract the fractal dimensions we plot $\langle n \ln n \rangle / \langle n \rangle$ and $\ln \langle n^q \rangle$ as functions of increasing size of phase space interval δX_η , taken symmetrically about the centroid of the η -distribution. The results are shown in Figure 4.5, where the experimental data are compared with the corresponding UrQMD and UrQMD+BEC simulations. Table 4.2 provides a comparison of the D_1 values obtained from the ^{16}O -Ag/Br and ^{32}S -Ag/Br interactions both at 200A GeV/c. The results suggest that a significant portion ($> 95\%$) of the η -space is filled up with the shower tracks. The $D_{q \geq 2}$ values obtained for the ^{16}O -Ag/Br interaction at 200A GeV/c are plotted against q in Figure 4.6. The D_q values obtained from the G_q and F_q -moment analysis are also included in this diagram. The $D_{q \geq 2}$ values obtained

Table 4.2: The values of information dimension D_1 obtained from the T_q moments for the ^{16}O -Ag/Br and ^{32}S -Ag/Br interactions at 200A GeV/c.

Interaction	Experiment	UrQMD	UrQMD+BEC
^{16}O -Ag/Br	0.957 ± 0.003	0.965 ± 0.003	0.961 ± 0.003
^{32}S -Ag/Br	0.978 ± 0.001	0.978 ± 0.001	0.979 ± 0.001

**Figure 4.6:** Generalized dimensions D_q with order number q calculated from the SFM F_q , G_q -moment and T_q -moment analysis for ^{16}O -Ag/Br interaction at 200A GeV/c. The lines joining points are shown to guide the eye.

from the T_q -moments show a general decreasing trend with increasing q . The observation is common for the experiments and simulations. We notice that the fractal dimensions obtained from the T_q -moment analysis for the ^{32}S -Ag/Br interaction are approximately equal to those obtained from the ^{16}O -Ag/Br data. It is also observed that D_q computed from F_q and G_q -moment analysis for the UrQMD and UrQMD+BEC simulations on ^{16}O -Ag/Br interaction are close to unity. The D_q values obtained from the T_q moments for all the data sets are consistently lower than those obtained from the F_q and G_q -moments. There may be a reason of such deviation. The T_q moments are not free from the statistical noise. The moments are defined in different ways, which might be another source of such inconsistencies. For a simple Poisson type multiplicity distribution in a given interval δX_η , the generalized dimensions should all be equal to the topological dimension of the supporting space. Any deviation from unity, as it is observed in our analysis, should therefore be considered as a signature of nonstatistical elements being present in the underlying distribution. If a monofractal to multifractal phase transition is present in the particle production mechanism, and if the distribution has only Bernoulli type of fluctuations, then one can introduce a thermodynamic interpretation to describe such fluctuations. According to Bershadski [36], for such a transition a multifractal specific heat C can be introduced as,

$$D_q = D_\infty + C \frac{\ln q}{(q-1)} \quad (4.21)$$

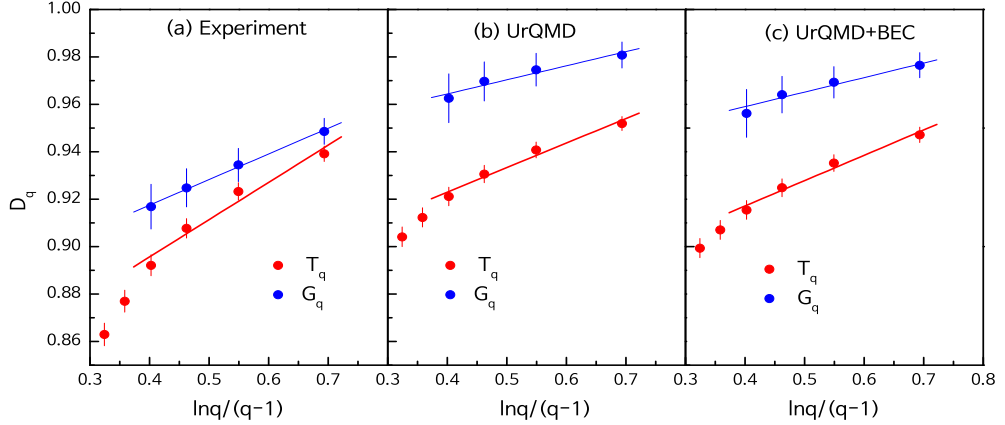


Figure 4.7: Plot of D_q with $\ln q/(q-1)$ for the $^{16}\text{O-Ag/Br}$ interaction at $200A$ GeV/c. The D_q values obtained from G_q and T_q moment analysis are compared. The lines represent the best linear fits to the data points.

Table 4.3: The values of multifractal specific heat C calculated from the F_q , G_q and T_q moment analysis for the $^{16}\text{O-Ag/Br}$ and $^{32}\text{S-Ag/Br}$ interactions at $200A$ GeV/c.

Interaction	Method Employed	Experiment	UrQMD	UrQMD+BEC
$^{16}\text{O-Ag/Br}$ interaction at $200A$ GeV/c	Hwa's moments	0.1079 ± 0.0047	0.0594 ± 0.0098	0.0612 ± 0.0314
	Takagi's moments	0.1571 ± 0.0215	0.1035 ± 0.0118	0.1068 ± 0.0108
	SFM	0.1148 ± 0.0199	0.0028 ± 0.0004	0.0179 ± 0.0030
$^{32}\text{S-Ag/Br}$ interaction at $200A$ GeV/c	Hwa's moments	0.0533 ± 0.0034	0.0010 ± 0.0032	0.0062 ± 0.0024
	Takagi's moments	0.1984 ± 0.0413	0.0772 ± 0.0064	0.0918 ± 0.0101
	SFM	0.0257 ± 0.0019	0.0102 ± 0.0022	0.0073 ± 0.0010

A monofractal to multifractal transition corresponds to a gap in the value of C from zero to a finite non-zero value. The variation of D_q with $\ln q/(q-1)$ is shown in Figure 4.7 for the experimental and simulated data sets on the $^{16}\text{O-Ag/Br}$ interaction under consideration. From the D_q against $\ln q/(q-1)$ plot we compute C for the G_q and T_q -moments. This quantity is also estimated from our SFM analysis. Table 4.3 presents the values of C computed from all three methods, as well as for both the $^{16}\text{O-Ag/Br}$ and $^{32}\text{S-Ag/Br}$ interactions at $200A$ GeV/c.

4.5 Detrended multifractal moments

Here we provide a brief description of the multifractal detrended fluctuation analysis (MFDFA) method and the multifractal detrended moving average (MFDMA) method. The details about these methods can be found in [12, 13].

The MFDFA method: Let $\{x_k : k = 1, 2, \dots, N\}$ be a series of outcomes of N consecutive measurements. The MFDFA procedure consists of the following four steps:

1. Determine a profile series as,

$$Y(i) = \sum_{k=1}^i [x_k - \langle x \rangle], \quad i = 1, 2, \dots, N \quad (4.22)$$

where $\langle x \rangle = \frac{1}{N} \sum_{k=1}^N x_k$ is the mean value of $\{x_k\}$.

2. Divide the profile $Y(i)$ into $N_n = \text{int}(N/n)$ non-overlapping segments of equal length n . If N is not a multiple of n , a short part at the end of the profile remains as a left over. To retain this part of the profile, the dividing procedure is repeated from the opposite end of the series. That will result in $2N_n$ segments of the series.
3. Obtain the local trend of $\{x_k\}$ for each of the $2N_n$ segments. This is done by a segment wise least square fit. Linear, quadratic, or even higher, say m -th order polynomials can be used to recover the local trend, and accordingly the procedure is named as the MF DFA1, MF DFA2, \dots , MF DFA m analysis. If Y_ν is the best fitted polynomial to any arbitrary section ν of the series, then the corresponding variance is given by,

$$W^2(\nu, n) = \frac{1}{n} \sum_{i=1}^n \{Y[(\nu - 1)n + i] - Y_\nu(i)\}^2 \quad (4.23)$$

for $\nu \in (1, N_n)$, while for $\nu \in (N_n + 1, 2N_n)$ it is given by,

$$W^2(\nu, n) = \frac{1}{n} \sum_{i=1}^n \{Y[N - (\nu - N_n)n + i] - Y_\nu(i)\}^2 \quad (4.24)$$

4. Finally, the q -th order MF DFA moment is defined as,

$$\begin{aligned} W_q(n) &= \left\{ \frac{1}{2N_n} \sum_{\nu=1}^{2N_n} [W^2(\nu, n)]^{q/2} \right\}^{1/q}, \quad \text{for all } q \neq 0 \\ W_q(n) &= \exp \left\{ \frac{1}{4N_n} \sum_{\nu=1}^{2N_n} \ln[W^2(\nu, n)] \right\}, \quad \text{for } q = 0 \end{aligned} \quad (4.25)$$

Note that the fluctuation function W_q can be defined only for $n \geq m + 2$, where m is the degree of the detrending polynomial. Moreover, W_q is statistically unstable at very large n , typically at $n \geq N/4$.

The MFDMA method: The MFDMA moments (W_q) are calculated from the profile series (4.22) following the steps listed below:

1. Calculate the moving average function in a moving window of size n , an integer number. The average is given by,

$$\tilde{Y}(i) = \frac{1}{n} \sum_{k=-\lfloor(n-1)\theta\rfloor}^{\lceil(n-1)(1-\theta)\rceil} Y(i-k) \quad (4.26)$$

where $\lfloor\xi\rfloor$ is the largest integer not larger than ξ , and $\lceil\xi\rceil$ is the smallest integer not smaller than ξ . The parameter $\theta \in [0, 1]$ specifies the position of the moving window. In general, the moving average function includes $\lceil(n-1)(1-\theta)\rceil$ data points from the backward region, and $\lfloor(n-1)\theta\rfloor$ data points from the forward region with respect to the value to be detrended, x_α say. Here we consider $\theta = 0.5$ for which the function $\tilde{Y}(i)$ is equally extended over both sides of x_α , and hence the moving window may be called the ‘central moving’ window. Note that for $\theta = 0$ the moving average function is calculated from all the n backward points ($x_{k<\alpha}$), while for $\theta = 1$ the function is calculated from all the n forward points ($x_{k>\alpha}$) with respect to x_α , and accordingly the detrending windows may be called backward and forward moving windows, respectively.

2. Detrend the sequence $Y(i)$ by subtracting the moving average function $\tilde{Y}(i)$ and obtain the residue series as,

$$e(i) = Y(i) - \tilde{Y}(i), \quad (4.27)$$

where i satisfies a criterion like, $n - \lfloor(n-1)\theta\rfloor \leq i \leq N - \lfloor(n-1)\theta\rfloor$.

3. Divide the residue $e(i)$ into $N_n = \lfloor N/n - 1 \rfloor$ non-overlapping segments of equal length n . Let a sequence be denoted by e_ν so that $e_\nu(i) = e(l+i)$ for $1 \leq i \leq n$ with $l = (\nu-1)n$. For any arbitrary segment ν , the mean square fluctuation function $\mathcal{W}^2(\nu, n)$ is calculated as,

$$\mathcal{W}^2(\nu, n) = \frac{1}{n} \sum_{i=1}^n \{e_\nu(i)\}^2 \quad (4.28)$$

4. Finally define the q -th order MFDMA moment as,

$$\begin{aligned} \mathcal{W}_q(n) &= \left\{ \frac{1}{N_n} \sum_{\nu=1}^{N_n} [\mathcal{W}^2(\nu, n)]^{q/2} \right\}^{1/q}, \quad \text{for all } q \neq 0, \\ \mathcal{W}_q(n) &= \exp \left\{ \frac{1}{2N_n} \sum_{\nu=1}^{N_n} \ln[\mathcal{W}^2(\nu, n)] \right\}, \quad \text{for } q = 0 \end{aligned} \quad (4.29)$$

The scaling behavior of the function $W_q(n)$ and $\mathcal{W}_q(n)$ are examined for a set of exponents. If the signal $\{x_i\}$ contains multifractality (long-range correlation), both $W_q(n)$ and $\mathcal{W}_q(n)$

for large values of n would follow a scaling relation like,

$$W_q \sim n^{h(q)}, \quad \text{and} \quad \mathcal{W}_q \sim n^{h(q)} \quad (4.30)$$

The $h(q)$ parameter, called the generalized Hurst exponent, would be a nonlinear function of q . For a stationary series $h(2)$ is the well-defined Hurst exponent H [12]. The exponent $h(2) = H$ can be used to analyze correlations present in the signal $\{x_k\}$. The scaling exponent $H = 0.5$ means that the signal under consideration is uncorrelated. A value $0.5 < H < 1$ implies a long-term persistence and $0 < H < 0.5$ implies a short-term persistence [48]. For a monofractal series $h(q)$ is independent of q , since the variances $W^2(\nu, n)$ and $\mathcal{W}^2(\nu, n)$ are identical for all the sub-series, and therefore Equations (4.25) and (4.29) yield identical values for all q . If the scaling behavior for small and large fluctuations are different, there will be a significant dependence of $h(q)$ on q . For positive values of q the fluctuation functions (4.25) and (4.29) will be dominated by large variances which corresponds to large deviations from the detrending function. Whereas for negative values of q , major contributions in those functions arise from small fluctuations coming from the detrending function. Thus, for positive/negative values of q , the exponent $h(q)$ describes the scaling behavior of the segment with large/small fluctuations.

4.5.1 Detrended methods and multifractal parameters

From our knowledge on $h(q)$ we can easily derive the multifractal scaling exponent $\tau(q)$, and subsequently some other parameters such as the multifractal singularity spectrum $f(\alpha)$, the generalized multifractal dimensions D_q etc. In order to examine the connection between the $h(q)$ exponent and the multifractal exponent $\tau(q)$, the series $\{x_k\}$ is considered as a stationary and normalized one. The variance of such a series is given by,

$$W_N^2(\nu, n) = \{Y(\nu n) - Y[(\nu - 1)n]\}^2 \quad (4.31)$$

The fluctuation function and its scaling-law are given by,

$$W_q(n) = \left[\frac{1}{2N_s} \sum_{n=1}^{2N_s} |Y(\nu n) - Y[(\nu - 1)n]|^q \right]^{\frac{1}{q}} \sim s^{h(q)} \quad (4.32)$$

Now if we assume that the length of the series N is an integer multiple of the scale s , then the above relation can be rewritten as,

$$\sum_{n=1}^{N/s} |Y(\nu n) - Y[(\nu - 1)n]|^q \sim s^{qh(q)-1} \quad (4.33)$$

where the term under $||$ is nothing but a sum of $\{x_k\}$ -s within an arbitrary ν -th segment of length n . In the standard theory of multifractals it is known as the box probability $\mathcal{P}(\nu, n)$ for the series $\{x_k\}$. Therefore,

$$\mathcal{P}(\nu, n) \equiv \sum_{k=(\nu-1)n+1}^{\nu n} x_k = Y(\nu n) - Y((\nu-1)n) \quad (4.34)$$

The multifractal scaling exponent $\tau(q)$ is defined via the partition function $Z_p(n)$ as,

$$Z_p(n) \equiv \sum_{\nu=1}^{N/n} |\mathcal{P}(\nu, n)|^q \sim s^{\tau(q)} \quad (4.35)$$

where q is a real parameter. From Equations (4.33)–(4.35) it is clear that the multifractal exponent $\tau(q)$ is related to $h(q)$ through the following relation,

$$\tau(q) = q h(q) - 1 \quad (4.36)$$

For a multifractal set $\tau(q)$ is also a nonlinear function of q , whereas for a monofractal set $\tau(q)$ is linear in q . The multifractal spectrum is given by Equation (4.5). From $\tau(q)$ one can derive the fractal dimension D_q as,

$$D_q \equiv \frac{\tau(q)}{q-1} = \frac{q h(q) - 1}{q-1} \quad (4.37)$$

This relation shows that even for a monofractal signal D_q depends on q .

4.5.2 Results of MF DFA and MFDMA methods

In the detrended fluctuation analysis we consider the event-wise η -distributions as the signal. The MF DFA and MFDMA fluctuation functions are first calculated on an e-by-e basis and then they are averaged over all the events. The scaling behavior of the event averaged fluctuation functions is schematically represented in Figure 4.8 for the MF DFA method and in Figure 4.9 for the MFDMA method. To maintain clarity we consider only some selective values of q like, $q = 0, \pm 2, \pm 5$ to plot the fluctuation functions. In each figure the experimental results are compared with the UrQMD+BEC simulated data. For both ^{16}O -Ag/Br and ^{32}S -Ag/Br interactions the fluctuation functions obtained from the experimental data show more or less similar trend as the corresponding UrQMD+BEC simulation. It is to be noted that the variations of $\ln \langle W_q(n) \rangle$ and $\ln \langle \mathcal{W}_q(n) \rangle$ are not linear over the entire region of $\ln n$. In each case significant nonlinearities are observed, particularly in the $q < 0$ region and at small values of the scale parameter $\ln n$. The nonlinearity in $\ln \langle W_q \rangle$ is more prominent than that in $\ln \langle \mathcal{W}_q \rangle$. Therefore, in our calculation a scale range

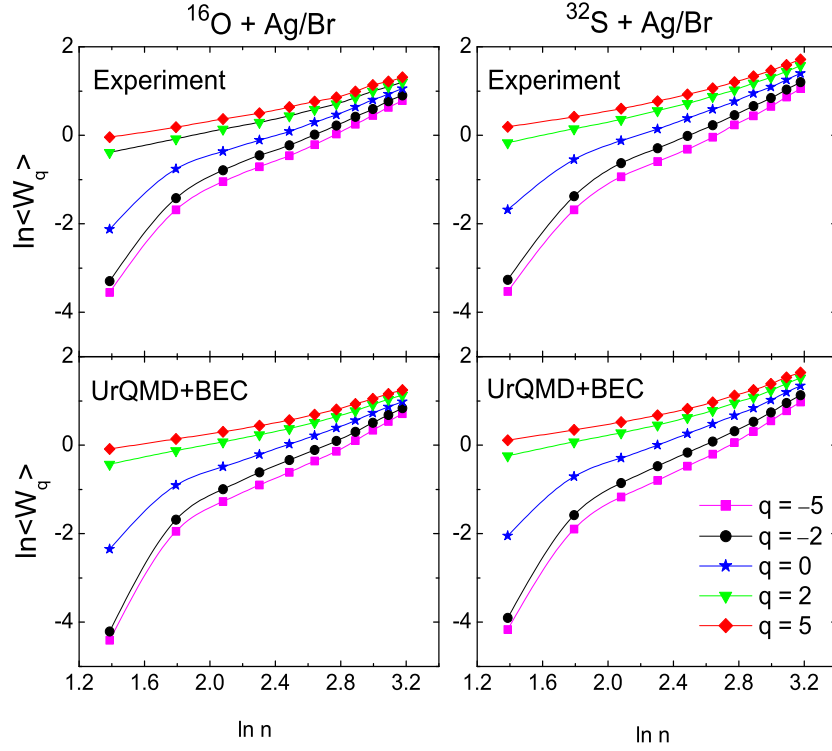


Figure 4.8: Scaling behavior of the event averaged MFDFFA moments $\langle W_q(s) \rangle$ for $q = 0, \pm 2$ and ± 5 . Left panel: ^{16}O -Ag/Br collision at 200A GeV/c and right panel: ^{32}S -Ag/Br collision at 200A GeV/c.

of $8 \leq n \leq 24$ for the MFDFFA method and $6 \leq n \leq 24$ for the MFDMA method is considered to evaluate the multifractal exponent $h(q)$. These regions produce better scaling for the average fluctuation functions. We note that the difference between the UrQMD and UrQMD+BEC computed results is very marginal, and hence the UrQMD values are not quoted/shown in our detrended analysis. The nature of fractality in the particle density function can be analyzed with the help of the generalized Hurst exponent $h(q)$. We extracted the values of $h(q)$ from the $\ln \langle W_q \rangle$ versus $\ln n$ in the MFDFFA, and $\ln \langle W_q \rangle$ versus $\ln n$ in the MFDMA plots in the n -regions mentioned above. The q values in our calculation vary from -5 to $+5$ in steps of 0.25 . The q -dependence of $h(q)$ is graphically shown in Figure 4.10 for the MFDFFA method and in Figure 4.11 for the MFDMA method. In each of the figures mentioned above, the experimental results are compared with the corresponding UrQMD+BEC simulation. It is clear from Figure 4.10 that the $h(q)$ values for the simulated data are slightly higher than those obtained from the corresponding experiment in the $q < 0$ region, while in the $q > 0$ region the differences are not statistically significant. However, for the MFDMA method as we see in Figure 4.11, just the opposite behavior is observed. The $h(q)$ spectra obtained from the MFDMA is more smoothly varying than that from the MFDFFA case for both ^{16}O -Ag/Br and ^{32}S -Ag/Br interactions. In each case the observed variation is nonlinear and $h(q)$ decreases with q , which signifies multifractal nature of the

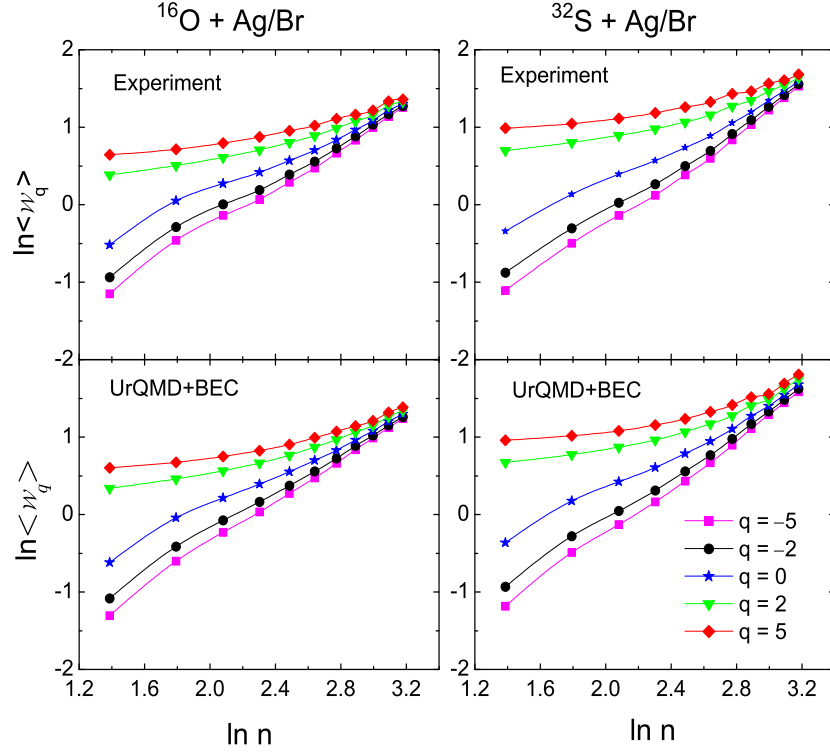


Figure 4.9: The same as in Figure 4.8 but for the MFDMA method.

η -distribution as manifested by different scaling behaviors for large and small fluctuations. The $h(q = 2)$ values obtained from the MFDFA method are always very close to unity. On the other hand, the $h(q = 2)$ values obtained from the MFDMA method are a little higher than 0.5. The $h(q = 2)$ values are quoted in Table 4.4. It is mentioned above that $H > 0.5$ indicates a long-range correlation for a stationary signal. Therefore, as the present analysis suggests, the η -distribution functions for the ^{16}O -Ag/Br and ^{32}S -Ag/Br interactions are long-range correlated. The observed variation of the multifractal mass exponents $\tau(q)$ is nonlinear in each case as can be seen from the bottom panels of Figures 4.10 and 4.11. However, the difference between the experiment and UrQMD+BEC simulation in this regard is statistically not very significant. The degree of non-linearity present in $\tau(q)$ plot gives us an idea about the degree of multifractality. The observed nonlinearity supports the presence of multifractal pattern in the particle density distributions for both the interactions studied.

In order to study the local scaling patterns and to get a quantitative idea about multifractality, the multifractal spectrum $f(\alpha) = q\alpha(q) - \tau(q)$ for the ^{16}O -Ag/Br and ^{32}S -Ag/Br interactions are obtained, and the experimental results in this regard are compared with the simulated one. Figure 4.12 and 4.13 show the $f(\alpha)$ -spectra plotted with $\alpha(q)$. From Figure 4.12 it is clear that in the MFDFA method, in the higher α region the simulated results

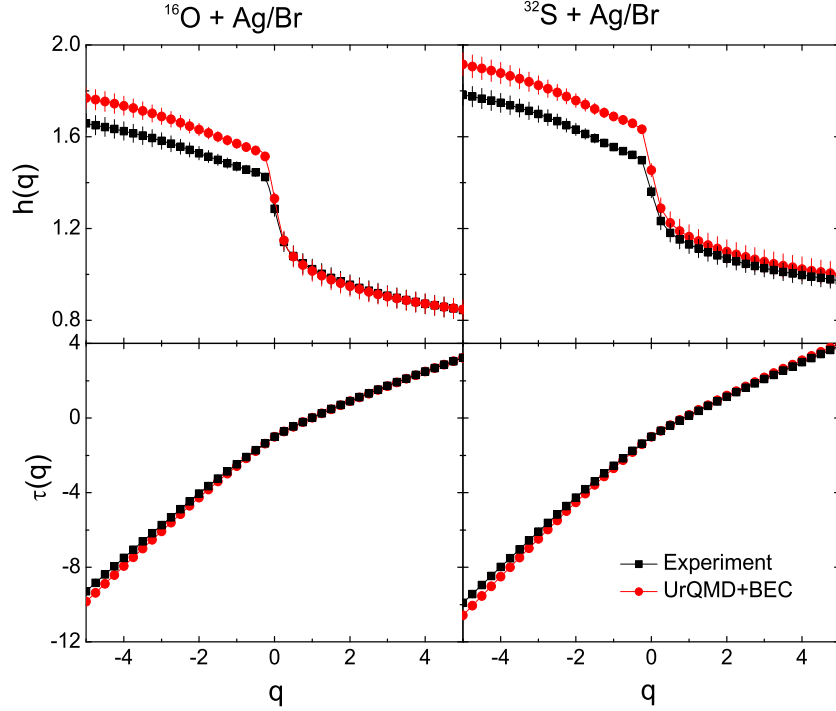


Figure 4.10: The generalized Hurst exponent $h(q)$ and the multifractal exponent $\tau(q)$ obtained from the MFDFA method. Left panel: ^{16}O -Ag/Br collision at $200A$ GeV/c, right panel: ^{32}S -Ag/Br collision at $200A$ GeV/c.

Table 4.4: The values of generalized Hurst exponent $h(q = 2)$.

Data sample	MFDFA	MFDMA
	$h(q = 2)$	$h(q = 2)$
$^{16}\text{O}+\text{Ag}/\text{Br}$ (Experiment)	0.9558 ± 0.0438	0.6165 ± 0.0407
$^{16}\text{O}+\text{Ag}/\text{Br}$ (UrQMD+BEC)	0.9486 ± 0.0436	0.6660 ± 0.0370
$^{32}\text{S}+\text{Ag}/\text{Br}$ (Experiment)	1.0700 ± 0.0388	0.6162 ± 0.0333
$^{32}\text{S}+\text{Ag}/\text{Br}$ (UrQMD+BEC)	1.0998 ± 0.0513	0.7221 ± 0.0463

deviate significantly from the respective experiment. Whereas in the MFDMA method significant deviations between experiment and simulation are observed only in the low α region for both interactions. Moreover, in the MFDFA method due to lack of smoothness in the $h(q)$ versus q plot, some points near the peak region of the spectrum could not be obtained. The spectrum is fitted with a fourth degree polynomial function around the position of its maximum at α_0 , and we have extrapolated the curves to $f(\alpha) = 0$ on either side of the maxima. Slightly right-skewed spectrum denotes relatively strongly weighted high fractal exponents, corresponding to finer structures of particle density function [49]. The width of the spectrum defined by $\Delta\alpha = \alpha_{\max} - \alpha_{\min}$, with $f(\alpha_{\min}) = f(\alpha_{\max}) = 0$, and the skewness parameter $r = (\alpha_{\max} - \alpha_0)/(\alpha_0 - \alpha_{\min})$ are also calculated. The strength of multifractality is measured by $\Delta\alpha$. If the η -distributions are multifractal in nature, then the width $\Delta\alpha$

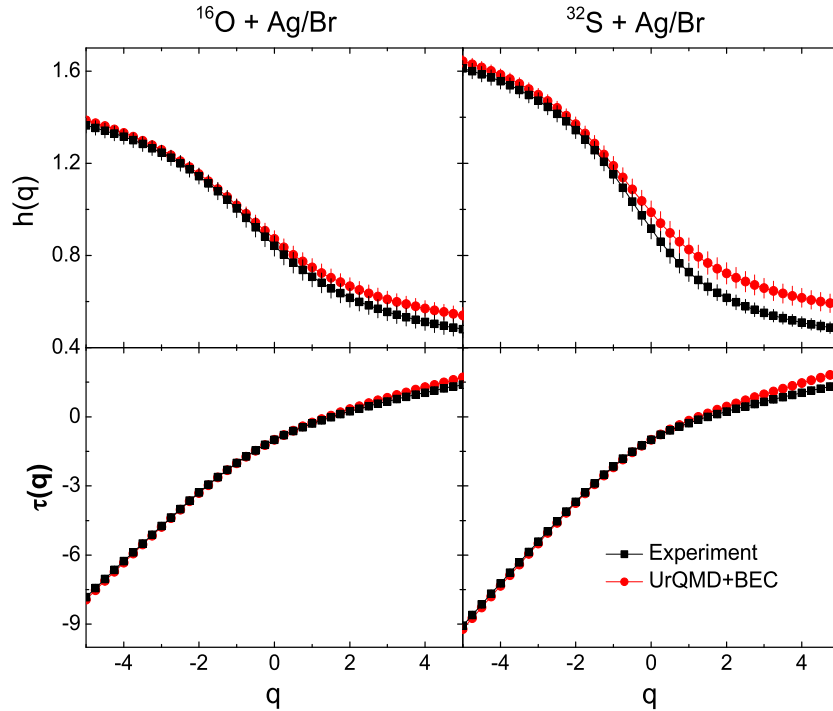


Figure 4.11: The same as in Figure 4.10 but for the MFDMA method.

Table 4.5: The centroid (α_0), the width ($\Delta\alpha$) and the skewness (r) parameters of the multifractal spectra for the studied interactions.

Data sample	MFDFA			MFDMA		
	α_0	$\Delta\alpha$	r	α_0	$\Delta\alpha$	r
$^{16}\text{O}+\text{Ag}/\text{Br}$ (Experiment)	1.242	1.177	1.023	0.830	1.277	1.318
$^{16}\text{O}+\text{Ag}/\text{Br}$ (UrQMD+BEC)	1.277	1.282	1.057	0.840	1.231	1.438
$^{32}\text{S}+\text{Ag}/\text{Br}$ (Experiment)	1.321	1.170	1.175	0.872	1.530	1.517
$^{32}\text{S}+\text{Ag}/\text{Br}$ (UrQMD+BEC)	1.389	1.271	1.136	0.932	1.469	1.479

should be positive definite. On the contrary, $\Delta\alpha \rightarrow 0$ indicates a monofractal η -distribution. The centroid, the width and the asymmetry (skew) parameters of the spectral functions are presented in Table 4.5. The spectrum width appears to be a little wider in the present case than what was obtained earlier using the G_q -moments for the ^{32}S -Ag/Br interaction [25]. The generalized fractal dimensions D_q are plotted against the order number q in Figure 4.14. The D_q values obtained from the experiment and simulation for both MFDFA and MFDMA methods are plotted together for an easy comparison. From the left panel of the figure it is clear that the experimental and simulated results for the ^{16}O -Ag/Br interactions almost coincide with each other, and practically very little deviation is seen while applying the MFDFA method. However, significant deviations between the experiment and simulation are observed in the MFDMA case. For both interactions the D_q values are less in the

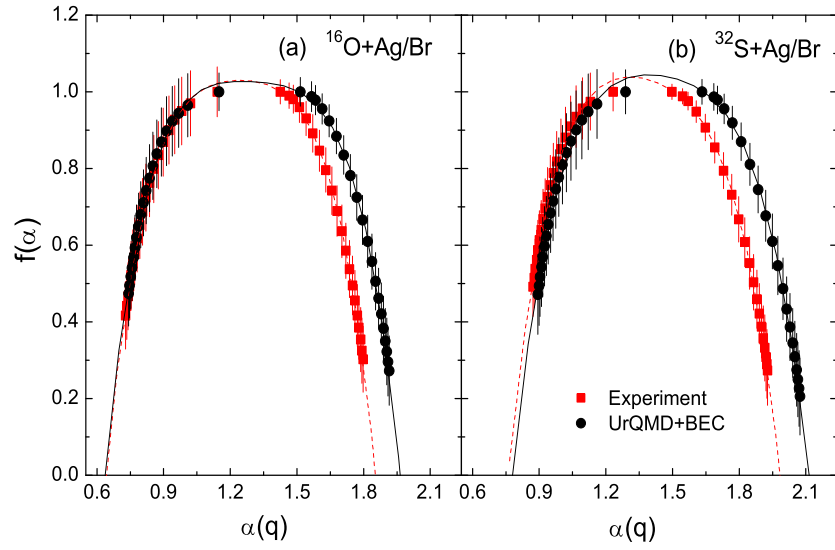


Figure 4.12: The multifractal singularity spectra obtained from the MF DFA method for (a) $^{16}\text{O}+\text{Ag}/\text{Br}$ interaction and (b) $^{32}\text{S}+\text{Ag}/\text{Br}$ interaction both at 200A GeV/c. Lines joining points are shown only to guide the eye.

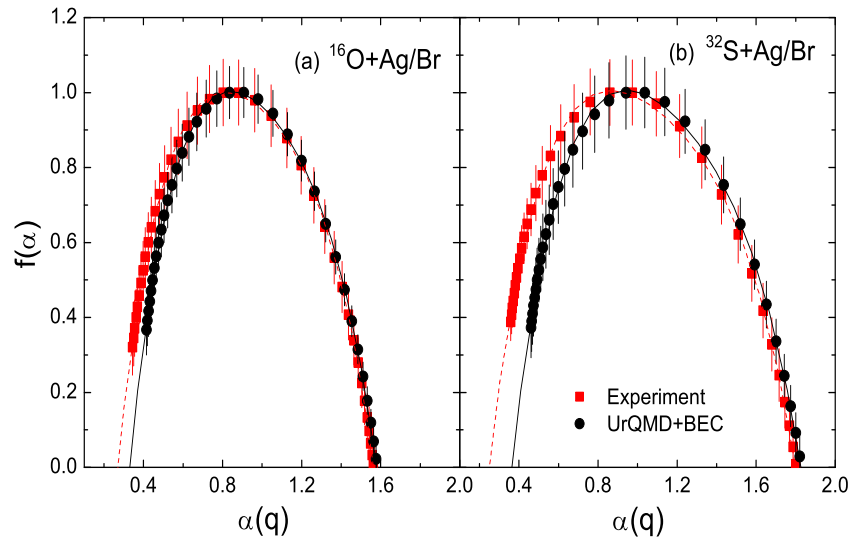


Figure 4.13: The same as in Figure 4.12 but for the MF DMA method.

MF DMA case compared to the MF DFA. It is also noticed that the dependence of D_q on q as observed here, is weaker than that observed either in the G_q or the T_q -method. Our general conclusions are therefore, the experiment as well as the simulated distributions for both interactions considered in this analysis are multifractal in nature. The multifractal spectra are slightly right skewed, but the results depend on the method of analysis.

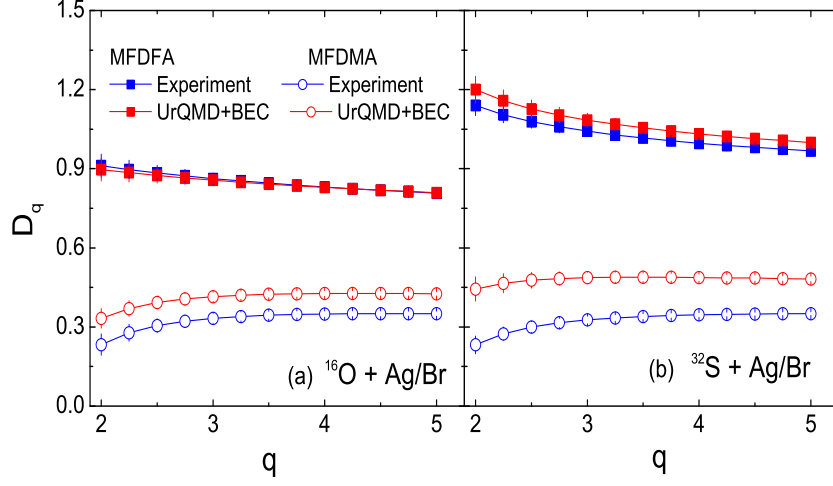


Figure 4.14: Order dependence of the generalized fractal dimension D_q for (a) ^{16}O -Ag/Br interaction and (b) ^{32}S -Ag/Br interaction both at 200A GeV/c.

4.6 Visibility graph and sandbox algorithm

4.6.1 Visibility graph

A graph is a collection of objects or nodes, and links or edges each of which identifies a relation or interaction between any two nodes. Lacasa *et al.* [50] introduced a simple computational method to convert a time series into a visibility graph (VG). Accordingly, a VG of N -nodes is obtained from a time ordered sequence of N -measurements $(t_i, x_i) : i = 1, 2, \dots, N$, so that two measurements (t_i, x_i) and (t_j, x_j) have mutual visibility and are therefore two connected nodes, provided any third measurement in the graph (t_k, x_k) satisfies the criterion,

$$x_k < x_i + (x_j - x_i) \frac{t_k - t_i}{t_j - t_i} \quad (4.38)$$

where $i < k < j$. A simplified form of the above visibility criterion is employed to obtain the horizontal visibility graph (HVG) [51], where two nodes i and j are connected if one can draw a horizontal line joining x_i and x_j that does not intersect with any x_k located in between. The visibility criterion for HVG is,

$$x_k < \min\{x_i, x_j\} \quad (4.39)$$

Figure 4.15 illustrates the mechanism of making visibility graphs from the time series data, where the graph in diagram (a) is obtained following the criterion specified in Equation (4.38), and the graph in diagram (b) is obtained following Equation (4.39). As noted in [52], the structural complexity of a time series is inherited by the graph associated with the series.

As for instance periodic, random and fractal series map into motif-like random, exponential and scale-free networks, respectively. Our visibility graph analysis is performed in the η -space. As for illustration, we show in Figure 4.16(a) the η -distribution of shower tracks for an event with $n_s = 240$. A single event η -distribution of shower tracks naturally shows widely varying and random fluctuations. The local peaks in the single event η -distribution are of our interest. The fluctuations are obviously washed out when the η -distribution is drawn for the whole sample, and a smooth Gaussian shaped distribution is retrieved. The analysis is therefore, performed on an e-by-e basis. Note that the background, very roughly Gaussian in nature, undesirably obstructs the visibility of the height, i.e. the number of tracks located at a particular η (nodes of visibility graphs) from that located at other nodes. Particularly, the nodes located on the left hand side of the peak of the Gaussian get obstructed from those located on the right hand side of the peak and vice versa. In order to

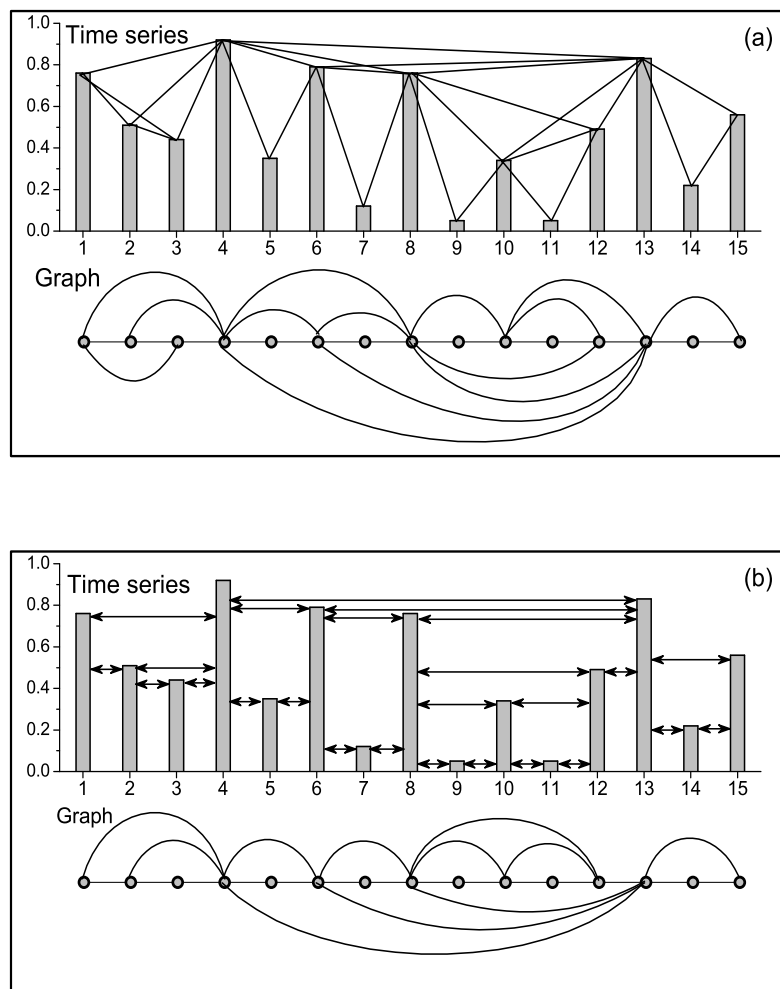


Figure 4.15: An illustration of converting a time series to the corresponding visibility graph: (a) A time series of 15 measurements is converted to a visibility graph and (b) the same series is converted to a horizontal visibility graph.

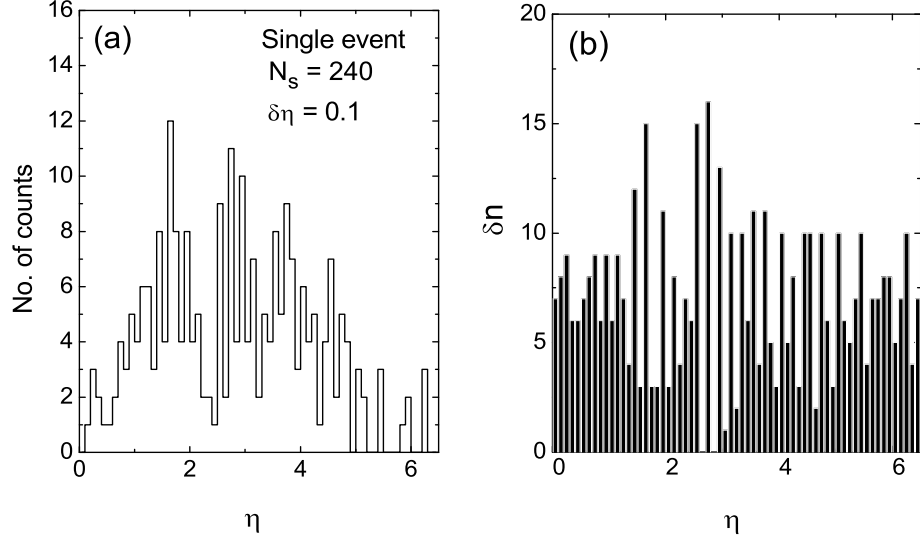


Figure 4.16: (a) Pseudorapidity distribution of an ^{16}O -Ag/Br event having shower track multiplicity 240. (b) The η distribution shown in diagram (a) is modified using Equation (4.40).

get rid of this problem we have considered the differences of successive bin contents at every resolution $\delta\eta$ as,

$$\delta n(\eta_i) = dn_{\eta_{i+1}} - dn_{\eta_i} \quad (4.40)$$

and as required by the mapping criteria (4.38) and (4.39) we project the modified distribution onto a positive $(\delta n, \eta)$ -plane. Here dn_i is the number of tracks falling within $\delta\eta$ about a particular η_i . Figure 4.16(b) shows the modified form of the distribution that we see in Figure 4.16(a). It seems that the single event η -distribution so modified, reasonably eliminates the background, while the relative fluctuations present in the event are retained. Note that the local fluctuations also could have been detrended by subtracting the fitted Gaussian background from the data, but the χ^2 value of such a fit would never be reliable. On an e-by-e basis the modified η -distributions are converted in the corresponding graphs. The HVG for the event shown Figure 4.16 is illustrated in Figure 4.17.

4.6.2 Degree distribution of visibility graph

We compute the degree(s) of each of the nodes present in the graphs constructed on an e-by-e basis. For each sample we have as many graphs as the number of events present. The degree distributions of individual events are then combined to obtain the degree distribution $P(k)$ for an entire event sample. In Figure 4.18 we show such distributions for both the interactions studied, where the upper panels show the results derived from the VG and the lower panels represent the corresponding HVG. The UrQMD simulated distributions are also plotted

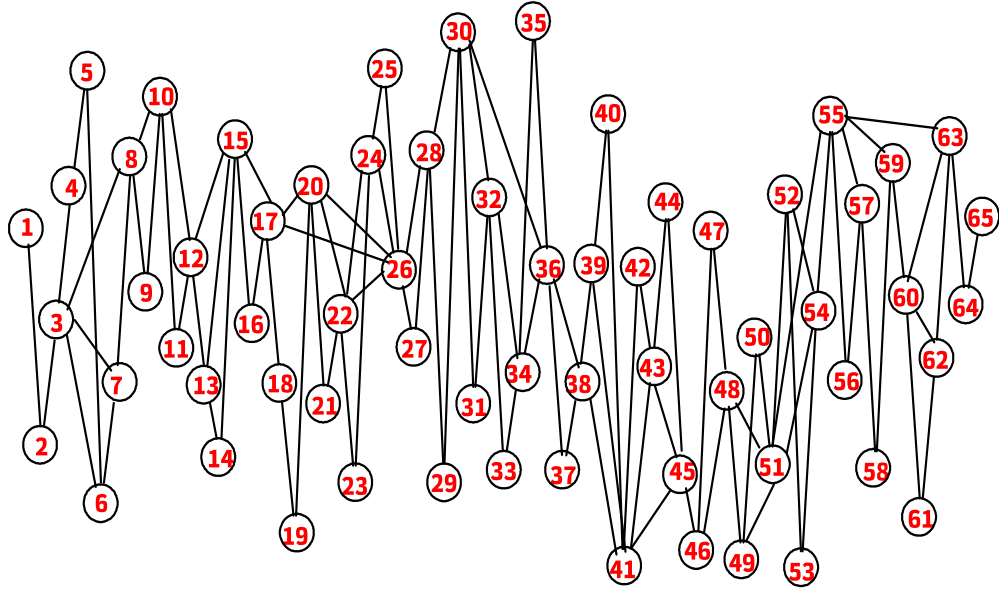


Figure 4.17: A schematic of the HVG constructed from the distribution shown in Figure 4.16(b). The numbers within circles indicate the nodes of the graph and the lines represent the connectivity between a pair of nodes.

along with the respective experiment. The degree distribution of the HVG associated with a purely random process can be analytically computed [51], and the resultant formula for that would be,

$$P(k) = \frac{1}{3} \left(\frac{2}{3} \right)^{k-2} \quad (4.41)$$

The tail regions ($k \geq 10$) of the degree distribution plots are fitted to a power-law $P(k) \sim k^{-\gamma}$ like equation to evaluate the tail exponent γ . The exponent is an important parameter in the visibility graph analysis. It is a scale free parameter for a large number of real networks, and in some cases the exponent is related to the Hurst exponent of the underlying signal [52, 53] over which the graph is constructed. We find that for both interactions as well as for both VG and HVG $\gamma \sim 8$. Also we do not see any statistically significant difference between the data and the simulation. Though the shape of the $P(k)$ distribution obtained from the VGs is not quite identical to that obtained from the HVGs, specially in the low k (< 10) region. But that does not significantly affect the tails of the distributions. It has been pointed out that the γ -exponent calculated using the aforementioned method, has some intrinsic disadvantages, and its value should be determined on the basis of a maximum-likelihood

(ML) method as [54],

$$\gamma = 1 + n \left[\sum_{i=1}^n \log \frac{k_i}{k_{\min}} \right]^{-1} \quad (4.42)$$

Here n is the total number of measured values of k_i taken into account, and k_{\min} is the smallest value of k ($= 10$) for which the power-law behavior holds good. The ML-estimated γ -values are given in Table 4.6. The exponents obtained from the HVG analysis are slightly larger in magnitude than the corresponding values obtained from the VGs. However, all these values are significantly larger than what was observed for a long-range correlated time series [53]. The overall results of our degree distributions show that the scale freeness property of $P(k)$ is retained even in the visibility and horizontal visibility graphs generated from the η -distributions of shower tracks produced in the ^{16}O -Ag/Br and ^{32}S -Ag/Br interactions both at 200A GeV/c, but the exponent γ cannot distinguish the experiment from the simulation. Therefore, we argue that the degree distribution and its power-law scaling cannot be taken as suitable measure for the heavy-ion collision data.

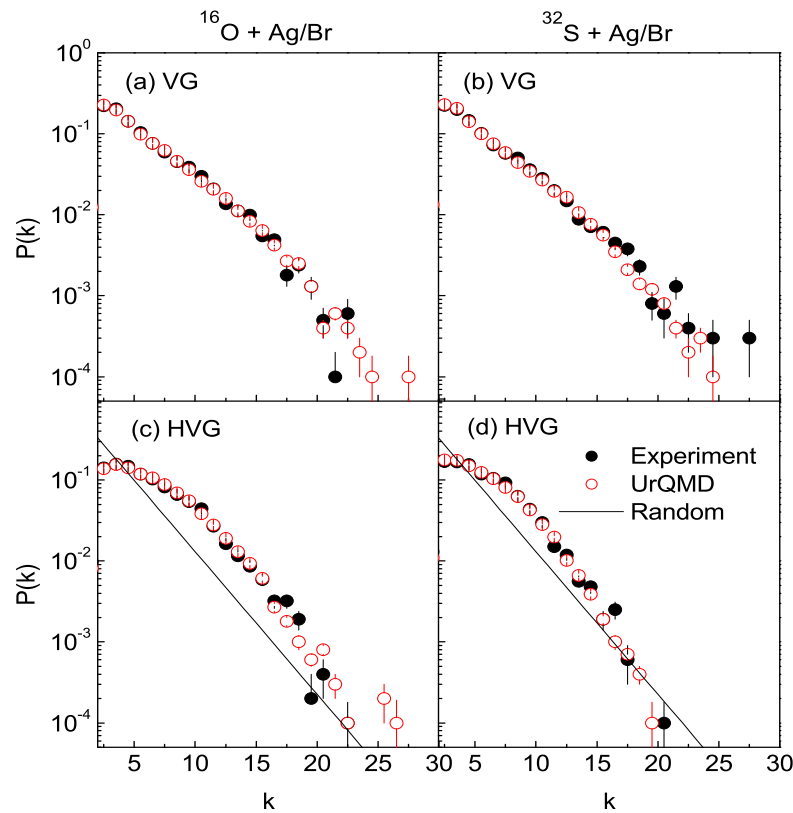


Figure 4.18: Combined degree distributions of all the VGs (upper panel) and HVGs (lower panel) generated from the ^{16}O -Ag/Br data (left) and ^{32}S -Ag/Br data (right). The straight lines in the HVG plots follow Equation (4.41).

Table 4.6: The ML estimated values of the exponent γ , see Equation (4.42).

Data sample	VG		HVG	
	^{16}O	^{32}S	^{16}O	^{32}S
Experiment	4.756	4.566	5.207	5.681
UrQMD	4.710	4.838	5.335	5.764

4.6.3 Sandbox method of multifractality analysis

The sandbox algorithm of multifractal analysis of complex networks is well described in [19, 55]. The algorithm is based on a fixed-size box-covering method suggested by Halsey [56]. To ensure completeness of the discussion we outline below the sandbox method. For a given probability measure μ (say), with a compact support in a metric space, one can define a partition sum as,

$$Z_r(q) = \sum_{\mu(B) \neq 0} [\mu(B)]^q; \quad \forall q \in R \quad (4.43)$$

where the summation runs over all different non-empty boxes B of size r , and q is the order number. The mass exponent $\tau(q)$ of the measure μ is defined by,

$$\tau(q) = \lim_{r \rightarrow 0} \frac{\Delta \ln Z_r(q)}{\Delta \ln r} \quad (4.44)$$

The generalized fractal dimensions D_q of the measure μ are given by,

$$D_q = \frac{\tau(q)}{q-1}; \quad \forall q \neq 1 \quad (4.45)$$

and the information dimension is given by,

$$D_1 = \lim_{r \rightarrow 0} \frac{\ln Z_r(1)}{\ln r} \quad (4.46)$$

In the expression of information dimension the partition sum is defined as,

$$Z_r(1) = \sum_{\mu(B) \neq 0} \mu(B) \ln \mu(B) \quad (4.47)$$

In a complex network the probability measure μ of each box is taken as the ratio of the number of nodes covered by the box and the total number of nodes present in the entire network. The fixed-size box-covering algorithm is modified in the sandbox algorithm, where the center of each equal-sized (sand) box is chosen at random over the fractal object, and then the number of nodes present in the sandbox is counted. In the sandbox method the

generalized fractal dimensions D_q is defined as,

$$D_q = \frac{\partial}{\partial(\ln r)} \ln \langle [M(r)/M_0]^{q-1} \rangle \frac{1}{q-1}; \quad \forall q \neq 1 \quad (4.48)$$

where $M(r)$ is the number of nodes in a sandbox of radius r , M_0 is the total number of nodes in the network and $\langle \rangle$ indicates that the quantity within the bracket is averaged over many sandbox centers chosen at random over the network. The information dimension D_1 is then obtained through Taylor's expansion of D_q around $1 + dq$,

$$D_1 = \frac{\partial}{\partial(\ln r)} \langle [M(r)/M_0] \rangle \quad (4.49)$$

In order to implement the sandbox algorithm into computation the following steps are taken:

1. Set a radius $r \in [1, d]$ for the sandbox which will be used to cover the network of dimension d (say).
2. Cover the entire network with sandboxes of size r whose central nodes are selected at random over the entire network. Note that if a node with large degree (known as a hub) is selected as the center of the sandbox, a large number of nodes would be covered within one box. This is an efficient way of box-covering. On the other hand, if a node with small degree is selected as the center, a few nodes would be covered within the box. As a result, if we change the arrangement of sandboxes the partition sum in Equations (4.48) and (4.49) will also change. To get rid of this problem we optimize the number of sandboxes needed to cover the entire network. Out of ten random combinations we select one which has the minimum number of box count.
3. Count the number of nodes $M(r)$ in each sandbox of radius r , and calculate the average $\langle [M(r)/M_0]^{q-1} \rangle$ and $\langle [M(r)/M_0] \rangle$ over the optimal number of sandboxes as described in the previous step.
4. Repeat steps 1 to 3 for several different values of r and for a given q . Compute the slope of the $\ln(r)$ versus $X_q(r)$ plots, where $X_q(r) \equiv \ln \langle [M(r)/M_0]^{q-1} \rangle$ for $q \neq 1$, and $X_1(r) \equiv \langle [M(r)/M_0] \rangle$. Then vary q over a desired range.

The sandbox algorithm for $r = 1$ is illustrated in Figure 4.19. For $r = 1$ node 1 has been chosen at random as the central node along with four other nodes covered in a box connected with node 1, which are shown in red color except node 3 (yellow). For the second pick, node 2 has been chosen at random as the sandbox centre, and two other nodes are covered in the same box with node 2. In this step node 3 (yellow), which has already been covered in a box with node 1, is excluded. This procedure is repeated unless and

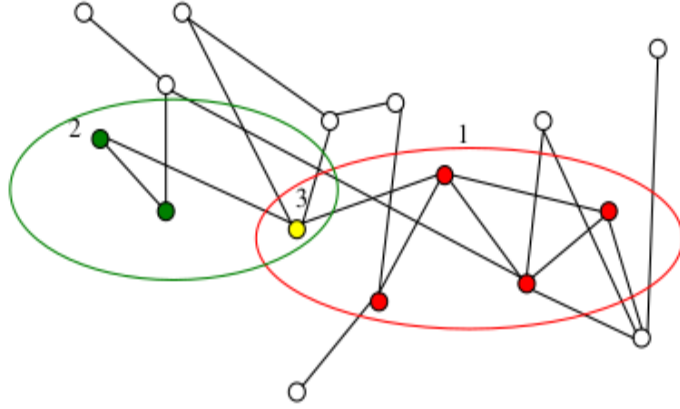


Figure 4.19: An illustration of the sandbox algorithm.

until all the nodes are covered by sandbox centres of radius $r = 1$, and then steps 3 to 4 are followed. The multifractal mass exponent $\tau(q)$ is related to the generalized fractal dimension D_q through $\tau(q) = (q - 1) D_q$. Knowing $\tau(q)$ the multifractal spectrum $f(\alpha)$ is computed via a Legendre transformation [Equation (4.5)]. Following the sandbox algorithm we compute $X_q(r) \equiv \ln \langle [M(r)/M_0]^{q-1} \rangle$ for $q \neq 1$ and $X_1(r) \equiv \langle [M(r)/M_0] \rangle$ from the VGs as well as from the HVGs obtained on an e-by-e basis, and then the quantities are averaged over the event space. In that sense the multifractal parameters studied here are actually their sample averaged values. $X_q(r)$ calculated in the sandbox approach from the VGs are plotted against $\ln(r)$ in Figure 4.20. Similar plots obtained from the HVGs are shown in Figure 4.21. In both figures the $X_q(r)$ functions are shown only for some selective values of q , though they are calculated over a wide range $q \in [-10, +10]$ with an incremental step of 0.25. The box-size is varied as, $r \in (1, 15)$ for both $^{16}\text{O-Ag/Br}$ and $^{32}\text{S-Ag/Br}$ interactions. Apparently, the $X_q(r)$ versus $\ln(r)$ plots for both interactions are identical, and the difference between the experiment and corresponding simulation predictions are also marginal. At this moment we do not give much importance to the apparent similarity in the behavior of the $X_q(r)$ functions obtained for different interactions and simulated events. Rather a linear rise of these functions over a reasonable range of $\ln(r)$ is what we require, since this is going to affect the accuracy of measurement of multifractal parameters to be derived. From Figures 4.20 and 4.21 we see that the functions $X_q(r)$ are approximately linear over the interval $7 \leq r \leq 15$.

The generalized fractal dimensions D_q are calculated from a linear regression of the partition functions X_q . The D_q values are plotted against the order number q in the upper panels of Figures 4.22 and 4.23 respectively, obtained from the VGs and HVGs. The UrQMD results are also included in these figures. In the lower panels of these figures we show the multifractal

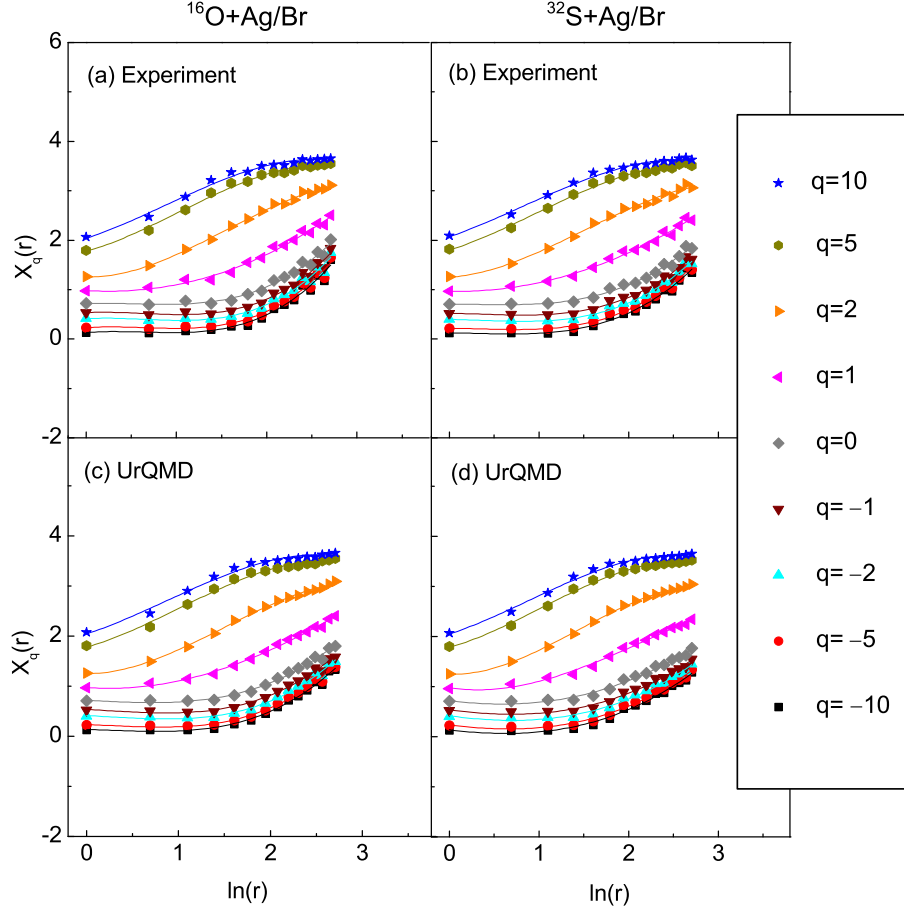


Figure 4.20: X_q versus $\ln r$ plots for several different q values for ^{16}O -Ag/Br (left) and ^{32}S -Ag/Br (right) interactions at 200A GeV/c obtained from the visibility graphs. In the lower panels we show the UrQMD simulations of the data.

mass exponents $\tau(q)$ plotted against q . Now we see the relative difference between the interactions considered and two approaches followed. It is known that for a monofractal signal the fractal dimensions are independent of the order number q . Consequently $\tau(q)$ is a linear function of q . A multifractal signal on the other hand, results in an order dependent D_q and the corresponding τ_q is a nonlinear function of q . The difference $\Delta D_q = \max .D_q - \min .D_q$ is sometimes considered as a measure of the degree of multifractality in the underlying process. In the present investigation we shall quantify the degree of multifractality from the singularity spectrum $f(\alpha)$. Our first impression from Figures 4.22 and 4.23 is that, the sandbox algorithm applied to the VG and HVG networks constructed from the η -distributions, efficiently reproduces the multifractal behavior as previously observed in our analyses for the same sets of data [25, 35]. Some important observations related to these figures are, (i) the ΔD_q value is greater for the ^{16}O -Ag/Br interaction than for the ^{32}S -Ag/Br interaction, (ii) the experimental D_q values, for $q \lesssim 2$, are consistently higher than the respective simulated values, (iii) the difference between the experimental and simulated values of D_q for $q \lesssim 2$ is

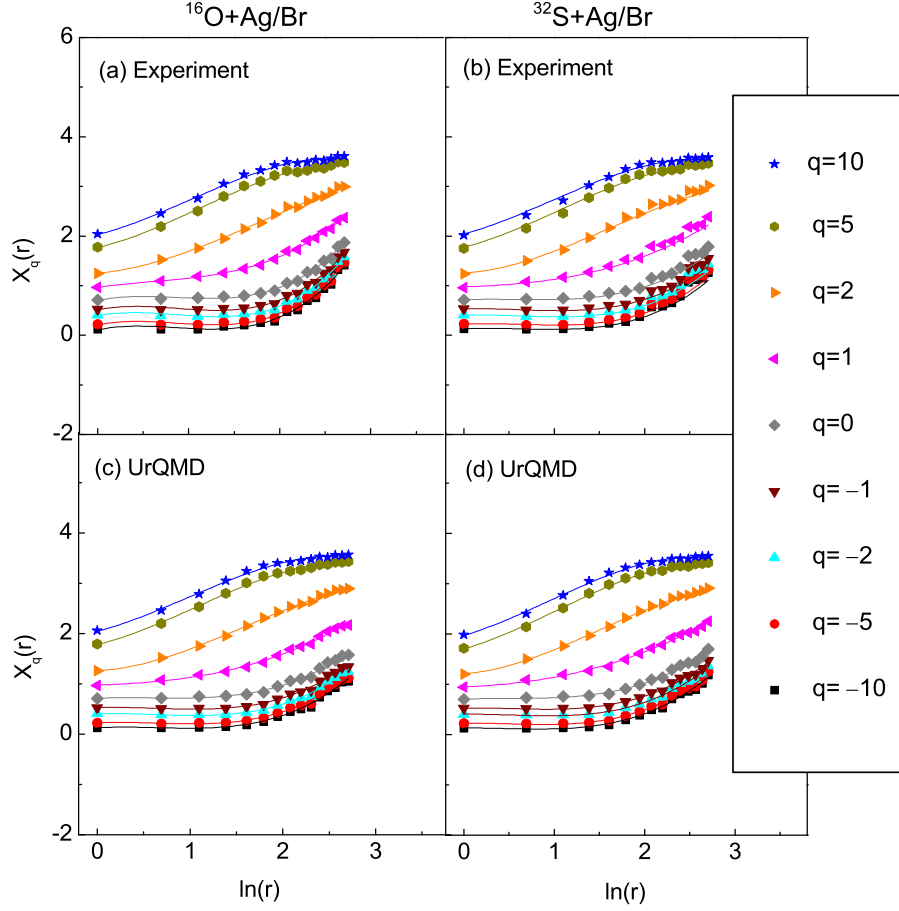


Figure 4.21: The same as in Figure 4.20 but for the horizontal visibility graphs.

also greater in the ^{16}O -Ag/Br interaction than in the ^{32}S -Ag/Br interaction, and (iv) in all the cases the values obtained from the VGs and HVGs do not differ significantly from each other. The $\tau(q)$ plots are consistent with the respective D_q plots. Observation (ii) implies that for $q < 1$ the quantity $\langle [M(r)]^{(q-1)} \rangle$ in Equation (4.43) is dominated by a comparatively smaller number of large fluctuations, whereas for $q > 1$ a large number of small fluctuations contribute to the overall coarse structure of the distributions. In AB collisions at the present energy scale the chance of a few large fluctuations occurring in every event is rare, whereas a large number of small fluctuations predominantly arise due to statistical reasons, resonance decays and kinematic conservations. In that sense the observed differences in $D_{q>1}$ between the experiment and simulation may be attributed to the existence of some large fluctuations in the experiment which are absent in the simulation.

The multifractal spectral functions $f(\alpha)$ obtained from this analysis are plotted against the Hölder exponents $\alpha(q)$ in Figure 4.24. Results from the VG (upper panel) and HVG (lower panel) analysis are included in the same figure along with the corresponding UrQMD and

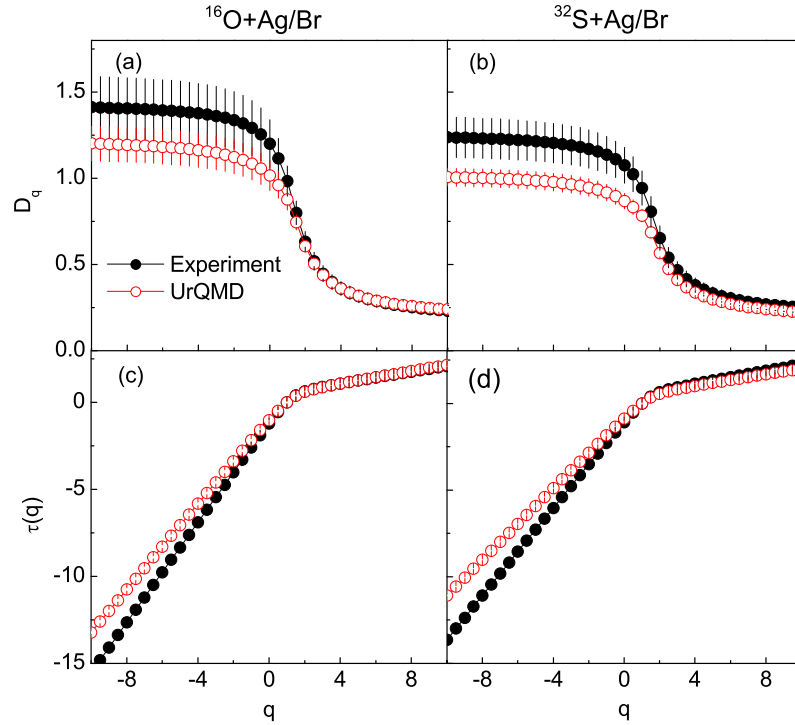


Figure 4.22: The order dependence of the generalized fractal dimensions (upper panel) and the multifractal mass exponents (lower panel) calculated from the visibility graph analysis.

mixed event predictions. The mixed event samples are prepared by mixing the track information belonging to the individual events taken at random, keeping the overall multiplicity and η -distributions unchanged. Our intention is to eliminate the noise present in the experimental event samples. Since the random mixing procedure unambiguously destroys particle correlations (if there are any) present in the data sample, a mixed event sample is a good representation of the statistical noise. The $f(\alpha)$ spectra as shown in the figure, support our previous findings that the η -distributions of the interactions studied are multifractal in nature. As expected the event mixing process reduces the degree of multifractality present in the data, and the $f(\alpha)$ spectra for mixed events almost coincide with the model simulation. However, within the error bars the multifractality strength in the UrQMD-mixed events is identical to the actual UrQMD generated value. From this observation we understand that the multifractal characteristics of the UrQMD simulated events is mainly due to statistical noise. Therefore, the difference in multifractal measures between an experiment and its UrQMD/mixed-event counterpart might be due to one or more dynamical reasons associated with the particle production mechanism. The degree of multifractality is determined from the $f(\alpha)$ spectrum by the following a parametrization like [49, 57],

$$f(\alpha_q) = A + B(\alpha - \alpha_0) + C(\alpha - \alpha_0)^2 + D(\alpha - \alpha_0)^3 + E(\alpha - \alpha_0)^4 \quad (4.50)$$

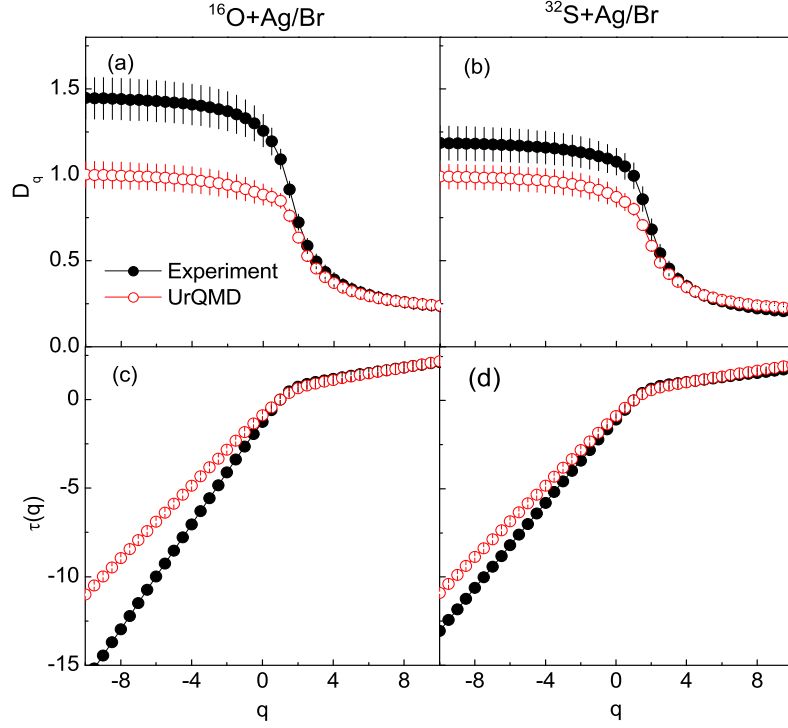


Figure 4.23: The same as in Figure 4.22 but for the horizontal visibility graph analysis.

where α_0 is the peak position of the spectrum, the first and third order coefficients B and D , respectively determine the overall asymmetry of the spectrum. The left side of $f(\alpha)$ spectrum corresponds to $q > 0$ and it filters out the large fluctuations, while the right side of the spectrum corresponds to $q < 0$ and it is associated with the small noise-like fluctuations. Another parameter of interest is the width of the spectrum $\Delta\alpha = \alpha_{\max} - \alpha_{\min}$, where α_{\max} and α_{\min} are the values of α for which $f(\alpha) = 0$. Parameters α_0 , B and $\Delta\alpha$ are used as a measure of the ‘complexity’ of the process under consideration [57], and therefore they are known as the ‘complexity parameters’. Multifractal spectrum generated from a random process is expected to peak at $\alpha_0 = 0.5$ with a marginal width. For a long-range correlated signal $\alpha_0 > 0.5$. The width $\Delta\alpha$ measures the range of fractal exponents required to describe the signal, and therefore, it measures the degree of multifractality present in the signal. The wider the range of fractal exponent is, wider will be the $f(\alpha)$ spectrum, which indicates a richer structure of the underlying process. Formally an asymmetry parameter can be defined as [57],

$$r = (\alpha_{\max} - \alpha_0) / (\alpha_0 - \alpha_{\min}) \quad (4.51)$$

For a symmetric spectrum $r = 1$, for a right skewed distribution $r > 1$, and for a left skewed distribution $r < 1$. The asymmetry parameter r indicates which fractal exponents are dominant. For instance a right skewed spectrum is dominated by small values of $\alpha(q)$

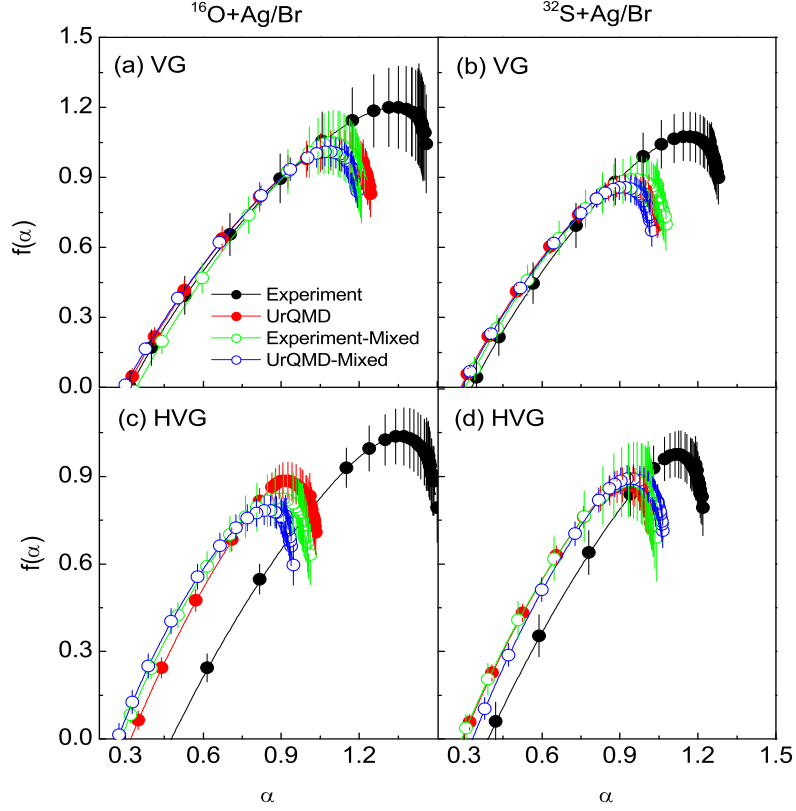


Figure 4.24: Multifractal spectra obtained from the VG (upper panel) and HVG (lower panel) analysis for the interactions studied. Predictions from the mixed events are shown (follow text for details). The lines joining points represent Equation (4.50) with the best fitted parameters given in Table 4.7.

that indicates multifractal nature of small noise-like fluctuations, while a left skewed spectrum indicates dominance of large $\alpha(q)$ values and therefore, a multifractal nature of large fluctuations. The former one is characterized by more regular smooth looking processes, while the latter corresponds to finer structures. In short, a wide right skewed spectrum with $\alpha_0 > 0.5$ corresponds to a more complex process. To measure the complexity of the underlying mechanism of particle production, each $f(\alpha)$ spectrum is fitted to Equation (4.50). The fits are shown by solid curves in the diagram. Note that instead of measuring the width $\Delta\alpha$ of the $f(\alpha)$ -spectrum we measure its half width at full maximum (FWHM) $\Delta\omega$, as because the spectra obtained here are truncated much above $f(\alpha_{max}) = 0$. The set of chaoticity parameters, namely the peak position α_0 , the FWHM $\Delta\omega$ and the asymmetry parameter r are shown in Table 4.7. From the table it is now clear that fine structured small fluctuations dominate the η -distributions of the interactions considered in the present investigation. However, the contribution of some nontrivial hitherto unknown dynamics is also not negligible in the ^{16}O -Ag/Br and ^{32}S -Ag/Br interactions at 200A GeV/c.

Table 4.7: The peak position α_0 , the FWHM $\Delta\omega$ and the asymmetry parameter r of the multifractal spectra shown in Figure 4.24.

Data sample	VG			HVG		
	α_0	$\Delta\omega$	r	α_0	$\Delta\omega$	r
¹⁶ O-Ag/Br						
Experiment	1.297	0.964	0.557	1.317	0.759	0.530
UrQMD	1.085	0.758	0.556	0.910	0.545	0.580
Experiment-Mixed	1.067	0.659	0.580	0.874	0.569	0.572
UrQMD-Mixed	1.051	0.706	0.562	0.828	0.533	0.549
³² S-Ag/Br						
Experiment	1.128	0.762	0.565	1.088	0.638	0.607
UrQMD	0.914	0.591	0.559	0.907	0.574	0.573
Experiment-Mixed	0.937	0.602	0.572	0.918	0.573	0.561
UrQMD-Mixed	0.896	0.568	0.569	0.934	0.574	0.586

At this point it would be prudent to discuss the effectiveness of the VG method vis-a-vis that of the detrended method(s) of analysis of multiparticle emission data [40]. One can speculate that (i) the strength of a local singularity will be higher if both statistical and non-statistical components contribute to it, and (ii) being Poisson distributed it is very unlikely only for a noise to yield a very strong local singularity. Equivalently, if in the singularity spectrum one finds a systematic reduction in the values of the singularity strength, then a probable reason of that should be the noise elimination. The spectrum of the singularity strength obtained by using the detrended method(s) is quite different in nature from that obtained by using the VG-sandbox algorithm. The detrended methods gave us smooth, almost symmetric and/or slightly right sided spectra, which were never significantly different from the respective simulation. In [40] this feature was interpreted in terms of a large number of small fluctuations and a small number of large fluctuations [58, 59], which were in principle present both in the experiments and in the simulations. When it comes to the question of VG/HVG method, we first observe that the $f(\alpha)$ spectra are strongly left sided, and on several occasions the experimental singularity spectrum is significantly different from the corresponding simulation. The left side of each spectrum gradually rises to reach the respective peak value, is dominated by small $\alpha(q)$ values, and therefore by ‘rough’ fluctuations. The spectrum then abruptly drops down to some extent from the peak position marginally towards its right, suppressing the ‘smooth’ fluctuations almost to a monofractality. This kind of left sided asymmetry in $f(\alpha)$ may arise due to superposition of partonic/hadronic level cascades [27, 45].

Ideally the detrended methods of analysis should be applied to a sufficiently long time (or equivalent) series, so that the local trend(s) or the local average(s) are minimally influenced by statistical uncertainties, and the fluctuations considered either about a local trend or about a local average become statistically significant. For a finite sized η -distribution that

can at best be divided into $\sim 10^2$ intervals, this unfortunately is not the case, and therefore, the results obtained in this analysis are to some extent representative in nature. Moreover, in the detrended method we have used only a linear local trend, which may not always be the case. The limitation of the detrended method is also reflected in the fact that we rarely find significant difference between experiment and simulation. Though our data could be characterized in terms of (multi)fractality, we have never been sure about how to eliminate the statistical components present in the data. On the contrary, in the VG/HVG method, the issue of statistical noise has perhaps been taken care of. This is reflected in the $f(\alpha)$ spectrum and also in the plots of other (multi)fractal parameters. At least in some regions significant differences between experiment and simulation are observed. The experimental values obtained from the VG/HVG-sandbox method are quite different from the corresponding simulation. The rise in the $f(\alpha)$ spectrum in the left side of the peak position is gradual, and is never as sharp as it is in the detrended method(s). The region dominated by ‘rough’ (large) fluctuations is therefore multifractal in nature. In the right side of the $f(\alpha)$ distribution we notice that the singularity strengths obtained from the VG/HVG method(s) are restricted within a very narrow range, and are never quite as large as those obtained from the detrended methods ($\alpha \approx 1.9$). This shows that the contribution of statistical noise has perhaps been taken care of, restricting thereby the small fluctuations almost to a monofractality. We therefore, conclude that while addressing the issue of statistical noise, if we have to analyze a data series that is not very long, the VG-sand box algorithm is certainly a better choice, and the results obtained thereof are more accurate than those obtained from the detrended method(s).

4.7 Summary

To summarize, we have presented some results on multifractal analysis of shower tracks (singly charged produced particles) in ^{16}O -Ag/Br interaction at 200A GeV/c. The experimental results are systematically compared with the UrQMD and UrQMD+BEC simulations. We present the results obtained from the G_q and T_q -moments, two conventional methods of multifractal analysis of particle density fluctuations. The results obtained from ^{16}O -Ag/Br interaction are sometimes compared with similar results obtained from ^{32}S -Ag/Br interaction at 200A GeV/c. We also employ the detrended multifractal methods, the visibility graphs and sandbox algorithm to characterize shower track emission data in terms of multifractality. In these cases we systematically compare the results obtained from ^{16}O -Ag/Br interaction with those from ^{32}S -Ag/Br interaction at 200A GeV/c. The experimental results are compared with UrQMD+BEC simulations. The observations of our multifractal analysis are enumerated below.

1. The multifractal G_q -moments follow a scale invariant power-law scaling with diminishing phase space resolution size. The UrQMD and UrQMD+BEC simulated results too show identical trends like the experiments for both $^{16}\text{O-Ag/Br}$ and $^{32}\text{S-Ag/Br}$ interactions at 200A GeV/c. This is in contrast to our previous investigation of intermittency phenomenon for the same set of experimental data where UrQMD and UrQMD+BEC failed to reproduce the experimental observations. The reason is, while defining the scaled factorial moments, statistical noise is automatically taken care of.
2. The q -dependence of mass exponent $\tau(q)$ and Lipschitz-Hölder exponent $\alpha(q)$ obtained from the experiments is very much similar to the corresponding UrQMD results. The parameters themselves are probably not very sensitive to the nature of fluctuations present in the data. However, it is observed that $[q - 1 - \tau(q)]$ is significantly different from the intermittency exponent ϕ_q . When statistical contribution is properly taken care of $[q - 1 - \tau^{\text{dyn}}(q)]$ comes very close to the ϕ_q values, and this happens for both experiments and both simulations considered in this analysis.
3. The multifractal spectrum, consistent in all aspects with its expected behavior, has a slightly smaller width in the UrQMD generated curve. In this regard the UrQMD+BEC generated spectrum lies in between the experiment and the UrQMD. Therefore, the multifractal spectrum might be considered as a sensitive tool that can distinguish the dynamical contribution from the statistical noise in the density fluctuations. This is a common feature for both $^{16}\text{O-Ag/Br}$ and $^{32}\text{S-Ag/Br}$ interactions.
4. We have analyzed the multifractal spectral function to compute the Lévy stable index μ . Irrespective of the data set used we have obtained different μ -values in different q -regions. The μ -values in the low- q region are not consistent with the values obtained from our intermittency analysis. The values are far above the upper acceptable limit ($\mu = 2$) allowed by the Lévy stability law [44, 45]. However, in the high- q region the experimental μ -values within errors are very close to that upper limit of the parameter. In the high- q region, the differences in the μ -values obtained from simulation and experiment are not statistically significant.
5. Takagi's multifractal moments also exhibit the expected power-law scaling with decreasing phase space resolution size for experiments and simulations. Though Takagi's technique has a few advantages over Hwa's technique of analysis, the T_q moments are also contaminated by statistical noise. This limitation is reflected in the multifractal parameters derived by using this method. The experimental D_q values obtained from the T_q moments are not significantly different from the corresponding simulated values for the $^{16}\text{O-Ag/Br}$ interaction, though it is marginally different in the $^{32}\text{S-Ag/Br}$ case. A systematic deviation in D_1 from the topological dimension, that increases with the

order number q , is an indication of the presence of multifractality in the single particle density distribution. The parameter D_q , unlike $\tau(q)$ and α , is found to be sensitive to the nature of fluctuation. The variation of D_q with $\ln q/(q-1)$ is consistent with the thermodynamic interpretation of a monofractal to multifractal transition. The magnitude of specific heat however, does not corroborate any kind of universality as claimed in [36].

6. In the framework of MF DFA and MFDMA techniques we have presented a systematic study on the density fluctuations present in the η -distributions of shower tracks coming from $^{16}\text{O-Ag/Br}$ and $^{32}\text{S-Ag/Br}$ collisions at 200A GeV/c. The results show that for both the interactions the η -distributions having sharp spikes and empty valleys, are long-range correlated and highly multifractal in nature. Comparison of multifractal parameters like the generalized Hurst exponents $h(q)$, the mass exponents $\tau(q)$ and the spectral function $f(\alpha)$, obtained from the experiments and UrQMD+BEC simulations, reveal that the multifractality observed in the experiment goes beyond UrQMD+BEC prediction, and contribution of some nontrivial hitherto unknown dynamics has to be taken into account to interpret the observation. However, the observations presented here qualitatively agree with our previous findings [40, 41], and also with the particle production mechanism of the UrQMD model. However, quantitative differences between the results of the MF DFA and MFDMA methods are prominent in some cases.
7. From the detrended analysis we understand that as far as the multiparticle production data are concerned, the signal length is an important issue. The MF DFA method like the MFDMA method is not quite capable of filtering out the statistical noise from the signal. However, unlike the MF DFA (first order) method the MFDMA analysis produces a complete and stable singularity spectrum. The multifractal spectrum of MFDMA analysis indicates the existence of a few events with large fluctuations, whereas the coarse fluctuations arise from statistical noise. The observation is grossly identical for both the interactions considered in the present investigation.
8. Using the visibility graph and sandbox algorithm, event-wise η -distributions of shower tracks coming out from $^{16}\text{O-Ag/Br}$ and $^{32}\text{S-Ag/Br}$ interactions both at 200A GeV/c, have been analyzed to find out the multifractal parameters. The degree distributions of the visibility graphs obtained from each experimental event sample and the respective UrQMD simulation are identical in nature. Both result in approximately the same tail exponent (γ). The scale freeness property of the degree distribution as observed for long-range correlated signals [51, 53], is therefore retained in the multiparticle emission data as well [42]. However, the γ value is found to be far above the limiting value ($\gamma \sim 3$) required for a long-range series. The sandbox algorithm applied to the VGs

and HVGs generated from the η -distributions, successfully reproduce the multifractal properties of the interactions studied [25, 35]. We also observe that the present graph theoretical approach of multiparticle data analysis, apparently has the potential to distinguish between the dynamical (non-statistical) contribution of fluctuations in the η -distributions from the statistical noise.

Bibliography

- [1] R. C. Hwa, Phys. Rev. D 41, 1456 (1990).
- [2] W. Florkowski and R. C. Hwa, Phys. Rev. D 43, 1548 (1991).
- [3] C. B. Chiu and R. C. Hwa, Phys. Rev. D 43, 100 (1991).
- [4] C. Albajar *et al.* (UA1 Collaboration), Z. Phys. C - Particles and Fields 56, 37 (1992).
- [5] I. Derado *et al.*, Phys. Lett. B 283, 151 (1992).
- [6] R. K. Shivpuri and V. Anand, Phys. Rev. D 50, 287 (1994).
- [7] M. I. Adamovich *et al.* (EMU01 Collaboration), Europhys. Lett. 44, 571 (1998).
- [8] E. K. Sarkisyan, L. K. Gelovani and G. G. Taran, Phys. Lett. B 302, 331 (1993); Phys. Lett. B 347, 439 (1995).
- [9] R. C. Hwa, Phys. Rev. D 51, 3323 (1995).
- [10] R. C. Hwa and J. Pan, Phys. Rev. D 45, 1476 (1992).
- [11] F. Takagi, Phys. Rev. Lett. 72, 32 (1994).
- [12] J. W. Kantelhardt *et al.*, Physica A 316, 87 (2002).
- [13] G.-F. Gu and W. X. Zhou, Phys. Rev. E 82, 011136 (2010).
- [14] T. Tél, À. Fülöp and T. Vicsek, Physica A 159, 155 (1989).
- [15] C.-K. Peng *et al.*, Phys. Rev. E 49, 1685 (1994).
- [16] S. M. Ossadnik *et al.*, Bio-phys. J 67, 64 (1994).
- [17] N. Vandewalle and M. Ausloos, Phys. Rev. E 58, 6832 (1998).
- [18] E. Alessio, A. Carbone, G. Castelli and V. Frappietro, Eur. Phys. J. B 27, 197 (2002).
- [19] J. L. Liu, Z. G. Yu and V. Anh, Chaos 25, 023103 (2015).

- [20] P. Mali *et al.*, Mod. Phys. Lett. A 32, 1750024 (2017).
- [21] R. C. Hwa and J. C. Pan, Phys. Rev. D 45, 106 (1992).
- [22] P. L. Jain, K. Sengupta and G. Singh, Physics Letters B 241, 273 (1990).
- [23] K. Sengupta *et al.* (KLM Collaboration), Phys. Rev. D 48, 3174 (1993).
- [24] G. Singh and P. L. Jain, Phys. Rev. C 50, 2508 (1994).
- [25] M. K. Ghosh, A. Mukhopadhyay and G. Singh, J. Phys. G 32, 2293 (2006).
- [26] N. Parashar, J. Phys. G 22, 59 (1996).
- [27] W. Ochs, Phys. Lett. B 247, 101 (1990).
- [28] R. E. Ansorge *et al.* (UA5 Collaboration), Z. Phys. C 43, 357 (1989).
- [29] W. Braunschweig *et al.* (TASSO Collaboration), Z. Phys. C 45, 159 (1988).
- [30] P. Abreu *et al.* (DELPHI Collaboration), Z. Phys. C 52, 271 (1991).
- [31] D. Ghosh, A. Deb *et al.*, J. Phys. G: Nucl. Part. Phys. 29, 983 (2003); D. Ghosh *et al.*, Nucl. Phys. A 720, 419, (2003);
- [32] D. Ghosh *et al.*, Phys. Rev. C 70, 054903 (2004); D. Ghosh, P. Ghosh, A. Deb, A. Ghosh and J Roy, Phys. Letts. B 272, 5 (1991).
- [33] S. Ahmad and M. Ayaz Ahmad, Nucl. Phys. A 780, 206 (2006).
- [34] S. Ahmad, A. R. Khan, M. Zafar and M. Irfan, Chaos, Solit. Frac. 42, 538 (2009).
- [35] P. Mali, A. Mukhopadhyay and G. Singh, Fractals 20, 203 (2012).
- [36] A. Bershadski, Phys. Rev. C 59, 364 (1999).
- [37] S. Khan and S. Ahmad, Adv. High Eng. Phys. 2018, 1 (2018).
- [38] Y. X. Zhang, W. Y. Qian and C. B. Yang, Int. J. Mod. Phys. A 23, 2809 (2008).
- [39] P. Mali, S. K. Manna *et al.*, Chaos, Solitons and Fractals 94, 86 (2017).
- [40] P. Mali, A. Mukhopadhyay and G. Singh, Physica A 450, 323 (2016).
- [41] P. Mali *et al.*, Physica A 424, 25 (2015).
- [42] P. Mali, S. K. Manna *et al.*, Physica A 493, 253 (2018).
- [43] J. Feder, Fractals, Plenum Press, New York (1988).

-
- [44] Ph. Brax and R. Peschanski, *Phys. Lett. B* 253, 225 (1991).
- [45] W. Ochs, *Z. Phys. C* 50, 339 (1991).
- [46] Y. Hu, M. Yu and L. Liu, *Chin. Phys. Lett.* 16, 553 (1999).
- [47] H. G. E. Hentschel and I. Proccacia, *Physica D* 8, 435 (1983).
- [48] M. S. Movahed *et al.*, *J. Stat. Mech.* 02003 (2006);
P. Mali, *J. Stat. Mech.* 013201 (2016)
- [49] Y. Shimizu, S. Thurner and K. Ehrenberger, *Fractals* 10, 103 (2002).
- [50] L. Lacasa *et al.*, *Proc. Natl. Acad. Sci. USA* 105, 4972 (2008).
- [51] B. Luque, L. Lacasa, F. Ballesteros and J. Luque, *Phys. Rev. E* 80, 046103 (2009).
- [52] L. Lacasa and R. Toral, *Phys. Rev. E* 82, 036120 (2010).
- [53] L. Lacasa, B. Luque, J. L. Luque and J. C. Nuño, *Europhys. Lett.* 86, 30001 (2009).
- [54] M. E. J. Newmann, *Contemp. Phys.* 46, 323 (2005).
- [55] Z.-G. Yu, H. Zhang, D.-W. Huang, Y. Lin and V. Anh, *J. Stat. Mech.* 033206 (2016).
- [56] T. C. Halsey *et al.*, *Phys. Rev. A* 33, 1141 (1986); 34, 1601 (erratum) (1986).
- [57] A. Muñoz-Diosdado and J. L. D. Ro-Correa, *Proc. of 28th IEEE EMBS Ann. Int. Conf. New York City* (2006).
- [58] P. Oświęcimka, J. Kwapien and S. Drożdż, *Phys. Rev. E* 74, 016103 (2006).
- [59] S. Drożdż and P. Oświęcimka, *Phys. Rev. E* 91, 030902(R) (2015).

Chapter 5

Ring-jet structure and wavelet analysis

5.1 Introduction

One of the primary objectives of this investigation is to understand the cluster structures, if any, present in our experimental data. It has been speculated that the emission of Cerenkov gluons within the intermediate fireball might be a primary source of local density fluctuations and therefore might be a source of cluster formation [1]. An alternative but somewhat similar speculation is the formation of a shock wave traveling through the partonic/nuclear medium of the fireball [1, 2]. These macroscopic phenomena correspond respectively, to the transverse and longitudinal excitations of the medium concerned. In either case however, the emission pattern is characterized by a conical structure defined in terms of a semi-vertex angle ξ as,

$$\cos \xi = \frac{c_{med}}{v} = \frac{c}{\mu v} \quad (5.1)$$

Here depending upon the case, as it may be, c_{med} is either the velocity of the gluon or that of the shock wave in the fireball medium, v is the velocity of the partonic/hadronic jet that triggers either the Cerenkov gluon or the shock wave emission, μ is the refractive index of the medium concerned, and c is either the velocity of the gluon in vacuum or the velocity of sound wave in air. The incident nucleus can be treated as a bunch of quarks, each of which is capable of emitting Cerenkov gluons while traversing through the target nucleus.

Experimentally the real part of the elastic forward scattering amplitude of all hadronic processes in high-energy collisions have been found to be positive [3]. This condition is necessary for the Cerenkov emission to take place, as the excess of nuclear refractive index over unity is proportional to the real part of the forward scattering amplitude. Under favorable circumstances the conical structure, if so formed, may withstand the impact of collision and retain its original shape. If the initial/triggering parton direction is same as that of the incident beam, and if the number of minijet emitting gluons is large, then in the distributions of the particles one may observe ring-like structures that are clustered within narrow regions of pseudorapidity (η). The particles may however be distributed more or less uniformly over the entire azimuth $\varphi \in [0, 2\pi]$. On the other hand, if the number of jet emitting gluons is small, then it is more likely that several jets, each restricted to narrow intervals of both η and φ , will be formed, resulting thereby jet-like structures in the distributions of final state hadrons. A quark-gluon jet created by a high-energy parton can as well give rise to a collective behavior that is similar to the Mach shock wave formation. For thin targets like the nuclei, due to their small confinement lengths, just like the Cerenkov gluons shock wave emission can also take place [4]. A partonic jet moving with a velocity close to that of the light can be considered as a body moving in the nuclear/partonic medium with a supersonic speed, which may cause a large pressure variation, and therefore can give rise to shock waves. The Mach angle depends upon the state of the matter through which the partonic jets are moving. Once again depending on the nature of the medium, the sound (elastic) wave speed is expected to vary in between $0.4c - 0.9c$ [5].

The wavelet analysis technique is mainly used in signal processing, image analysis, communication systems, fractals and in several other branches of physics. For a review one can for example see [6, 7]. The wavelets have also been used for pattern recognition in high-multiplicity AB events [8, 9]. The key idea of wavelet analysis is the expansion of the signal with respect to a self-similar set of orthogonal basis functions, the so-called wavelets. The entire basis is constructed through dilation and translation of one single function, known as the mother wavelet. It provides a convenient representation to study self-similar processes, in which an arbitrary distribution can be resolved simultaneously in many scales. Singularities, i.e. large fluctuations can be identified through wavelet decomposition, as and where the wavelet coefficients are large. At lower (higher) resolution wavelet algorithm returns gross (finer) pictures of the signal under scrutiny. In this chapter, along with an analysis on the angular distributions of the shower tracks in the context of ring and/or jet like structures, we also present some results obtained from a wavelet analysis in the context of cluster formation. In order to study any unusual structure in the particle emission data, we compare the results obtained from ^{16}O -Ag/Br and ^{32}S -Ag/Br interactions at an incident energy $E_{lab} = 200$ GeV/nucleon. We also compare the experiments with the UrQMD and UrQMD+BEC simulations.

5.2 Literature review

Ring-like structures were first studied in a cosmic-ray induced nuclear interaction [10]. Subsequently in several accelerator based experiments ring and jet-like structures were further investigated in high-energy AB interactions [11–16]. The results of azimuthal structure analysis in $^{16}\text{O-Ag/Br}$, $^{32}\text{S-Ag/Br}$ and $^{32}\text{S+Au}$ interactions at $200A$ GeV/c (EMU01 experiment) were compared with the FRITIOF-1.7 simulations taking the γ -conversion and HBT effects into account [11]. It was observed that the FRITIOF model combined with the γ -conversion factor, could reproduce the experimental data well, while the effect of HBT was found to be marginal. In $^{197}\text{Au+Ag/Br}$ interactions at $11.6A$ GeV/c ring-like structures were observed in the target azimuth [17]. The angular structure of particle emission in $^{208}\text{Pb+Ag/Br}$ interaction at $158A$ GeV/c obtained from EMU12 experiment [18] was investigated by Vokál, *et al.* [19], and the data were compared with the FRITIOF model. These results also supported the presence of ring-like substructures in the target azimuth, and the creation mechanism of such substructures are similar to that of the Cerenkov radiation. The EMU12 data also suggest that there are two preferred regions of pseudorapidity where ring-like events are observed, one in the forward and another in the backward hemisphere in the center-of-mass system. The ring/jet-like structures were also studied in $^{28}\text{Si-Ag/Br}$ interaction at $14.5A$ GeV and in $^{32}\text{S-Ag/Br}$ interaction at $200A$ GeV [20]. The experimental results were compared with the RQMD and UrQMD models where the BEC effect was also taken into account. There was an indication of ring-like structures being present in the $^{28}\text{Si-Ag/Br}$ interaction, while in the $^{32}\text{S-Ag/Br}$ interaction jet-like structures were found. The microscopic transport models could not match the experiments.

In high multiplicity AB events cluster structures in multiparticle emission data were studied with the help of wavelet analysis [8, 21–23]. The pseudorapidity distributions in the JACEE events were analyzed in terms of the wavelet transform technique [24]. The wavelet spectra of one Ca-C and another Si-Ag/Br event were compared with Monte-Carlo simulations using Poisson distributed random numbers, uniformly distributed random numbers and a p -model. The experimental results followed a trend similar to that observed in the uniformly distributed random numbers as well as in the Poisson distributed random numbers [21]. The wavelet results obtained from the EMU15 Pb+Pb data at 158 GeV/nucleon showed the presence of ring and jet-like structures in some of the high multiplicity events [25]. A two-dimensional wavelet analysis of a high-multiplicity Pb+Pb event at 158 GeV/nucleon (EMU15 experiment) [26] has been presented in [27]. In [27] the (η, φ) -space was divided into 24 equal sectors. In each sector the wavelet power spectra was calculated and the most densely populated regions in the (η, φ) -plane was identified. The g_2 wavelets (second derivatives of the Gaussian function) were used to analyze the Au+Emulsion data at $11.6A$ GeV/c

[28]. Some irregularities in the wavelet pseudorapidity spectra were observed, which were attributed to the preferred emission angles of groups of particles [28]. The wavelet technique was used to analyze the data acquired from the EMU12 experiment [18]. The observations of EMU12 experiment were more or less similar to that of [28]. The pseudorapidity distributions of shower tracks in $^{28}\text{Si-Ag/Br}$ and $^{32}\text{S-Ag/Br}$ interactions, respectively at 14.5A GeV and 200A GeV, were analyzed by using the continuous wavelet transform technique [29]. In this investigation experimental results were compared with UrQMD where the BEC effect was mimicked into the simulation. Presence of some non-trivial effects was found in the particle emission data that was beyond the UrQMD or UrQMD+BEC prediction. There are some reports where wavelet technique has also been employed to study particle correlations [8, 9, 30].

5.3 Ring and jet-like structures

The method of ring-jet analysis has been elaborated in [11]. A brief description of the same is presented below only for the sake of completeness. For an individual event, we start with a fixed number ($n \leq n_s$) of particles (shower tracks). Each n -tuple of particles is sequentially arranged either in the ascending or descending order along the η -axis. This subgroup of particles is then characterized by a size $\Delta\eta = |\eta_{m+i-1} - \eta_i|$, $i = 1 \cdots n_s$, a mean $\eta_m = \sum_{i=1}^n \eta_i/n$, and a density $\rho = n/\Delta\eta$. Each subgroup of particles having same multiplicity n can be statistically compared with each other. The azimuthal structure of a particular subgroup can be parameterized in terms of the following quantities,

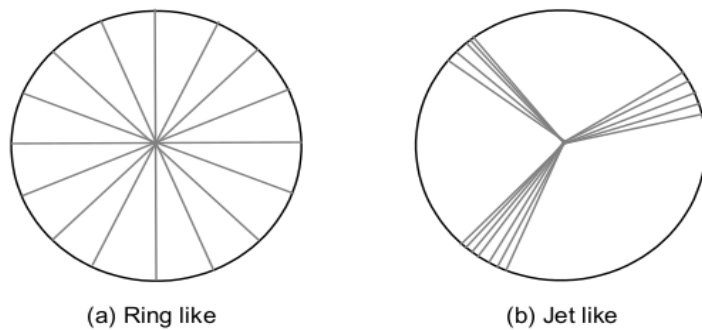


Figure 5.1: Schematic representation of (a) a ring-like distribution and (b) a jet-like distribution of tracks in the target azimuth.

$$S_1 = - \sum_{i=1}^n \ln(\Delta\varphi_i) \quad \text{and} \quad S_2 = \sum_{i=1}^n (\Delta\varphi_i)^2 \quad (5.2)$$

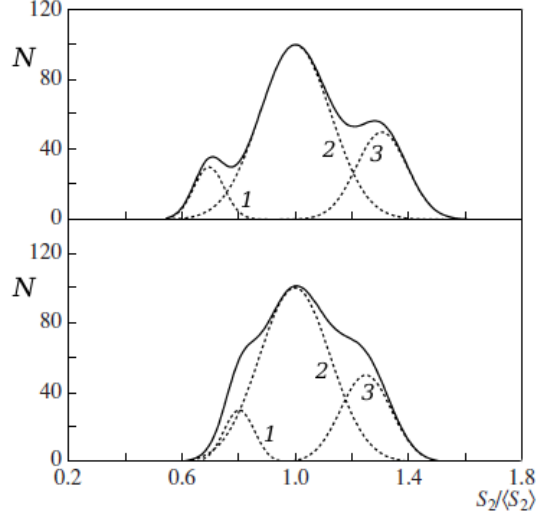


Figure 5.2: A schematic of $S_2/\langle S_2 \rangle$ distributions obtained for three cases, namely (1) ring-like events, (2) stochastic distribution and (3) jet-like events. The solid curve represents the resultant distribution.

Here $\Delta\varphi_i$ is the φ -difference of two neighboring particles, i.e., between the i -th and the $(i+1)$ -th particle belonging to a particular subgroup, starting from first and second and ending at the n -th and first. One can measure φ in units of a complete revolution [$\varphi \in (0, 2\pi)$]. Each $\Delta\varphi_i$ would then be a fraction of the total azimuth 2π . The difference between a ring-like and a jet-like structure has been schematically explained in Figure 5.1 using the target azimuth. For a ring-like structure the tracks are almost isotropically distributed over the entire azimuth. On the other hand for a jet-like structure some of the tracks are clustered within a narrow region of φ , but each cluster is well separated from the other in the azimuthal plane. Note that for a perfect ring-like emission of particles both $S_1 \rightarrow n \ln n$ and $S_2 \rightarrow 1/n$ will be small valued. On the other hand for a perfect jet-like emission $S_1 \rightarrow \infty$ and $S_2 \rightarrow 1$. While S_1 is sensitive to small gaps S_2 is sensitive only to large gaps. For a purely stochastic emission the $\Delta\varphi$ -distribution is given by [11, 31],

$$f(\Delta\varphi)d(\Delta\varphi) = (n-1)(1-\Delta\varphi)^{(n-2)}d(\Delta\varphi) \quad (5.3)$$

The expectation values of the S -parameters are therefore given by,

$$\langle S_1 \rangle = n \sum_{k=1}^{n-1} \frac{1}{k} \quad \text{and} \quad \langle S_2 \rangle = \frac{2}{n+1} \quad (5.4)$$

The distributions of S_1 and S_2 would be peaked around the corresponding expectation values. Presence of jet-like substructures would result in bulging and small local peaks in the distributions to the right side, whereas ring-like substructures would do the same

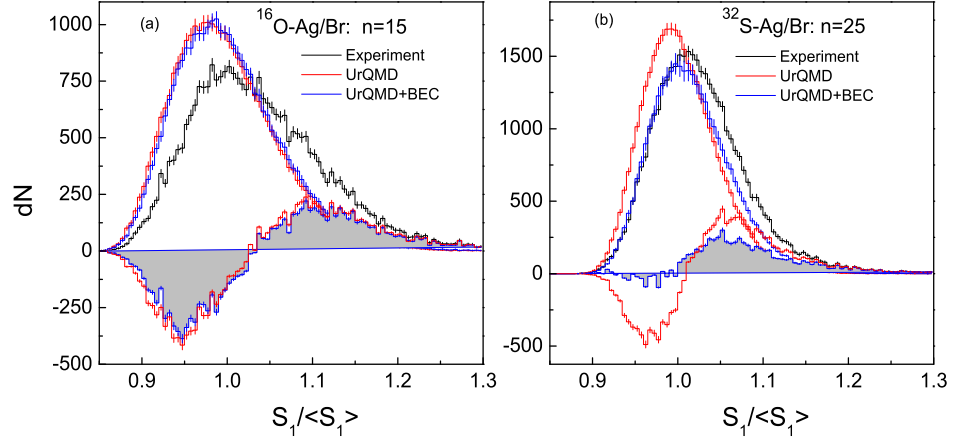


Figure 5.3: Distributions of the S_1 parameter normalized by its stochastic expectation value $\langle S_1 \rangle$ for (a) $^{16}\text{O-Ag/Br}$ and (b) $^{32}\text{S-Ag/Br}$ interactions both at 200A GeV/c. The shaded region is experimental excess over UrQMD+BEC distribution and without shaded region is over UrQMD.

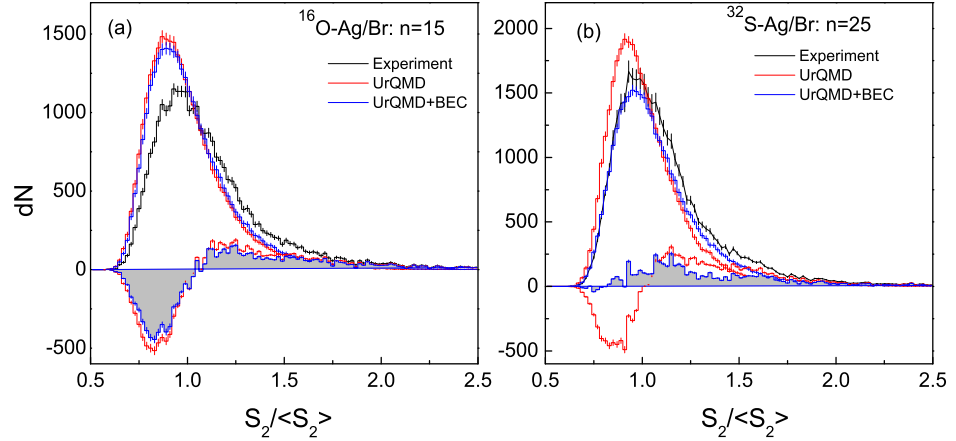


Figure 5.4: Same as in Figure 5.3 but for the S_2 parameter.

towards the left side of the expectation values. A schematic of the distributions of S_2 expected from three different processes are shown in the Gaussian form in Figure 5.2. In this figure the distributions marked by 1, 2 and 3 (dotted lines) represent, respectively the ring-like, stochastic and jet-like structures. All three distributions are then combined to form a resultant distribution. In order to extract the information about any unusual azimuthal structure, one therefore needs to first eliminate the contributions coming from the stochastic processes.

We have taken $n = 15$ and 25, respectively for the $^{16}\text{O-Ag/Br}$ and $^{32}\text{S-Ag/Br}$ event samples. For these choices of n the stochastic expectation values [see Equation (5.4)] come out as $\langle S_1 \rangle \approx 48.8$ and 94.4, and $\langle S_2 \rangle \approx 0.125$ and 0.077 respectively. Distributions of the S_1 parameter normalized by the corresponding stochastic expectation value $\langle S_1 \rangle$ are plotted in Figure 5.3 for both interactions. For a particular interaction the experiment, the UrQMD

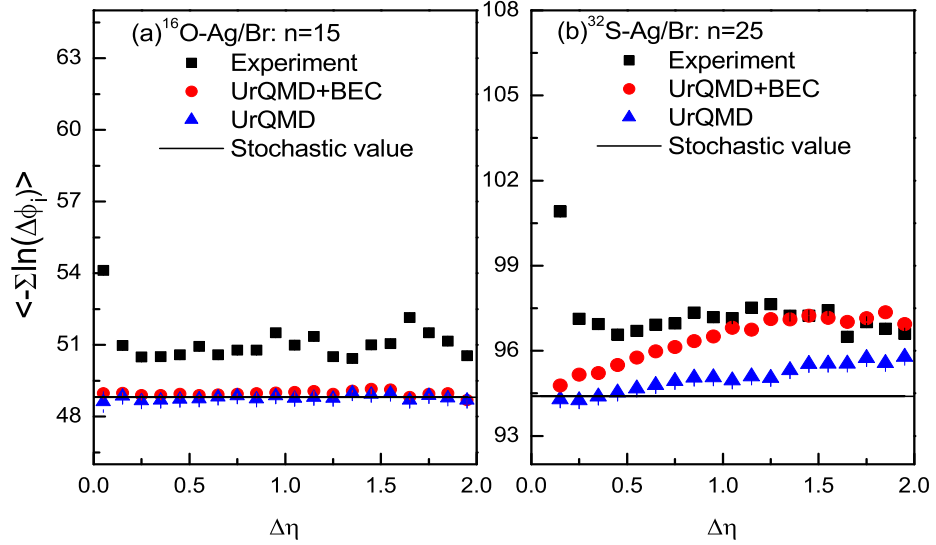


Figure 5.5: Average behavior of the S_1 parameter $\langle -\sum \ln(\Delta\varphi_i) \rangle$ for (a) $^{16}\text{O-Ag/Br}$ and (b) $^{32}\text{S-Ag/Br}$ interactions both at 200A GeV/c.

and UrQMD+BEC generated distributions are plotted together. As expected the UrQMD and UrQMD+BEC generated distributions peak around $S_1/\langle S_1 \rangle = 1.0$. The simulated distributions are taller, smoother and slightly narrower than the $^{16}\text{O-Ag/Br}$ experiment. On the other hand in the $^{32}\text{S-Ag/Br}$ case the UrQMD generated distribution is slightly taller while the UrQMD+BEC generated distribution is slightly shorter than the corresponding experimental distribution. All distributions are asymmetric, slightly right skewed, and the asymmetry is more pronounced in the experimental distributions. In each case the experimental distribution is slightly shifted towards right with respect to the corresponding simulation(s). Large S_1 values in the experimental distributions signify presence of jet-like structures. The differences between the experiment and the respective simulated data are also shown in these figures. We find experimental excesses in the $S_1/\langle S_1 \rangle > 1.0$ region, a feature common to both the interactions. In the $S_1/\langle S_1 \rangle < 1.0$ region of the $^{16}\text{O-Ag/Br}$ interaction both UrQMD and UrQMD+BEC simulations overpredict the experiment. On the other hand in the $^{32}\text{S-Ag/Br}$ case, only the UrQMD simulation has an excess whereas the UrQMD+BEC simulation matches reasonably well with the experiment. In Figure 5.4 graphical plots of $S_2/\langle S_2 \rangle$ are shown. The behavior is more or less same as that of the $S_1/\langle S_1 \rangle$ distributions. In both interactions there are slight experimental excesses over the corresponding simulated distributions in the right side of the peak ($S_2/\langle S_2 \rangle > 1.0$). In the left side of the peak ($S_2/\langle S_2 \rangle < 1.0$) both the simulations exceed the experiment in the $^{16}\text{O-Ag/Br}$ case, whereas in the $^{32}\text{S-Ag/Br}$ case only the UrQMD over-predicts the experiment, whereas the experiment marginally exceeds the UrQMD+BEC distribution. The overall nature of the distributions of S -parameters indicates the presence of jet-like structures in the target azimuth, the contribution however is small.

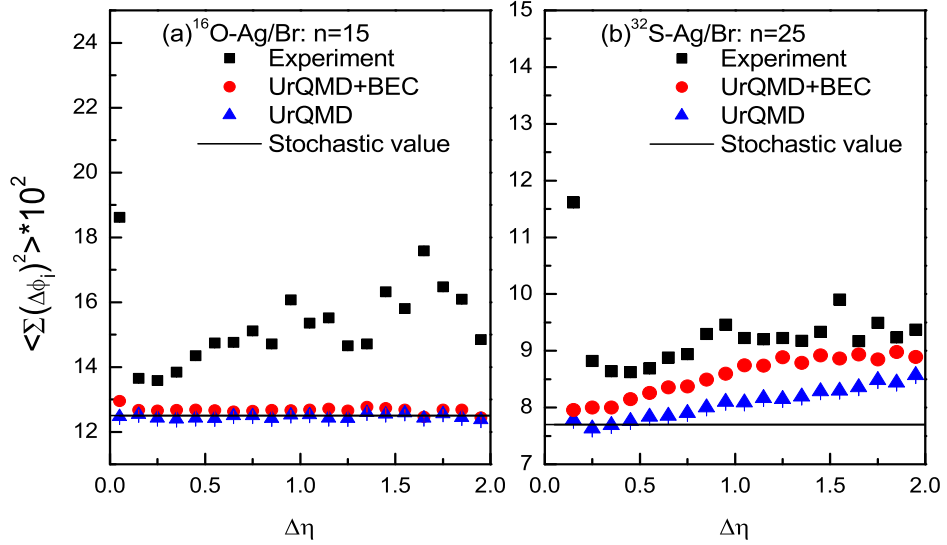


Figure 5.6: Same as in Figure 5.5 but for the S_2 parameter.

The variations of $\langle -\sum \ln(\Delta\varphi_i) \rangle$ and $\langle \sum (\Delta\varphi_i)^2 \rangle$ against $\Delta\eta$ are shown respectively, in Figure 5.5 and Figure 5.6 for both the interactions. Note that these quantities are different from the stochastic expectations values, $\langle S_1 \rangle$ and $\langle S_2 \rangle$. The dashed lines in these figures correspond to Equation (5.4). The UrQMD and UrQMD+BEC results are also included in these diagrams. One can see that the experimental values lie consistently above the stochastic expectation values. For the $^{16}\text{O-Ag/Br}$ interaction the simulated values of both parameters lie more or less around the corresponding stochastic expectation lines. On the other hand in the $^{32}\text{S-Ag/Br}$ case they are slowly increasing with $\Delta\eta$. At large $\Delta\eta$ the UrQMD+BEC values even lie in the range of the experiment. However, inadequacy of an independent emission model of the particles to replicate the experimental results is clearly visible in our analysis. It has been observed that to a large extent the experimentally observed average behavior of the S -parameters can be reproduced by the FRITIOF model calculation, where γ -conversion and the Hanbury-Brown-Twiss (HBT) effect have been included [11]. However, it has also been argued that before coming to a definite conclusion regarding such azimuthal structures, along with the average behavior of the S -parameters detailed distributions of some other relevant cluster parameters should be examined [15, 16].

The cluster size of the azimuthal substructures can be investigated with the help of their distributions against $\Delta\eta$. For both the interactions under our consideration, these distributions are plotted in Figures 5.7 and 5.8. A distinction between the ring and jet-like structures has been made by separating the $S_2/\langle S_2 \rangle < 1$ and $S_2/\langle S_2 \rangle > 1$ categories. These distributions are once again right skewed, having a rapid growth in the left to the peak followed by a comparatively slower fall on the right side. The width of the experimental distribution in each case is more or less same as that of the UrQMD and UrQMD+BEC distributions. For

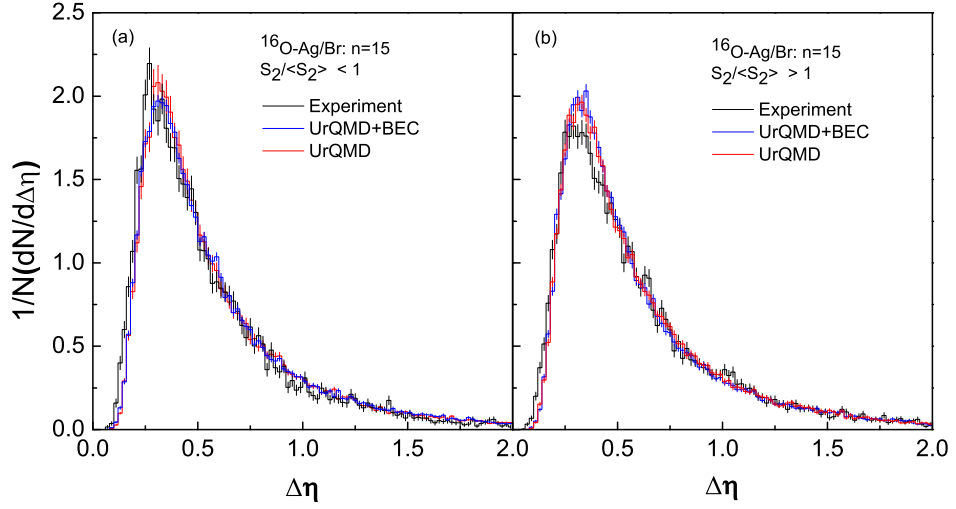


Figure 5.7: Cluster density distributions for (a) the ring-like region, $S_2/\langle S_2 \rangle < 1$ and (b) the jet-like region, $S_2/\langle S_2 \rangle > 1$ for ^{16}O -Ag/Br interactions at $200A$ GeV/c.

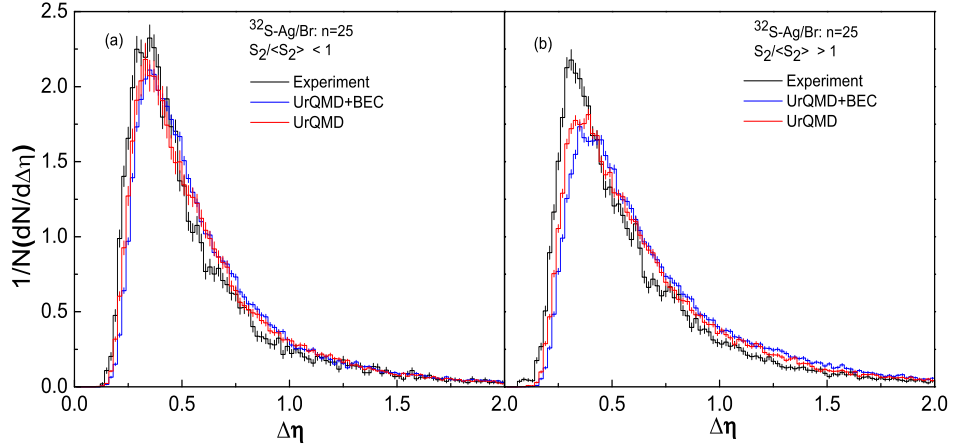


Figure 5.8: Same as in Figure 5.7 but for ^{32}S -Ag/Br interactions at $200A$ GeV/c.

both data sets one can see that small sized clusters around the peak region and to left of the peak region, have slight experimental excesses over the corresponding simulated data for the $S_2/\langle S_2 \rangle < 1$ category. On the other hand, clusters of large size (right to the peak) are either reproducible by the simulations or the simulations exceed the experimental values.

The location of jet and ring-like substructures can be investigated by studying the η_m -distributions of the S -parameters. Following the prescriptions of [15, 16] the distributions are divided into three categories, namely (i) $S_2/\langle S_2 \rangle < 0.95$, (ii) $0.95 \leq S_2/\langle S_2 \rangle \leq 1.1$ and (iii) $S_2/\langle S_2 \rangle > 1.1$. The ring-like, stochastic and jet-like structures, respectively dominate these three regions. Figure 5.9 and Figure 5.10 show the distributions of η_m for all three categories mentioned above. The average behavior of each distribution is roughly symmetric about a central value, which for each type of interaction is close to the corresponding central value of the basic η -distribution of the shower tracks. However, there are some small

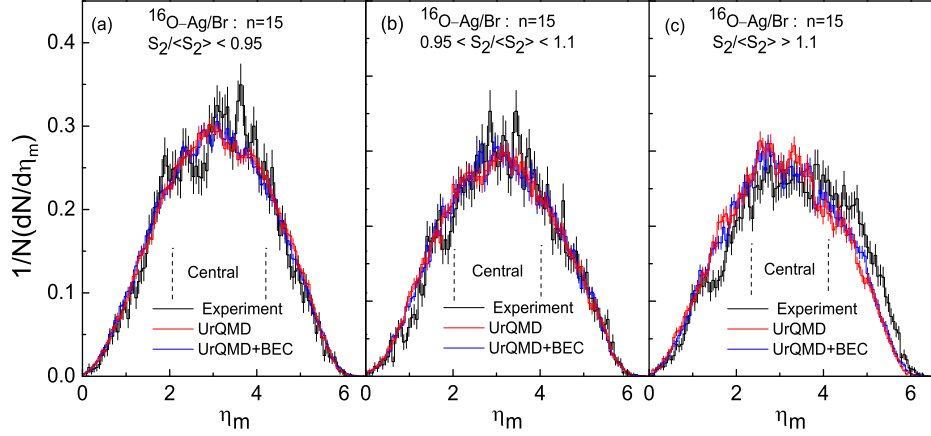


Figure 5.9: Comparison of the φ -subgroup position distributed along the η axis for three different regions of $S_2/\langle S_2 \rangle$ for ^{16}O -Ag/Br interaction at 200A GeV/c.

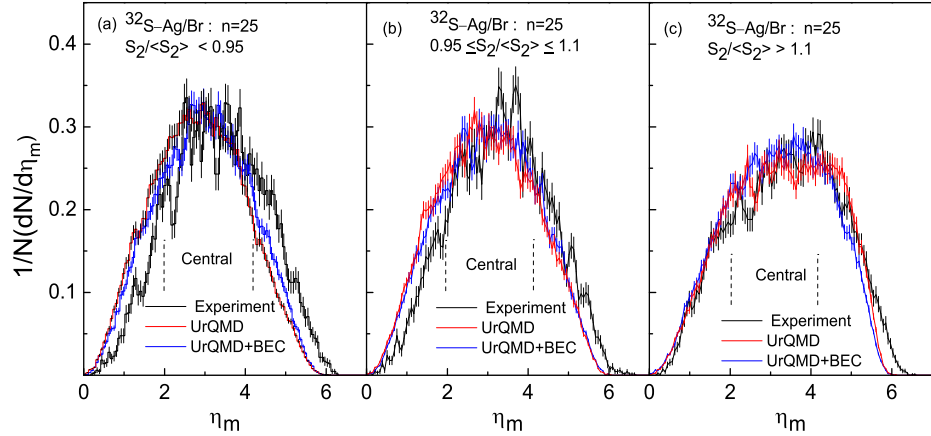


Figure 5.10: Same as in Figure 5.9 but for ^{32}S -Ag/Br interactions at 200A GeV/c.

experimental excesses beyond statistical uncertainties over the UrQMD and UrQMD+BEC simulations. For the $S_2/\langle S_2 \rangle < 0.95$ category of the ^{16}O -Ag/Br interaction, excess experimental counts are present in the form of several sharp and narrow spikes particularly around the central maximum and in the left to the central maximum regions. On the other hand for the ^{32}S -Ag/Br interaction, simulations show excess over experiment in the left to the central region, whereas in the right to the central region experiment shows excess over the simulations. The experimental excesses over the simulation can probably be attributed to ring-like substructure(s) of particle emission. However, the effect is not statistically very significant. Probably, by using a larger statistics and by choosing events for a particular centrality class, one could have reduced the noise that are otherwise present in the data. For the $0.95 \leq S_2/\langle S_2 \rangle \leq 1.1$ category, a few prominent narrow spikes are seen in the central region of the experimental distributions in both types of interactions, which cannot be replicated either by the UrQMD or by the UrQMD+BEC simulations. These structures are

more prominent in the ^{32}S induced interaction, the physical origin of which is not very much clear. For the $S_2/\langle S_2 \rangle > 1.1$ category, the experimental excesses are continuous and extend over a region of about 1 unit of η on the right-hand side of the central maxima of both interactions. This effect can be attributed to jet-like structures in the forward hemisphere.

5.4 Wavelet analysis

Wavelets are mathematical functions that can decompose signals into different frequency components so that one can study each component with a resolution matched to its scale. The mother wavelet is chosen according to the properties and patterns of the signal under consideration [6, 7]. If $\psi(x)$ is the mother wavelet then the continuous wavelet transform of a function $f(x)$ is given by,

$$W_\psi(a, b)f = \frac{1}{\sqrt{C_\psi}} \int_{-\infty}^{+\infty} f(x) a^{-1/2} \psi\left(\frac{x-b}{a}\right) dx \quad (5.5)$$

where the normalization constant

$$C_\psi = 2\pi \int_{-\infty}^{+\infty} |\tilde{\psi}(\omega)|^2 |\omega|^{-1} d\omega \quad (5.6)$$

and $\tilde{\psi}(\omega)$ is the wavelet transform of $\psi(x)$. Note that the wavelet $\psi(x)$ is characterized by a translation parameter b and a dilation parameter a . The coefficients $W_\psi(a, b)$ of the signal $f(x)$ can be interpreted as contributions of the wavelet $\psi\{(x-b)/a\}$ to the signal. Alternatively, $W_\psi(a, b)$ is a measure of the correlation between the function $f(x)$ and the mother wavelet $\psi(x)$ at the scale a and at location b . Higher correlation results in a larger coefficient and conversely. In our analysis the signal is the η -distribution of shower tracks. If we arrange the η -values of N number of tracks present in an event as $\eta_1, \eta_2, \dots, \eta_N$ etc., then the distribution of η can be expressed as,

$$f(\eta) = \frac{dn}{d\eta} = \frac{1}{N} \sum_{k=1}^N \delta(\eta - \eta_k) \quad (5.7)$$

For multiparticle data analysis derivatives of the Gaussian function like,

$$\Psi(x) \equiv g_n(x) = (-1)^{n+1} \frac{d^n}{dx^n} e^{-x^2/2} \quad (5.8)$$

are often used as mother wavelets. In particular the second derivative

$$g_2(x) = (1 - x^2)e^{-x^2/2} \quad (5.9)$$

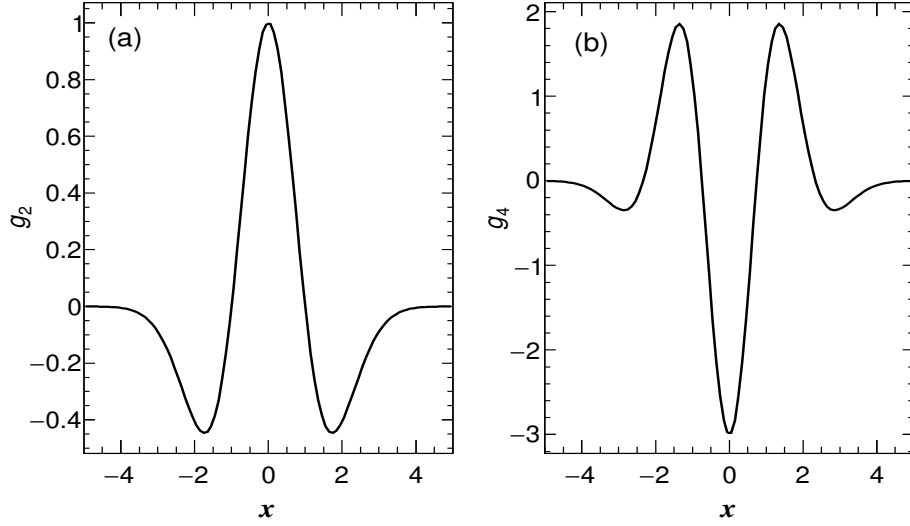


Figure 5.11: (a) Second derivative (Mexican hat wavelet) and (b) fourth derivative of the Gaussian function.

popularly known as the Mexican hat (MHAT) wavelet, and the fourth derivative

$$g_4(x) = -(x^4 - 6x^2 + 3)e^{-x^2/2} \quad (5.10)$$

are customarily used to analyze multiparticle emission data. In our analysis g_2 and g_4 are considered as the mother wavelets, the schematics of which are shown in Figure 5.11. The g_p ($p = 2$ and 4) wavelet transform of $f(\eta)$ is then given by [9],

$$W_{g_p}(a, b)f(\eta) = \frac{1}{N} \sum_{k=1}^N a^{-1/2} g_p \left(\frac{\eta_k - b}{a} \right) \quad (5.11)$$

The wavelet distributions of pseudorapidity spectra W_{g_2} are plotted in Figure 5.12 against the translation parameter b taken along the horizontal axis and the dilation parameter a taken along the vertical axis. The b -values are nothing but the locations of the particle clusters on the pseudorapidity axis. The values of wavelet coefficients are high where the gray-leveled scale has a lighter shade, and they are low where the distribution has a deeper shade. Large values of wavelet coefficient signify large number of particles crowding around a particular η -value. It is observed that the information about individual events are revealed in the small scales ($a < 0.1$), whereas in the large scales ($a > 0.5$) individual information is lost, indicating that more than one cluster combine to form a large group. For the same a -parameter, the wavelet distributions are of different intensities at different b -values, which indicates that the clustering of particles is not uniform at different locations. It is to be noted that three large groups of particles are centered around $\eta = 1.8, 2.6$ and 4.0 in the $^{16}\text{O-Ag/Br}$ events, and around $\eta = 2.2, 3.8$ and 5.2 in the $^{32}\text{S-Ag/Br}$ events. To further

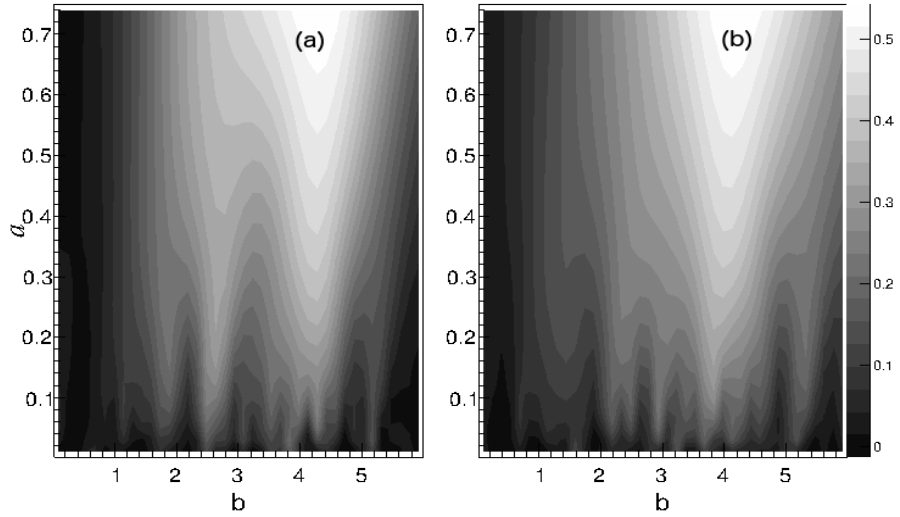


Figure 5.12: Wavelet coefficients $W_{g_2}(a, b)$ for a ^{16}O -Ag/Br event ($n_s = 202$) and a ^{32}S -Ag/Br event ($n_s = 276$) are plotted as functions of scale parameter a and translation parameter b [Equation (5.11)].

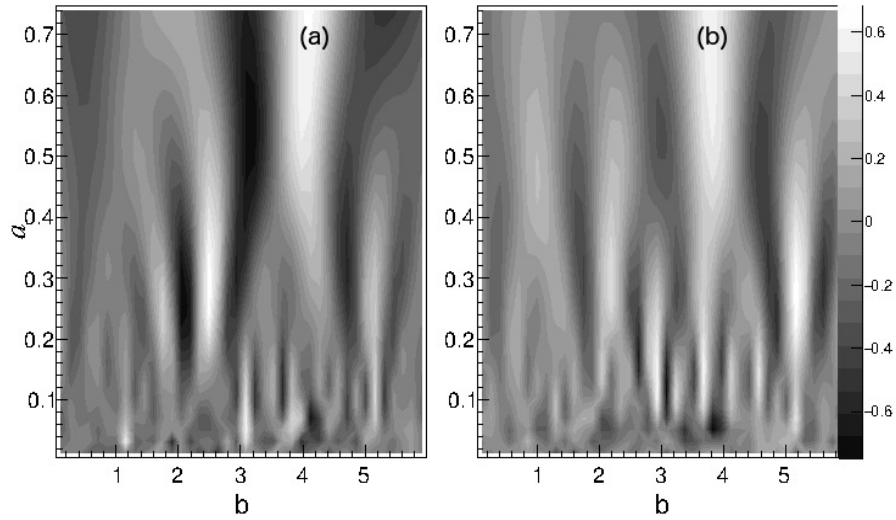


Figure 5.13: The same as in Figure 5.12 but for the g_4 wavelet.

scrutinize the cluster formation in our data, the g_4 wavelet spectra for the same events are plotted in Figure 5.13. One can see that for the ^{16}O -Ag/Br events the g_4 coefficients have several prominent maxima at $\eta = 1.2, 1.8, 2.6, 3.0, 4.0$ and 5.2 . For the ^{16}O -Ag/Br events, the local maxima of g_4 coefficients are connected with the positions of the centers of the group of particles at $\eta = 1.8$ and 2.6 in the scale range $a > 0.56$, and particles falling within $\eta = 3.0 - 4.6$ range are connected via their g_4 coefficient in the scale range $a > 0.4$. In the ^{32}S -Ag/Br events the clusterization of particles is observed at $\eta = 1.2, 2.0, 2.4, 3.0, 3.2, 3.6, 4.2, 4.6$ and 5.2 . Groups of particles having centers at $\eta = 2.0$ and 2.4 , at $\eta = 3.6, 4.2$

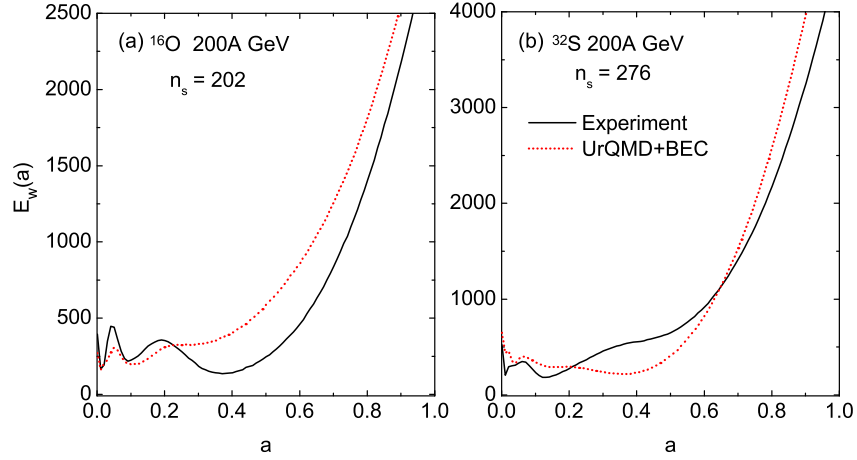


Figure 5.14: Scalograms of the events for which the g_2 wavelets are shown in Figure 5.12.

and 4.6 and the particles in the $\eta = 5.0 - 5.2$ range are connected by their wavelet maxima in the scale range $a > 0.36$. The minima at different pseudorapidity values correspond to disintegration of larger groups. Therefore, using the g_2 and g_4 spectra we can examine the cluster properties of particles at different pseudorapidity locations and at appropriate pseudorapidity resolutions. The most dominant scale at which the clusters are formed, can be obtained from the scalogram, defined as,

$$E_w(a) = \int W_{g_2}(a, b)^2 db \quad (5.12)$$

Some of the characteristic features of an event are also reflected in a scalogram. As for example, a local minimum on a scalogram represents the average distance between the particle clusters, while a local maximum signifies the most compact group of particles. Figure 5.14 shows the scalograms for the same ^{16}O -Ag/Br and ^{32}S -Ag/Br events for which the contour plots of W_{g_2} and W_{g_4} coefficients are shown respectively in Figures 5.12 and 5.13. For each event the experimental result is compared with the corresponding UrQMD+BEC simulation. In the ^{16}O -Ag/Br event the maxima occur at $a \approx 0.04$ and 0.2, whereas the minima occur at $a \approx 0.01$ and 0.1. In the ^{32}S -Ag/Br event the maxima occur at $a \approx 0.06$ and 0.37, while the minima occur at $a \approx 0.01$ and 0.12. For both the events UrQMD+BEC simulation cannot match the experiment satisfactorily. We have checked that most of the local maxima (minima) in the event samples are found within $0.05 \leq a \leq 0.5$ range, and in most of the events only a few such maxima (minima) are found.

In a wavelet analysis the g_2 spectrum plays an important role, as it can detect the coarse structures of the signal, event-wise pseudorapidity distributions in the present case. In Figure 5.15 the g_2 spectra, obtained respectively for the ^{16}O -Ag/Br and ^{32}S -Ag/Br interactions at 200A GeV/c are schematically presented. For each event sample the spectra are plotted

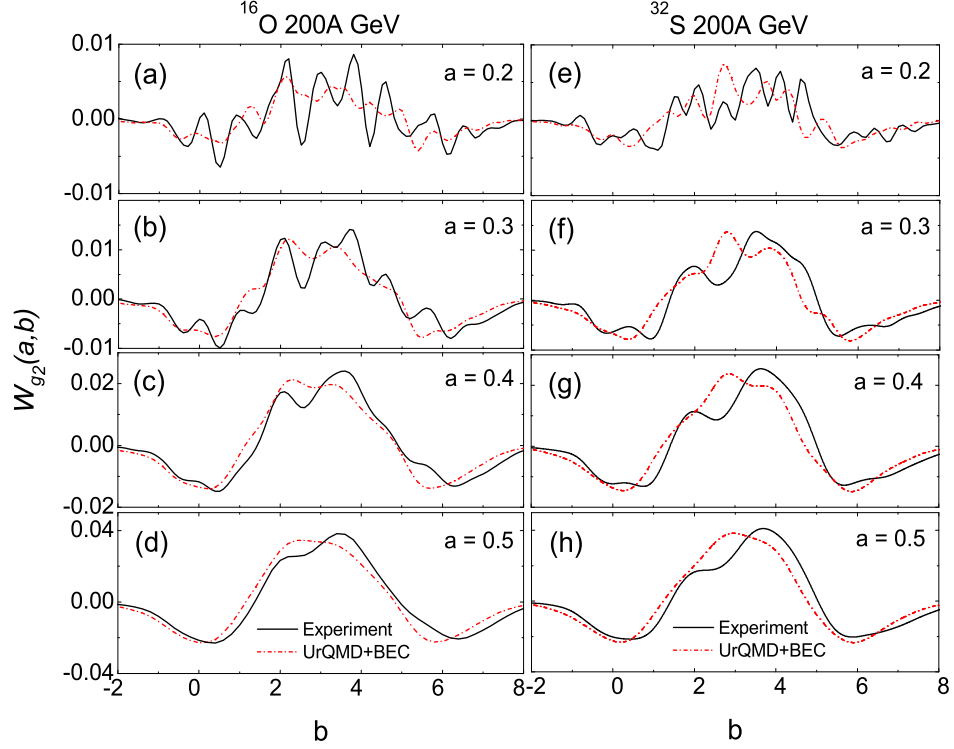


Figure 5.15: g_2 wavelet pseudorapidity spectra for ^{16}O (left) and ^{32}S (right) interactions for different values of scale parameter a . In both the cases the experimental results are compared with the corresponding UrQMD+BEC simulation.

at four different scales, $a = 0.2, 0.3, 0.4$ and 0.5 . For an easy comparison experimental results are plotted along with the corresponding UrQMD+BEC simulations. At small scale each spectrum fluctuates rapidly while with increasing scale size it gradually becomes more regular. Each distribution ultimately converges to the mother wavelet g_2 . Several peaks are seen within the $1 \leq b \leq 5$ range for both ^{16}O -Ag/Br and ^{32}S -Ag/Br experiments. Overall fluctuations in the simulated event samples are less rapid compared to the respective experiment, a fact that can clearly be noticed in Figure 5.15 at $a = 0.2$. The observed maxima of the spectra are associated with preferred pseudorapidity locations where cluster formation takes place. Clusters are present in the target fragmentation, central particle producing, and projectile fragmentation regions. The number of particles involved in separate groups can be estimated from the size of the area lying under the local maxima. To study the cluster formation further, we have graphically presented the g_4 -spectra for the ^{16}O -Ag/Br and ^{32}S -Ag/Br interactions in Figure 5.16. In each diagram the experimental and simulated results are compared. We see more rapid fluctuations than the g_2 spectra at a particular resolution. The locations of maxima (minima) are more or less in the same range of b as they are in the g_2 -spectra. In the g_4 -spectra there are however more number of peaks than that in the corresponding g_2 -spectra. The other features of the g_4 wavelet spectra are more or less same as that of the g_2 -wavelet. Peaks in the target fragmentation, the central

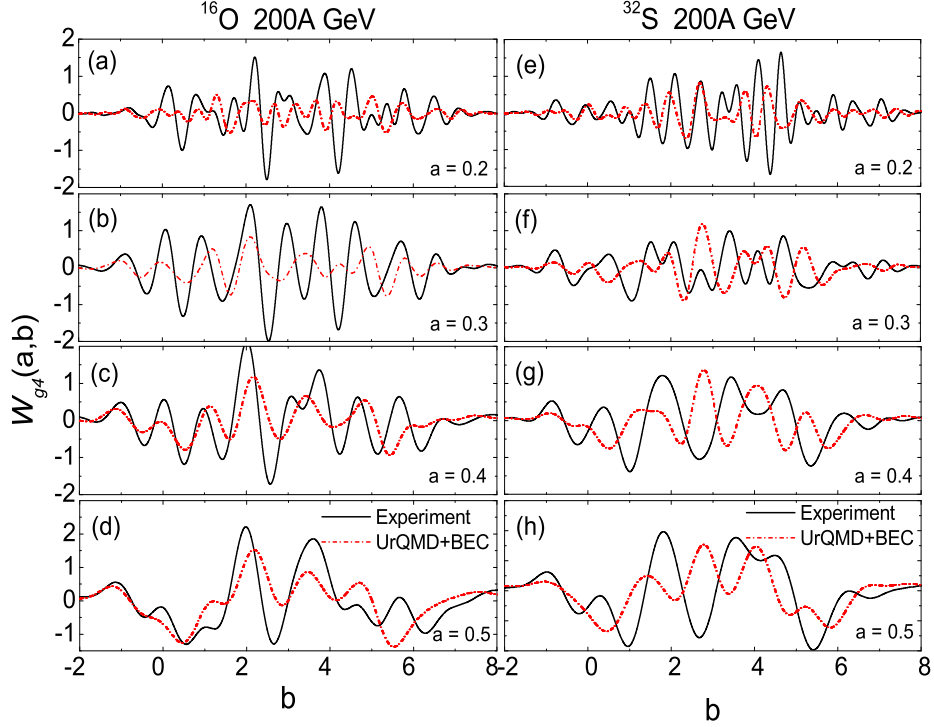


Figure 5.16: The same as in Figure 5.15 but for the g_4 wavelet.

particle producing, and projectile fragmentation regions are clearly observed in the wavelet g_4 -spectra too for both interactions. In this case also the simulated results cannot exactly replicate the experimental results.

The results described above enable us to fix the characteristic scales and the preferred pseudorapidity locations where particle clusters are formed. Using the scalograms we can further examine whether the maxima (minima) occurring in individual events have any systematic behavior or they are occurring at random. We need to study the distributions of the scale parameter, denoted by a_{\max} (a_{\min}), at which such maxima (minima) occurs. Frequency distributions of a_{\max} and a_{\min} are plotted in Figures 5.17 and 5.18, respectively for the ^{16}O -Ag/Br and ^{32}S -Ag/Br interactions with two different bin widths i.e. $\Delta a_{\max/\min} = 0.02$ and $\Delta a_{\max/\min} = 0.04$. In order to better understand the mechanism of cluster formation, experimental results are compared with the UrQMD+BEC simulation. No appreciable difference between the experiment and the corresponding simulation can be seen in these distributions. As such no significant difference in the nature of $a_{\max(\min)}$ distribution is observed between the ^{16}O -Ag/Br and ^{32}S -Ag/Br interactions either, except that the tail of the distributions are stretched a bit more in the ^{16}O -Ag/Br rather than in the ^{32}S -Ag/Br case. Both a_{\max} and a_{\min} distributions are peaked at a very small value like, $a_{\max/\min} \approx 0.1$. The diagrams suggest that the cluster size is always less than one pseudorapidity unit, which perhaps indicates dominance of short range correlations in the data. In the framework of the UrQMD

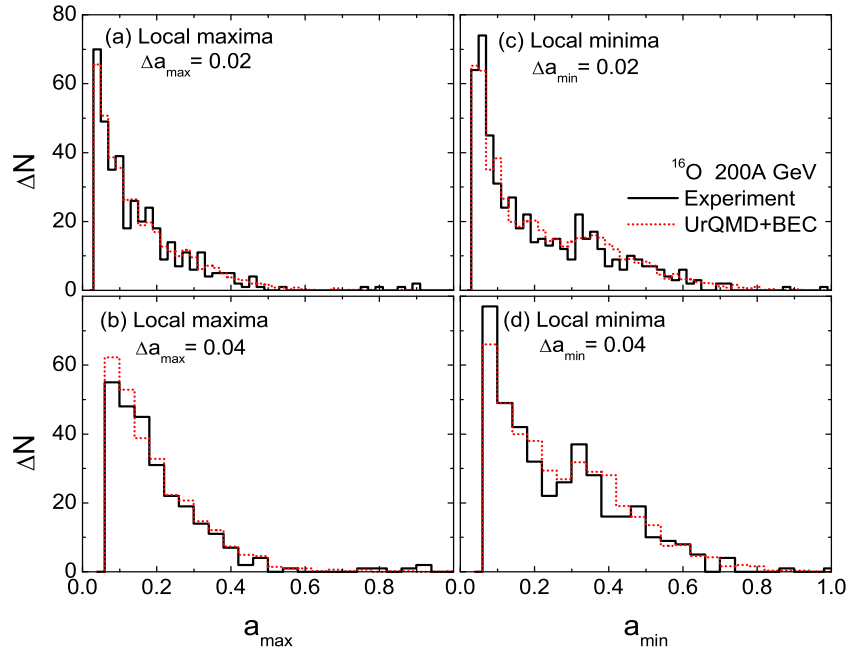


Figure 5.17: Distributions of the local maxima (left) and the local minima (right) of the scalograms in ^{16}O -Ag/Br interactions at 200A GeV/c.

model short range correlations are manifested because of resonance decays, jet fragmentation etc. The pseudorapidity values preferred by the particle clusters are represented by the local maxima seen in the pseudorapidity distributions. This signature is magnified in the

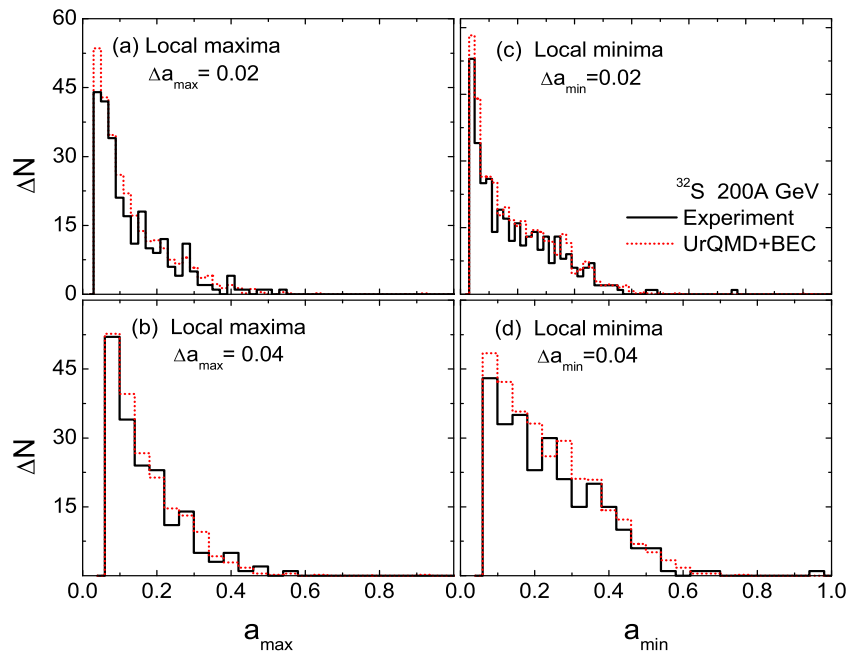


Figure 5.18: The same as in Figure 5.17 but for the ^{32}S -Ag/Br interactions.

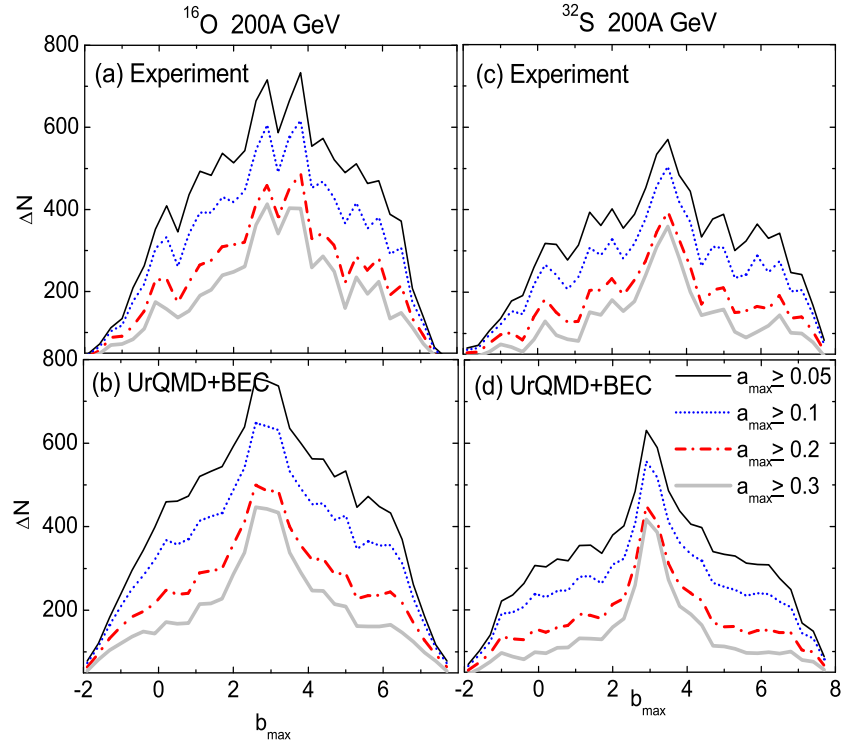


Figure 5.19: Distributions of b_{\max} for different values of a_{\max} cut in ^{16}O -Ag/Br (left) and ^{32}S -Ag/Br (right) interactions at $200A$ GeV/c. In the lower panel shown are the results from the UrQMD+BEC simulations.

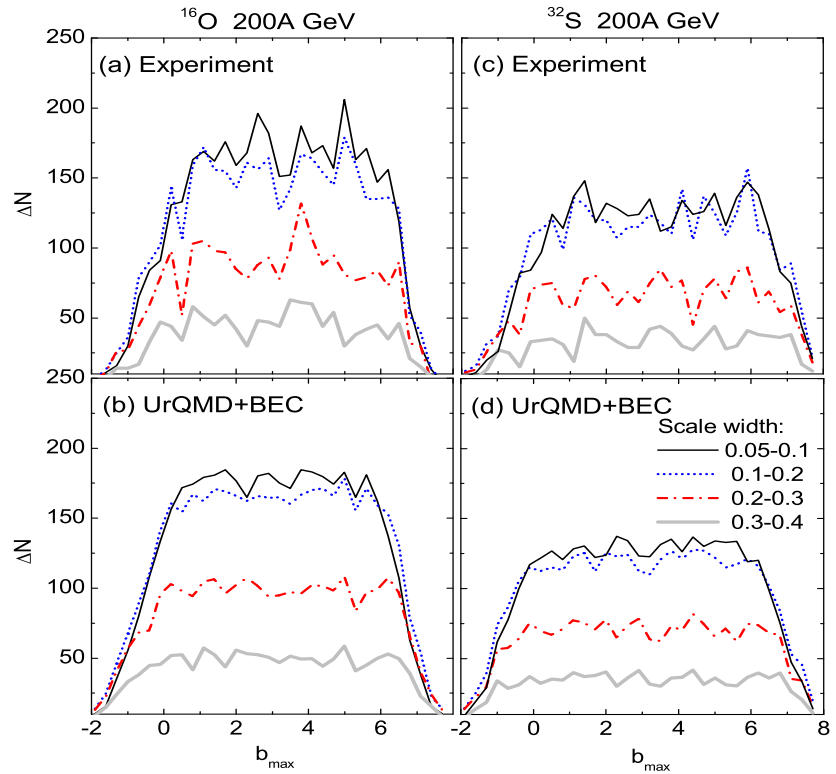


Figure 5.20: The same as in Figure 5.19 but for different scale windows (Δa_{\max}).

distributions of b_{\max} , which actually is the pseudorapidity coordinate of the wavelet maxima $W_{g_2}(a_{\max}, b_{\max})$. We examine the b_{\max} distribution with the help of different choices of a_{\max} cut as well as using different scale intervals. Such distributions for the $^{16}\text{O-Ag/Br}$ and $^{32}\text{S-Ag/Br}$ event samples (both experiment and simulation) are graphically presented in Figure 5.19. It is clear that with increasing a_{\max} the fluctuations get reduced and the patterns become smooth. For all the scale intervals the peaks however remain fixed at the same position. In comparison with the experiment, perhaps due to a larger statistics the UrQMD+BEC distributions vary less rapidly. Otherwise no significant difference between either the experimental and the corresponding simulated distributions, or between the two interactions considered are seen. In Figure 5.20, we plot b_{\max} -distribution for different scale intervals for the experimental and simulated event samples for both interactions. As expected, in all the cases the fluctuations are more in the scale interval $0.05 \leq a \leq 0.1$, which get reduced with increasing a .

5.5 Summary

From the azimuthal structure analysis we find that the average behavior of the S -parameters exhibits unusual structures in both $^{16}\text{O-Ag/Br}$ and $^{32}\text{S-Ag/Br}$ interactions that are limited in narrow regions of η and/or φ -space. Small but significant experimental departure from independent emission model, particularly at small $\delta\eta$ are seen. This suggests that short range correlations are present in the experimental data. In this regard our observation matches with another similar experiment where nuclear emulsion technique was used [11]. A closer look at the distributions of structure size ($\Delta\eta$) and their positions (η_m) indicates that features pertaining to both ring-like and jet-like structures are present in our data samples that cannot be fully reproduced by a simple random number generated independent emission model. The effects however, are always not too strong in either type of interaction concerned. Within the framework of the Cerenkov gluon emission model [1] we can therefore, conclude that in some events there are only a few emitted gluons, whereas in some other their numbers are large. It would be a worthwhile exercise to determine either the nuclear refractive index or the speed of the sound wave in the fireball medium, either of which can further be utilized to find out a proper equation of state of the hadronic/partonic matter.

In the wavelet analysis once again we find significant differences between the experiment and corresponding UrQMD+BEC simulation. For all the parameters studied in connection with the g_2 and g_4 wavelets, usually larger and somewhat ordered fluctuations are observed in both $^{16}\text{O-Ag/Br}$ and $^{32}\text{S-Ag/Br}$ experimental data samples. These differences should be interpreted in terms of certain nontrivial dynamical reason(s), like short range correlation. A detailed and more involved analysis in a higher-dimensional phase space is necessary to

unravel the dynamics of cluster formation more clearly. However, we understand that the wavelet analysis is a powerful statistical tool for an event-by-event analysis of fluctuation patterns in high-energy nuclear collisions.

Bibliography

- [1] I. M. Dremin, *Pis'ma Zh. Eksp. Teor. Fiz.* 30, 152 (1979).
- [2] A. E. Glassgold, W. Heckrotte, K. M. Watson, *Ann. Phys.* 6, 1 (1959).
- [3] I. M. Dremin, *Yad. Fiz.* 33, 1357 (1981).
- [4] I. M. Dremin, *Pis'ma Zh. Eksp. Teor. Fiz.* 34, 594 (1981).
- [5] I. M. Dremin, *Nucl. Phys. A* 467, 233 (2006).
- [6] I. Daubechies, *Ten Lectures on Wavelets: Society for Industrial and Applied Mathematics, Philadelphia* (1992).
- [7] J. C. Van Den Berg (ed.), *Wavelets in Physics: Cambridge University Press* (2004).
- [8] D.-W. Huang, *Phys. Rev. D* 56, 3961 (1997).
- [9] V. V. Uzhinsky *et al.*, *Phys. of Atom. Nucl.* 67, 156 (2004).
- [10] A. B. Apanasenko *et al.*, *Pis'ma Zh. Eksp. Teor. Fiz.* 30, 157 (1979).
- [11] M. I. Adamovich, *et al.* (EMU01 Collaboration), *J. Phys. G* 19, 2035 (1993).
- [12] A. El-Naghy, K. S. Abdel-Khalek, *Phys. Lett. B* 299, 370 (1993).
- [13] G. L. Gogiberidge *et al.*, *Nucl. Phys. B (Proc. Suppl.)* 92, 75 (2001);
- [14] G. L. Gogiberidge, L. K. Gelovani and E. K. Sarkisyan, *Phys. Atom. Nucl.* 64, 143 (2006); *Phys. Lett. B* 430, 368 (1998).
- [15] S. Vokál *et al.*, *Phys. Atom. Nucl.* 71, 1395 (2008).
- [16] S. Vokál, G. I. Orlova and S. Lehocká, *Phys. Atom. Nucl.* 72, 237 (2009).
- [17] G. I. Orlova, *et al.*, *Proc. International Conference Hadron Structure 2002, Herľany, Slovakia, 2002* (P. J. Šafárik Univ., Košice, 2003), p. 155.
- [18] A. Sh. Gaitinov *et al.* (EMU12), *Talk given at XVII. Meeting of the EMU01 Collaboration, Dubna, Russia, May 18-20 (1999).*

-
- [19] S. Vokál, A. Vokálová *et al.*, Proc. Hadron Structure 2004, Smolenice castle, Slovakia, 30.8.-30.9 (2004).
- [20] P. Mali *et al.*, Int. J. Mod. Phys. E 23, 1450027 (2014).
- [21] N. Suzuki, M. Biyajima and A. Ohsawa, Prog. Theor. Phys. 94, 91 (1995).
- [22] Z. Huang *et al.*, Phys. Rev. D 54, 750 (1996).
- [23] B. K. Nandi *et al.* (WA98 Collaboration), in Proc. of the 3rd Intern. Conf. on Physics and Astrophysics of Quark-Gluon Plasma, Jaipur, India, (1997).
- [24] T. H. Burnett *et al.*, Phys. Rev. Lett. 50, 2062 (1983).
- [25] I. M. Dremin, Physics - Uspekhi 43, 1137 (2000).
- [26] O. D. Chernavskaya *et al.* (EMU15 Collaboration), Proc. 24th ICRC, Rome (1996).
- [27] N. M. Astafyeva, I. M. Dremin, K. A. Kotelnikov, Mod. Phys. Lett. A 12, 1185 (1997).
- [28] J. Fedorišin and S. Vokál, JINR Preprint E1-2007-4., Dubna, (2007).
- [29] P. Mali *et al.*, Adv. High Eng. Phys. 2013, 1 (2013).
- [30] J. Fedorišin and S. Vokál, Fizika B 17, 273 (2008).
- [31] E. Stenlund, *et al.* (EMU01 Collaboration), Nucl. Phys. A 498, 541c (1989).

Chapter 6

Multiplicity fluctuation and forward-backward multiplicity correlation

6.1 Introduction

The multiparticle emission data obtained from the RHIC and LHC experiments have inspired many to investigate the fluctuations of particle densities in nuclear collisions, and to examine the rapid formation of QGP that expands hydrodynamically with very low specific viscosity [1, 2]. The initial density fluctuations are found to transfer very efficiently into collective flow correlations in the momentum space. Experimental measurement of such correlations provide us therefore, with an opportunity to look into the space-time evolution of the collective expansion as well as the medium properties that drives such expansion. Observables like e-by-e fluctuations of the charged hadron multiplicity, fluctuations of dynamical variables like the total transverse momentum (p_t) or total rapidity (y) of particles per event, and correlations among these particles, are often used as statistical tools for such kind of investigations. The equation of state of the fireball matter is sensitive to the above mentioned fluctuation and correlation measures. The initial state density fluctuations are also studied in the longitudinal direction [3]. The longitudinal fluctuations are directly related to the entropy production at the early stages of the collision, well before the onset

of the collective flow, and in terms of the multiplicity of produced particles they appear as long-range correlations well separated in the rapidity (y) or pseudorapidity (η) space. On the other hand, short-range correlations are usually generated through resonance decays, jet fragmentation and Bose-Einstein correlations. The short-range correlations are localized over a relatively smaller range of y or η , and are sensitive to the final-state effects. Recently short range correlations between two hard knocked nucleons has been studied by using the inverse kinematics in the Baryonic Matter at Nuclotron (BM@N) experiment conducted at the Nuclotron-based Ion Collider (NICA) facility at Joint Institute of Nuclear Research at Dubna, Russia [4]. The results have significant implications in nuclear, high-energy and astro-particle physics.

In this chapter we report some results on the short and long-range longitudinal correlations, and e-by-e fluctuations of charged particle multiplicities. The observables of our interest are the correlation among singly charged particles emitted in the forward and backward hemispheres of the η -space [5], a roughness parameter associated with the η -distributions of the singly charged particles produced [6], the scaled variance of charged particles [7, 8], and an e-by-e fluctuation measure of the charged particle multiplicities [9, 10]. We analyze the particle emission data obtained from ^{16}O -Ag/Br and ^{32}S -Ag/Br interactions at an incident beam energy of 200A GeV. Following the trend of our analysis we systematically compare the experimental results with the UrQMD simulation [11, 12]. The Bose-Einstein correlation (BEC), considered to be the major source of short-range correlations among identical bosons, has been mimicked into our simulated data sample(s) as an after-burner by using a charge reassignment algorithm [13]. The objectives are, (i) to study the longitudinal dynamics of short and long-range particle correlations generated by the density fluctuations at the early stages of collisions, (ii) to confirm the presence of dynamical fluctuations in the particle emission data by using standard statistical methods, (iii) to set a reference baseline for the experimental measures by using a hadronic transport model like the UrQMD, (iv) to examine the degree of mismatch between the experiment(s) and simulation(s), and (v) to check if that can be compensated by mimicking the BEC into our simulated data.

6.2 Literature review

Large density of particles produced within a narrow region of η is traditionally called a spike, which was first observed by the JACEE collaboration in very high-energy cosmic-ray events [14]. Since that observation several statistical techniques have been developed, some of which are already discussed in the previous chapters of this thesis, to understand the spike structures in the pseudorapidity distributions of JACEE events. However, a systematic comparison of the experimental density fluctuations with model simulations may

bring out some useful information related to multiparticle production [6, 15–17]. While large multiplicity fluctuations could be a signal of particle production via clusters [18] or super-cooled droplets of QCD matter [19], small fluctuations in the final state of conserved charges, electric or baryonic, are seen when the fluctuations generated in the plasma phase are frozen due to rapid expansion of the fireball system [20]. It was found that if the hot and dense fireballs hadronize near the critical QCD end-point, significant transverse momentum and multiplicity fluctuations would be observed [21]. In this line the lattice calculations are presented in [20, 21]. The results on electric charge and transverse momentum fluctuations, particularly in terms of the Φ -measure [9, 10], are presented in [22, 23]. Though, on several occasions the Φ -measure is used to quantify the p_t and net-charge fluctuations only [24–26], in this analysis we have used it to measure the fluctuations in the η -space.

In several studies on the forward-backward (FB) correlation of particle multiplicities like in e^+e^- [27], pp [28–31] and AB [32, 33] collisions, significant correlation between the forward and backward multiplicities have been observed. The PHOBOS collaboration at RHIC have studied the FB multiplicity correlation in Au+Au interaction at $\sqrt{s_{NN}} = 200$ GeV [32]. Aziz *et al.* [34] proposed a model to extract the effective cluster multiplicity K_{eff} from the PHOBOS data. The K_{eff} -values were found to be 2.2 for the 0 – –20% centrality, and 2.7 for the 40 – –60% centrality intervals. These values surely exceed the prediction of a hadron resonance gas (HRG) model which reported $K_{\text{eff}} \approx 1.5$ [35]. The STAR Au+Au collision results at top RHIC energy showed that the FB correlation strength decreases rapidly from central to peripheral interactions [33]. The UrQMD prediction matches the RHIC Au+Au data for the peripheral collisions while the model overestimates the experimental results for the central collisions. The HIJING model however, exhibits an opposite behavior of the UrQMD [36]. Recently, a study on multiplicity correlations has been generalized by decomposing the correlation function into orthogonal Legendre polynomial functions, more generally into the principal components, each representing a unique component of the measured FB correlation [37, 38]. Particle production in pp collisions is usually described by the QCD-inspired models like PYTHIA [39] and EPOS [40]. Previous studies show that these models can grossly describe the pseudorapidity and transverse momentum dependence of the inclusive charged-particle spectra [41], as well as the underlying dynamics accompanying various hard-scattering processes [42]. In many such models, events with large charged-particle multiplicities are produced through several multi-parton interactions (MPI), which naturally serves as sources for the FB multiplicity asymmetry described above. Presence of long-range FB correlation has been predicted in the Dual Parton model (DPM) and in the Color Glass Condensate (CGC)/Glasma model [43, 44], both of which contain one form of the color flux tubes or the other, e.g. color strings in the DPM and Glasma flux tubes in the CGC, that actually lead to long-range correlations [45].

6.3 Roughness in η -distribution

A standard χ^2 test has been performed to investigate the roughness present in the single particle pseudorapidity distributions. The method has been elaborated in [6]. Accordingly, if n_{ik} is the number of shower tracks emitted in the i -th η -bin of the k -th event, $\langle n_i \rangle = N_{\text{ev}}^{-1} \sum_k n_{ik}$ is the event sample averaged multiplicity in the i -th bin, and $n_k = \sum_i n_{ik}$ is the corresponding multiplicity of the k -th event, then the χ^2 value for the k -th event is defined as,

$$\chi_k^2 = \sum_{i=1}^M (n_{ik} - \langle n_i \rangle)^2 / \sigma_{ik}^2 \quad (6.1)$$

Here M is the number of η -bins and $\sigma_{ik} = \sqrt{n_{ik}}$ is the statistical error associated with n_{ik} . χ_k^2 is sensitive to the e-by-e fluctuations in the shower track multiplicity per event with respect to its event sample averaged value $\langle n_k \rangle$. Therefore, another variable γ_k^2 , which depends only on the shape of the single particle η -distribution, is introduced as,

$$\gamma_k^2 = \sum_{i=1}^M \left(n_{ik} - \frac{n_k}{\langle n_k \rangle} \langle n_i \rangle \right)^2 / \sigma_{ik}^2 \quad (6.2)$$

γ_k^2 measures the roughness of the η -distribution function. A large value of γ_k^2 implies that n_{ik} is far from its event sample mean $\langle n_i \rangle$, thereby denoting a probable cluster of particles. In the above $\langle \rangle$ denotes an averaging over the entire event sample.

The probability distributions of γ_k^2 for our experiments are compared with the respective UrQMD simulations in Figure 6.1. The presence of spikes, i.e. high probabilities of finding

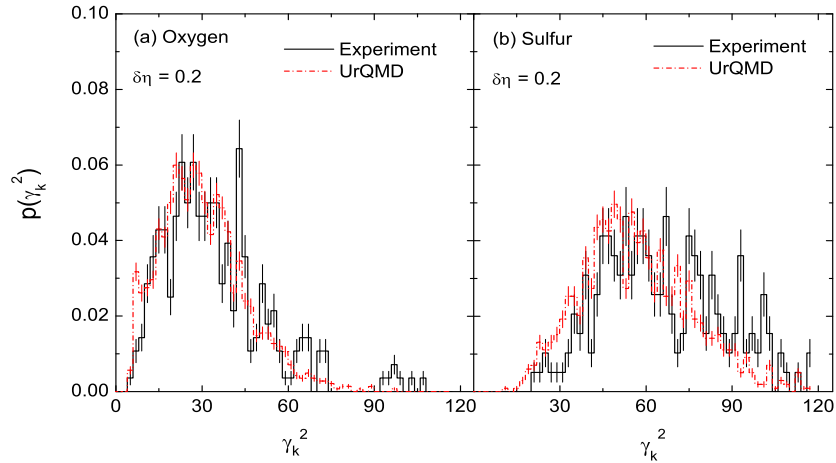


Figure 6.1: Distributions of γ_k^2 for pseudorapidity bin $\delta\eta = 0.2$.

γ_k^2 -values within a narrow $\delta\eta$, as well as valleys are quite prominent in these distributions. In particular, spikes are seen in several places in the large γ_k^2 -region of each experimental

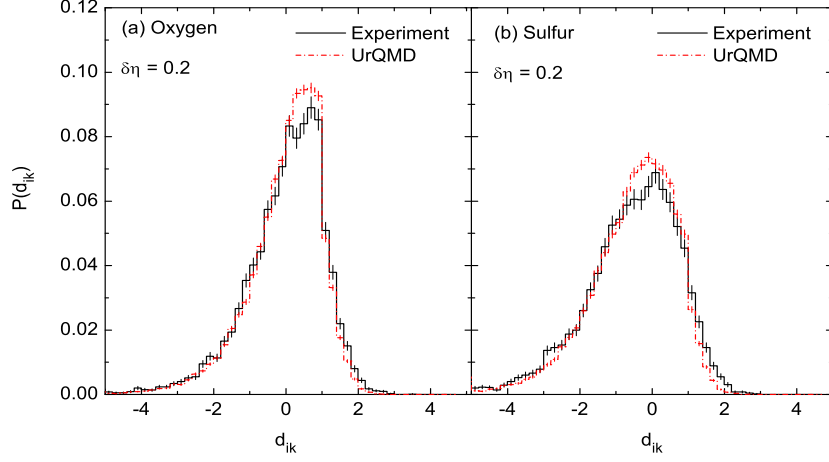


Figure 6.2: Distributions of d_{ik} for pseudorapidity bin $\delta\eta = 0.2$.

distribution, which the corresponding simulation could not match. Such fluctuations may arise due to (a) statistical reasons, (b) kinematic constraints, (c) BEC between identical particles, or (d) some non-trivial dynamics associated with multiparticle production. The mean and standard deviation values of the γ_k^2 -distributions are calculated for two pseudorapidity bin widths i.e. $\delta\eta = 0.1$ and 0.2 , and their values are listed in Table 6.1. We see that the $\langle\gamma_k^2\rangle$ and $\sigma(\gamma_k^2)$ -values for the experiment are consistently greater than, though not significantly different from, the simulated values. For both the interactions the UrQMD+BEC simulations yield slightly larger values of parameters than the UrQMD generated values. There is an indication that by mimicking BEC into our simulations we may to some extent, though not completely, account for the particle correlations. The $\langle\gamma_k^2\rangle$ and $\sigma(\gamma_k^2)$ values calculated for $\delta\eta = 0.1$ are higher than the corresponding values obtained for $\delta\eta = 0.2$. A larger η -window perhaps smooths out the roughness present in the e-by-e fluctuation. In this regard an obvious and significant projectile mass dependence in the results is observed from Table 6.1. We next find out large local densities of particles that correspond to large entropy contained within small domains of η -space. The parameter [6],

$$d_{ik} = \left(n_{ik} - \frac{n_k}{\langle n_k \rangle} \langle n_i \rangle \right) / \sigma_{ik} \quad (6.3)$$

measures the deviation in the particle number from its event average in the i -th bin of width $\delta\eta$ of the k -th event, and therefore, it also measures the fluctuation in the local density of particle number. The probability distributions of d_{ik} for the ^{16}O -Ag/Br and ^{32}S -Ag/Br experimental data are compared schematically with the respective simulations in Figure 6.2. We have noted that in terms of the single particle distributions, the UrQMD and UrQMD+BEC predictions are quite identical. Therefore, in this diagram only the UrQMD generated distributions are plotted against the respective experiment. For both

Table 6.1: The values of $\langle \gamma_k^2 \rangle$ and $\sigma(\gamma_k^2)$ for the ^{16}O - and ^{32}S -induced Ag/Br interactions at 200A GeV/c. The values are calculated for pseudorapidity window $\delta\eta = 0.2$ and 0.1.

Data	^{16}O -Ag/Br		^{32}S -Ag/Br	
	$\langle \gamma_k^2 \rangle$	$\sigma(\gamma_k^2)$	$\langle \gamma_k^2 \rangle$	$\sigma(\gamma_k^2)$
$\delta\eta = 0.2$				
Experiment	34.58 ± 1.09	18.26 ± 0.77	66.38 ± 1.61	23.47 ± 1.13
UrQMD	30.41 ± 0.39	14.74 ± 0.74	57.55 ± 0.66	20.15 ± 0.47
UrQMD+BEC	31.19 ± 0.42	15.73 ± 0.29	59.28 ± 0.60	20.83 ± 0.42
$\delta\eta = 0.1$				
Experiment	39.17 ± 1.33	22.26 ± 0.77	83.40 ± 2.24	31.71 ± 1.58
UrQMD	36.33 ± 0.51	19.20 ± 0.74	78.72 ± 1.07	30.35 ± 0.71
UrQMD+BEC	37.91 ± 0.37	19.91 ± 0.37	79.67 ± 0.59	30.67 ± 0.59

types of interactions probability distributions of d_{ik} are smooth and slightly left-skewed. The simulated distribution functions, perhaps due to their larger statistics, are smoother than the respective experimental distribution. In the peak region of the distribution of each type of interaction, the UrQMD prediction slightly exceeds the experiment. The experiment and the simulated data do not otherwise differ very significantly.

6.4 Forward-backward multiplicity correlation

In high-energy collisions multiparticle production takes place mainly through two different classes of sub-processes. One of them consists of soft processes that can be explained in terms of multiple parton interactions at low p_t . Processes of this kind are often characterized by correlations in the local particle number density $\rho(\eta) = N_{\text{ev}}^{-1} (dn_{\text{ch}}/d\eta)$ that usually extends over a long η -range [46]. On the other hand, at high p_t values hard perturbative processes like radiative transitions or parton scattering take place through single and/or a few-parton exchange. These processes generate particle jets, which by definition are characterized by short-range correlations. Such processes are associated with high multiplicity, found typically within a unit of η or so, and quickly diminish with increasing η -gap. Thus a soft process results in a smaller particle multiplicity with weaker correlation prevailing over a wider η -separation, the so-called long-range correlation. In comparison, hard processes result in a small number of jets that are characterized by a high multiplicity within a small η -interval, the so called short-range correlation. As the p_t value increases above a few hundred MeV, there is a gradual transition from the soft to the hard processes. Therefore, particle correlations examined as a function of separation in the η -space and η -interval size, can be used to measure the contribution of each category of sub-processes mentioned above. Forward-backward (FB) correlation measure as a function of rapidity (y) or pseudorapidity

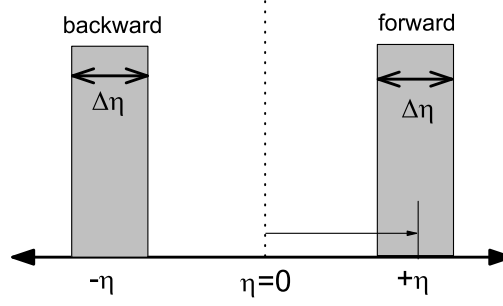


Figure 6.3: A schematic diagram showing how the forward and backward windows are selected in η -distribution.

(η) can be used to examine the longitudinal characteristics of the fireball system produced in high-energy AB interactions.

We consider two η -windows of width $\Delta\eta$ each at positions $\pm\eta$, located symmetrically about the centroid of the overall η -distribution of the event sample. A schematic diagram in Figure 6.3 describes the above consideration. Let the number of charged particles in the forward window be denoted by n_f and that in the backward window be denoted by n_b . For correlated emission of particles, one observes the following linear dependence [47],

$$\langle n_b \rangle = a + b n_f \quad (6.4)$$

Here b is a measure of the correlation strength. The FB-correlation is also measured in terms of a FB-asymmetry parameter (C) defined as,

$$C = \frac{n_f - n_b}{\sqrt{n_f + n_b}} \quad (6.5)$$

The variance of charged particle multiplicities is then given by $D_{qq} = \langle n_q^2 \rangle - \langle n_q \rangle^2$, where $q = f$ for the forward and $q = b$ for the backward window, and $\langle \rangle$ stands for an averaging over the event sample. The covariance of n_f and n_b is defined as $D_{fb} = \langle n_f n_b \rangle - \langle n_f \rangle \langle n_b \rangle$. The fluctuation in C can be expressed in terms of the variance and covariance of the asymmetry parameter as [5],

$$\sigma_c^2 = \frac{D_{ff} + D_{bb} - 2D_{fb}}{\langle n_f + n_b \rangle} \quad (6.6)$$

In principle σ_c^2 should have contributions from both short and long-range correlations [34]. The short-range contribution comes from particle production due to cluster decay. A cluster in general can be a resonance state, a partonic jet or a QGP droplet. When $\Delta\eta$ is larger than the cluster size, all particles belonging to the cluster should be within that interval. The long-range contribution on the other hand, comes perhaps from the fragmentation of stretched color strings or color flux tubes that may be extended over a longer y or η -range. If the bins centered around $\pm\eta$ are largely separated in the η -axis, contribution of long-range

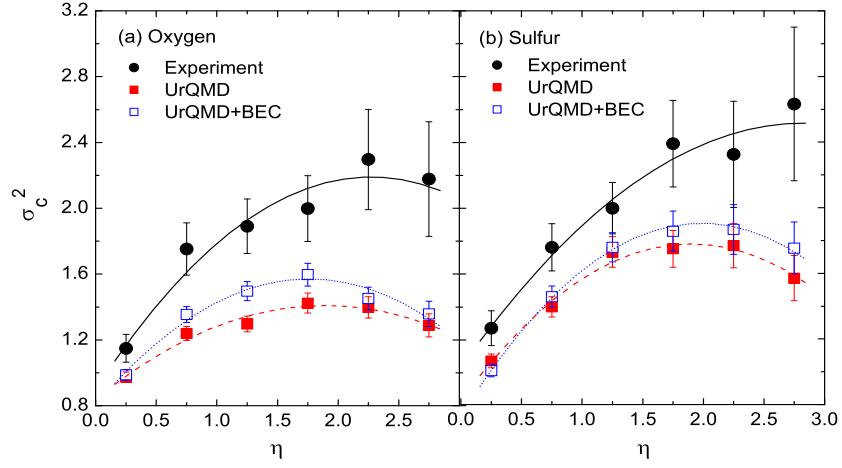


Figure 6.4: σ_c^2 as a function of pseudorapidity η measured about the centroid of the η -distribution. Continuous curves are drawn to visualize the trend of the data points.

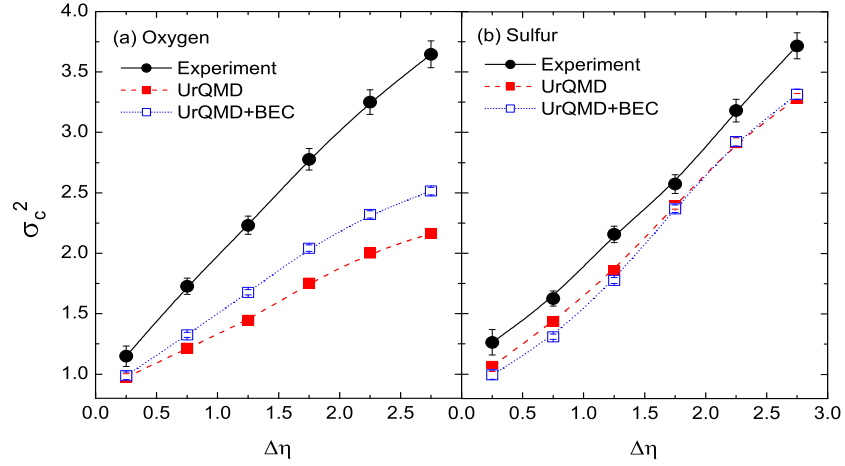


Figure 6.5: σ_c^2 as a function of pseudorapidity windows $\Delta\eta$ at $\eta = \pm 1.5$ about the centroid of the η -distribution. Continuous curves are drawn to visualize the trend of the data points.

correlation becomes negligibly small. Only under such circumstances one can approximate as $\sigma_c^2 \approx K_{\text{eff}}$, where K_{eff} is the effective multiplicity in a cluster. The correlation strength parameter b can also be obtained in terms of the covariance as [48],

$$b = D_{fb}/D_{ff} \quad (6.7)$$

In the absence of any correlation among the particles, when the covariance D_{fb} is vanishing, or when the separation between forward and backward windows is very large, the dynamical correlation approaches its Poisson limit. In either case $\sigma_c^2 \approx K_{\text{eff}} = 1$, which indicates no cluster.

We calculate fluctuations in the FB-multiplicity asymmetry (σ_c^2) as functions of η and $\Delta\eta$. The results are graphically shown respectively in Figures 6.4 and 6.5, where we consider a

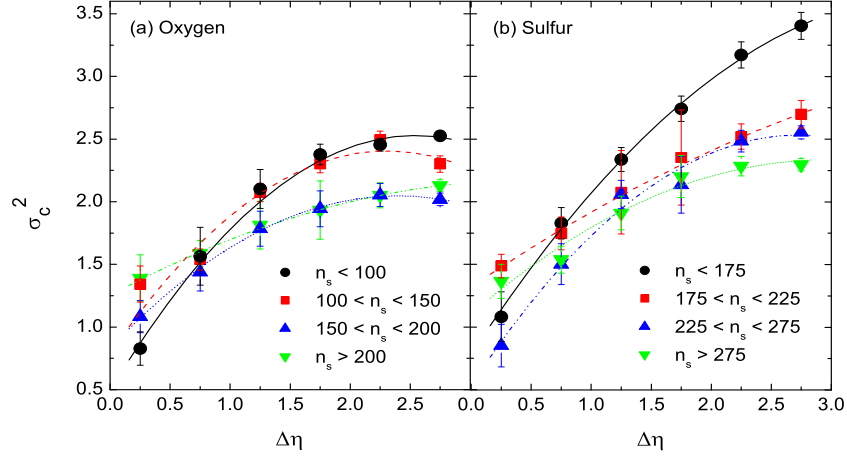


Figure 6.6: σ_c^2 as a function of pseudorapidity windows $\Delta\eta$ at $\eta = \pm 1.5$ about the centroid of the η -distribution for four different multiplicity classes. Continuous curves are drawn to visualize the trend of the data points.

pair of η -bins each of equal width $\Delta\eta$ located symmetrically at $\pm\eta$ about the centroid η_0 of the overall distribution. In Figure 6.4 we then vary the η -value keeping window size fixed at $\Delta\eta = 0.5$. Whereas in Figure 6.5 overlapping η -windows of varying width are taken at a fixed separation $|\eta - \eta_0| = 1.5$. In Figure 6.4 we see that for each type of interaction the experimental value of σ_c^2 starts from $\sigma_c^2 \approx 1.2$ at $\eta = 0.25$, it grows with increasing η -gap up until $\eta \approx 2.0$ units or so, and then attains a kind of saturation, e.g. at $\sigma_c^2 \approx 2.0$ in the $^{16}\text{O-Ag/Br}$ and at $\sigma_c^2 \approx 2.4$ in the $^{32}\text{S-Ag/Br}$ interaction. On the other hand, the UrQMD and the UrQMD+BEC generated values are initially found to increase with increasing η , attain maximum in the intermediate stage before finally dropping down to some extent at the end. Perhaps due to hadronic rescattering embedded into the UrQMD model, the initial fluctuations present in the FB-correlation are to some extent destroyed at large η . The simulated values of σ_c^2 are significantly smaller than the experiment, the difference being larger in $^{16}\text{O-Ag/Br}$ interaction than in the $^{32}\text{S-Ag/Br}$ interaction. Inclusion of BEC into the UrQMD model, though statistically not very significant, slightly enhances the values of σ_c^2 . In Figure 6.4 we also see a definite system size dependence. The values of σ_c^2 in $^{32}\text{S-Ag/Br}$ interaction are consistently higher than the corresponding values obtained from the $^{16}\text{O-Ag/Br}$ interaction. Moreover, the saturation as mentioned above, has perhaps been attained a little earlier in the $^{16}\text{O-Ag/Br}$ interaction than in the $^{32}\text{S-Ag/Br}$ interaction. Figure 6.5 shows that σ_c^2 increases linearly with increasing $\Delta\eta$ over almost the entire range under consideration ($0.25 \leq \Delta\eta \leq 2.75$). Once again we see that the simulated values are consistently lower than the experiment in both cases. In the $^{32}\text{S-Ag/Br}$ interaction the model predictions are to some extent closer to the experiment than that in the $^{16}\text{O-Ag/Br}$ interaction. Absence of any kind of saturation in these plots indicates that all correlated particles could not be accommodated even within the widest $\Delta\eta$ considered.

This observation perhaps indicate presence of long-range correlations in the η -space. In order to reduce the effects of widely varying collision geometry, to the extent it is possible within a limited statistics that is typical to an emulsion experiment, we have divided each experimental event sample into four sub-samples by using the shower track multiplicity cuts. In Figure 6.6 only the experimental σ_c^2 values are plotted against $\Delta\eta$ at a fixed gap $|\eta - \eta_0| = 1.5$. The general nature of the variation in σ_c^2 with $\Delta\eta$, as we see in these plots, is quite different from that of the Figure 6.5. At higher $\Delta\eta$ ($\approx 2.0 - 2.5$) the σ_c^2 values attain saturation. We may therefore conclude that the linear rise observed in Figure 6.5 is nothing but a trivial artifact originating from varying collision geometry. As expected, we observe that in both the interactions considered, the fluctuation measures, particularly at large $\Delta\eta$, are smaller in more central events. The overall nature of our data is almost similar to that observed in the peripheral (40-60% central) Au+Au collisions [49]. Our results indicate that the particle production in both interactions are so correlated that cannot be matched with the UrQMD model. Inclusion of BEC in the simulation does not make any significant change in the outcome either.

In Figure 6.7 we plot the correlation strength b against η -gap for a fixed window size $\Delta\eta = 0.5$. Equation (6.7) is used to determine b . We see that in ^{16}O -Ag/Br interaction the

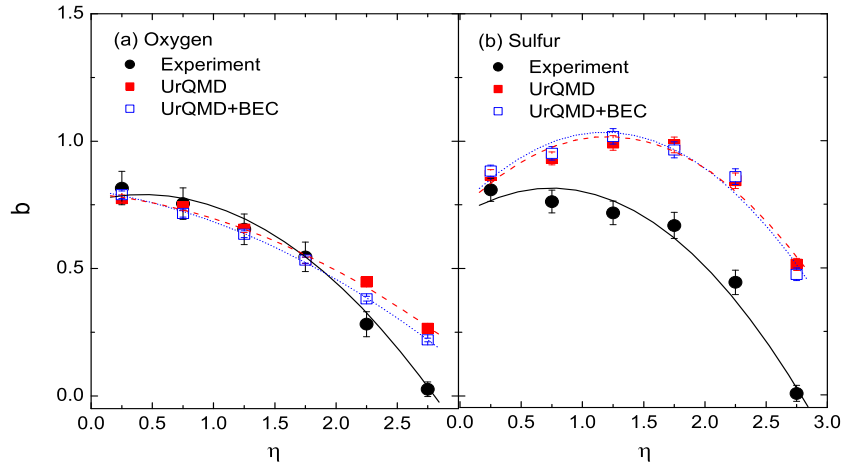


Figure 6.7: Plot of forward-backward correlation parameter b as a function of pseudorapidity gap η . Continuous curves are drawn to visualize the trend of the data points.

correlation strength monotonically decreases with increasing gap between η -windows located in the forward and backward hemispheres. In ^{32}S -Ag/Br interaction the variation of b with η is almost similar to that of the ^{16}O -Ag/Br interaction. Both the model predictions are very close to the experiment in the ^{16}O -Ag/Br case except for the largest gap $\eta = 2.75$. In the ^{32}S -Ag/Br case the simulations however significantly exceed the experiment and remain relatively flat over a comparatively larger η -range. This can be interpreted

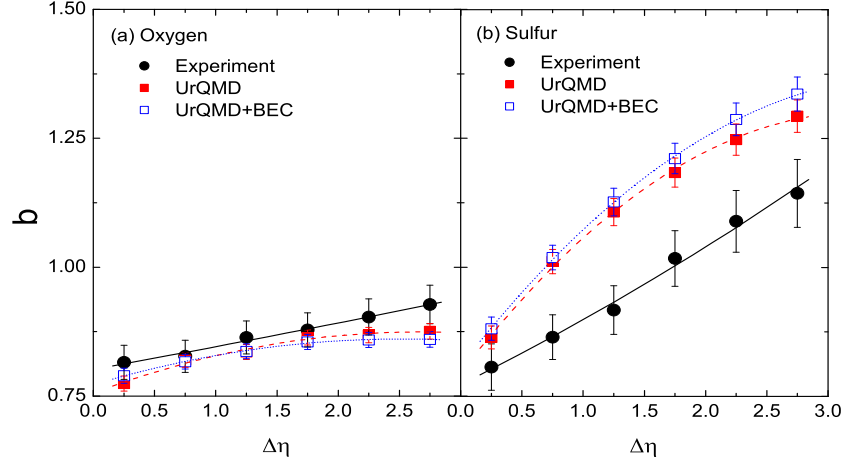


Figure 6.8: b parameter plotted against pseudorapidity window size $\Delta\eta$. Continuous curves are drawn to visualize the trend of the data points.

in terms of long-range correlations present in the ^{32}S -Ag/Br simulation data, for which the string fragmentation and transport mechanisms like diffusion present in the UrQMD model may be held accountable. The hadronic rescattering embedded in the UrQMD may not be strong enough to melt the cluster structure. In Figure 6.8 we plot the correlation strength against $\Delta\eta$ for a fixed η -gap. We see that in both ^{16}O -Ag/Br and ^{32}S -Ag/Br interactions the experimental b -values increase linearly with $\Delta\eta$, while the corresponding simulations exhibit some kind of saturation at large $\Delta\eta$. The linear rise is sharper in ^{32}S -Ag/Br interaction than in the ^{16}O -Ag/Br interaction. Once again, while in the ^{16}O -Ag/Br interaction the simulations approximately reproduce the experiment, in the ^{32}S -Ag/Br case they significantly exceed the experiment. It seems that the fireballs produced in the latter interaction are in general closer to equilibrium, and therefore, thermodynamically more random in nature.

6.5 ω -measure

As mentioned above, a QGP to hadron phase transition may give rise to large rapidity and multiplicity fluctuations of produced particles and have distinct effects on the dynamics or the space-time evolution of the fireball. One way to measure the multiplicity fluctuations is to use the scaled variance (ω) of the multiplicity distribution. ω is defined as [7, 8],

$$\omega = \frac{\text{Var}(n)}{\langle n \rangle} = \frac{\langle n^2 \rangle - \langle n \rangle^2}{\langle n \rangle} \quad (6.8)$$

where $\text{Var}(n) = \sum_k (n_k - \langle n \rangle)^2 P(n_k)$ and $\langle n \rangle = \sum_k n_k P(n_k)$ are respectively the variance and mean of the multiplicity distribution $P(n_k)$. For an independent particle emission, i.e

for a purely statistical mechanism $P(n_k)$ follows Poisson distribution which results in $\omega = 1$. We measure the η -dependence of ω for the shower tracks and show the results schematically

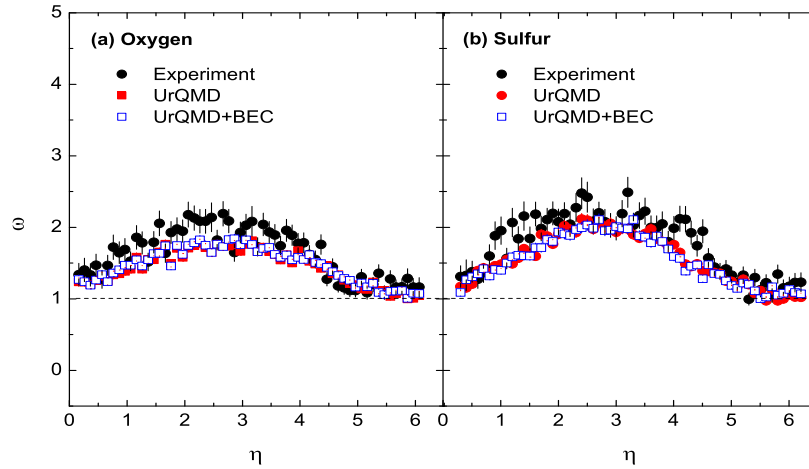


Figure 6.9: Pseudorapidity dependence of the scaled variance ω of the multiplicity distribution.

in Figure 6.9. For comparison the UrQMD and UrQMD+BEC simulated results are also included in the same graph. For both $^{16}\text{O-Ag/Br}$ and $^{32}\text{S-Ag/Br}$ interactions the ω versus η plot looks like a bell-shaped distribution within $0 \leq \eta \leq 6$. The ω -values are almost always greater than their Poisson limit except for $\eta \geq 5$, where the ω -value tends to saturate towards its Poisson limit. In both interactions the experimental values of ω are marginally greater than the corresponding UrQMD and/or UrQMD+BEC prediction. However, under no circumstances the difference between the experiment and simulation is so significant as to augment any excess fluctuation typically required near a critical point. Figure 6.9 reflects the presence of particle correlations in the experimental data as well as in the model simulations. The degree of correlation, i.e. deviation from the Poisson limit is maximum in the central η -region ($2.5 \leq \eta \leq 3.5$) in the experiments as well as in the simulations. The charge reassignment algorithm implemented into the UrQMD simulation, does not affect the ω -measure significantly. In a rather detailed analysis of the NA49 data, it is seen that UrQMD can approximately reproduce the energy as well as the rapidity dependence of the ω -values associated with the charge hadron multiplicity in Pb+Pb collisions at 20A and 158A GeV incident beam energies [50].

6.6 Φ -measure

The Φ -measure of net-charge fluctuation was introduced in [9, 10]. The observable Φ potentially removes the trivial statistical contributions and determines the dynamical e-by-e

fluctuations. The definition of Φ is not limited to measure the net-charge fluctuation only, but it is also applicable to dynamical variables like p_t , y and/or η . Following [9, 10] we define the deviation in the variable x_i from its inclusive mean \bar{x} as, $\Delta x_i = x_i - \bar{x}$. In our case for the i -th shower track $x_i \equiv \eta_i$. By definition the mean $\overline{\Delta x} = 0$, and the mean square deviation is $\overline{\Delta x^2} = \overline{(x_i - \bar{x})^2}$. Analogously for each event the deviation is introduced as,

$$\Delta X = \sum_{i=1}^{n_k} \Delta x_i \quad (6.9)$$

where n_k is the number of shower tracks (particles) present in the k -th event. The Φ_η -measure is then defined as,

$$\Phi_\eta = \sqrt{\frac{\langle \Delta X^2 \rangle}{\langle n \rangle}} - \sqrt{\overline{\Delta x^2}} \quad (6.10)$$

Here $\langle \rangle$ denotes an event averaging. In absence of any inter-particle correlation $\Phi_\eta \rightarrow 0$. Moreover, the fluctuation measure Φ_η would be independent of the number of particle producing sources provided the sources are identical and independent, and provided an AB collision can be treated as an incoherent superposition of many such sources.

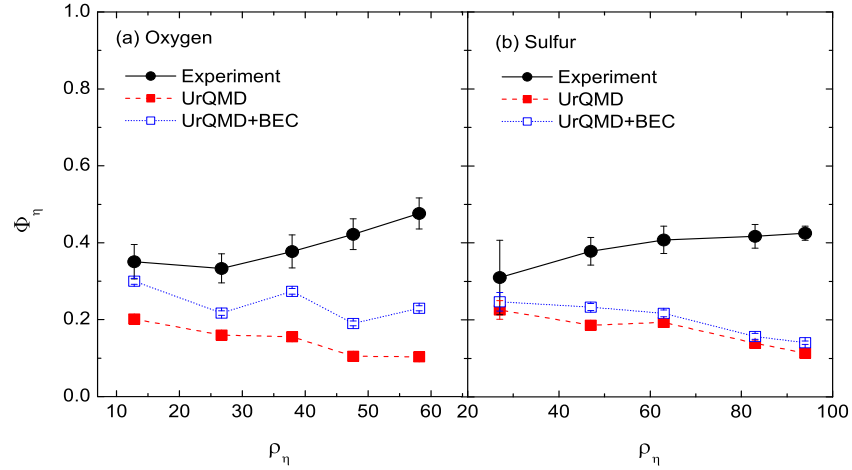


Figure 6.10: The values of Φ_η -measure are shown as a function of pseudorapidity density ρ_η .

The centrality dependence of Φ_η is shown in Figure 6.10. The centrality is measured in terms of the central pseudorapidity density of the produced particles $\rho_\eta = N_{\text{ev}}^{-1} (dn/d\eta)|_{\eta_0}$. For both the experiments Φ_η values are found to slowly and marginally increase with increasing ρ_η . For both interactions the experimental Φ_η -values vary within a narrow range ($\sim 0.30 - 0.45$). In the $^{32}\text{S-Ag/Br}$ case, beyond $\rho_\eta = 60$ the Φ_η -values remain almost unchanged, indicating a dominance of independent particle producing sources in semicentral and central events. There is a definite indication of particle correlations being present in

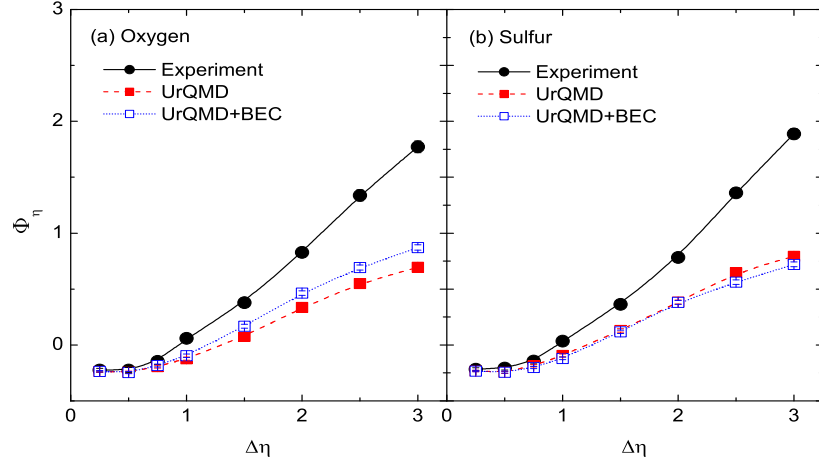


Figure 6.11: The values of Φ_η measure are shown as a function of overlapping pseudorapidity window $\Delta\eta$

both the experimental data samples. The strength of correlation at least in the $^{16}\text{O-Ag/Br}$ events, increases as one moves from peripheral to central collisions. In contrast, the UrQMD simulated values are consistently smaller than the corresponding experimental values. The simulated values show slightly decreasing trend with increasing ρ_η . This implies that the Φ_η measure is sensitive even to the correlations present in the UrQMD model, originating mainly due to resonance decays, jet fragmentation etc. The hadronic re-scattering effect present in the model, might have diluted the correlation to some extent at more central collisions having large particle densities. The BEC effect adds some extra correlation to the UrQMD simulation, which is more prominent in the $^{16}\text{O-Ag/Br}$ case than in the $^{32}\text{S-Ag/Br}$ case. The $\Delta\eta$ -dependence of Φ_η is shown in Figure 6.11. In both experiments we see that beyond $\Delta\eta = 1.0$ the fluctuation measure Φ_η is positive, it increases almost linearly with increasing $\Delta\eta$, and its variation is almost independent of the mass number of the projectile nucleus. The simulated values of Φ_η on the other hand are consistently smaller than the respective experiment, and their rise with increasing $\Delta\eta$ is also not as sharp as they are in the experiments. The differences between the UrQMD and UrQMD+BEC simulations are not very significant in either case. Φ_η is negative valued below $\Delta\eta = 1.0$ in both the experiments and in the corresponding simulations, which should be attributed to lack of correlation due to a small size of the phase-space interval, some of the correlated particles may have been excluded. Even the kinematic conservation laws may not be valid for such a limited interval.

6.7 Summary

The forward-backward multiplicity correlations and e-by-e fluctuations in various correlation measures have been investigated by using two sets of nuclear emulsion data on ^{16}O -Ag/Br and ^{32}S -Ag/Br interactions at an incident beam energy of 200 GeV/nucleon. The experimental results are compared with the UrQMD simulation, as well as with the UrQMD simulation modified with a charge reassignment algorithm that mimics the Bose-Einstein correlation. In spite of the limitations regarding the statistics, which is typical to any emulsion experiment, we have been able to make several important observations, which are summarized below.

1. The roughness distribution of particles are examined through a χ^2 test, and large concentrations of particles within small η -intervals are observed that cannot be reproduced by the UrQMD and UrQMD+BEC simulations. On some occasions the particle densities are too large to be merely due to statistical reasons or kinematic constraints.
2. Fluctuations in the forward-backward asymmetry parameter show dominance of short-range correlation in the pseudorapidity space, which in the ^{16}O -Ag/Br interaction gets diluted to some extent. However, in the ^{32}S -Ag/Br interaction the correlation strength sustains even at the large η -gaps as well as in large $\Delta\eta$. Small sized clusters are responsible for the short-range correlations observed. The UrQMD simulation, even after inclusion of the BEC effect, can not reproduce the experimental results. At large η re-scattering among hadrons significantly dilutes the fluctuation observed. Inclusion of the BEC marginally improves the simulation results.
3. Our observation on the correlation strength parameter is more or less consistent with that of the fluctuations observed in the FB asymmetry parameter. While the UrQMD and UrQMD+BEC simulations can almost predict the ^{16}O -Ag/Br experiment, they significantly over predict the ^{32}S -Ag/Br results. In the latter case it seems that in the experiment, inter-particle correlations are more susceptible to the fireball environment than what has been assumed in the simulation.
4. Presence of particle correlations is reaffirmed through the ω -measure. Non-Poissonian multiplicity distribution within small η -interval is established through this test. The experimental results however are very close to the simulations which do not warrant any critical phenomenon.
5. The Φ_η -measure of dynamical fluctuations indicate that both ^{16}O -Ag/Br and ^{32}S -Ag/Br collision events can perhaps be approximated as incoherent superpositions of many binary NN collisions. Hadronic re-scattering dilutes the simulated values to noticeable extent.

The statistical tools used in this analysis have their own limitations [51], and the AB collision events have a widely varying geometry. The results presented in this analysis however certainly indicate that the mechanism of particle production in UrQMD is in no way sufficient to describe the real dynamics of AB interactions.

Bibliography

- [1] H. Song, Euro. Phys. J. A 48, 163 (2012).
- [2] W. Busza, K. Rajagopal and W. van der Schee, Ann. Rev. Nuc. Part. Sci. 68, 1 (2018).
- [3] M. Gaździcki, M. I. Gorenstein and S. Mrówczyński, Phys. Lett. B 585, 115 (2004).
- [4] A. Galavanov *et al.*, J. Phys: Conf. Series, 1390, 012025 (2019).
- [5] B. B. Back *et al.* (UA5 Collaboration), Z. Phys C 37, 191 (1998).
- [6] M. Cherry *et al.* (KLM Collaboration), Acta Phys. Pol. B 29, 2129 (1998).
- [7] V. V. Begun *et al.*, Phys. Rev. C 70, 034901 (2004).
- [8] B. Lungwitz and M. Bleicher, Phys. Rev. C 76, 044904 (2007).
- [9] M. Gaździcki and S. Mrówczyński, Z. Phys. C 54, 127 (1992).
- [10] S. Mrówczyński, Phys. Lett. B 465, 8 (1999).
- [11] S. A. Bass *et al.*, Prog. Part. Nucl. Phys. 41, 255 (1998).
- [12] M. Bleicher *et al.*, J. Phys. G 25, 1859 (1999).
- [13] O. V. Utyuzh, G. Wilk and Z. Wlodarczyk, Phys. Lett. B 522, 273 (2001).
- [14] T. H. Burnett *et al.* (JACEE Collaboration), Phys. Rev. Lett. 50, 2062 (1962).
- [15] B. Wosiek (KLMM Collaboration), Proc. XXV Int. Symp. on Multiparticle Dynamics, World Scientific (1996) p.271.
- [16] P. Deines-Jones *et al.* (KLM Collaboration), Phys. Rev. C 53, 3044 (1996).
- [17] G. Roland *et al.* (PHOBOS Collaboration), Nucl. Phys. A 774, 113 (2006).
- [18] E. V. Shuryak, Nucl. Phys. A 715, 289 (2003).
- [19] G. Baym and H. Heiselberg, Phys. Lett. B 469, 7 (1999).
- [20] S. Jeon and V. Koch, Phys. Rev. Lett. 85, 2076 (2000);
M. Asakawa, U. Heinz, and B. Müller, Phys. Rev. Lett. 85, 2072 (2000).

- [21] N. G. Antoniou *et al.*, Phys. Lett. B 432, 8 (1998).
- [22] C. Alt *et al.* (NA49 Collaboration), Phys. Rev. C 70, 064903 (2004).
- [23] T. Anticic *et al.* (NA49 Collaboration), Phys. Rev. C 70, 034902 (2004).
- [24] G. Roland (for the NA49 Collaboration), Nucl. Phys. A 638, 91c (1998);
H. Appelshauser *et al.* (NA49 collaboration), Phys. Lett. B 459, 679 (1999).
- [25] M. Bleicher *et al.*, Phys. Lett. B 435, 9 (1998).
- [26] A. Capella, E. G. Ferreira and A. B. Kaidalov, Euro. Phys. J. C 11, 163 (1999).
- [27] W. Braunschweig *et al.* (TASSO Collaboration), Z. Phys. C 45, 193 (1989).
- [28] S. Uhlig, I. Derado, R. Meinke and H. Preissner, Nucl. Phys. B 132, 15 (1978).
- [29] R. Ansorge *et al.* (UA5 Collaboration), Z. Phys. C 37, 191 (1988).
- [30] ATLAS Collaboration, J. High Energy Phys. 07, 019 (2012).
- [31] J. Adam *et al.* (ALICE Collaboration), J. High Energy Phys. 05, 097 (2015).
- [32] B. B. Back *et al.* (PHOBOS Collaboration), Phys. Rev. C 74, 011901(R) (2006).
- [33] B. I. Abelev *et al.* (STAR Collaboration), Phys. Rev. Lett. 103, 172301 (2009).
- [34] M. Abdel-Aziz and M. Bleicher, arXiv:nucl-th/0605072.
- [35] M. Stephanov, K. Rajagopal and E. Shuryak, Phys. Rev. D 60, 114028 (1999).
- [36] S. Haussler, M. Abdel-Aziz and M. Bleicher, Nucl. Phys. A 785, 253c (2007).
- [37] A. Bzdak and D. Teaney, Phys. Rev. C 87, 024906 (2013).
- [38] R. S. Bhalerao *et al.*, Phys. Rev. Lett. 114, 152301 (2015).
- [39] T. Sjöstrand *et al.*, Comput. Phys. Commun. 178, 852 (2008).
- [40] T. Pierog *et al.*, Phys. Rev. C 92, 034906 (2015).
- [41] G. Aad *et al.* (ATLAS Collaboration), Phys. Lett. B 758, 67 (2016);
M. Aaboud *et al.* (ATLAS Collaboration), Eur. Phys. J. C 76, 502 (2016).
- [42] G. Aad *et al.* (ATLAS Collaboration), Eur. Phys. J. C 74, 2965, *ibid* 3195 (2014).
- [43] A. Capella and J. T. T. Van, Phys. Lett. B 93, 146 (1980); Z. Phys. C 10, 249 (1981).
- [44] T. Lappi and L. McLerran, Nucl. Phys. A 772, 200 (2006).

- [45] T. J. Tarnowsky (STAR Collaboration), Proceedings of the 22nd Winter Workshop on Nuclear Dynamics, California, USA (2006).
- [46] W. Kittel and E. A. de Wolf, *Soft Multihadron Dynamics*, World Scientific (2005).
- [47] S. Lim, Y. Lim, C. Oh and K. Phua, *Z. Phys. C* 43, 621 (1989).
- [48] A. Capella, U. Sukhatme, C.-I. Tan and J. T. T. Van, *Phys. Rep.* 236, 225 (1994).
- [49] G. Roland (NA49 Collaboration), *Proc. of the Quark Matter 1997*, Japan (1997).
- [50] C. Alt *et al.* (NA49 Collaboration), *Phys. Rev. C* 78, 034914 (2008).
- [51] O. V. Utyuzh, G. Wilk and Z. Wlodarczyk, *Phys. Rev. C* 64, 027901 (2001).

Concluding remarks

Multiparticle production at $E_{\text{lab}} = 200A \text{ GeV}/c$ is predominantly a soft hadronic process that pertains to very late stages of a high-energy AB collision. By studying the debris of particles produced in the final state particles, most of which are hadrons, it is extremely difficult to draw definite conclusions about an early and/or intermediate stage. One only hopes that the characteristic features of the early stages can withstand the impact of the collision and retain their foot prints even in the later stages. The method of analysis should therefore be sensitive enough so that it can disentangle the characteristic features of a signal from all kinds of background noise. One can develop theories and/or simulation codes based on some presumptive dynamical processes, come up with predictions and try to match the experimental observations, and then fine tune the theory and/or code. It is claimed that a strongly interacting QGP matter has already been created in very high-energy AB experiments ($\sqrt{s_{NN}} \sim \text{TeV}$) held at the RHIC/LHC. The QGP state so created, is almost baryon free and has a very high temperature, a state perhaps similar to that filled up the entire universe a few microseconds after its birth. Such a claim however does not make the experiments at lower collision energies redundant. It is quite possible that even at much lower energies (typical SPS, FAIR or NICA energies, or the lower end of RHIC energy) there will be large baryon stopping. As a result an extended QCD matter at high baryon density and moderate temperature will be created. A similar QGP state perhaps can be found within the cores of very compact stars. AB collisions should therefore be examined from different perspectives using a wide variety of colliding systems over a vastly different collision energies.

An investigation on the local structures in the phase space distribution of singly charged particles produced in high-energy AB collisions has been made. The data used in this

investigation are collected from a nuclear emulsion experiment (EMU-08) held at the Super-proton Synchrotron at CERN, Geneva. Several statistical methods are employed to analyze the multiparticle emission data in ^{16}O -Ag/Br interaction at $p_{\text{lab}} = 200A \text{ GeV}/c$. A comparison with the ^{32}S -Ag/Br results at the same incident momentum per nucleon is made. The experiments are compared with a set of simulated data generated by the Ultra-relativistic Quantum Molecular Dynamics (UrQMD). A charge reassignment algorithm that mimics the Bose-Einstein Correlation (BEC), is implemented to the UrQMD output as an after burner. The experimental results are also compared with the simulation after the UrQMD output is modified by the charge reassignment algorithm. The UrQMD model(s) set a good reference baseline to the experiment(s). In this thesis we review some aspects of the high-energy AB collision, i.e. its importance in the context of QGP formation, describe gross characteristics of the experimental data samples used, explain some general features of the UrQMD model, outline the charge reassignment scheme, describe the statistical techniques adopted in our analysis, and discuss the results obtained thereof. We now summarize the major conclusions of this investigation and conclude the thesis.

We observe that the gross features of the ^{16}O -Ag/Br experiment like, the η -distribution, the φ -distribution, the distribution of particle density, $N_{ev}^{-1} (dn_s/d\eta)$ -values of the shower tracks, are more or less well reproduced by the UrQMD model. Corresponding distributions obtained for the ^{32}S -Ag/Br interaction are similar in nature, but are different from the ^{16}O -Ag/Br results only quantitatively. UrQMD reproduces the ^{32}S -Ag/Br results too. There is however a little mismatch between the φ -distributions obtained from the experiments and that from the corresponding simulations. The differences observed in the $0 \leq \varphi \leq \pi/2$ and $3\pi/2 \leq \varphi \leq 2\pi$ regions, may be attributed to an inefficiency in measurements, a smaller statistics used in the experiments and/or to the collective flow of hadronic matter. The η -distributions of charged hadrons can be approximated by single Gaussian curves. Corresponding UrQMD generated distributions also have similar characteristics. In both experiments the initial energy density values estimated from the central pseudorapidity densities, are very close to the LQCD predicted threshold of QGP formation, which is \sim a few GeV/fm^3 . The single Gaussian shape of the η -distributions, as expected at such collision energies, is compatible to a significant baryon stopping in the central region. Large values of η -density in the central particle producing regions are seen in the η -distributions of shower tracks in individual events. One of the main objectives of this investigation is to characterize these high particle densities.

The η -distributions of charged hadrons belonging to individual events, fluctuate at random between sharp spikes and deep valleys apparently devoid of any definite pattern. For a large event sample, these fluctuations are however averaged out resulting in smooth Gaussian shaped distributions. With decreasing size of phase space intervals down to the experimental

resolution, such fluctuations increase in magnitude. Particles in large numbers accumulate in narrow phase space intervals for three different reasons, due to statistical uncertainties, due to kinematic conservation rules and due to some underlying dynamics. A part of the dynamics may be known whereas a part of it may still be unknown. We use the scaled factorial moments (SFM) and characterize the fluctuating distributions in terms of a finite set of regularly behaving parameters. For the experimental distributions, the SFMs follow a power law and increase in magnitude with decreasing phase space resolution size. This is observed in both η and φ -spaces. In high-energy physics the phenomenon is known as intermittency. On the other hand, for the UrQMD generated samples we do not see any significant change in the SFM values. Inclusion of BEC in the UrQMD output only marginally recovers the power law type of scaling. The main sources of short range particle correlations in UrQMD are resonance decays and mini-jet fragmentation. Inclusion of BEC perhaps enhances the correlation to a small extent, which is not there in the UrQMD. The intermittency strengths are however much larger in the experiments than in the simulations. There is a definite indication that some degree of short range correlations present in the experiments cannot be accounted for by the simulation. We speculate that a kind of hadronic/partonic cascade mechanism or some other unknown dynamics is responsible for the differences. Some other observations regarding the intermittency are listed below.

1. Intermittency in the φ -space is stronger than that in the η -space. The observation may partially be attributed to a stronger influence of kinematic conservation in the transverse (azimuthal) plane.
2. At the same incident momentum per nucleon, intermittency in the $^{16}\text{O-Ag/Br}$ interaction is stronger than that in the $^{32}\text{S-Ag/Br}$ interaction. The observation is attributed to a larger number of particle producing sources in a larger colliding system.
3. Intermittency in the (η, φ) -plane is stronger than that either in the η or φ -space. In $1d$ intermittency is self-similar, whereas in $2d$ it is self-affine. Self-similarity in $2d$ is retrieved when the phase space is partitioned unequally along the η and φ -directions by using the roughness (Hurst) parameter.

The intermittency technique also allows us to characterize the bin-to-bin correlations. A two fold SFM or the factorial correlator (FC) is used for this purpose. In the η -space, as the bin-to bin distance (the correlation length) is decreased, the FCs follow a power-law type of scaling. The FCs however are independent of the phase space interval size. Our results on the FCs are consistent with the predictions of a simple intermittency model (α -model). The experimental results could not be reproduced either by the UrQMD or by the UrQMD+BEC model. Once again presence of short range correlations in the data is established that the models can not account for.

Presence of genuine higher order correlations are examined by using the factorial cumulant moments or the normalized cumulant moments, where contributions coming from lower order correlations are eliminated. According to a QCD-based parton shower cascade model, the normalized cumulant moments should undergo an oscillation with the order number. This prediction has been verified in our experiments in small sized η -intervals ($\Delta\eta \lesssim 0.25$) in the central region. With increasing width of the η -interval considered, the oscillatory behavior gradually disappears, and the experiment starts to coincide with the respective simulation. However, as long as the η -interval remains small sized, our experimental results on the oscillatory moments are not exactly reproduced by the UrQMD model(s).

We have obtained the distributions of single event SFMs for a particular partition number in the η -space. We observe that while most of the SFM-values are restricted within a small range, events with quite high SFM-values are also not very rare. It is speculated that this kind of event space fluctuations of the SFMs is chaotic in nature. Such fluctuations can be characterized in terms of the erraticity moments. We find that the erraticity moments in both experiments and simulations increase with increasing partition number following once again a power-law type of scaling. A chaoticity parameter, similar to the entropy index used in the pp interaction, was obtained. We find that the event space fluctuations are more chaotic in the $^{32}\text{S-Ag/Br}$ than in the $^{16}\text{O-Ag/Br}$ interaction. Fluctuations in the simulated event samples are significantly less chaotic than that in the experiment.

We have used several statistical methods to characterize the particle density fluctuations in the η -space in terms of a set of (multi)fractal parameters. The results of $^{16}\text{O-Ag/Br}$ interaction are sometimes compared with the $^{32}\text{S-Ag/Br}$ results. We also use the detrended methods and visibility graph(s) for our multifractal analysis. Our observations on multifractality are summarized below.

1. With diminishing phase space resolution size the G_q -moments increase in magnitude following a scale invariant power-law. The UrQMD and UrQMD+BEC simulated moments show similar trends. This is in contrast to our intermittency results for the same sets of data, where the simulations fail to reproduce the experiments. The SFMs take care of the statistical noise which the multifractal moments do not. Perhaps it is this reason that makes all the differences in our observations between intermittency and multifractality.
2. The multifractal spectrum, consistent in all respects with its expected behavior, has slightly smaller width in the UrQMD than in the corresponding experiment. Width of the UrQMD+BEC generated spectrum lies in between. The multifractal spectrum may be considered as a sensitive tool that can distinguish the dynamics of experiment from the dynamics of simulation.

3. Takagi's multifractal moments also exhibit a power-law scaling with decreasing phase space resolution size for the experiments and simulations. In the $^{16}\text{O-Ag/Br}$ interaction the fractal dimensions obtained from the experiment are marginally different from the UrQMD simulated values. The D_q results are consistent with a thermodynamic interpretation of a monofractal to multifractal phase transition.
4. Multifractal analysis has been performed by using the MFDFA and MFDMA techniques too. The results show that for both interactions the η -distributions are long-range correlated and multifractal in nature. The multifractality observed in the experiments goes beyond the UrQMD+BEC prediction. The MFDFA method too is not quite capable of filtering out the statistical noise from the signal. Unlike the first order MFDFA method, the MFDMA analysis produces a complete and stable singularity spectrum, which indicates the presence of a small number of events with large fluctuations. Coarse fluctuations are attributed mostly to statistical reasons.
5. Using the visibility graph and sandbox algorithm, event-wise η -distributions of shower tracks are analyzed. Degree distributions of visibility graphs obtained for each experiment and the respective UrQMD simulation are similar in nature. The scale freeness of the degree distribution indicates presence of long-range correlated signals in our multiparticle emission data. The sandbox algorithm applied to the visibility graphs successfully reproduces the multifractal properties. We observe that the graph theoretical approach has the potential to differentiate between the dynamical and statistical components.

We have looked for unusual structures in the azimuthal space. The S -parameters used for this purpose, behave consistently with ring and/or jet-like structures in the experiments. Small but significant departures from an independent emission model are seen in the experiments. In the framework of a Cerenkov gluon emission model we conclude that, in some events only a few gluons are emitted, whereas in some others their numbers are large. It would be worthwhile to find out the nuclear refractive index and use the same to constrain the nuclear equation of state. In our wavelet analysis once again we find statistically significant differences between the experiment and corresponding UrQMD+BEC simulation. All the parameters studied in connection with the g_2 and g_4 -wavelets indicate that large and ordered fluctuations are present in both $^{16}\text{O-Ag/Br}$ and $^{32}\text{S-Ag/Br}$ data. The differences are attributed to short range correlations.

The forward-backward multiplicity correlations and e-by-e fluctuations in various correlation measures are investigated. The roughness distribution of particles are examined through a χ^2 test. Large concentration of particles within small η -intervals are observed, that cannot

be reproduced by the simulations used. On some occasions the particle densities are too large to be merely due to statistical and/or kinematic reasons.

Fluctuations in the forward-backward asymmetry parameter show dominance of short-range correlations in the η -space. Small sized clusters are responsible for the short-range correlations observed. The UrQMD simulation, even after inclusion of the BEC effect, can not reproduce the experimental results. At large η , re-scattering among hadrons significantly dilutes the fluctuations. Our observation on the correlation strength parameter is more or less consistent with that of the fluctuations in the FB asymmetry parameter. The UrQMD and UrQMD+BEC simulations are close to the $^{16}\text{O-Ag/Br}$ experiment, but they over predict the $^{32}\text{S-Ag/Br}$ results.

Presence of particle correlations is reaffirmed through the ω -measure. Non-Poissonian multiplicity distribution within small η -intervals is established through this test. The experimental results however are very close to the simulations. The Φ_η -measure of dynamical fluctuations indicate that both $^{16}\text{O-Ag/Br}$ and $^{32}\text{S-Ag/Br}$ collision events can perhaps be approximated as incoherent superpositions of many particle producing sources. Hadronic re-scattering dilutes the simulated values to a noticeable extent.

List of publications

The publications marked by an asterisk (*) are related to the thesis.

- *14. Forward–backward multiplicity correlation and event-by-event multiplicity fluctuation in nucleus–nucleus collisions at 200A GeV, S. K. Manna, A. Mukhopadhyay and P. Mali, *Int. J. Mod. Phys. E*, 2150021 (2021).
- *13. Wavelet analysis of particle density functions in nucleus–nucleus interactions, S. K. Manna, P. K. Haldar, P. Mali, A. Mukhopadhyay and G. Singh, *Int. J. Mod. Phys. E* 27(1), 1850009 (2018).
- *12. Multifractal analysis of multiparticle emission data in the framework of visibility graph and sandbox algorithm, P. Mali, S. K. Manna, A. Mukhopadhyay, P. K. Haldar and G. Singh, *Physica A* 493, 253 (2018).
- *11. Multifractal analysis of charged particle distributions using horizontal visibility graph and sandbox algorithm, P. Mali, A. Mukhopadhyay, S. K. Manna, P. K. Haldar and G. Singh, *Mod. Phys. Lett. A* 32(8), 1750024 (2017).
- *10. Detrended analysis of shower track distribution in nucleus-nucleus interactions at CERN SPS energy, P. Mali, S. K. Manna, P. K. Haldar, A. Mukhopadhyay and G. Singh, *Chaos. Sol. and Fractals* 94, 86 (2017).
- 9. Multidimensional intermittency study of target fragments at CERN SPS energies, P. K. Haldar, S. K. Manna, P. Saha and D. Ghosh, *Astropart. Phys.* 42, 76 (2013).
- 8. Ring and jet study on the azimuthal substructure of pions at CERN SPS energy, P. K. Haldar, S. K. Manna, P. Saha and D. Ghosh, *Pramana-J. Phys.* 80(4), 631 (2013).
- 7. Dynamical fluctuations of pions for ring and jet-like events at SPS energy: an in-depth study with factorial correlator, P. K. Haldar, S. K. Manna, P. Saha and D. Ghosh, *Ind. J. Phys.* 86(12), 1155 (2012).

6. Peculiarities in the distribution of produced particles emission in $^{24}\text{Mg-Ag/Br}$ interactions at $4.5A$ GeV, P. K. Haldar, S. K. Manna, P. Saha and D. Ghosh, *Ind. J. Pure. & App. Phys.* 50, 156 (2012).
5. Non-statistical fluctuations of pions for ring- and jet-like events at CERN SPS energy – An in-depth analysis with factorial correlator, P. K. Haldar, S. K. Manna, P. Saha and D. Ghosh, *Int. J. Mod. Phys. E* 20(9), 2027 (2011).
4. Factorial correlators and oscillatory multiplicity moments at the CERN SPS energy for ring-like and jet-like events, P. K. Haldar and S. K. Manna, *Chin. Phys. Lett.* 28(1), 012502 (2011).
3. Factorial correlators and oscillatory multiplicity moments of ring-like and jet-like events in $^{16}\text{O-Ag/Br}$ interactions at $60A$ GeV, P. K. Haldar and S. K. Manna, *Can. J. Phys.* 89, 713 (2011).
- *2. Ring and jet-like structures and two-dimensional intermittency in nucleus–nucleus collisions at $200A$ GeV/c, M. K. Ghosh, P. K. Haldar, S. K. Manna, A. Mukhopadhyay and G. Singh, *Nucl. Phys. A* 858, 67 (2011).
- *1. Intermittency and related issues in $^{16}\text{O-Ag/Br}$ collision at $200A$ GeV/c, M. K. Ghosh, P. K. Haldar, S. K. Manna, A. Mukhopadhyay and G. Singh, *Can. J. Phys.* 88, 575 (2010).

Reprints



Multifractal analysis of multiparticle emission data in the framework of visibility graph and sandbox algorithm

P. Mali ^a, S.K. Manna ^b, A. Mukhopadhyay ^{a,*}, P.K. Haldar ^c, G. Singh ^d

^a Department of Physics, University of North Bengal, Siliguri 734013, India

^b Department of Physics, Chakdaha College, Chakdaha, Nadia 741222, India

^c Department of Physics, Dinhatra College, Dinhatra, Cooch Behar 736135, India

^d Department of Computer and Information Sciences, SUNY at Fredonia, NY 14063, USA

HIGHLIGHTS

- Multiparticle emission data in high-energy heavy-ion collisions are analyzed.
- Fractal characteristics of single particle density fluctuations are established.
- Visibility graph and sandbox algorithm are used.
- Experimental results are compared with UrQMD simulation.
- Effectiveness of visibility graph method and detrended method are compared.

ARTICLE INFO

Article history:

Received 10 May 2017

Received in revised form 20 September 2017

Available online 3 November 2017

Keywords:

High-energy heavy-ion collisions

Visibility graph and sandbox methods

Degree distribution of visibility graph

Multifractality and long-range correlation

ABSTRACT

Multiparticle emission data in nucleus–nucleus collisions are studied in a graph theoretical approach. The sandbox algorithm used to analyze complex networks is employed to characterize the multifractal properties of the visibility graphs associated with the pseudorapidity distribution of charged particles produced in high-energy heavy-ion collisions. Experimental data on $^{28}\text{Si}+\text{Ag}/\text{Br}$ interaction at laboratory energy $E_{\text{lab}} = 14.5A$ GeV, and $^{16}\text{O}+\text{Ag}/\text{Br}$ and $^{32}\text{S}+\text{Ag}/\text{Br}$ interactions both at $E_{\text{lab}} = 200A$ GeV, are used in this analysis. We observe a scale free nature of the degree distributions of the visibility and horizontal visibility graphs associated with the event-wise pseudorapidity distributions. Equivalent event samples simulated by ultra-relativistic quantum molecular dynamics, produce degree distributions that are almost identical to the respective experiment. However, the multifractal variables obtained by using sandbox algorithm for the experiment to some extent differ from the respective simulated results.

© 2017 Published by Elsevier B.V.

1. Introduction

A collection of nodes or objects, and the mutual interactions between them, technically called the edges, is commonly referred to as a network. Studies of complex networks play an important role to explore complexities present in the dynamics of a natural and/or social process [1]. On several occasions it has been shown that the complex network analysis might be an efficient tool to extract information embedded in time series and sequential measurements [2–7]. An usual time series analysis provides us with the information regarding the dynamics of a system, while a network analysis of time series

* Corresponding author.

E-mail address: amitabha_62@rediffmail.com (A. Mukhopadhyay).

provides a structural framework of complex systems along with their dynamics. In recent times quite a few algorithms are proposed that can construct complex networks from time series, such as complex networks from pseudo-periodic time series [2], visibility graphs [4,5], state space networks [8], recurrence networks [7,9], nearest-neighbor networks [3,10], and complex networks based on phase-space reconstruction [11] etc. Among the aforementioned techniques, the visibility graphs (VGs) and horizontal visibility graph (HVGs) are used in many applications belonging to diverse fields. The operational procedure of constructing a VG/HVG from a set of time ordered measurements is discussed in the next section. It has been observed that the VGs converted from some long-range correlated time series are scale-free [6,12], and that there exists a definite relationship between the Hurst exponent H of the series and the exponent of the power-law type degree distribution of the graph concerned [6]. The relationship between the H of fractional Brownian motion (fBm) and topological/fractal properties of the associated HVG and recurrence networks has also been examined [13,14]. The analysis of networks/graphs thus provides an alternative way to characterize time series.

Fractal analysis of complex networks underwent a paradigm shift when the box-counting algorithm of fractals were generalized [1]. Over the years the box-counting algorithm has been scrutinized in several different ways, and is applied widely to a number of emerging fields such as financial modeling, biology, social and communication networks [15–18]. Recently the sandbox (SB) algorithm, originally proposed in [19], has been employed for multifractal analysis (MFA) of complex networks [20]. They show that the SB algorithm is the most effective and accurate technique to determine multifractal parameters of complex networks. In this work we employ the SB algorithm to characterize the pseudorapidity (η) distribution of singly charged particles produced in relativistic nucleus–nucleus (AB) collisions. On an even-by-event basis the η -distributions of singly charged particles produced in $^{28}\text{Ar}/\text{Br}$ interaction at $E_{\text{lab}} = 14.5\text{A GeV}$, $^{16}\text{O}/\text{Ar}/\text{Br}$ interaction at 200A GeV , and $^{32}\text{S}/\text{Ar}/\text{Br}$ interaction at 200A GeV , are converted into the corresponding VGs and HVGs. The SB algorithm is then employed to determine the respective set of multifractal parameters.

Hadronization takes place at a late stage of the evolution of an AB collision process. It is therefore, quite a challenging task to characterize multiparticle emission data by using statistical tools, and trace back the thermodynamic properties of the intermediate ‘fireball’ produced in an AB collision. However, the ‘fireball’ property has some cosmological relevance if it is produced under a high-temperature and low baryo-chemical potential, in the sense that at a minuscule scale it can replicate the early universe scenario (\sim a few micro-seconds after the ‘big bang’). On the other hand at low to moderate temperature and at high baryo-chemical potential the ‘fireball’ has an astrophysical relevance, as the QCD matter contained within it is perhaps similar to that filling up the core of very compact stars [21]. Like fractal analysis of complex networks, fractal analysis of multiparticle production data is also not a new topic of research. It started in the late 1980’s with the observation that large fluctuations present in the η -distributions of charged particles produced in a few very high-multiplicity cosmic-ray events [22], possess some kind of scale invariant self-similarity that can be formulated in terms of a power-law type of scaling of the factorial moments with the resolution of the scale in which it is measured [23]. The phenomenon known as ‘intermittency’ in high-energy interactions, is closely connected to fractality. This was first recognized when the intermittent behavior of turbulent fluids was studied in terms of fractal dimensions [24]. This observation prompted the fractal formalism to be adopted into multiparticle data analysis. Several techniques based on the theory of fractals are available in literature [24–27]. Recently, the detrended methods of time series analysis [28,29] are also used to analyze particle emission data [30,31]. The combination of visibility graph and sandbox algorithm is perhaps for the first time used in [32] to analyze particle emission data in AB interaction. In this paper the following issues are addressed: (i) whether or not the graph theoretical approach can provide a multifractal description of the particle emission data at varying collision energies for different colliding systems, and (ii) to check if the method can consistently distinguish between the experiment and corresponding Monte-Carlo (MC) simulation based on ultra-relativistic quantum molecular dynamics (UrQMD) [33,34]. Throughout the analysis a systematic comparison has been made between the results derived from VG–SB and HVG–SB algorithms, as well as between the experiment and corresponding MC simulation. We therefore, expect to be able to extract the non-statistical effects present in the experiment, if there is any.

2. Visibility graph and horizontal visibility graph

In graph theory a graph is a collection of objects or nodes and links or edges, each of which identifies the relation or interaction between any two nodes. Lacasa et al. [4] introduced a simple computational method to convert a time series into a VG. Accordingly, a VG of N nodes is obtained from a time ordered sequence of N measurements so that any two data points (t_i, x_i) and (t_j, x_j) have mutual visibility, and consequently are two connected nodes in the graph associated, if any other point (t_k, x_k) satisfy the criterion:

$$x_k < x_i + (x_j - x_i) \frac{t_k - t_i}{t_j - t_i}. \quad (1)$$

where $i < k < j$. Fig. 1(a) illustrates the mapping of an arbitrary time series of 15 measurements. It is shown [12] that the structural complexity of time series is inherited by the associated graph. As for instance, periodic, random and fractal series map into motif-like random, exponential and scale-free networks, respectively. A much more simplified form of the above visibility criterion is employed to obtain the HVG [5], where two nodes i and j are connected if one can draw a horizontal

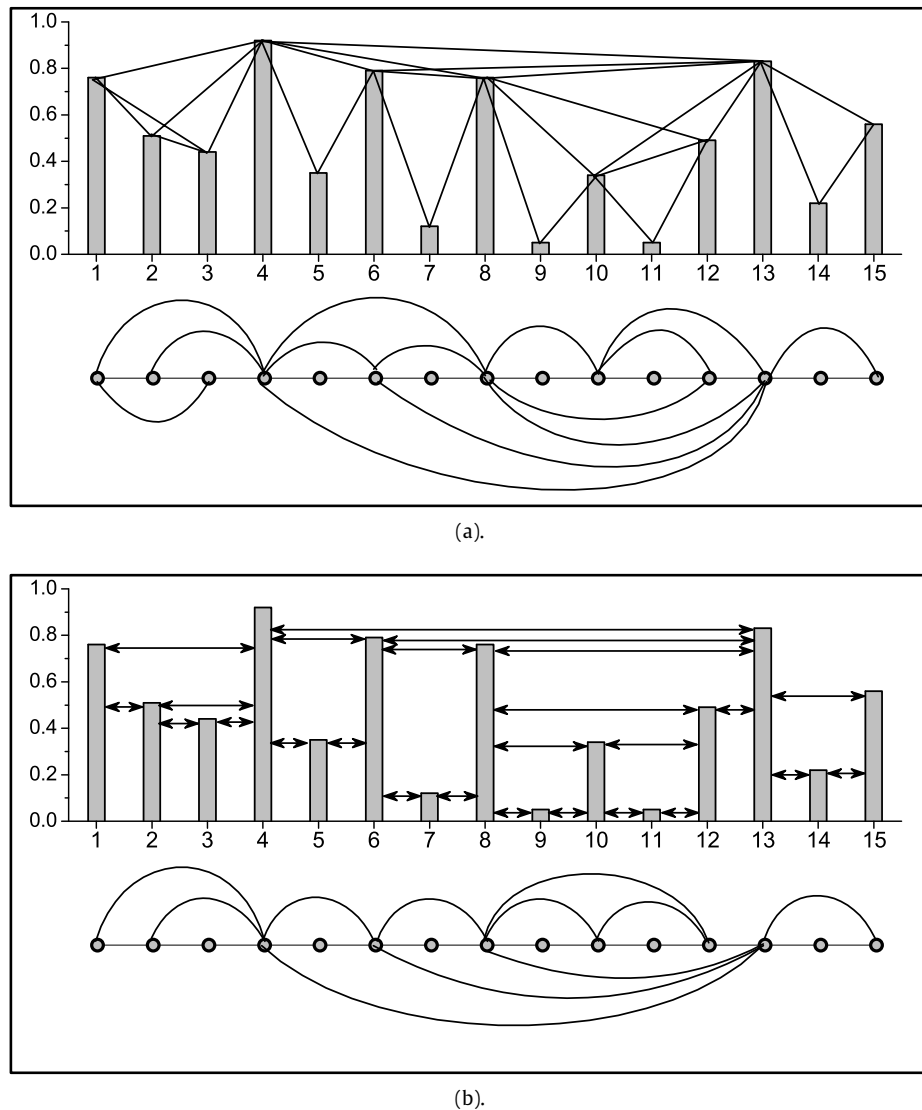


Fig. 1. An illustration of converting a time ordered measurement to the corresponding visibility graph: (a) A time series of 15 measurements is converted to a visibility graph and (b) the same series is converted to a horizontal visibility graph.

line joining x_i and x_j that does not intersect with any x_k located in between. The visibility criterion for HVG reads as

$$x_k < \min\{x_i, x_j\}, \tag{2}$$

and it is shown geometrically in Fig. 1(b) for the same time series shown in Fig. 1(a).

3. Sandbox algorithm

The SB algorithm for multifractal analysis of complex networks is well described in [20,35]. The algorithm is based on the fixed-size box-covering algorithm [36]. For the sake of completeness, here we provide the outline of the fixed-size box-covering algorithm, and subsequently the SB algorithm without claiming any originality. For a given probability measure μ (say) with a compact support in a metric space, one can define a partition sum as

$$Z_r = \sum_{\mu(B) \neq 0} [\mu(B)]^q; \quad \forall q \in R \tag{3}$$

where the summation runs over all different non-empty boxes B of size r , and q is the order number. The mass exponent $\tau(q)$ of the μ -measure is computed as

$$\tau(q) = \lim_{r \rightarrow 0} \frac{\ln Z_r(q)}{\ln r}. \tag{4}$$

The generalized fractal dimensions D_q of the measure μ are given by

$$D_q = \frac{\tau(q)}{q-1}; \quad \forall q \neq 1, \quad (5)$$

and for $q = 1$ the information dimension is given by,

$$D_1 = \lim_{r \rightarrow 0} \frac{Z_{1,r}}{\ln r}. \quad (6)$$

In the above expression the partition sum is measured as

$$Z_{1,r} = \sum_{\mu(B) \neq 0} \mu(B) \ln \mu(B). \quad (7)$$

In a complex network the probability measure μ of each box is taken as the ratio of the number of nodes covered by the box and the total number of nodes present in the entire network. The characteristics of the parameters like $\tau(q)$ and/or D_q , and other derived quantities like the multifractal spectrum $f(\alpha_q)$, provide important information on whether the network under consideration is multifractal or monofractal in nature. As for instance, if for a given object/series/distribution D_q is constant (varying) and $\tau(q)$ is a linear (nonlinear) function of q , then the object is mono- (multi-)fractal. Moreover, multifractality results in an inverted bell shaped spectrum of the Hölder exponent (α_q), whereas the same spectrum corresponding to a monofractal object converges to a delta function about the centroid $\alpha \approx 0.5$. The fixed-size box-covering algorithm is modified in the sandbox algorithm, where the center of each equal-sized (sand) box is chosen at random over the fractal object, and then the number of nodes present in the sandbox is counted. In the sandbox method the generalized fractal dimensions D_q are then evaluated as,

$$D_q = \frac{\partial}{\partial(\ln r)} \ln \langle [M(r)/M_0]^{q-1} \rangle \frac{1}{q-1}; \quad \forall q \neq 1 \quad (8)$$

where $M(r)$ is the number of nodes in a sandbox of radius r , M_0 is the total number of nodes in the network and $\langle \dots \rangle$ indicates that the quantity within the brackets is averaged over many SB centers chosen at random over the network. The information dimension D_1 is obtained through Taylor's expansion of D_q around $1 + dq$, and it reads as

$$D_1 = \frac{\partial}{\partial(\ln r)} \langle [M(r)/M_0] \rangle. \quad (9)$$

In order to implement the SB algorithm into computation now we outline the steps to be followed:

1. Set the radius $r \in [1, d]$ of the sandbox which will be used to cover the network having dimension d (say).
2. Cover the entire network by sandboxes of size r whose central nodes are selected at random over the network. Note that, if a node with large degree (known as a hub) is selected as the center of a sandbox, a large number of nodes would be covered within one box. This is an efficient way of box-covering. On the other hand, if a node with small degree is selected first, a few nodes would be covered within the box. As a result the partition sum in Eqs. (8) and (9) will change if we change the arrangement of sandboxes. To get rid of this problem we optimize the number of sandboxes needed to cover the entire network. Out of ten random combinations we select one which has the minimum number of box count.
3. Count the number of nodes $M(r)$ in each sandbox of radius r , and calculate the average $\langle [M(r)/M_0]^{q-1} \rangle$ and $\langle [M(r)/M_0] \rangle$ over the optimal number of sandboxes as described in the previous step.
4. Repeat steps (i)–(iii) for several different values of r and for a given q compute the slope of the $\ln(r)$ versus $X_q(r)$ plots, where we denote $X_q(r) \equiv \ln \langle [M(r)/M_0]^{q-1} \rangle$ for $q \neq 1$ and $X_1(r) \equiv \langle [M(r)/M_0] \rangle$, and then vary the exponent q over the desired range.

The multifractal mass exponent $\tau(q)$ is related to the generalized fractal dimension D_q through $\tau(q) = (q-1)D_q$. Knowing $\tau(q)$ the multifractal spectrum $f(\alpha_q)$ is computed via a Legendre transformation

$$f(\alpha_q) = q\alpha_q - \tau(q), \quad (10)$$

where $\alpha_q = -\partial\tau(q)/\partial q$ called the Lipschitz–Hölder exponent, is a measure of the strength of the singularity. While small α_q values are associated with large fluctuations, the large α_q values characterize small noise-like fluctuations.

4. Data

Nuclear emulsion data are used in this analysis. Ilford G5 nuclear emulsion pellicles of size $16 \text{ cm} \times 10 \text{ cm} \times 600 \mu\text{m}$ were horizontally irradiated with the ^{28}Si beam at an incident energy of 14.5 GeV/nucleon from the Alternating Gradient Synchrotron of Brookhaven National Laboratory. Similarly pellicles of size $18 \text{ cm} \times 7 \text{ cm} \times 600 \mu\text{m}$ were irradiated with the ^{16}O and ^{32}S beams at an incident energy of 200 GeV/nucleon each, obtained from the Super Proton Synchrotron at CERN. The primary interactions (also called events or stars) within the emulsion plates are found by following individual projectile

tracks along the forward as well as along the backward direction. The process is known as line scanning, and it was performed with Leitz microscopes under a total magnification of $300\times$. In emulsion experiment, on an event-by-event basis we count the multiplicity of tracks, identify the category of particles coming out of an interaction using the characteristics of the tracks formed by them, and measure the polar (θ) and azimuthal (φ) angles of the tracks. Koristka microscopes having a combined magnification of $1500\times$ were utilized for track counting and angle measurement purpose. According to the convention followed in emulsion experiments [37], the tracks resulting from secondary charged particles coming out of an event are categorized in the following way.

- (i) The shower tracks – caused by singly charged particles moving at relativistic speed. Most of which are charged π mesons. In an event their number is denoted by n_s .
- (ii) The gray tracks – caused mostly by the protons knocked out of the target nuclei due to the impact of the collision. In an event their number is denoted by n_g .
- (iii) The black tracks – caused by the heavy fragments that evaporate out of the spectator part of the target nuclei. In an event their number is denoted by n_b , and the total $n_h (= n_g + n_b)$ denotes the number of target fragments in an event.
- (iv) The projectile fragments – caused by the spectator part of the incident projectile nucleus. In an event their number is denoted by n_{pf} .

The details of emulsion experiments, track selection criteria and data acquisition techniques are well elaborated in [37]. To ensure that the target is either an Ag or a Br nucleus we impose a cut $n_h > 8$. For each incident beam 150 events were selected with the following criterion: $n_s > 50$ for the ^{28}Si events, $n_s > 100$ for the ^{16}O events and $n_s > 150$ for the ^{32}S events. The average shower multiplicity of the samples are, 81.68 ± 1.77 , 163.5 ± 2.61 and 246.85 ± 2.89 , respectively for the $^{28}\text{Si}+\text{Ag}/\text{Br}$, $^{16}\text{O}+\text{Ag}/\text{Br}$, and $^{32}\text{S}+\text{Ag}/\text{Br}$ events. The pseudorapidity (η), an approximation of the dimensionless boost parameter rapidity (y), is taken as the dynamical variable over which the analysis is performed. The η value of a track is computed from its polar angle (θ) as,

$$\eta = -\ln[\tan(\theta/2)]. \quad (11)$$

An accuracy of $\delta\eta = 0.1$ unit is achieved through the reference primary method of angle measurement. A single event η -distribution of shower tracks are highly fluctuating in nature over a more or less Gaussian shaped background. As for illustration, we show in Fig. 2(a) the η -distribution of shower tracks for an event taken from our ^{32}S sample with a bin width $\delta\eta = 0.1$. However, when summed/averaged over events, such fluctuations are smoothed out. The η -distribution shown in Fig. 2(b) is for the ^{32}S event sample, where one can see that the distribution can be well approximated by a Gaussian function as shown by the red smooth line. The local peaks of single event η -distribution, as shown in Fig. 2(a), are of our interest. The analysis is therefore, performed on an even-by-event (e-by-e) basis. It is to be noted that the Gaussian background undesirably obstructs the visibility of the height (number of tracks) located at a particular η (nodes of visibility graphs) from that located at other. Especially the nodes located on the left hand side of the peak of the Gaussian get obstructed from those located on the right hand side of the peak and vice versa. In order to get rid of this problem we take the difference of successive bin contents as,

$$\delta n(\eta_i) = dn_{\eta_{i+1}} - dn_{\eta_i}, \quad (12)$$

and as required by the mapping criteria (1) and (2), project the modified distribution onto a positive (δn , η) plane. Here dn_i is the number of tracks falling within $\delta\eta$ about a particular η_i . Fig. 2(c) shows the modified form of the distribution that is presented in Fig. 2(a). It seems that the single event η distribution so modified reasonably eliminates the Gaussian background, while relative fluctuations present in the event are retained. Note that the local fluctuations could have also been detrended by subtracting the fitted Gaussian background, but the χ^2 value of such a fit is never reliable.

5. Simulation

As mentioned before, the experimental results are systematically compared with the Ultra-relativistic Molecular Dynamics (UrQMD) [33,34] simulation. The rationale of using a transport model like the UrQMD is that it treats the final freeze-out stage dynamically, does not make any equilibrium assumption and describes the dynamics of a hadron gas like system very well in and out of the chemical and/or thermal equilibrium. In the present case neither the colliding nuclei are too heavy, nor the collision energies are extremely high. Hence a local thermal and/or chemical equilibrium are/is very unlikely to be achieved. To describe a non-equilibrium many-body dynamics, a transport model is a natural choice. The UrQMD model is applicable over a wide range of energies starting from $\sqrt{s_{NN}} \sim 5$ GeV and ending up at $\sqrt{s_{NN}} = 200$ GeV. In this scheme particle production at high-energy interactions is implemented by the color string fragmentation mechanism similar to that of the Lund model. The UrQMD code has been successfully used to reproduce the particle density distributions and the transverse momentum spectra of various particle species in proton–proton, proton–nucleus and nucleus–nucleus collisions.

We use the UrQMD code (version 3.4) in its default setting and generate the minimum bias event samples in the laboratory frame, separately for the Ag and Br targets, and for ^{28}Si , ^{16}O and ^{32}S projectile nuclei at their respective incident energies mentioned above. For each projectile the Ag and Br events are mixed up maintaining the proportional abundances of these

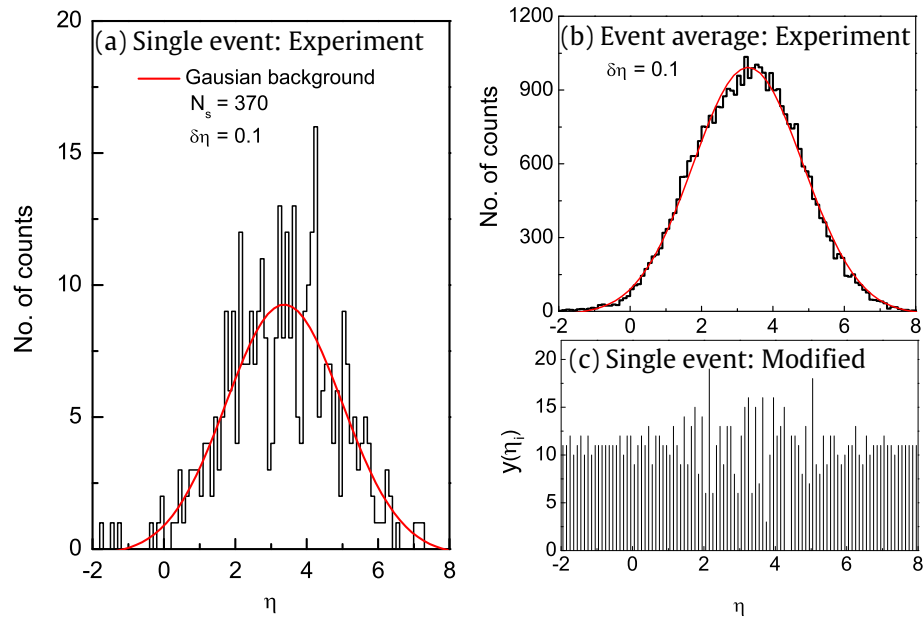


Fig. 2. (a) Pseudorapidity distribution of an event from the ^{32}S event sample. The shower track multiplicity of the event is 370, (b) pseudorapidity distribution of the ^{32}S event sample with Gaussian fit (red smooth line) and (c) a modified distribution [Eq. (12)] of the same event as shown in (a).

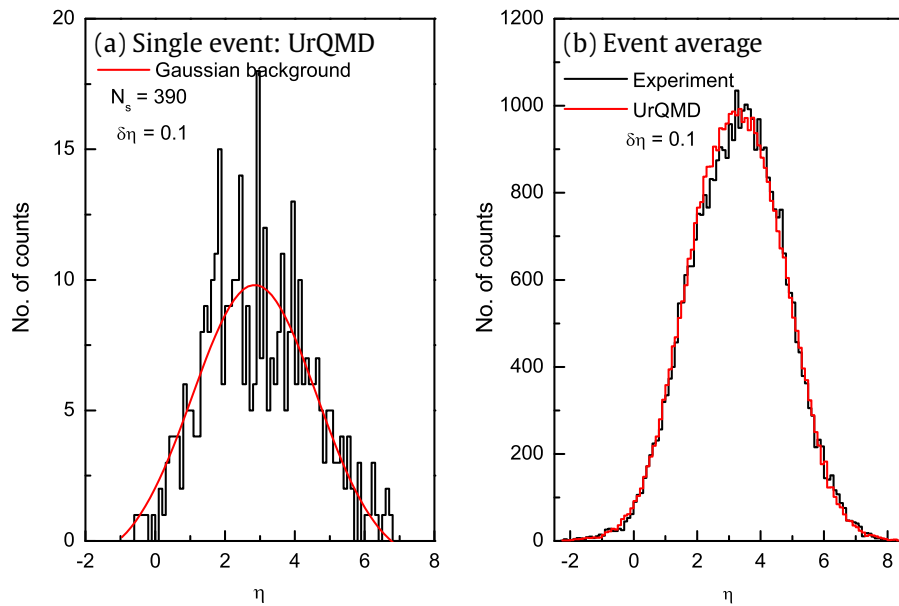


Fig. 3. (a) Pseudorapidity distribution of a $^{32}\text{S}+\text{Ag}/\text{Br}$ event, (b) pseudorapidity distribution of the experimental $^{32}\text{S}+\text{Ag}/\text{Br}$ sample is compared with the UrQMD simulation.

nuclei in G5 emulsion. Information regarding the charged mesons are retained for subsequent analysis. From each minimum bias sample we select a subsample that matches the respective experimental multiplicity and pseudorapidity distributions. For each projectile the final sample of simulated events is five times as large as the corresponding experiment. Like the single event η -distributions of experiment, the simulated events too exhibit rapid fluctuations as shown in Fig. 3(a). In Fig. 3(b) we compare the UrQMD generated η -distribution for the $^{32}\text{S}+\text{Ag}/\text{Br}$ interaction with the corresponding experiment. One can see that the agreement between experiment and simulation is fairly good. Similar observation could also be made for the other two (^{28}Si and ^{16}O induced) interactions.

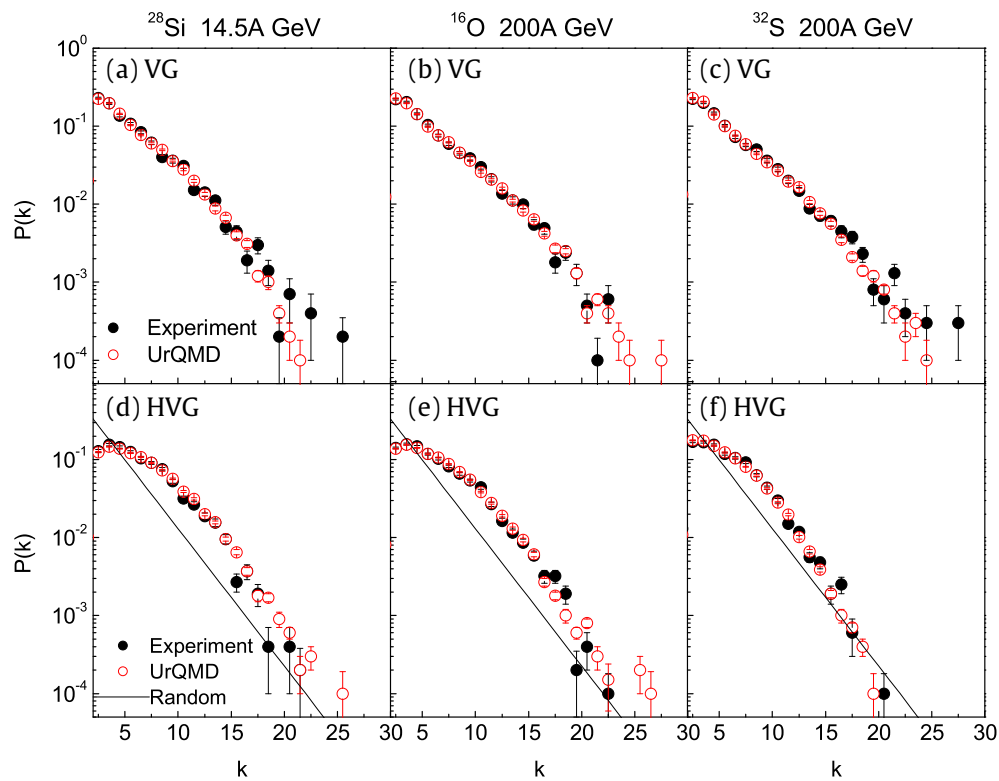


Fig. 4. Combined degree distributions of all the VGs (upper panel) and HVGs (lower panel) generated from the ^{28}Si data (left), ^{16}O data (middle) and ^{32}S data (right). The straight lines in the HVG plots follow Eq. (13).

6. Results

6.1. Degree distribution of visibility graph

On an e-by-e basis we convert the modified η -distributions (as mentioned before) into the corresponding visibility and horizontal visibility graphs, and then compute the degree of each of the nodes present in the graphs. For each sample we have as many graphs as the number of events present in the sample. The degree distributions of individual events are then combined to obtain the degree distribution $P(k)$ for an entire event sample. In Fig. 4 we show such distributions for all three interactions studied, where the upper panels show the results derived from the VG and the lower panels represent the corresponding HVG. The UrQMD simulated distributions are also plotted along with the respective experiment. The straight lines in the HVG plots follow the equation:

$$P(k) = \frac{1}{3} \left(\frac{2}{3} \right)^{k-2}. \quad (13)$$

This represents the analytical form of the degree distribution of the HVG associated with a random (time ordered) series [5]. To evaluate the exponent γ the tail region ($k \geq 10$) in the log–log plot of $P(k)$ can be fitted to a power-law like $P(k) \sim k^{-\gamma}$. The exponent is an important parameter in visibility graph analysis. It is a scale free parameter for a large number of real networks, and in some cases the exponent is related to the Hurst exponent of the underlying signal [6,12] from where the graph is constructed. We find that for all three interactions as well as for both VG and HVG $\gamma \sim 8$. Also we do not see any statistically significant difference between the data and the simulation. Though the shape of the $P(k)$ distribution obtained from VGs is not quite identical to that obtained from the HVGs, specially in the low k (< 10) region, but that does not significantly affect the γ value. It has been pointed out that the γ exponent calculated from the aforementioned method has some intrinsic disadvantages, and its value should be determined on the basis of a maximum-likelihood (ML) method as [38],

$$\gamma = 1 + n \left[\sum_{i=1}^n \log \frac{k_i}{k_{\min}} \right]^{-1}. \quad (14)$$

Here n is the total number of measured values of k_i taken into account, and k_{\min} is the smallest value of k ($= 10$) for which the power-law behavior holds. The ML estimated γ values are given in Table 1. The exponents obtained from the HVG approach are slightly larger than the corresponding VG values. However all these values are significantly larger than what

Table 1The ML estimated values of the exponent γ , see Eq. (14).

Data sample	VG			HVG		
	^{28}Si	^{16}O	^{32}S	^{28}Si	^{16}O	^{32}S
Experiment	4.892	4.756	4.566	5.503	5.207	5.681
UrQMD	4.960	4.710	4.838	5.252	5.335	5.764

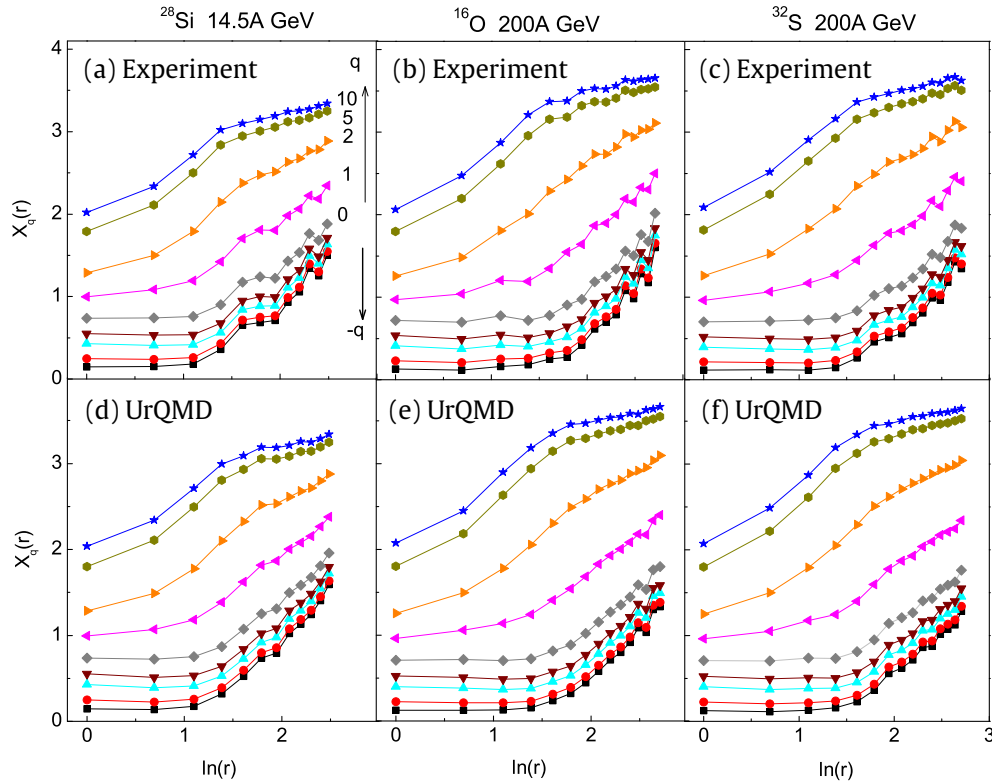


Fig. 5. Scaling curves for the sandbox algorithm applied to the visibility graph networks constructed from the event-wise modified η -distributions. Results obtained from the ^{28}Si -data, ^{16}O -data and ^{32}S -data are shown side by side, and the corresponding UrQMD predictions are given in the lower panel. The curves are drawn for $q = 0, \pm 1, \pm 2, \pm 5, \pm 10$.

was observed for long-range correlated time series [6]. The overall results of our degree distribution show that the scale freeness property of $P(k)$ is retained even in the visibility and horizontal visibility graphs generated from the η -distributions of charged mesons produced in high-energy AB collisions, but the exponent γ cannot distinguish the experiment from the simulation, the particle production mechanism to a large extent being purely speculative in nature in the latter case. Therefore, we argue that the degree distribution and its power-law scaling cannot be taken as suitable measures for the heavy-ion collision data.

6.2. Multifractality by sandbox method

Following the sandbox algorithm we compute $X_q(r) \equiv \ln\langle [M(r)/M_0]^{q-1} \rangle$ for $q \neq 1$ and $X_1(r) \equiv \langle [M(r)/M_0] \rangle$ from the visibility as well as from the horizontal visibility graphs obtained on an e-by-e basis, and then the quantities are averaged over the entire event sample. In that sense the multifractal parameters that we are going to study, have actually their sample averaged values. The event averaged values of $X_q(r)$ for $q \neq 1$ and $X_1(r)$ calculated in the VG-SB approach are plotted against $\ln(r)$ in Fig. 5, and similar plots obtained from the HVG-SB approach are shown in Fig. 6. In both the figures the $X_q(r)$ functions are shown for some selective values of q , though they are calculated for $q = -10$ to $+10$ with an incremental step of 0.25. The box-size is varied as: $r \in (1, 12)$ for the ^{28}Si data, and $r \in (1, 15)$ for the ^{16}O and ^{32}S data. Apparently, the $X_q(r)$ versus $\ln(r)$ plots for all three different interactions are identical, and the difference between the data and corresponding simulation predictions are also marginal. At this moment we do not give much emphasis on the apparent similarity in the behavior of the $X_q(r)$ functions obtained for different interactions and for the simulated data sets. Rather a linear rise of these functions over a reasonable range of $\ln(r)$ is what we require, as this is going to affect the accuracy of measurement of multifractal parameters to be derived from the $X_q(r)$ plots. From Figs. 5 and 6 we see that the functions $X_q(r)$ are approximately linear over the interval $5 \leq r \leq 12$ for the ^{28}Si data and over $7 \leq r \leq 15$ for the ^{16}O and ^{32}S data.

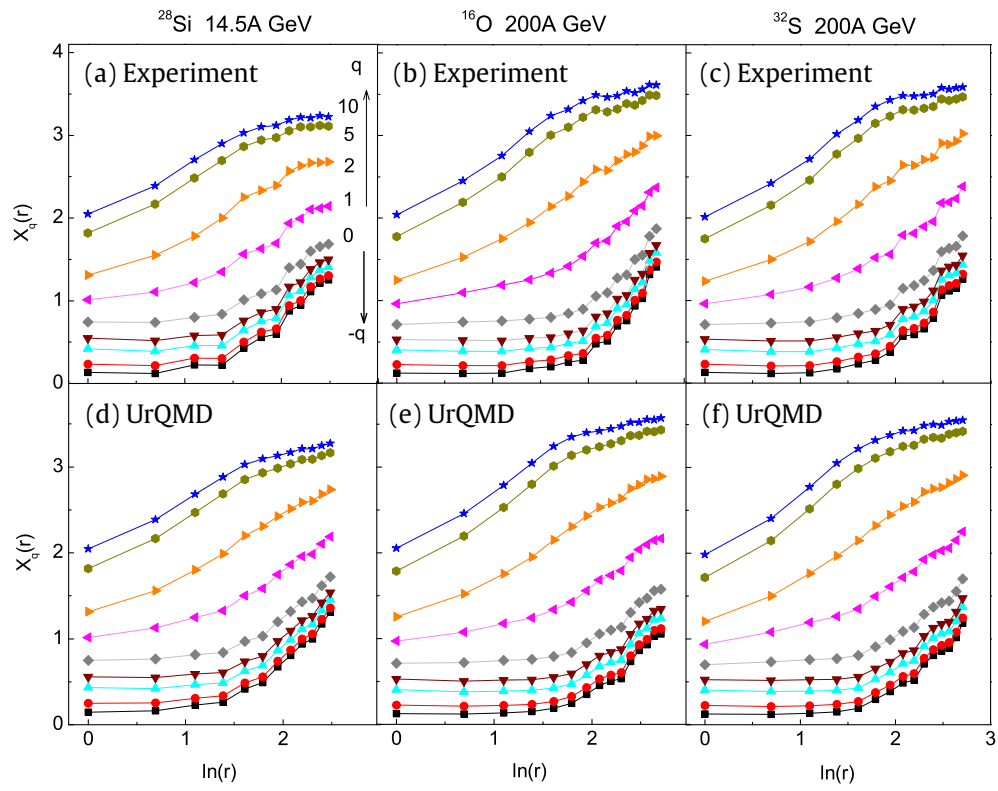


Fig. 6. The same as in Fig. 5 but for the horizontal visibility graph analysis.

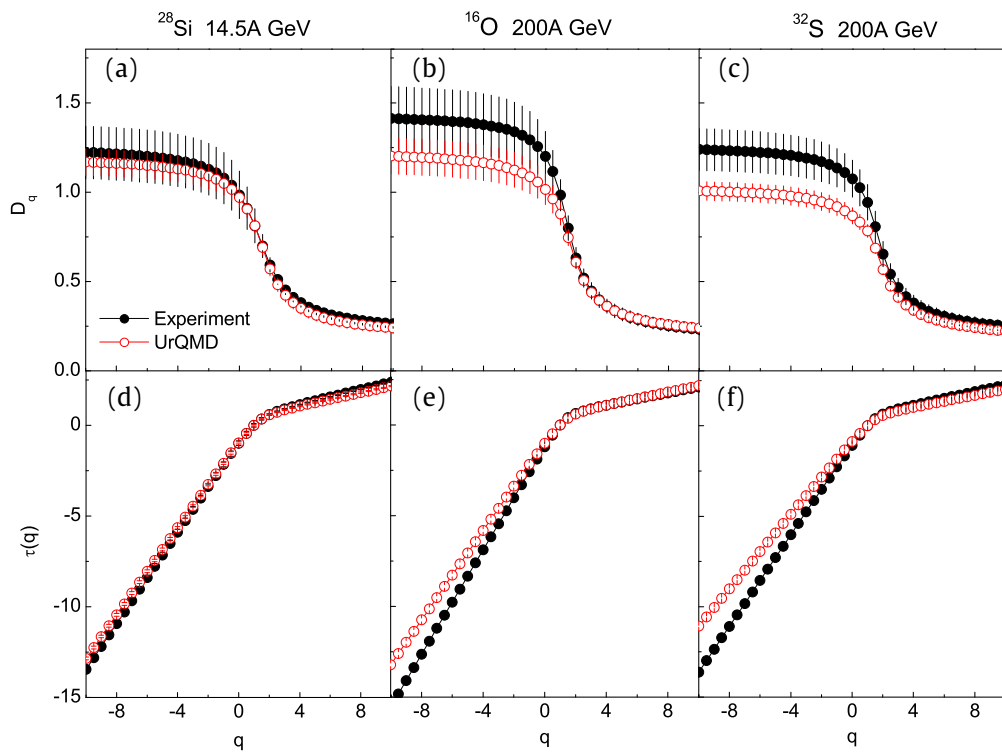


Fig. 7. The order dependence of the generalized fractal dimensions (upper panel) and the multifractal mass exponents (lower panel) calculated from the visibility graph analysis.

The generalized fractal dimensions D_q are calculated from a linear regression of the partition functions as shown in Figs. 5 and 6. The D_q values are plotted against order number q in the upper panel of Figs. 7(a-c) and 8(a-c), respectively for

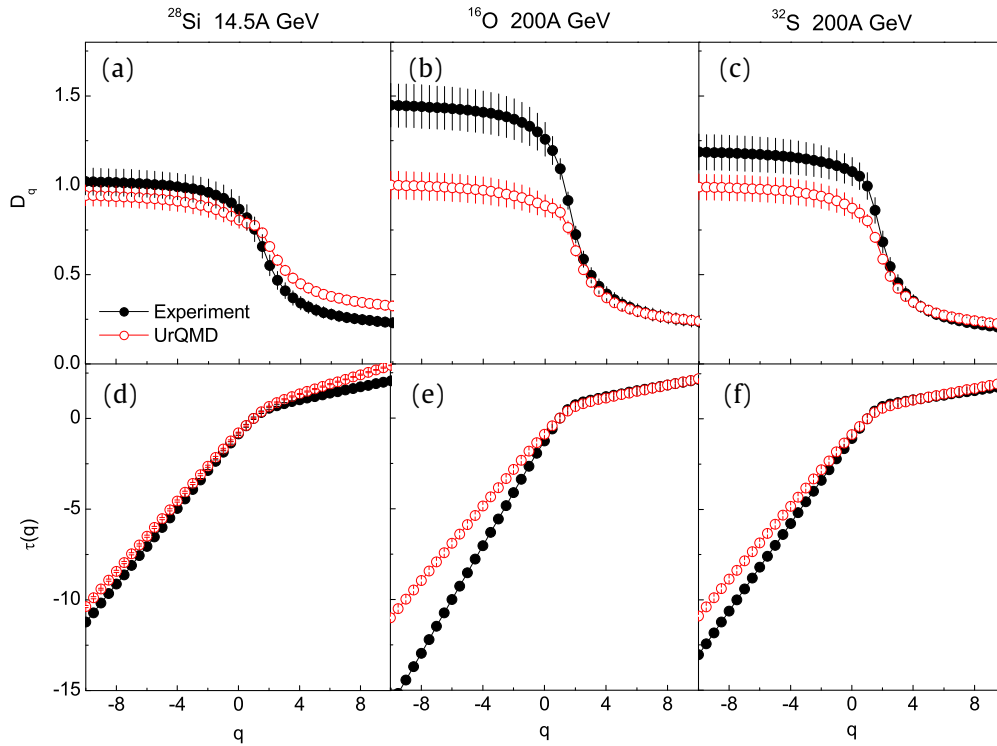


Fig. 8. The same as in Fig. 7 but for the horizontal visibility graph analysis.

the VG–SB and HVG–SB methods. The UrQMD model estimates are also included in these figures. In the lower panel of these figures we show the plots of corresponding multifractal mass exponents $\tau(q) = (q - 1)D_q$. Now we see the relative difference among the three interactions and two approaches. It is known to us that the fractal dimensions of monofractal signals are independent of order number, and consequently $\tau(q)$ becomes a linear function of q . Multifractal signals on the other hand, result in an order dependent D_q and the corresponding $\tau(q)$ is a nonlinear function of q . The difference $\Delta D_q = \max D_q - \min D_q$ is sometimes considered as a measure of the degree of multifractality (DoM) in the underlying process. In the present investigation we shall quantify the DoM from multifractal singularity spectrum $f(\alpha_q)$, which is known to be a better parameter for measuring DoM. Our first impression from Figs. 7 and 8 is that, the sandbox algorithm applied to the VG as well as to the HVG networks constructed from the η -distributions of the charged mesons produced in nuclear collisions, efficiently produces the multifractal behavior as observed in our previous analyses for the same sets of data [39,40]. Some important observations related to these figures are: (a) the ΔD_q value is maximum for the ^{16}O data and minimum for the ^{28}Si data, (b) the experimental D_q values are consistently higher than the respective simulated values for $q \lesssim 2$, but excepting the HVG–SB result for $^{28}\text{Si}+\text{Ag}/\text{Br}$ interaction [Fig. 8(a)] the simulated values for $q > 2$ almost match the corresponding experiment, (c) the difference between the experimental and simulated values of D_q for $q \lesssim 2$ is also largest for the ^{16}O -induced interaction and it is smallest for the ^{28}Si -induced interaction, while the values for ^{32}S events lie in between the other two, and lastly (d) in all cases the VG–SB and HVG–SB methods do not differ too much from each other. The $\tau(q)$ plots are consistent with the respective D_q plots. Observation (b) implies that for $q < 1$ the quantity $\langle [M(r)]^{q-1} \rangle$ in Eq. 4 is dominated by a comparatively smaller number of large fluctuations, whereas for $q > 1$ a large number of small fluctuations contribute to the overall coarse structure of the distributions. In AB collisions at the present energy scale the chance of a few large fluctuations occurring in every event is rare, whereas a large number of small fluctuations basically arise due to statistical reasons. In that sense the observed difference in $D_{q>1}$ between the experiment and simulation may be attributed to the existence of some large fluctuations in the experiment which are absent in the simulation. Lastly, for the ^{28}Si interaction identical values of D_q observed from the experiment and simulation might be due to the dominance of the statistical noise since the event multiplicity for the interaction is not as large as the other two interactions studied.

As far as multifractal analysis is concerned, the multifractal spectrum $f(\alpha_q)$ is probably the most important quantity. The $f(\alpha_q)$ spectrum can be used to quantify the DoM in the underlying process. To do that the spectrum is parametrized as [41]

$$f(\alpha_q) = A + B(\alpha_q - \alpha_0) + C(\alpha_q - \alpha_0)^2, \quad (15)$$

where α_0 is the peak position of the spectrum, B is an asymmetry parameter that vanishes for a symmetric spectrum, $B > 0$ for left-skewed and $B < 0$ for right skewed spectrum, and parameters A and C decide the overall shape of the spectrum. The left side of $f(\alpha_q)$ spectrum corresponds to $q > 0$ and it filters out the large fluctuations, while the right side of the

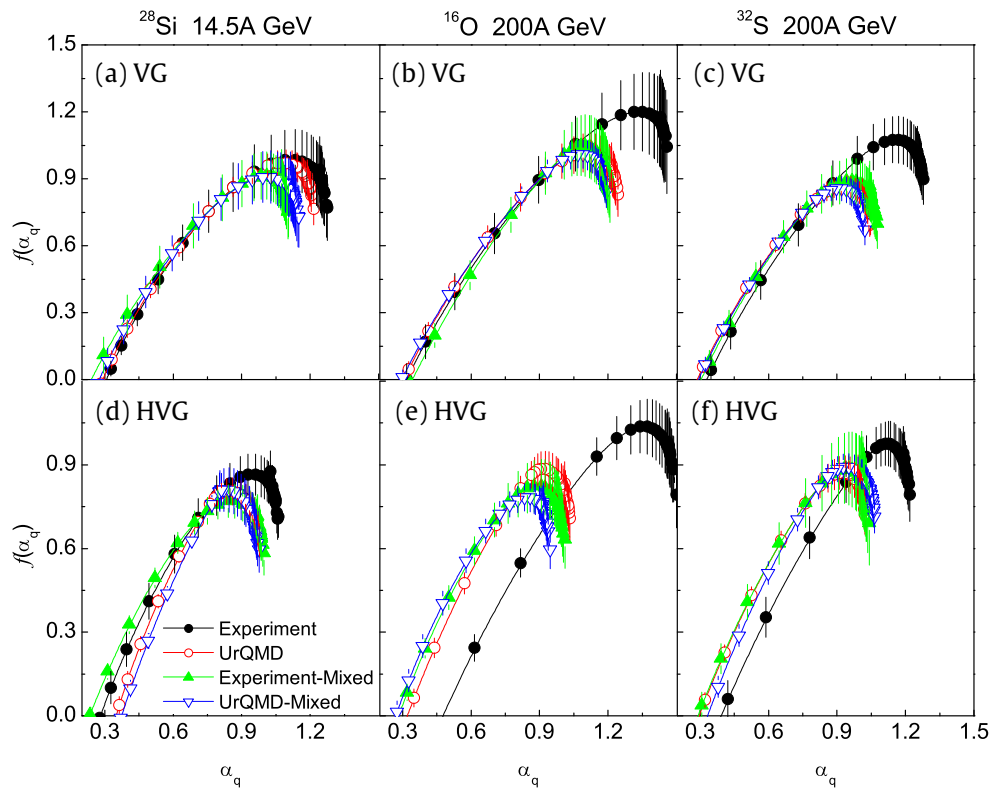


Fig. 9. Multifractal spectra obtained from the VG (upper panel) and HVG (lower panel) analysis for the interactions studied. Predictions from the mixed events are shown (follow text for details). The lines joining points represent Eq. (17) with the best fitted parameters given in Table 2.

Table 2

The peak position α_0 , the FWHM $\Delta\omega$ and the asymmetry parameter r of the multifractal spectra shown in Fig. 9.

Data sample	VG			HVG		
	α_0	$\Delta\omega$	r	α_0	$\Delta\omega$	r
²⁸Si 14.5A GeV						
Experiment	1.091	0.806	0.550	0.927	0.629	0.553
UrQMD	1.052	0.755	0.550	0.853	0.504	0.585
Experiment-Mixed	0.990	0.712	0.555	0.844	0.613	0.588
UrQMD-Mixed	0.967	0.684	0.558	0.850	0.459	0.594
¹⁶O 200A GeV						
Experiment	1.297	0.964	0.557	1.317	0.759	0.530
UrQMD	1.085	0.758	0.556	0.910	0.545	0.580
Experiment-Mixed	1.067	0.659	0.580	0.874	0.569	0.572
UrQMD-Mixed	1.051	0.706	0.562	0.828	0.533	0.549
³²S 200A GeV						
Experiment	1.128	0.762	0.565	1.088	0.638	0.607
UrQMD	0.914	0.591	0.559	0.907	0.574	0.573
Experiment-Mixed	0.937	0.602	0.572	0.918	0.573	0.561
UrQMD-Mixed	0.896	0.568	0.569	0.934	0.574	0.586

spectrum corresponds to $q < 0$ and it is associated with the small noise-like fluctuations. Another parameter of interest is the width of the spectrum $W = \alpha_{\max} - \alpha_{\min}$, where α_{\max} and α_{\min} are the values of α_q for which $f(\alpha_q) = 0$. Parameters α_0 , B and W are used as a measure of the “complexity” of the process under consideration [42], and therefore, they are known as the “complexity parameters”. Multifractal spectrum generated from a random process is expected to peak at $\alpha_0 = 0.5$ with a marginal width. For long-range correlated signals $\alpha_0 > 0.5$. The width W measures the range of fractal exponents required to describe the signal, and therefore, it measures the degree of multifractality of the signal. The wider the range of fractal exponents is, wider will be the $f(\alpha_q)$ spectrum that indicates a richer structure of the process. Formally an asymmetry parameter can be defined as [42]

$$r = (\alpha_{\max} - \alpha_0) / (\alpha_0 - \alpha_{\min}). \quad (16)$$

For a symmetric spectrum $r = 1$, for a right skewed distribution $r > 1$ and for a left skewed distribution $r < 1$. The asymmetry parameter indicates which fractal exponents are dominant. For instance a right skewed spectrum is dominated by small values of α_q that indicates multifractal nature of small noise-like fluctuations, while a left skewed spectrum indicates dominance of large α_q values and therefore, a multifractal nature of large fluctuations. The former one is characterized by more regular *smooth looking* processes, while the latter corresponds to rough *fine structure* processes. In short, a wide right skewed spectrum with $\alpha_0 > 0.5$ corresponds to a more complex process. Note that a quadratic function may not always be able to describe the observed $f(\alpha_q)$ spectrum, as it is found in the present analysis. In such cases a fourth degree polynomial

$$f(\alpha_q) = A + B(\alpha_q - \alpha_0) + C(\alpha_q - \alpha_0)^2 + D(\alpha_q - \alpha_0)^3 + E(\alpha_q - \alpha_0)^4, \quad (17)$$

is used [42]. The asymmetry in this case depends on the first and third order coefficients, namely B and D .

The multifractal spectra $f(\alpha_q)$ obtained from this analysis are plotted against the Hölder exponents α_q in Fig. 9. Results from the VG–SB (upper panel) and HVG–SB (lower panel) techniques are included in the same figure. Along with the UrQMD results, predictions for mixed events are also included in this figure. The mixed event samples are prepared by mixing the track information belonging to individual events at random, keeping the overall multiplicity and η -distributions unchanged. Our intention is to eliminate the noise present in the experimental event samples. Since the random mixing procedure unambiguously destroys particle correlations (if there are any) present in the data sample, a mixed event sample is a good representation of the statistical noise. According to the theory of fractals an inverted parabolic nature of $f(\alpha_q)$ spectrum is a sign of multifractality of the underlying dynamics. The $f(\alpha_q)$ spectra as shown in the figure are all indicating similar nature of multifractality in the respective η -distributions. Expectedly the event mixing process reduces the DoM in the data, and the $f(\alpha_q)$ spectra for mixed events almost coincide with the model simulation. However, the DoM in the UrQMD-mixed events is, within error bars, identical to the actual UrQMD generated value. From this observation we understand that the multifractal characteristics of the UrQMD simulated events is mainly due to statistical noise. Therefore, the difference in multifractal measures between an experiment and its UrQMD /mixed-event counterpart might be due to one or more dynamical effects present in the particle production mechanism.

To quantify the DoM or complexity, each $f(\alpha_q)$ spectrum is fitted to Eq. (17) and is shown by a solid curve in the diagrams. Note that instead of measuring the width W of the $f(\alpha_q)$ spectrum we measure its half width at full maximum (FWHM) $\delta\omega$, since the spectra obtained here are truncated much above $f(\alpha_{\max}) = 0$. The set of chaoticity parameters, namely the peak position α_0 , the FWHM $\delta\omega$ and the asymmetry parameter r are given in Table 2. From the table it is now clear that fine structure like small fluctuations dominate the η -distributions of the interactions considered in the present investigation. However, the contribution of some nontrivial hitherto unknown dynamics is not negligible, especially for the $^{16}\text{O}+\text{Ag}/\text{Br}$ and $^{32}\text{S}+\text{Ag}/\text{Br}$ interactions.

At this point it would be prudent to discuss the effectiveness of the visibility graph method vis-a-vis that of the detrended method(s) of analysis of multiparticle emission data [31]. Particle density fluctuations contain a statistical component (called noise), which is ordinarily Poisson distributed, and a non-statistical one whose character is not known. We are interested in characterizing the latter in terms of (multi)fractality. However, we are not very much aware of any quantitative method that can filter the statistical part out of the total fluctuation. One can only speculate that (i) the strength of a local singularity will be higher if both statistical and non-statistical components contribute to it, and (ii) being Poisson distributed it is very unlikely only for a noise to yield a very strong local singularity. Equivalently, if in the singularity spectrum one finds a systematic reduction in the values of the singularity strength then a probable reason of that should be the noise elimination. The spectrum of the singularity strength obtained by using the detrended method(s) is quite different in nature from that obtained by using the VG–sand box algorithm. The detrended methods gave us smooth, almost symmetric and/or slightly right sided spectra, which barring the left hand side of the $^{28}\text{Si}+\text{Ag}(\text{Br})$ experiment, was never significantly different from the respective simulation. In [31] this feature was interpreted in terms of a large number of small fluctuations and a small number of large fluctuations [43,44], which were in principle present both in the experiments and in the simulations. When it comes to the question of VG/HVG method(s), we first observe that the $f(\alpha_q)$ spectra are strongly left sided, and on several occasions the experimental singularity spectrum is significantly different from the corresponding simulation. The left side of each spectrum which is dominated by small α_q values and therefore, by ‘rough’ fluctuations, gradually rises to reach the respective peak value. The spectrum then abruptly drops down to some extent from the peak position towards its right, suppressing the ‘smooth’ fluctuations almost to a monofractality. This kind of left sided asymmetry in $f(\alpha_q)$ may arise out of superimposition of partonic/hadronic level cascades [45,46].

Ideally the detrended methods of analysis should be applied to a sufficiently long time (or equivalently any other) series, so that the local trend(s) or the local average(s) are minimally influenced by statistical uncertainties, and the fluctuations either about a local trend or about a local average are statistically significant. For a finite sized η -distribution that can at best be divided into $\sim 10^2$ intervals, this unfortunately is not the case, and therefore, the results obtained are to some extent representative in nature. Moreover, in the detrended method we have used only a linear local trend, which may not always be the case. The limitation of the detrended method is also reflected in the fact that we rarely find significant difference between experiment and simulation. Though our data could be characterized in terms of (multi)fractality, we have never been sure about how to eliminate the statistical components present in the fluctuations. On the contrary in the VG/HVG method, the issue of statistical noise has perhaps been taken care of. This is reflected in the $f(\alpha_q)$ spectrum and also in the plots of other (multi)fractal parameters. At least in some regions significant differences between experiment and simulation are observed. In ^{16}O and ^{32}S cases the VG/HVG experiments are in particular quite different from the corresponding simulation. The rise in

the $f(\alpha_q)$ spectrum in the left side of the peak position is gradual, and is never as sharp as it is in the detrended method(s). The region dominated by ‘rough’ (large) fluctuations is therefore, multifractal in nature. In the right side of the $f(\alpha_q)$ distribution we notice that the singularity strengths obtained from the VG/HVG method(s) are restricted within a very narrow range, and are never quite as large as those obtained from the detrended methods ($\alpha_q \approx 1.9$). This shows that the contribution of statistical noise has perhaps been taken care of, restricting thereby the small fluctuations almost to a monofractality. We therefore, conclude that in the context of addressing the issue of statistical noise, when we have to analyze not a very long data series, the VG–sand box algorithm is certainly a better choice, and the results obtained thereof are more accurate than those obtained from the detrended method(s).

7. Discussion

In this article we present a multifractal analysis of multiparticle production data using the visibility graph and sandbox algorithm. The event-wise η -distribution of charged particles produced in $^{28}\text{Si}+\text{Ag}/\text{Br}$ interaction at 14.5A GeV, and $^{16}\text{O}+\text{Ag}/\text{Br}$ and $^{32}\text{S}+\text{Ag}/\text{Br}$ interactions both at 200A GeV, are converted to the corresponding visibility and horizontal visibility graphs. The sandbox algorithm is then applied to measure the multifractal parameters. The degree distributions of the visibility graphs obtained from each experimental event sample and the respective UrQMD simulation are identical in nature. Both result in approximately the same tail exponent (γ). The scale freeness property of the degree distribution as observed for long-range correlated signals [5,6], is therefore, retained in the multiparticle emission data as well. However, the γ value is found to be far above the limiting value ($\gamma \sim 3$) required for long-range series. The sandbox algorithm applied to the VGs and HVGs generated from the η -distributions successfully produce the multifractal properties of the interactions studied [39,40]. We also observe that the present graph theoretical approach of multiparticle data analysis has the potential to differentiate between the dynamical (non-statistical) contribution of fluctuations in the underlying η -distributions from the statistical noise. In our previous studies it was found that the detrended and other methods are not very effective to discriminate the data from the simulation [30,31,39,40]. In this regard the method presented here appears to be more useful than the conventional methods used for multifractal characterization. The small noise-like fluctuations associated with a very narrow range of Hölder exponents, are almost monofractal in nature. The large fluctuations on the other hand exhibit multifractal characteristics, which can potentially be seen as the augmentation of a scale invariant cascade mechanism in particle production process.

References

- [1] C. Song, S. Havlin, H.A. Makse, *Nature* 433 (2005) 392.
- [2] J. Zhang, M. Small, *Phys. Rev. Lett.* 96 (2006) 238701.
- [3] X.-K. Xu, J. Zhang, M. Small, *Proc. Natl. Acad. Sci. USA* 105 (2008) 19601.
- [4] L. Lacasa, B. Luque, F. Ballesteros, J. Luque, J.C. Nuno, *Proc. Natl. Acad. Sci. USA* 105 (2008) 4972.
- [5] B. Luque, L. Lacasa, F. Ballesteros, J. Luque, *Phys. Rev. E* 80 (2009) 046103.
- [6] L. Lacasa, B. Luque, J.L. Luque, J.C. Nuño, *Europhys. Lett.* 86 (2009) 30001.
- [7] R.V. Donner, Y. Zou, J.F. Donges, N. Marwan, J. Kurths, *Phys. Rev. E* 81 (2010) 015101.
- [8] C.B. Li, H. Yang, T. Komatsuzaki, *Proc. Natl. Acad. Sci. USA* 105 (2008) 536.
- [9] N. Marwan, J.F. Donges, Y. Zou, R.V. Donner, J. Kurths, *Phys. Lett. A* 373 (2009) 4246.
- [10] C. Liu, W.X. Zhou, *J. Phys. A* 43 (2010) 495005.
- [11] Z.-K. Gao, N.-D. Jin, *Chaos* 19 (2009) 033137.
- [12] L. Lacasa, R. Toral, *Phys. Rev. E* 82 (2010) 036120.
- [13] W.J. Xie, W.X. Zhou, *Physica A* 390 (2011) 3592.
- [14] J.L. Liu, Z.G. Yu, V. Anh, *Phys. Rev. E* 89 (2014) 032814.
- [15] E. Canessa, *J. Phys. A* 33 (2000) 3637.
- [16] V.V. Anh, Q.M. Tieng, Y.K. Tse, *Int. Trans. Oper. Res.* 7 (2000) 349.
- [17] Z.G. Yu, V. Anh, K.S. Lau, *Phys. Rev. E* 64 (2001) 031903.
- [18] G. Palla, I. Derényi, I. Farkas, T. Vicsek, *Nature* 435 (2005) 814.
- [19] T. Tél, Á. Fülöp, T. Vicsek, *Physica A* 159 (1989) 155.
- [20] J.L. Liu, Z.G. Yu, V. Anh, *Chaos* 25 (2015) 023103.
- [21] C.-Y. Wong, *Introduction to High-Energy Heavy-Ion Collisions*, World Scientific, Singapore, 1994.
- [22] T. Burnett, et al., JACEE Collaboration, *Phys. Rev. Lett.* 50 (1983) 2062.
- [23] A. Bialas, R. Peschanski, *Nuclear Phys. B* 273 (1986) 703.
- [24] G. Paladin, A. Vulpiani, *Phys. Rep.* 156 (1987) 147.
- [25] T.C. Halsey, M.H. Jensen, *Physica D* 23 (1986) 112.
- [26] R.C. Hwa, *Phys. Rev. D* 41 (1990) 1456.
- [27] F. Takagi, *Phys. Rev. Lett.* 72 (1994) 32.
- [28] J.W. Kantelhardt, S.A. Zschiegner, E. Koscielny-Bunde, S. Havlin, A. Bunde, H.E. Stanley, *Physica A* 316 (2002) 87.
- [29] G.-F. Gu, W.X. Zhou, *Phys. Rev. E* 82 (2010) 011136.
- [30] P. Mali, S. Sarkar, S. Ghosh, A. Mukhopadhyay, G. Singh, *Physica A* 424 (2015) 25.
- [31] P. Mali, A. Mukhopadhyay, G. Singh, *Physica A* 450 (2016) 323.
- [32] P. Mali, A. Mukhopadhyay, S.K. Manna, P.K. Haldar, G. Singh, *Modern Phys. Lett. A* 32 (8) (2017) 1750024.
- [33] S.A. Bass, M. Belkacem, M. Bleicher, M. Brandstetter, L. Bravina, C. Ernst, L. Gerland, M. Hofmann, S. Hofmann, J. Konopka, G. Mao, L. Neise, S. Soff, C. Spieles, H. Weber, L.A. Winckelmann, H. Stöcker, W. Greiner, C. Hartnack, J. Aichelin, N. Amelin, *Prog. Part. Nucl. Phys.* 41 (1998) 225.
- [34] M. Bleicher, E. Zabrodin, C. Spieles, S.A. Bass, C. Ernst, S. Soff, W. Weber, H. Stöcker, W. Greiner, *J. Phys. G* 25 (1999) 1859.
- [35] Z.-G. Yu, H. Zhang, D.-W. Huang, Y. Lin, V. Anh, *J. Stat. Mech.* (2016) 033206.

- [36] T.C. Halsey, M.H. Jensen, L.P. Kadanoff, I. Procaccia, B.I. Shraiman, *Phys. Rev. A* 33 (1986) 1141; *Phys. Rev. A* 34 (1986) 1601 (erratum).
- [37] W.H. Barkas, *Nuclear Research Emulsions Vol I and II*, Academic, New York, 1963.
- [38] M.E.J. Newmann, *Contemp. Phys.* 46 (2005) 323.
- [39] M.K. Ghosh, A. Mukhopadhyay, G. Singh, *J. Phys. G* 32 (2006) 2293.
- [40] P. Mali, A. Mukhopadhyay, G. Singh, *Fractals* 20 (2012) 1.
- [41] Y. Shimizu, S. Thurner, K. Ehrenberger, *Fractals* 10 (2002) 103.
- [42] A. Muoz-Diosdado, J.L.D. Ro-Correa, *Proc. of 28th IEEE EMBS Ann. Int. Conf. New York City*, 30 August 2006.
- [43] P. Oświęcimka, J. Kwapień, S. Drożdż, *Phys. Rev. E* 74 (2006) 016103.
- [44] S. Drożdż, P. Oświęcimka, *Phys. Rev. E* 91 (2015) 030902(R).
- [45] W. Ochs, *Phys. Lett. B* 247 (1990) 101.
- [46] W. Ochs, *Z. Phys. C* 50 (1991) 339.



Ring and jet-like structures and two-dimensional intermittency in nucleus–nucleus collisions at 200 A GeV/c

M.K. Ghosh ^a, P.K. Haldar ^b, S.K. Manna ^b, A. Mukhopadhyay ^{a,*},
G. Singh ^c

^a Department of Physics, University of North Bengal, Raja Rammohunpur, Darjeeling 734013, West Bengal, India

^b Physics Department, Dinhata College, Dinhata, Cooch Behar 736135, West Bengal, India

^c Department of Computer and Information Science, SUNY at Fredonia, NY 14063, USA

Received 17 September 2010; received in revised form 8 November 2010; accepted 2 December 2010

Available online 10 December 2010

Abstract

We have investigated the presence of ring and/or jet-like structures in the angular emission of secondary charged mesons (shower tracks) coming out of ^{16}O –Ag/Br and ^{32}S –Ag/Br interactions, each at an incident momentum of 200 A GeV/c. Nuclear photographic emulsion technique has been used to collect the experimental data. The experimental results have been compared with the results simulated by Monte Carlo method. The analysis indicates presence of ring and jet-like structures in the experimental data beyond statistical noise. This kind of jet structure is expected to give rise to a strong two-dimensional ($2d$) intermittency. The self-affine behaviour of $2d$ scaled factorial moments (SFM) has therefore been investigated and the strength of $2d$ intermittency has been determined. For each set of data the $2d$ results have been compared with the respective one-dimensional ($1d$) intermittency results.

© 2010 Elsevier B.V. All rights reserved.

Keywords: High-energy; Heavy-ion; Ring–jet; Intermittency

* Corresponding author.

E-mail address: amitabha_62@rediffmail.com (A. Mukhopadhyay).

1. Introduction

The space–time evolution of nucleus–nucleus (AB) collision can be broadly divided into three sub-stages, namely, (i) a very short lived pre-equilibrium stage, (ii) a comparatively longer lived central fireball stage, and lastly (iii) the longest lived freeze-out stage during which the central fireball expands and cools down to fragment into final state particles (predominantly hadrons). Depending entirely upon the initial kinematic conditions the intermediate fireball stage may or may not reach a thermal equilibrium that is necessary to achieve the colour deconfined Quark–Gluon Plasma (QGP) state [1]. If at all such a deconfinement takes place, then a subsequent phase transition from the QGP back to the multiparticle final state may lead to some collective behaviour manifested in the form of large local density fluctuations of produced particles [2]. Such local structures would obviously then correspond to the late freeze-out part of the history of the collision. Instead of a thermal phase transition there may however be other reasons behind such collective behaviour of particles within narrow intervals of phase space. One hypothesis is the emission of conical gluonic radiation, which is an outcome of a partonic jet traveling through the partonic/nuclear medium [3]. An alternative speculation is the formation of a shock wave traveling once again through a similar partonic/nuclear medium [4]. Both the macroscopic phenomena mentioned here have the same origin (i.e., electromagnetic) but they correspond respectively, to transverse and longitudinal excitations of the medium concerned. In either case the emission pattern is characterized by a conical structure defined through a semi-vertex angle ξ as

$$\cos \xi = \frac{c_{med}}{v} = \frac{c}{\mu v}. \quad (1)$$

Here, depending on the case as it may be, c_{med} is either the velocity of the gluons or it is the velocity of the shock wave, v is the velocity of the partonic jet that triggers the Cherenkov gluon or shock wave emission, and μ is the refractive index – all values pertaining to the medium concerned. Here c is either the velocity of the gluons in vacuum or the velocity of sound wave in air.

The phenomenon of gluon emission is similar to the emission of Cherenkov electromagnetic radiation. The incident nucleus can be treated as a bunch of quarks, each of which is capable of emitting Cherenkov gluons while traversing through the target nucleus. Experimentally the real part of the elastic forward scattering amplitude of all hadronic processes at high energy have been found to be positive [5]. This is necessary for Cherenkov emission as the excess of the nuclear refractive index over unity is proportional to this real part. For thin targets like the nuclei, an effect similar to the Cherenkov gluon emission can take place owing to the small confinement length [6]. Under favourable circumstances the conical structure so formed, may be able to withstand the impact of collision and retain its original shape. If the initial/triggering parton direction is the same as that of the incident beam direction, and if the number of gluons – each capable of emitting a minijet, is large, then one may observe ring-like structures in the distribution of particles that are clustered within a narrow region of pseudorapidity (η), but are distributed more or less uniformly over the entire azimuthal angle (φ) range ($0, 2\pi$). On the other hand, if the number of jet emitting gluons is small, then it is more likely that several jets, each restricted to narrow intervals in both η and φ will be formed, thereby resulting in jet-like structures in the distribution of final state hadrons.

As mentioned above, a quark–gluon jet created by a high-energy parton can produce a different type of collective behaviour similar to the Mach shock wave formation. A jet moving with a

velocity close to that of the light can be considered as a body moving with a supersonic speed, which may cause a large pressure variation inside a nuclear/partonic medium, and can therefore, give rise to shock waves. The Mach angle depends on the state of the matter through which the partonic jets are moving, and depending on the nature of the medium the sound (elastic wave) speed can vary between $\approx 0.4c$ and close to c [7]. Unfortunately, till date we possess only some speculative ideas (e.g., Fermi liquid to QGP) about the nature of the nuclear/partonic medium. Ring-like structures were first studied in a cosmic ray experiment [8]. Subsequently, in several accelerator based experiments involving high-energy nucleus–nucleus (AB) interactions ring and jet-like structures were further investigated [9–12].

With the introduction of a new methodology called the ‘intermittency’ [13] the investigation of event-to-event local fluctuations in particle density distributions in high-energy interactions entered into a new era. Intermittency is speculated to be a manifestation of some kind of scale invariant dynamics of particle production. The main tool of intermittency study as suggested by its proponents, is the statistical counting variable SFM, henceforth to be denoted by F_q . The main advantage of using this variable is that it can disentangle the statistical noise that contaminates the dynamical fluctuation, and can measure only the nonstatistical or dynamical contribution. A large number of experiments have already been performed to study the $1d$ intermittency phenomenon [14], while the actual process of particle emission occurs in three dimensions ($3d$). It has been pointed out [15] that in the lower-dimensional projection the fluctuations get reduced by the averaging process. The projection effect may even completely wash out the self-similar nature of fluctuations as predicted in the framework of intermittency. Thus, to get rid of the error due to dimensional reduction, the analysis should ideally be performed in $3d$. As mentioned before, for ring-like structures where the particles are confined to a limited η interval and distributed evenly over the entire φ range, a strong $1d$ intermittency is expected. On the other hand, for jet-like structures, where the particles are restricted over narrow regions of η and φ both, the $2d$ intermittency should be strong. It has been pointed out that the particle distributions are anisotropic in the longitudinal–transverse plane [16]. For example, in high-energy interactions the longitudinal momenta of produced particles can be large, whereas corresponding transverse momenta are restricted within a limited range with a universal average value $\langle p_t \rangle \approx 0.35 \text{ GeV}/c$. This kind of anisotropy leads to a self-affine (multi)fractal structure in the dynamical fluctuation. A self-similar behaviour can be retrieved when the $2d$ phase space is so partitioned as to properly take into account the above mentioned intrinsic anisotropy.

In some of our previous works (i) a weak $1d$ intermittency for the ^{16}O –Ag/Br data at $200 \text{ A GeV}/c$ [17], (ii) a weak $1d$ intermittency in ^{32}S –Ag/Br interaction at $200 \text{ A GeV}/c$, and (iii) a strong $2d$ intermittency for the same ^{32}S data have been reported [18]. From these analyses our data did not show any hint of any kind of phase transition. We are therefore, inclined to look for alternative mechanisms of local density fluctuations of produced particles. Hence in the present work we investigate the presence of ring and jet-like substructures within narrow intervals of phase space by analysing the angular distributions of final state charged particles produced in ^{16}O –Ag/Br and ^{32}S –Ag/Br interactions at $200 \text{ A GeV}/c$. To reaffirm the presence of jet-like structures for both sets of data we have in this paper presented a $2d$ intermittency analysis on the ^{16}O –Ag/Br interactions at $200 \text{ A GeV}/c$, and have compared the ^{16}O results with those of the ^{32}S –Ag/Br interaction. Following [19] the strength of intermittency has been quantified in each case. The organization of the paper goes like this – in Section 2 we have summarily described the experimental aspects, in Section 3 the statistical and computational methods adopted for ring–jet analysis along with a description of our results have been presented, in Section 4 the

methods and results of $2d$ self-affine intermittency analysis have been depicted, and in Section 5 we conclude with some critical comments on the outcome of our investigation.

2. Experiment

The experimental data used in the present analysis have been obtained from the stacks of Ilford G5 nuclear photo-emulsion pellicles of size $18\text{ cm} \times 7\text{ cm} \times 600\text{ }\mu\text{m}$, that were horizontally irradiated by the ^{16}O and ^{32}S beams, each with an incident momentum $200\text{ A GeV}/c$ from the super-proton synchrotron (SPS) of CERN. Leitz microscopes with a total magnification of $300\times$ have been used to scan the plates along the projectile tracks to find out primary interactions. Angle measurement and counting of tracks were performed under a total magnification $1500\times$ with the help of Koristka microscopes. According to the emulsion terminology, tracks emitted from an interaction (called a star) are classified into four categories namely, shower, grey and black tracks, and projectile fragments.

- (i) The shower tracks are due to the singly charged produced particles moving with relativistic speed ($\beta > 0.7$) caused mostly by the charged mesons. Their ionisation $I < 1.4I_0$, where I_0 (≈ 20 grains/ $100\text{ }\mu\text{m}$) is the minimum ionisation caused by any track in the Ilford G5 plates. Total number of such tracks in an event is denoted by n_s . Our analysis is confined only to the shower tracks.
- (ii) The black and grey tracks predominantly originate from the fragments of the target, and their ionisation $I \geq 1.4I_0$. The total number of such heavy fragments in a star is denoted by n_h , and $n_h > 8$ will ensure an interaction with an Ag/Br nucleus.
- (iii) The projectile fragments are due to the spectator parts of the incident projectile nuclei. They are emitted within a very narrow extremely forward cone whose semi-vertex angle is decided by the Fermi momenta of the nucleons present in the nucleus. Having almost same energy/momentum per nucleon as the incident projectile, these fragments exhibit uniform ionisation over a long range and suffer negligible scattering. Their number in an event is denoted by n_{pf} .

Events with no projectile fragment having charge $Q \geq +2e$ were selected for analysis. This criterion ensured that a complete fragmentation of the projectile nucleus has taken place in each event of the considered sample. For ^{16}O –Ag/Br interaction the sample size was 280 events, and that for the ^{32}S –Ag/Br interaction was 200 events. The average shower track multiplicities for these samples respectively, were $\langle n_s \rangle = 119.26 \pm 3.59$ and 217.79 ± 6.16 . To avoid any contamination between the produced charged mesons and the spectator protons belonging to the projectile, shower tracks falling within the Fermi cone have been excluded from our analysis. In an emulsion experiment η together with φ of a track constitutes a convenient pair of basic variables in terms of which the particle emission data can be analyzed. η is an approximation of the dimensionless boost parameter rapidity of a particle, and it is related to the emission angle θ of the corresponding shower track as $\eta = -\ln \tan(\theta/2)$. An accuracy of $\delta\eta = 0.1$ unit and $\delta\varphi = 1$ mrad could be achieved through the reference primary method of angle measurement. Nuclear emulsion experiments in spite of its many limitations are superior to other big budget experiments in one respect, that they offer a very high angular resolution. When distributions of particles within small phase-space regions are to be examined, this certainly is an important advantage. There are some excellent books where the details of an emulsion experiment including the event and track selection criteria can be found [20].

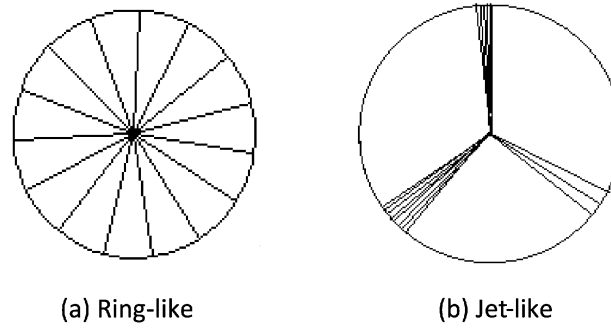


Fig. 1. Schematic representation of (a) the ring-like distribution of tracks and (b) the jet-like distribution of tracks in the target diagram.

3. Ring–jet analysis

There are several methods by which dense clusters of particles in an event can be identified and characterized. While distributing over a (or a set of) suitable phase-space variable(s), such clusters appear in the form of rapidly fluctuating density functions. In the resultant distribution, often trivial statistical noise is combined with one or more dynamical effect(s), and it is not always an easy task to separate out one from the other. One way to do so is to replace the basic phase-space variables associated with each particle by randomly generated numbers and distribute them according to the track multiplicity in an event. The random data set can then serve the purpose of a statistical background, because while generating these numbers neither any ring nor any jet structure is present in the form of an input. In the present investigation we have adopted the method of analysis that is prescribed in [9]. Without making any claim of originality we present below a brief description of the same for the purpose of completeness.

For an individual event we start with a fixed number n ($< n_s$) of particles (shower tracks). Each n -tuple of particles is arranged consecutively (either in ascending or in descending order) along the η -axis, and this subgroup of particles is then characterized by

- (i) a size: $\Delta\eta = |\eta_{n+i-1} - \eta_i|, i = 1, \dots, n_s,$
- (ii) a mean: $\eta_m = \sum_{i=1}^n \eta_i / n,$ and
- (iii) a density: $\rho = n / \Delta\eta.$

Thus each subgroup of particles, dense or dilute, has the same multiplicity n and hence they can be easily compared with each other. The azimuthal structure of a particular subgroup can now be parametrized in terms of the following quantities,

$$S_1 = - \sum_{i=1}^n \ln(\Delta\varphi_i) \quad \text{and} \quad (2)$$

$$S_2 = \sum_{i=1}^n (\Delta\varphi_i)^2, \quad (3)$$

Here $\Delta\varphi_i$ is the φ difference of two neighbouring particles, i.e., between the i th and the $(i + 1)$ th belonging to a particular subgroup (starting from first and second, and ending at the n th and first). One can, for example, measure φ in units of a complete revolution (2π), and then each $\Delta\varphi_i$ will be a fraction less than unity. The difference between a ring-like structure and a jet-like structure has been schematically explained in Fig. 1 with the help of target diagrams. In our case

the target diagram is nothing but the azimuthal plane. For a ring-like emission the tracks are almost isotropically distributed over the whole azimuth. Whereas, for a jet-like emission some of the tracks are clustered within a narrow region of φ , but each cluster is well separated from the other in the azimuthal plane. Note that both S_1 and S_2 are small ($S_1 \rightarrow n \ln n$ and $S_2 \rightarrow 1/n$) for a perfect ring-like structure and they are large ($S_1 \rightarrow \infty$ and $S_2 \rightarrow 1$) for a perfect jet-like structure. While S_1 is sensitive to small gaps, S_2 is sensitive only to large gaps. In a purely stochastic scenario the $\Delta\varphi$ -distribution is given by

$$f(\Delta\varphi) d(\Delta\varphi) = (n - 1)(1 - \Delta\varphi)^{(n-2)} d(\Delta\varphi). \quad (4)$$

The expectation values of the S -parameters $\langle S_i \rangle = \int S_i f(\Delta\varphi) d(\Delta\varphi)$: ($i = 1, 2$) are

$$\langle S_1 \rangle = n \sum_{k=1}^{n-1} \frac{1}{k} \quad \text{and} \quad \langle S_2 \rangle = \frac{2}{n + 1}, \quad (5)$$

when particles are emitted independently without any correlation. Distributions of S_1 and S_2 parameters would be peaked around these expectation values. Presence of jet-like substructures would result in bulging and small local peaks in the distributions to the right side of the mean, whereas ring-like substructures would do the same towards the left. A direct comparison between the experimental data and that representing an independent emission can be made by computer simulations. Experimental φ -distribution being more or less uniform between its allowed limits $(0, 2\pi)$, one can construct its stochastic equivalent by generating (pseudo)random numbers within the same range. This can be done with the help of a simple recursive linear congruential sequence [21]. Similarly, the η density is approximately normally distributed. Following the inverse of integral method the Gaussian distributed random numbers can also be generated. These Gaussian distributed random numbers should have the same centroid, peak density and width as those of the corresponding experimental set. Each pair of randomly generated (η, φ) will now represent a particle/track, and all such doublets, equal in number as the corresponding experimental set, have been assigned to individual events according to their shower track multiplicities (n_s). Both the average behaviour of the S -parameters as well as the detailed analysis of all relevant ring-jet variables are presented below.

We have chosen $n = 15$ for the ^{16}O -Ag/Br events, and $n = 25$ for the ^{32}S -Ag/Br events. For these two different choices of n values the stochastic expectation values [see Eq. (5)] for the two sets of data, respectively are: $\langle S_1 \rangle \approx 48.8$ and ≈ 94.4 , and $\langle S_2 \rangle = 0.125$ and ≈ 0.077 . Distributions of the S_1 parameter normalised by its stochastic expectation value $\langle S_1 \rangle$ for both sets of data are plotted in the form of histograms in Fig. 2(a) and (b). For a particular interaction the experimental distribution and the random number generated distribution are plotted together. As expected and as can be seen from these diagrams, the random number generated distributions are peaked around $S_1/\langle S_1 \rangle = 1$. In each case the peak of the randomly generated distribution is taller, smoother and narrower than the respective experimental distribution. The ^{16}O -Ag/Br distributions are broader than the ^{32}S -Ag/Br distributions. The distributions are asymmetric (left skewed), and this asymmetry is more pronounced in the experimental distributions. In each case, the experimental distribution is significantly shifted towards right with respect to the generated distribution. Thus large S_1 values signifying jet-like structures, cannot be generated as abundantly by a random number based independent emission model as it can be in the experiment. In the right-hand side of the respective peaks one can also find small bulging in the distributions, that are again more pronounced in experiment than in the random number generated distribution. In Fig. 3(a) and (b) similar graphical plots for $S_2/\langle S_2 \rangle$ can be found for the two types of

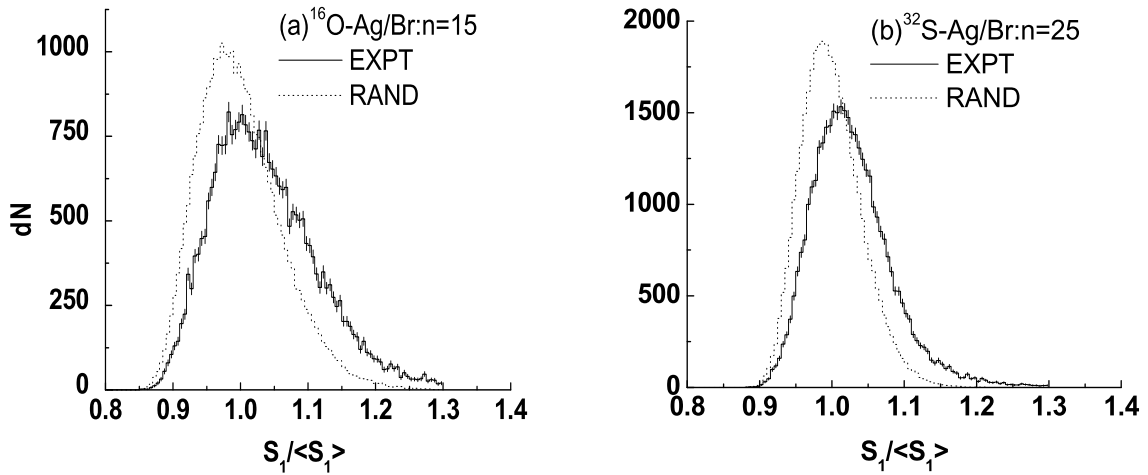


Fig. 2. Distributions of the S_1 parameter normalised by its stochastic expectation value $\langle S_1 \rangle$ for $^{16}\text{O-Ag/Br}$ and $^{32}\text{S-Ag/Br}$ interactions both at $200 \text{ A GeV}/c$.

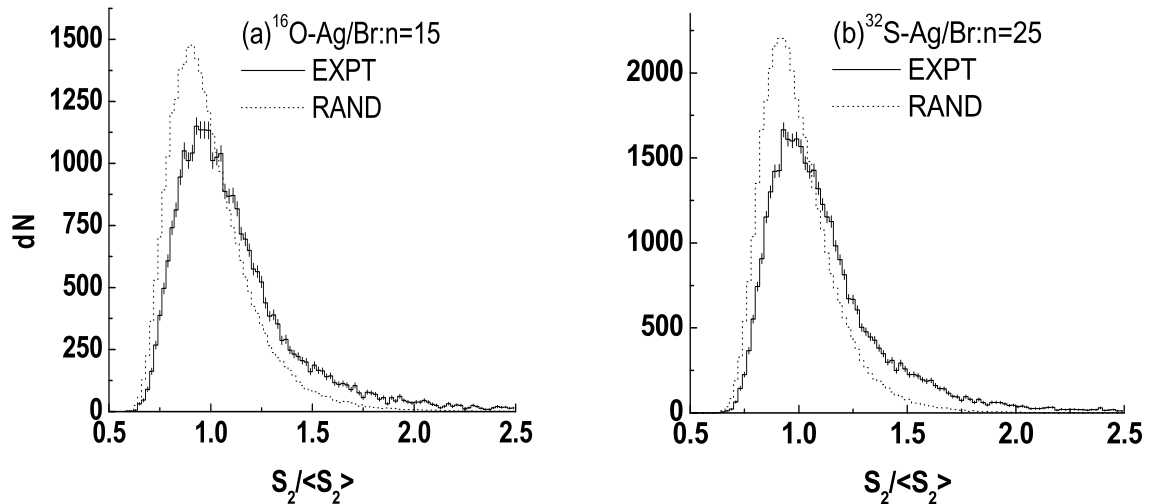


Fig. 3. Distributions of the S_2 parameter normalised by its stochastic expectation value $\langle S_2 \rangle$ for $^{16}\text{O-Ag/Br}$ and $^{32}\text{S-Ag/Br}$ interactions both at $200 \text{ A GeV}/c$.

interactions under consideration. In both cases once again the behaviour is more or less same as that of the $S_1/\langle S_1 \rangle$ distributions. There are obvious experimental excesses in the higher (right to the peak, i.e., $S_2/\langle S_2 \rangle > 1$) side over the corresponding random number prediction, indicating presence of nontrivial jet structures in the angular distribution of particles. The variation of the experimental average values of $\langle -\sum \ln(\Delta\varphi_i) \rangle$ and $\langle \sum (\Delta\varphi_i)^2 \rangle$ against the cluster size $\Delta\eta$ is shown respectively, in Figs. 4 and 5 for both types of interactions. Note that these quantities are different from the stochastic expectations values $\langle S_1 \rangle$ and $\langle S_2 \rangle$. Corresponding stochastic expectation values obtained from Eq. (5) represented by dashed lines in each graph, and random number generated values are also included in the same set of diagrams. One can see that the random number generated values lie more or less along the stochastic expectation lines, whereas the experimental values lie consistently above both the random number generated values and the stochastic prediction. At small $\Delta\eta$ significant difference between the experimental result and the stochastic (or random number) value can be observed. On the higher side of $\Delta\eta$ the experimental values in each diagram can be approximated by a plateau. Once again the inadequacy of an

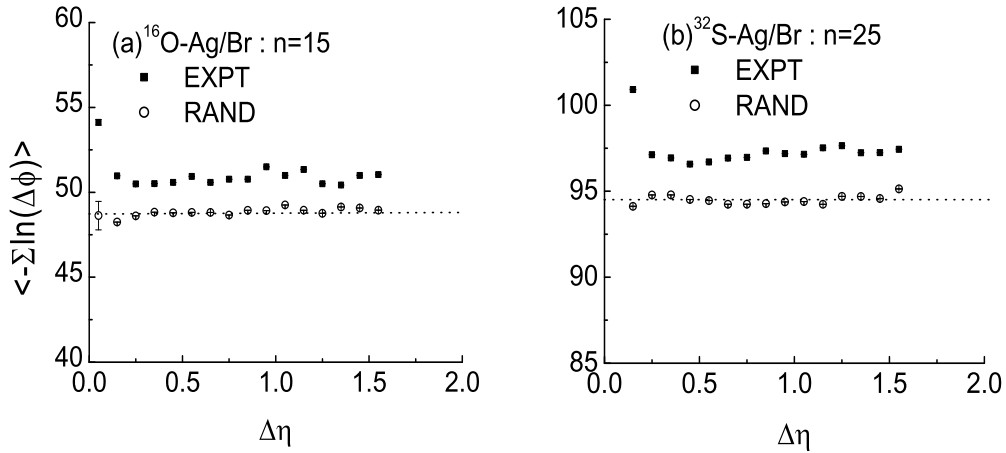


Fig. 4. Average behaviour of the S_1 parameter $\langle -\sum \ln \Delta\phi \rangle$ for $^{16}\text{O-Ag/Br}$ and $^{32}\text{S-Ag/Br}$ interactions both at 200 A GeV/c. The stochastic values are represented by dashed lines.

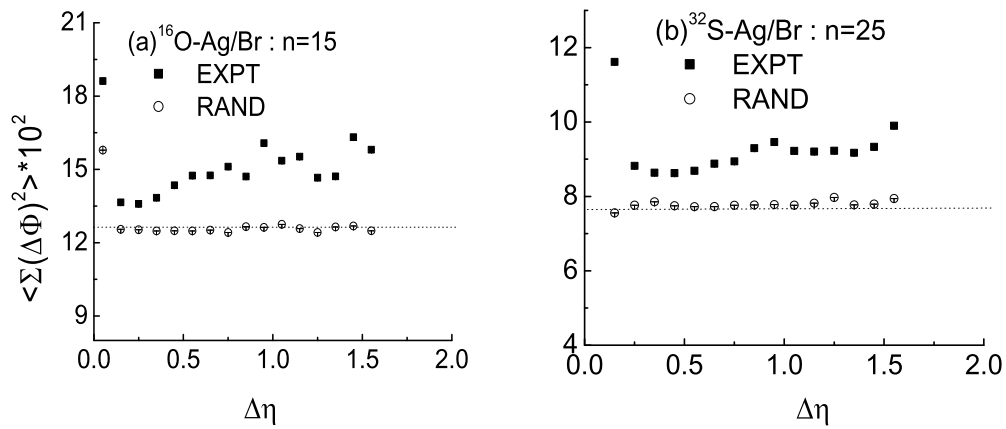


Fig. 5. Average behaviour of the S_2 parameter $\langle \sum (\Delta\phi)^2 \rangle$ for $^{16}\text{O-Ag/Br}$ and $^{32}\text{S-Ag/Br}$ interactions both at 200 A GeV/c. The stochastic values are represented by dashed lines.

independent emission of particles to replicate the experimental observation can be seen from our analysis.

It has been observed that to a large extent the experimentally observed average behaviour of the S -parameters can be reproduced with the Lund Monte Carlo code FRITIOF calculation, where γ -conversion and the Hanbury–Brown–Twiss (HBT) effect have been included [9]. However, it has also been argued that before coming to a definite conclusion regarding such azimuthal structures, the detailed distribution of some other relevant cluster variables should be examined along with the average behaviour of the S -parameters [12]. The cluster size of the azimuthal substructures can be investigated with the help of the $\Delta\eta$ distribution. For both types of interactions under consideration, these distributions are plotted in Figs. 6 and 7. A distinction between the ring and jet structure has been made by separately plotting distributions with $S_2/\langle S_2 \rangle < 1$ and $S_2/\langle S_2 \rangle > 1$. These distributions are once again left skewed, having a sharp rise in the left to the peak and a comparatively slower fall to the right side of the peak. The width of experimental distribution in each case is more or less same as that of the random number generated distribution. For both data sets one can see that the clusters of small size (peak region and left to the peak region) have significant experimental surplus over the corresponding statistical noise. On the other hand, clusters of large size (right side of the peak) are either reproducible by random numbers, or the randomly generated values exceed the experimental values. The location of jet/ring-like

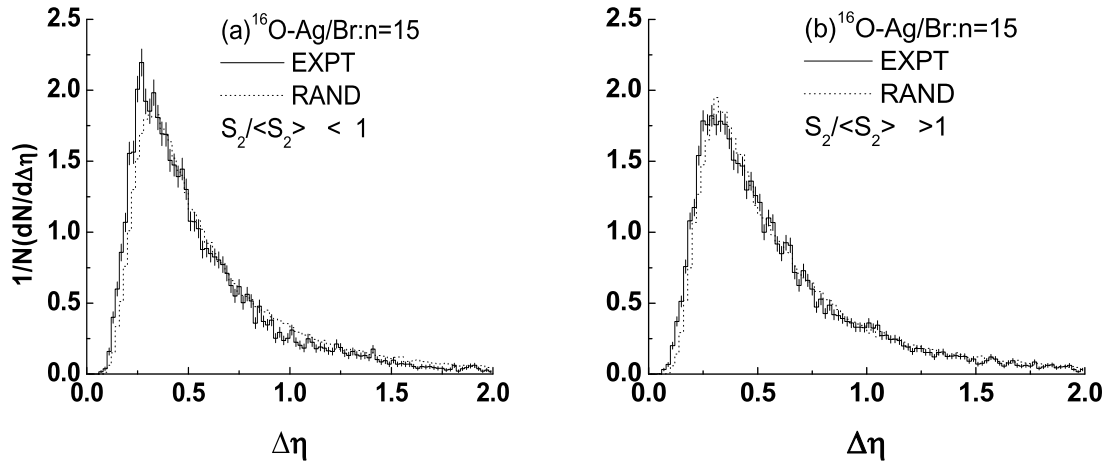


Fig. 6. Comparison of cluster size distribution between the experimental and the random number generated data sets for two different regions, i.e., (a) $S_2/\langle S_2 \rangle < 1$ and (b) $S_2/\langle S_2 \rangle > 1$ in $^{16}\text{O-Ag/Br}$ interaction at 200 A GeV/c.

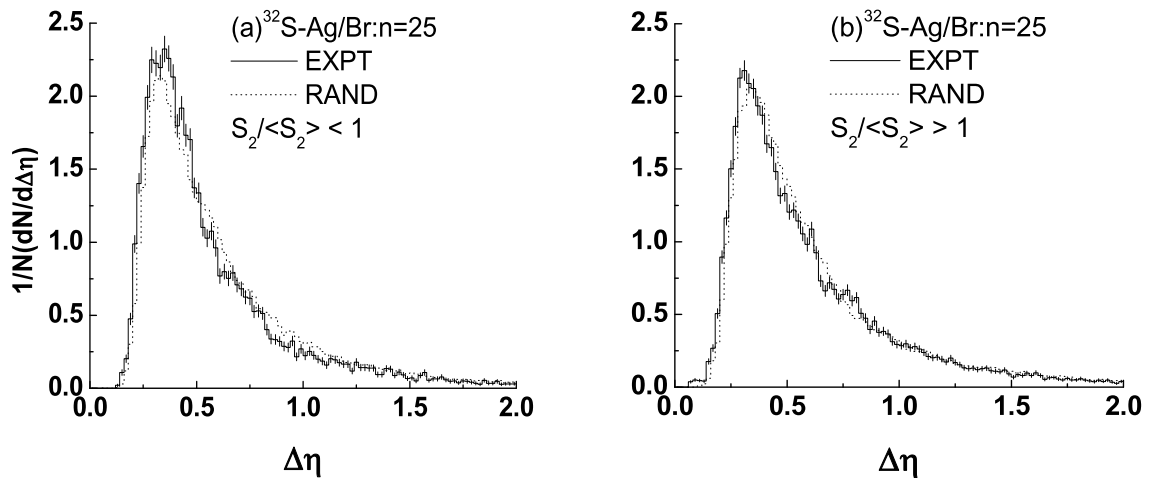


Fig. 7. Comparison of cluster size distribution between the experimental and the random number generated data sets for two different regions, i.e., (a) $S_2/\langle S_2 \rangle < 1$ and (b) $S_2/\langle S_2 \rangle > 1$ in $^{32}\text{S-Ag/Br}$ interaction at 200 A GeV/c.

substructures can on the other hand, be investigated by studying the η_m distribution. Following [12] the distributions can be divided into three categories:

- (i) $S_2/\langle S_2 \rangle < 0.95$ – the region where ring-like effects dominate,
- (ii) $0.95 \leq S_2/\langle S_2 \rangle \leq 1.1$ – the region of statistical background, and
- (iii) $S_2/\langle S_2 \rangle > 1.1$ – the region where jet-like structures dominate.

In Figs. 8 and 9 the η_m distributions for all three categories mentioned above, and respectively, for both types of interactions under consideration have been plotted. The average behaviour of each distribution is more or less symmetric about a central value, which for each type of interaction is close to the central value of the basic η -distribution of the shower tracks. However, there are some small experimental excesses beyond statistical errors over the random number generated values. For category (i) $S_2/\langle S_2 \rangle < 0.95$, these excesses are present in the form of several narrow peaks mainly in the central maximum and left to the central maximum region of the distributions. In the right to central region the experimental distribution for each type of interaction either matches

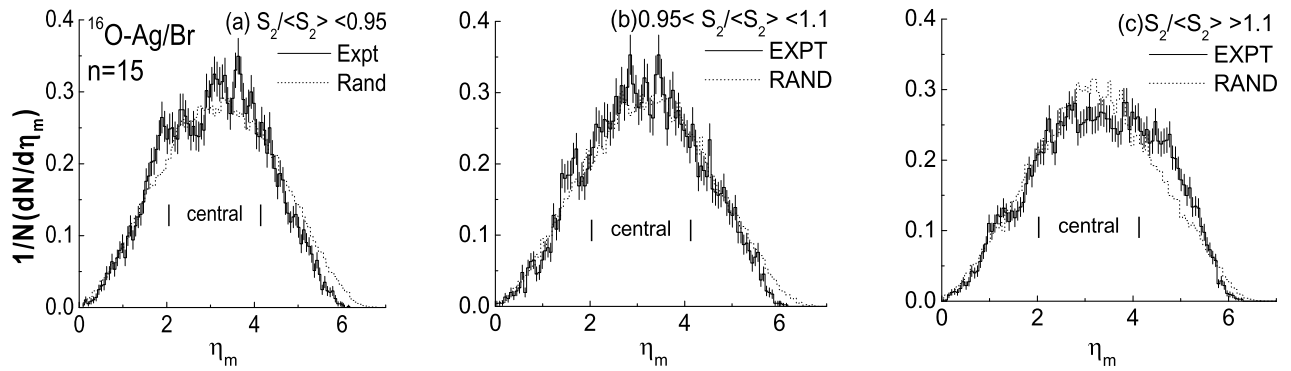


Fig. 8. Comparison of the φ -subgroup position distributed along the η -axis between the experimental and the random number generated data sets in three different regions of $S_2/\langle S_2 \rangle$ for ^{16}O -Ag/Br interaction at 200 A GeV/c.

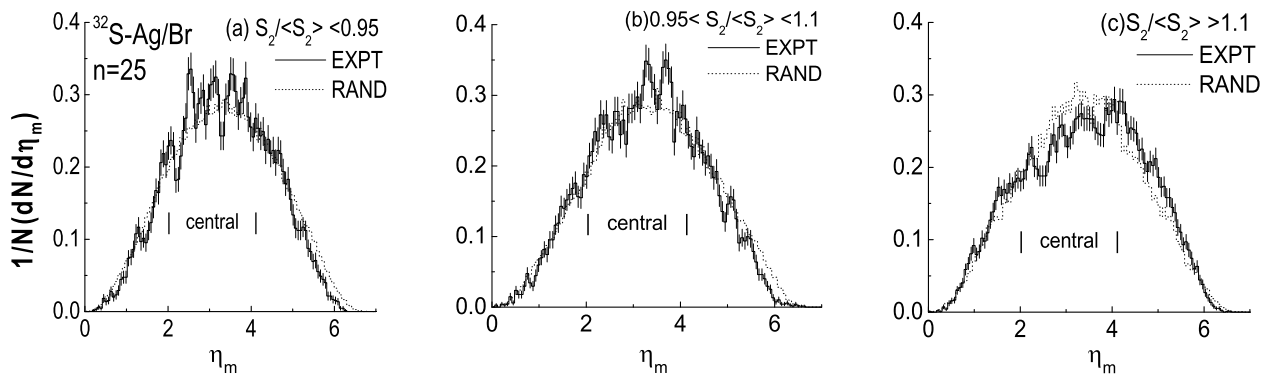


Fig. 9. Comparison of the φ -subgroup position distributed along the η -axis between the experimental and the random number generated data sets in three different regions of $S_2/\langle S_2 \rangle$ for ^{32}S -Ag/Br interaction at 200 A GeV/c.

with the respective random number generated one, or the latter dominates over the former. The features are equally prominent for both interactions under consideration, and can probably be attributed to the ring-like structure(s) of particle emission. The effect however, is statistically not too significant. Probably, by choosing events with a particular centrality one could have reduced the noise. For category (ii) $0.95 \leq S_2/\langle S_2 \rangle \leq 1.1$, there are two prominent narrow structures in the central region of the experimental distributions of both types of interactions, that cannot be replicated by the randomly generated data sets. These structures are more prominent in the ^{32}S induced interaction, and the physical origin of them is not very much clear. For category (iii) $S_2/\langle S_2 \rangle > 1.1$, the experimental excesses are continuous and extend over a region of about 1 unit of pseudorapidity exactly on the right-hand side of the central maxima for both sets of data. This effect is more prominent in the ^{16}O induced interaction than in the ^{32}S induced one, and it can be attributed to jet-like structures in the forward hemisphere.

4. Intermittency in $2d$

Our analysis of the angular emission data on singly charged particles produced in ^{16}O -Ag/Br and ^{32}S -Ag/Br interactions indicates presence of both ring and jet-like structures in the experimental data beyond the respective statistical noise. However small the effects may be, it is expected that a strong $2d$ intermittency would be observed for the same set of data. As mentioned before, we choose the (η, φ) plane as our basic phase space. As the shape of the distribution in respective directions may influence the scaling behaviour of the SFM, the (η, φ) set has been

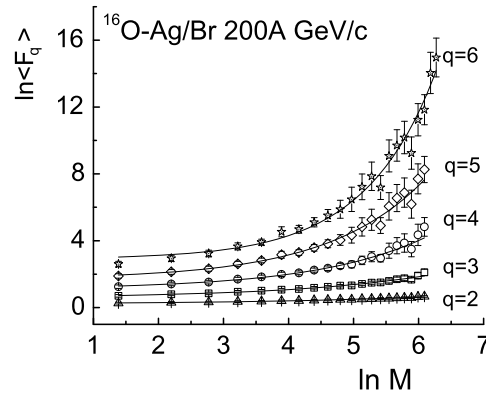


Fig. 10. Two-dimensional SFM of different order plotted against phase space (η, φ) partition number. The solid curves are drawn to guide the eye.

replaced by the ‘cumulative’ variables (X_η, X_φ) [22]. The distribution in terms of a cumulative variable is always uniform within a universal range $(\Delta X_i = 1: i = \eta, \varphi)$ between 0 and 1. Hence all particles are now distributed over a square of unit side. The SFM of order q is defined as [13]

$$\langle F_q \rangle = \frac{1}{M} \sum_{m=1}^M \frac{\langle n_{em}(n_{em} - 1) \cdots (n_{em} - q + 1) \rangle}{\langle n_m \rangle^q} \quad (6)$$

where n_{em} is the number of shower tracks falling within the m th interval of the e th event, $\langle \rangle$ denotes an averaging over the number of events,

$$\langle n_m \rangle = \frac{1}{N_{ev}} \sum_{e=1}^{N_{ev}} n_{em} \quad (7)$$

is the average shower track multiplicity in the m th interval, M ($= M_\eta \cdot M_\varphi$) is the total $2d$ phase space partition number, and M_η (M_φ) is the number of partitions along η (φ) direction. As it was in the $1d$ case, if in $2d$ the dynamical fluctuations are also self-similar at all scales, then one expects to see a linear rise like

$$\ln \langle F_q \rangle = \phi_q \ln M + \beta_q, \quad (8)$$

where β_q is the intercept, and the slope ϕ_q (> 0) is called the intermittency index that indirectly is a measure of the strength of intermittency. In Fig. 10 plots of $2d$ SFM of different orders have been plotted for the $^{16}\text{O-Ag/Br}$ data by setting $M_\eta = M_\varphi$. Due to the anisotropy in the fluctuations in different directions of phase space, the variation of $2d \ln \langle F_q \rangle$ against $\ln M$ is however, not linear over the entire range of $\ln M$. To obtain a measure of the self-affine intermittency index in $2d$ one can perform a polynomial fit to the $(\ln \langle F_q \rangle, \ln M)$ data, and can then retain the linear coefficient by setting all nonlinear coefficients to zero. For $^{16}\text{O-Ag/Br}$ interactions the results on $2d$ self-affine intermittency index obtained in this way along with the generalised Rényi dimensions (D_q) are presented in Table 1. Note that D_q is related to ϕ_q as

$$D_q = D - \frac{\phi_q}{q - 1}, \quad (9)$$

where D is the dimension of the supporting space, e.g., $D = 1$ for η or φ -space and $D = 2$ for the (η, φ) -space. Corresponding figure and fit results for the $^{32}\text{S-Ag/Br}$ data are available in [18].

Table 1
 $2d$ self-affine intermittency indices and the Rényi dimension in $^{16}\text{O}\text{--Ag/Br}$ interaction at 200 A GeV/c. The errors shown within brackets are of statistical origin.

Order	$\phi_q^{(2)}$	R^2	$D_q^{(2)}$
$q = 2$	0.125(0.025)	0.994	1.875(0.025)
$q = 3$	0.339(0.045)	0.987	1.831(0.023)
$q = 4$	0.857(0.115)	0.983	1.714(0.038)
$q = 5$	1.596(0.198)	0.986	1.601(0.049)
$q = 6$	3.059(0.270)	0.983	1.388(0.054)

In Table 1 the superscript (2) denotes the dimensionality of phase space, and the Pearson's R^2 coefficient [23] that is always very close to unity, denotes the goodness of polynomial (order 3 in our case) fit. The errors quoted in the $\phi_q^{(2)}$ values are only of statistical origin. Due to a strong correlation between the data points, e.g., $(\ln\langle F_q \rangle, \ln M)$ such errors are nontrivially estimated with the help of several simulated data samples by generating random numbers [24]. In the present case 10 such independent data samples have been generated, the ϕ_q values are obtained for each generated sample, and then the error in ϕ_q is obtained from the statistical dispersion,

$$\sigma(\phi_q) = \sqrt{\langle \phi_q^2 \rangle - \langle \phi_q \rangle^2}. \quad (10)$$

Here $\langle \rangle$ means averaging over all 10 generated samples. It has been conjectured [15] that beside the type of collective phenomena as mentioned in the introduction, there are other possibilities to observe intermittency within a scale invariant dynamics. They are, either a branching process or a second order phase transition. To check whether or not these mechanisms are acceptable as possibilities, in a way similar to our papers on $1d$ analysis [17,18] the $\phi_q^{(2)}$ values were put to different tests, and the following observations could be made.

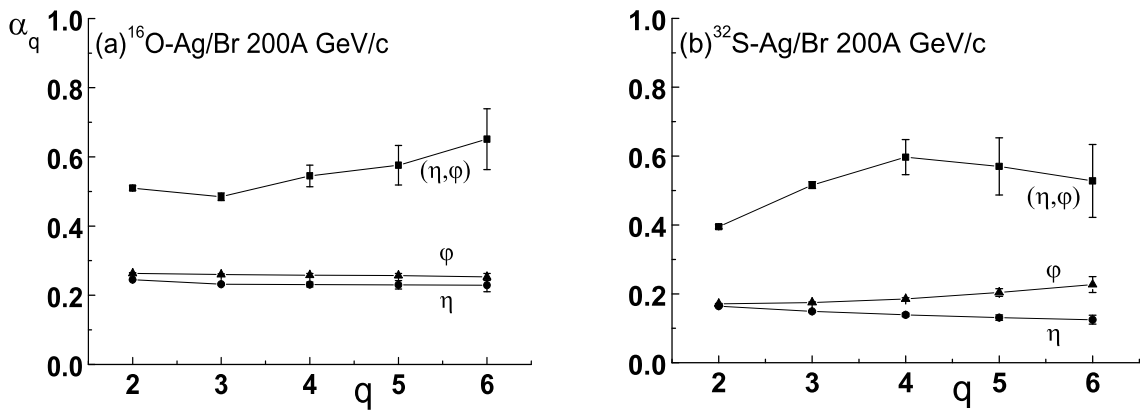
- (i) Unlike the $1d$ case the $\phi_q^{(2)}$ values either quoted above or given in [18] do not follow the predictions of a self-similar cascade mechanism. Neither a log-normal distribution under Gaussian approximation [13] nor a log-Lévy stable distribution work for the observed values [25], thereby ruling out a self-similar cascade process in $2d$. The Rényi dimensions are however fractional and decrease with increasing q , which indicates a (multi)fractal nature of the underlying dynamical fluctuation.
- (ii) The intermittency parameter $\lambda_q = \phi_q / (q + 1)$ does not exhibit any minimum, and so the possibility of coexistence of two different phases (e.g., liquid–gas) can also be ruled out [26].
- (iii) The $\phi_q^{(2)}$ values are also not consistent with a monofractal structure, as required for a system at the critical temperature of a second order phase transition [27]. The Landau–Ginzburg parameter ν is also significantly different from its universal value ($\nu = 1.304$) to warrant any kind of thermal (second order) phase transition [28].

However, the $\phi_q^{(2)}$ values indicate presence of a strong $2d$ intermittency, much stronger than the $1d$ case [17,18]. A more direct measure of the intermittency strength has been obtained for the hadronic interactions from its connection with the (multi)fractality, at first in the framework of a random cascading model (e.g., the α -model), and then in a model independent way irrespective

Table 2

 Intermittency strength based on random cascading α -model. The errors shown within brackets are of statistical origin.

Order (q)	$^{16}\text{O-Ag/Br 200 A GeV/c}$			$^{32}\text{S-Ag/Br 200 A GeV/c}$		
	$\alpha_q(\eta, \varphi)$	$\alpha_q(\eta)$	$\alpha_q(\varphi)$	$\alpha_q(\eta, \varphi)$	$\alpha_q(\eta)$	$\alpha_q(\varphi)$
2	0.487(0.006)	0.245(0.001)	0.263(0.002)	0.395(0.006)	0.164(0.002)	0.171(0.001)
3	0.502(0.012)	0.232(0.003)	0.260(0.002)	0.516(0.010)	0.149(0.002)	0.175(0.002)
4	0.549(0.032)	0.231(0.007)	0.258(0.005)	0.597(0.051)	0.139(0.005)	0.185(0.004)
5	0.612(0.063)	0.230(0.012)	0.257(0.006)	0.570(0.083)	0.131(0.008)	0.204(0.011)
6	0.643(0.084)	0.229(0.019)	0.253(0.010)	0.528(0.106)	0.125(0.013)	0.227(0.023)


 Fig. 11. Intermittency strength α_q based on random cascading model plotted against q for both types of interaction. The solid lines are drawn to guide the eye.

 of any particular mechanism of particle production [19]. According to the α -model the strength parameter α_q is related to D_q by a simple relation

$$\alpha_q = \sqrt{\frac{6 \ln 2}{q} (D - D_q)}. \quad (11)$$

As our $1d$ intermittency results [17,18] are consistent with the prediction of the random cascading model, using Eq. (11) we have calculated the α_q values in $1d$, and have shown them in Table 2. For comparison the α_q values in $2d$ are also included in this table. Corresponding graphical plots of α_q vs. q have been shown in Fig. 11(a) and (b). Results of both $1d$ and $2d$ analysis for both types of interaction have been included in these diagrams. One can see that the fluctuation strength is slightly but consistently greater in ^{16}O induced interactions than what it is in the ^{32}S induced interactions. The $2d$ strength parameters are always more than double the $1d$ values. Whereas, the $1d$ values either remain constant within statistical errors or exhibit very weak linear variation with q , the $2d$ values for ^{16}O interaction increase with q , and for ^{32}S interaction they exhibit an initial rise followed by a saturating effect at large q (> 4).

As mentioned above, the nonlinearity of the curves in Fig. 10 arises out of the anisotropy between the distributions along η and φ directions. For a particular interaction the η range depends on the kinematic parameter(s) like the collision energy, whereas the φ range irrespective of the colliding objects and/or collision energy is always the same between 0 and 2π . It is therefore, suggested that the phase space should be so partitioned as to appropriately take this anisotropy into account [29], which is usually done by introducing a ‘roughness’ parameter called the Hurst exponent (H). In Fig. 12 the unequal partitioning of two independent variables has been schemat-

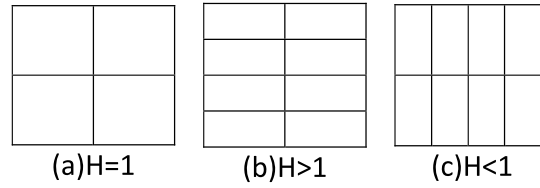


Fig. 12. Different ways of partitioning two independent phase-space directions using the Hurst exponent. (a) $H = 1$ corresponds to equal partitioning, (b) $H > 1$ corresponds say to partitioning the vertical direction finer, and (c) $H < 1$ corresponds to partitioning the horizontal direction finer.

ically represented. Only when such unequal division is made, a linear variation of $\ln\langle F_q \rangle$ over the entire range of $\ln M$, and hence a self-similar structure in the dynamical fluctuation of particles can be achieved. Otherwise the (multi)fractal structure is self-affine. Following [30] we have performed a self-affine analysis of our multiplicity fluctuation data with a continuously diminishing scale of phase-space resolution. The phase-space scale factors in different directions are related as

$$M_\eta = M_\varphi^H: 0 < H < 1, \quad \text{or} \quad M_\varphi = M_\eta^{(1/H)}: H > 1.$$

Both M_η and M_φ cannot simultaneously be integers. Any non-integer partition number M_i along the i th direction can be written as

$$M_i = N_i + f_i: i = \eta, \varphi, \tag{12}$$

where $N_i =$ an integer and $0 < f_i < 1$. Assuming that in terms of the cumulant variables X_η and X_φ both the particle distribution and its fluctuation are uniform, an averaging over any number of phase-space intervals should yield the same result. Therefore, for a non-integer partition number the smaller cell corresponding to the ‘ f th’ interval may be excluded from the summing (or averaging) process by putting it either at the beginning or at the end of the other N_i intervals. If the (X_η, X_φ) plane is considered as a unit square, then due to this exclusion particles falling within a rectangular slice of width $f_i \Delta X_i / M_i$ along the $j (\neq i)$ th side of the square are discarded. The self-affine analysis for $q = 2$ has been performed for a wide range of H values ($0.25 \leq H \leq 3.0$). In Figs. 13 and 14 our results on the self-affine analysis, respectively for the $^{16}\text{O-Ag/Br}$ and $^{32}\text{S-Ag/Br}$ data have been graphically presented for some representative values of H ($= 0.3, 0.6, 1.08, \text{ and } 2.0$). The nonlinear variation in each case is fitted with a quadratic function like

$$y = ax^2 + bx + c. \tag{13}$$

Here for each q the first two data points (corresponding to $M = M_0$ say) are omitted from the fit procedure to take care of the conservation rules [31]. Obviously $y = \ln\langle F_q(M) \rangle - \ln\langle F_q(M_0) \rangle$ and $x = \ln M - \ln M_0$. The parameter ‘ a ’ can be considered as a measure of nonlinearity in the variation. In Table 3 once again some representative values of the parameters ‘ a ’ and ‘ b ’ along with the R^2 coefficient with varying H are shown for $^{16}\text{O-Ag/Br}$ and $^{32}\text{S-Ag/Br}$ interactions. Once again the errors are only of statistical origin, and they are estimated in the same way as those associated with the $\phi_q^{(2)}$ values. One can see that, for both sets of data, as H differs from unity the variation is straightened out. A plot of the nonlinearity measure ‘ a ’ against H has been made in Fig. 15. For both types of interactions the ‘ a ’ parameter attains small values at $H = 0.3$ and maximum values at $H = 1.08$. On the other hand, for $H > 1$ the nonlinearity initially increases with increasing H , and then it starts to decrease attaining small values at $H = 2.5$ and at $H = 3.0$

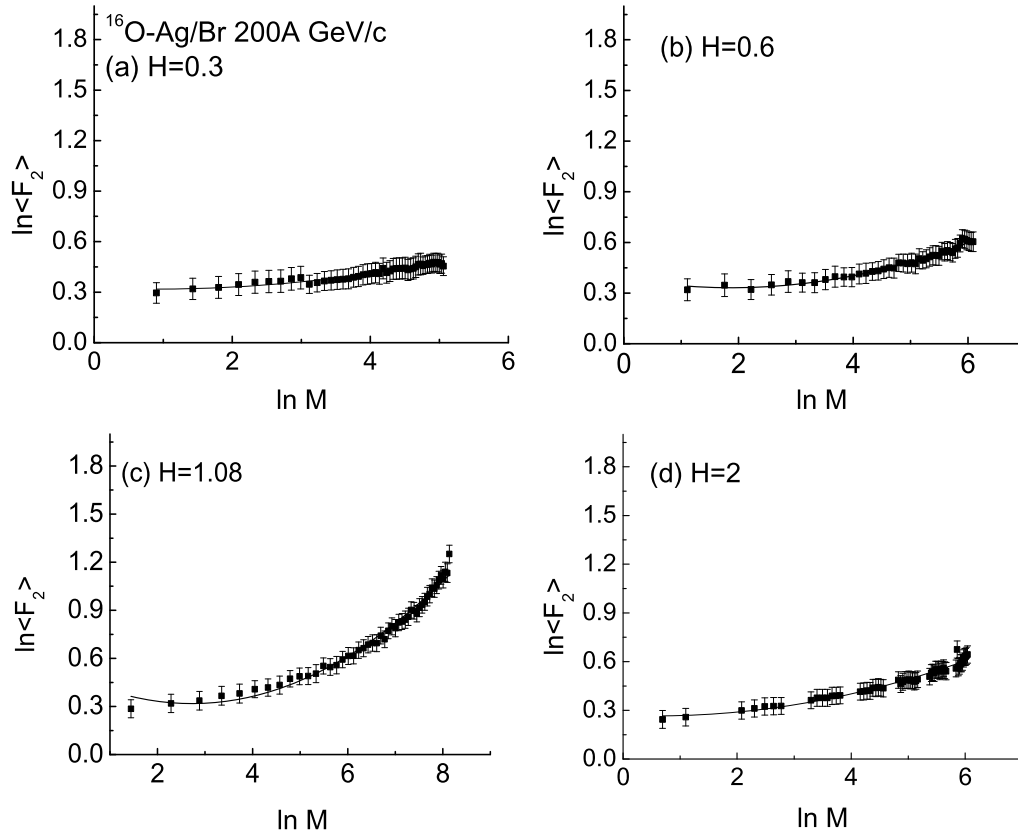


Fig. 13. Two-dimensional SFM $\ln\langle F_2 \rangle$ plotted against $\ln M$ for different Hurst parameters in ^{16}O –Ag/Br interaction at 200 A GeV/c. The solid curves represent quadratic fit to the data points.

respectively, for the ^{16}O and for the ^{32}S data. However, for $H > 1$ growing discontinuity in the variation of $\ln\langle F_2 \rangle$ with $\ln M$ could be seen with increasing H . Perhaps because the uniformity of both particle distribution and its fluctuation is too strict an assumption for a finite data sample, the method does not work equally well at all scales. Even after taking into account the correction factor suggested in [32] this problem could not be resolved for our AB data. Once, the self-similarity of dynamical fluctuation has been achieved it is now possible to estimate the effective fluctuation strength in $2d$ for any arbitrary process of particle production. A linear fit of the data as per Eq. (8) now gives the required $\phi_2^{(2)}$ values at $H = 0.3$ (which is almost linear) that is consistent with self-similarity: $\phi_2^{(2)} = 0.066 \pm 0.002$ for ^{16}O –Ag/Br and $\phi_2^{(2)} = 0.033 \pm 0.001$ for ^{32}S –Ag/Br interaction. Then following the relation [19]

$$\alpha_{\text{eff}} \approx \sqrt{2\phi_2}, \quad (14)$$

we obtain $\alpha_{\text{eff}}(\eta, \varphi) = 0.364 \pm 0.006$ for ^{16}O –Ag/Br interaction and $\alpha_{\text{eff}}(\eta, \varphi) = 0.257 \pm 0.006$ for ^{32}S –Ag/Br interaction. Note that the corresponding $1d$ values are, respectively, $\alpha_{\text{eff}}(\eta) = 0.240 \pm 0.005$ and $\alpha_{\text{eff}}(\varphi) = 0.258 \pm 0.0008$ for ^{16}O and $\alpha_{\text{eff}}(\eta) = 0.161 \pm 0.019$ and $\alpha_{\text{eff}}(\varphi) = 0.167 \pm 0.004$ for ^{32}S .

5. Discussion

In this paper we have presented an investigation on the ring and jet-like azimuthal angle substructures in the emission of secondary charged hadrons coming out of ^{16}O –Ag/Br and ^{32}S –Ag/Br interactions at 200 A GeV/c. To be more specific, presence of such substructures, their av-

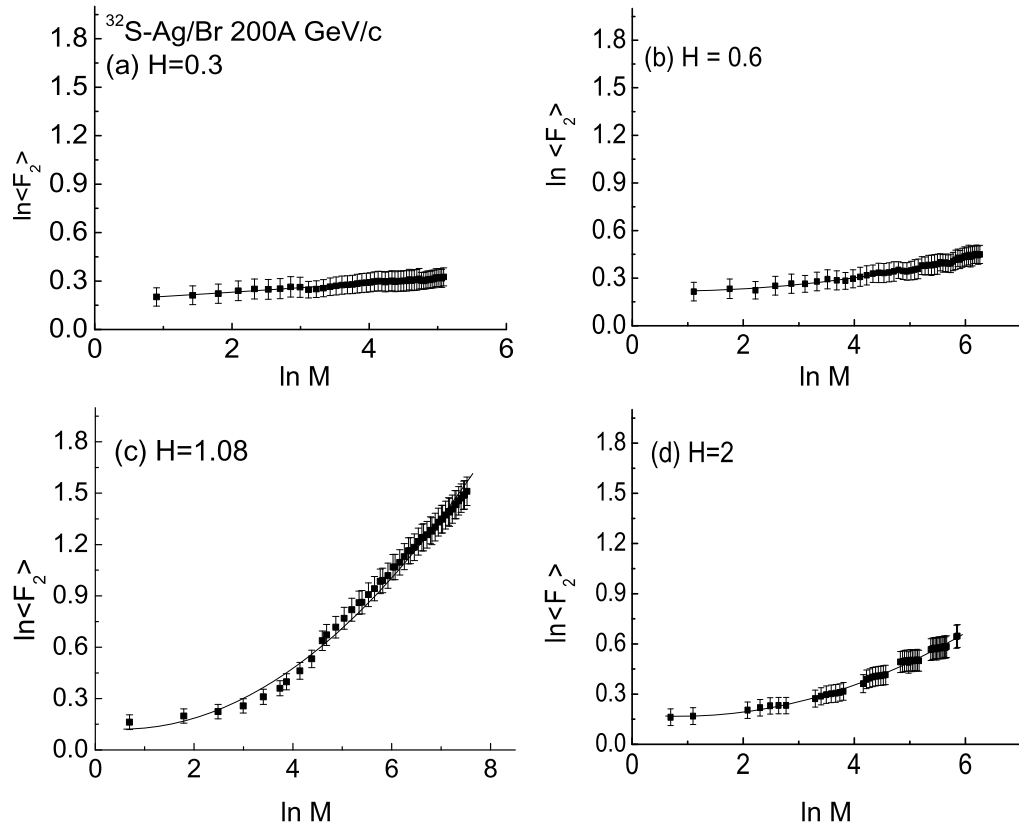


Fig. 14. Two-dimensional SFM $\ln\langle F_2 \rangle$ plotted against $\ln M$ for different Hurst parameters in ^{32}O –Ag/Br interaction at 200 A GeV/c. The solid curves represent quadratic fit to the data points.

erage behaviour, their size, and their position of occurrence have been examined. The analysis indicates presence of ring and jet-like structures in the experimental distributions of particles, that subsequently led us to perform a self-affine $2d$ intermittency analysis for the same sets of data on AB interaction. Major inferences from our analysis can be summarized in the following way.

- (i) The average behaviour of the S parameters exhibits presence of ring and jet-like structures in both types of interactions that are limited in narrow regions of η and φ . Small but significant experimental departure from independent emission particularly at small $\delta\eta$ suggests that short range correlations are present. In this regard our observation matches with another similar experiment using nuclear emulsion technique [9]. A closer look at the distributions of structure size ($\Delta\eta$) and its position (η_m) indicates that, features pertaining to both ring-like and jet-like structures are present in our data that cannot be fully reproduced by a simple random number generated independent emission model. The effects however, are always not too strong in either type of interaction concerned. Within the framework of Cherenkov gluon emission model [3] we can therefore, conclude that in some events there are only a few emitted gluons, whereas in some other their numbers are large. It is our future objective to confine the analysis to a particular centrality range and examine how these effects depend on geometry. It would be a worthwhile exercise to find out either the nuclear refractive index or the speed of sound wave in nuclear matter from the cone angle, each of which can further be utilized to find out a proper nuclear equation of state.

Table 3

Values of the fit parameters of $\ln\langle F_2 \rangle$ against $\ln M$ variation in terms of the quadratic function of Eq. (13). The errors shown within brackets are of statistical origin.

Interaction	Hurst exp. (H)	a	b	R^2
^{16}O –Ag/Br 200 A GeV/ c	0.25	0.0095(0.0029)	–0.0169(0.019)	0.998
	0.3	0.00946(0.0020)	–0.0165(0.015)	0.998
	0.35	0.0108(0.0019)	–0.0254(0.014)	0.995
	0.4	0.0137(0.0016)	–0.0448(0.0123)	0.939
	0.6	0.0154(0.0011)	–0.0566(0.0092)	0.978
	0.8	0.0205(0.0019)	–0.0905(0.0171)	0.963
	1.0	0.023(0.0018)	–0.105(0.0192)	0.995
	1.08	0.027(0.002)	–0.149(0.017)	0.967
	1.1	0.0261(0.0037)	–0.143(0.0305)	0.986
	1.2	0.0236(0.0029)	–0.118(0.0305)	0.985
	1.4	0.0219(0.0034)	–0.102(0.0326)	0.982
	1.6	0.0199(0.0038)	–0.0885(0.0351)	0.975
	1.8	0.0180(0.0042)	–0.075(0.036)	0.970
	2.0	0.0115(0.0012)	–0.0128(0.037)	0.961
	2.5	0.0102(0.0013)	0.0055(0.0098)	0.997
3.0	0.0101(0.0015)	–0.0058(0.0103)	0.924	
^{32}S –Ag/Br 200 A GeV/ c	0.25	0.0027(0.0009)	0.0114(0.0065)	0.995
	0.3	0.0005(0.0007)	0.0248(0.0048)	0.995
	0.35	0.0049(0.0007)	0.0015(0.0052)	0.998
	0.4	0.0029(0.0009)	0.0145(0.0071)	0.947
	0.6	0.0072(0.0006)	–0.0088(0.0049)	0.988
	0.8	0.0099(0.0006)	–0.0251(0.0060)	0.990
	1.0	0.0120(0.0006)	–0.0343(0.0070)	0.995
	1.08	0.025(0.0007)	0.0081(0.0165)	0.987
	1.1	0.0249(0.0017)	0.0052(0.0161)	0.991
	1.2	0.0245(0.0015)	–0.0056(0.0142)	0.992
	1.4	0.0241(0.0012)	–0.0266(0.0106)	0.994
	1.6	0.0227(0.0010)	–0.0339(0.0082)	0.995
	1.8	0.0209(0.0009)	–0.0355(0.0071)	0.994
	2.0	0.0186(0.0009)	–0.0306(0.0068)	0.994
	2.5	0.0117(0.0009)	–0.0076(0.0063)	0.997
3.0	0.0092(0.0011)	–0.0037(0.0073)	0.997	

- (ii) The $2d$ intermittency analysis of both ^{16}O and ^{32}S induced interactions suggests that the underlying fractal structure of the dynamical fluctuations is not self-similar at all scales, rather it is self-affine. The self-similarity could be retrieved only when the anisotropy issue (in the η – φ plane) is properly addressed with the help of the Hurst exponent. Unlike the observation of [31] we however, could not make any definite conclusion regarding as to which direction (i.e., η or φ) has to be partitioned finer to achieve self-similarity. In the $H < 1$ region our data behave in a more systematic and consistent manner, and for both data sets we have taken $H = 0.3$ as the point close to exact self-similarity. The fluctuation strength in $2d$ is significantly greater than that in $1d$, and the same is always greater for the ^{16}O –Ag/Br interaction than that in the ^{32}S –Ag/Br interaction. This indicates a dominance of the jet-like over the ring-like structures in both sets of our data. In the α -model the allowed range of α is $[0, 1]$. Hence we observe that for the ^{16}O case the intermittency strengths are about one third and one fourth of its maximum possible value, respectively, in $2d$ and

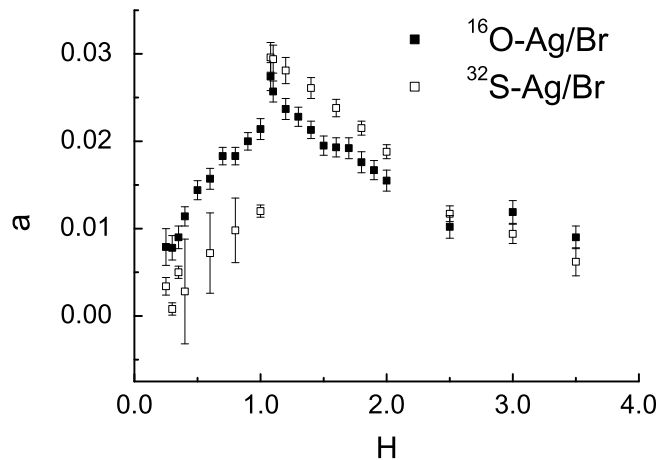


Fig. 15. The nonlinearity parameter ' a ' plotted against the Hurst parameter H for both types of interactions.

$1d$, whereas those for the ^{32}S data are, respectively, about one fourth and one sixth of the maximum strength.

Though some interesting observations could be made from our analysis of a set of data on ^{16}O -Ag/Br and ^{32}S -Ag/Br interactions at $200 A \text{ GeV}/c$, we feel that a more detailed analysis is necessary with other choices of n_d values and making appropriate n_s cut. It would also be a worthwhile exercise to compare our results with model predictions that takes into account collective phenomena like those prescribed in [3,4,7]. Recently, the wavelet technique [33] has been employed for fluctuation study of particle production, which is at present undergoing for our data.

Acknowledgements

P.K.H. and S.K.M. are grateful to the Department of Science and Technology, Govt. of India, for financial assistance through the SERC Fast Track scheme for young scientists (project No. SR/FTP/-21/2008). They also thank the IUCAA Reference Center of the North Bengal University (NBU) for offering local hospitality during their stay at NBU when a significant part of this work has been done.

References

- [1] E. Shuryak, Phys. Rep. 61 (1979) 71;
K. Yagi, T. Hatsuda, Y. Make, Quark–Gluon Plasma, Cambridge University Press, New York, 2005.
- [2] L. Van Hove, Z. Phys. C 21 (1984) 93;
E. Stenlund, et al., Nucl. Phys. A 498 (1989) 541c.
- [3] I.M. Dremin, Pis'ma Zh. Eksp. Teor. Fiz. 30 (1979) 152.
- [4] A.E. Glassgold, W. Heckrotte, K.M. Watson, Ann. Phys. 6 (1959) 1.
- [5] I.M. Dremin, Yad. Fiz. 33 (1981) 1357.
- [6] I.M. Dremin, Pis'ma Zh. Eksp. Teor. Fiz. 34 (1981) 594.
- [7] I.M. Dremin, Nucl. Phys. A 467 (2006) 233, arXiv:hep-ph/0507167v5.
- [8] A.B. Apanasenko, N.A. Dobrotin, I.M. Dremin, K.A. Kotel'nikov, Pis'ma Zh. Eksp. Teor. Fiz. 30 (1979) 157.
- [9] M.I. Adamovich, et al., EMU01 Collaboration, J. Phys. G 19 (1993) 2035.
- [10] A. El-Naghy, K.S. Abdel-Khalek, Phys. Lett. B 299 (1993) 370.
- [11] G.L. Gogiberidge, E.L. Sarkisyan, L.K. Gelovani, Nucl. Phys. B (Proc. Suppl.) 92 (2001) 75;
G.L. Gogiberidge, E.L. Sarkisyan, L.K. Gelovani, Phys. Atom. Nucl. 64 (2006) 143.

- [12] S. Vokál, A. Vokálová, A. Kravčáková, S. Lehocká, G.I. Orlova, Phys. Atom. Nucl. 71 (2008) 1395, arXiv:hep-ex/0412017v2;
S. Vokál, G.I. Orlova, S. Lehocká, Phys. Atom. Nucl. 72 (2009) 237, arXiv:hep-ex/0501025v1.
- [13] A. Bialas, R. Peschanski, Nucl. Phys. B 273 (1986) 703;
A. Bialas, R. Peschanski, Nucl. Phys. B 308 (1988) 857.
- [14] W. Kittel, E.A. De Wolf, Soft Multihadron Dynamics, World Scientific, Singapore, 2005;
E.A. De Wolf, I.M. Dremin, W. Kittel, Phys. Rep. 270 (1996) 1.
- [15] W. Ochs, Phys. Lett. B 247 (1990) 101;
W. Ochs, Z. Phys. C 50 (1991) 339.
- [16] L. Van Hove, Phys. Lett. B 28 (1969) 429.
- [17] M.K. Ghosh, P.K. Haldar, S.K. Manna, A. Mukhopadhyay, G. Singh, Can. J. Phys. 88 (2010) 575.
- [18] M.K. Ghosh, A. Mukhopadhyay, G. Singh, J. Phys. G 34 (2007) 177.
- [19] L. Lianshou, F. Jinghua, W. Yuanfang, Phys. Lett. B 444 (1998) 563, arXiv:hep-ph/9812291v1.
- [20] C.F. Powell, P.H. Fowler, D.H. Perkins, The Study of Elementary Particles by Photographic Method, Pergamon, Oxford, UK, 1959;
W.H. Barakas, Nuclear Research Emulsions, vols. I and II, Academic Press, New York, USA, 1963.
- [21] W.H. Press, S.A. Teukolsky, W.T. Vetterling, B.P. Flannery, Numerical Recipes in FORTRAN 90, Cambridge University Press, New York, 2002.
- [22] A. Bialas, M. Gazdzicki, Phys. Lett. B 252 (1990) 483.
- [23] P.R. Bevington, D.K. Robinson, Data Reduction and Error Analysis for the Physical Sciences, McGraw–Hill, New York, 2003.
- [24] M.I. Adamovich, et al., EMU01 Collaboration, Nucl. Phys. B 388 (1992) 3.
- [25] Ph. Brax, R. Peschanski, Phys. Lett. B 253 (1991) 225;
I. Sarcevic, H. Satz, Phys. Lett. B 233 (1989) 251.
- [26] A. Bialas, K. Zalewski, Phys. Lett. B 238 (1990) 413;
R. Peschanski, Int. J. Mod. Phys. A 6 (1991) 3681;
E.K. Sarkisyan, L.K. Gelovani, G.L. Gogiberidge, G.G. Taran, Phys. Lett. B 347 (1995) 439.
- [27] H. Satz, Nucl. Phys. B 326 (1989) 613.
- [28] R.C. Hwa, M.T. Nazirov, Phys. Rev. Lett. 69 (1992) 741.
- [29] W. Yuanfang, L. Lianshou, Phys. Rev. Lett. 70 (1993) 3197.
- [30] L. Lianshou, Y. Zhang, W. Yuanfang, Z. Phys. C 69 (1996) 323.
- [31] M.I. Adamovich, et al., EMU01 Collaboration, Z. Phys. C 76 (1997) 659.
- [32] C. Gang, L. Lianshou, G. Yanmin, Int. J. Mod. Phys. A 14 (1999) 3687.
- [33] V.V. Uzhinskii, V.Sh. Navotny, G.O. Ososkov, A. Polanski, M.M. Chernyavski, arXiv:hep-ex/0206003v1, 2002.